Perfusion and Diffusion Magnetic Resonance Imaging Studies of Cerebral Ischaemia

Submitted for the Degree of Doctor of Philosophy

Gaby S. Pell

Department of Medical Physics and Bioengineering,
University College London, London, UK

Department of Medical Physics & Bioengineering
University College London
1st Floor Shropshire House
11-20 Capper Street
London WC1E 6JA
United Kingdom

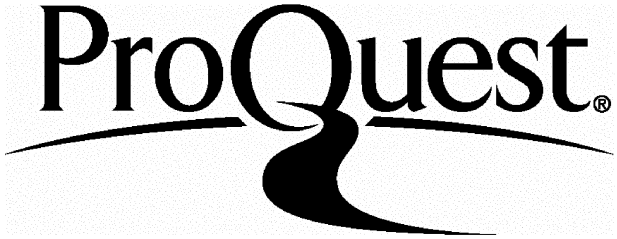

ABSTRACT

Magnetic resonance imaging (MRI) has opened up new avenues of anatomical and physiological research. Its non-invasive nature and the ability to obtain images with a high degree of spatial resolution, have been exploited in this research as well as in routine clinical investigations. However, the use of standard MRI techniques in the investigation of the acute phases of cerebrovascular diseases such as stroke, has been hampered by impaired sensitivity to detect areas of ischaemic damage. The relatively recent development of the MRI techniques of diffusion and perfusion imaging, described in this thesis, have the capability to fill this gap. The diffusive mobility of water is a sensitive indicator of tissue energy status, and perfusion imaging provides quantitative measurements of cerebral blood flow (CBF). This thesis describes the implementation of these two techniques in experimental studies of cerebral ischaemia. Special emphasis is placed upon the improvement of the temporal resolution of these methods in order that time course studies of the rapidly evolving pathophysiology can be carried out. In particular, an innovative modification of the spin-labelling perfusion technique of flow-sensitive alternating inversion recovery (FAIR), has been developed that allows rapid, mapping of CBF. This method was implemented in an important study of reperfusion injury. High time-resolution sequences for rapid, quantitative diffusion imaging were implemented on both high-field and low-field MRI systems. The high-field environment sensitises the images to various artefacts and a novel enhancement of a standard rapid imaging technique was required in order to obtain accurate measurements. On the low-field system, fast imaging of the trace of the diffusion tensor (trace(D)) was optimised and employed during a study of repeated ischaemic episodes that is a model of transient ischaemic attacks. The combination of these two MRI techniques has provided unique insights into experimental cerebral ischaemia.

DEDICATED TO THE MEMORY

OF MY BROTHER

DANIEL

(1956-1977)

Rabbi Tarphon said,

The day is short and the work is great...

It is not your duty to complete the work,

but neither are you free to desist from it.

Ethics of our Fathers 2:20-21

ACKNOWLEDGEMENTS

The PhD scheme in which I participated was EPSRC's Postgraduate Training Partnership and I am grateful to Sira Ltd for their support. No project of this nature could be accomplished without the help of others. I would especially like to thank David Thomas, Fernando Calamante and Mark Lythgoe for their assistance and friendship. I would also like to express my gratitude to Albert Busza, Matthew Clemence, Sally Dowsett, Jayne Gouge, Neil Harris, John Houseman, Alistair Howseman, Martin King, Mark Landeryou, Quyen Nguyen, Shonit Punwani, John Thornton and Steve Williams for their help in these projects. Thanks are owing to Uri Berkowitz for his advice on design matters, and Ted Proctor deserves special thanks for his enthusiastic support during the last few months of the PhD. I have greatly appreciated the guidance of my supervisor Roger Ordidge and his patient and good humoured direction was much valued. I am very grateful to David Gadian for his help and for allowing me to become part of his department at the Institute of Child Health, and I have also appreciated the assistance of my second supervisor, Robert Turner.

Last but not least, in true Hollywood style, the ultimate thanks must go to my parents and family for putting up with me, especially during the years spent trying to achieve the completion of this tome.

***Supervisors*:**

Professor Roger J. Ordidge, Department of Medical Physics and Bioengineering, University College London, London

Professor Robert Turner, Wellcome Department of Cognitive Neurology, Institute of Neurology, University College London, London

'The first ten million years were the worst', said Marvin, 'and the second ten million years, they were the worst too. The third ten million years, I didn't enjoy at all. After that I went into a bit of a decline.'

Douglas Adams, The Restaurant at the End of the Universe, 1980

Table of Contents

Table of Figures

Table of Tables

INTRODUCTION

Magnetic resonance imaging (MRI) is a technique that has been in common use for only a relatively short period of time in comparison with other scanning methodologies. Nevertheless, it has made an enormous impact on medical research and clinical practice especially for conditions such as stroke. The first human body images were published in 1977 (Damadian, 1977). Since that time, more than 10,000 MRI scanners have been built for use in hospitals and laboratories around the world. The technique is based on the magnetic property of the nuclei that make up matter. The distribution of positive charge in every nucleus is spinning on a diametric axis. As Faraday discovered over 150 years ago, this rotating charged body will produce a magnetic field. In fact the speed of rotation is closely related to the magnetic environment of the nucleus. The distribution of contributing spins can then be mapped by applying a magnetic field gradient that will tag each spin with a magnetic signature – the phase or the rotational frequency - that depends purely on its spatial position within the magnetic field. Moreover, the magnetic spinning state of the nucleus ascribes to each atom a magnetic *memory* that is dependent on the intrinsic state of the atom and its environment. This property of magnetic memory manifests itself in a number of time constants - measurable parameters - that can be recalled as the ensemble system is disturbed from its state of equilibrium. It is these memory time constants that can be manipulated to provide the contrast mechanisms that enable different tissue types to be distinguished – whether it be delineating grey and white matter or attempting to look for necrotic tissue. The technique of MRI re-forms both the spatial and contrast information into an image.

The central nervous system requires a regulated, constant supply of blood in order to function. Neurones are particularly sensitive to any imbalance between the supply and the demand of the vascular system. The blood perfuses the tissue of the central nervous system (CNS), thereby delivering oxygen and nutrients and removing the toxic waste products. In order to meet the tissue demand for this vascular supply under extreme conditions, a complex and sensitive autoregulatory system exists maintained by the peripheral nervous system. However, if this system fails and the flow of blood is disrupted, the outcome can be severe. The condition, manifested as a stroke, has defied considerable efforts to find an effective treatment and attempts to achieve this aim are ongoing.

The interference in blood flow causing a stroke may be due a variety of events (embolus, haemorrhage or thrombosis). The common outcome is that of cerebral ischaemia (deficient blood supply to the brain and the consequent impairment in the availability of oxygen and glucose). It has long been thought that a stroke causes immediate and irreversible damage and that it is, therefore, unlikely that any therapeutic strategy in the acute stage of the condition will prove to be effective. Indeed, the etymological source of the term itself derives from the pessimistically described "stroke of God's Hand" that became associated with the condition of apoplexy towards the end of the 16th Century. A number of promising drug treatments derived from research using experimental animal models of stroke, have been ineffectual when applied to the clinical setting. However, in 1996, the first successful, clinical trial of a therapeutic intervention for the treatment of acute stroke was reported (The National Institute of Neurological Disorders and Stroke rt-PA Stroke Study Group, 1996). The thrombolytic agent, recombinant tissue plasminogen activator (rt-PA), was found to improve outcome if applied within 3 hours of the onset of stroke. The investigation of this treatment had been accompanied by rigorous studies of thrombolysis performed using experimental models of cerebral and myocardial ischaemia. A more complete understanding of the pathogenesis of stroke remains the foundation of the development of such therapeutic strategies. The highly controllable and reproducible animal models of stroke are the optimal means to gain this information. The use of MRI in such investigations is attractive due to its inherent characteristics of non-invasiveness, sensitivity to a variety of contrast mechanisms, and its high temporal and spatial resolution. Longitudinal investigation of brain metabolism, function and physiology thereby becomes feasible.

The techniques of diffusion and perfusion MR imaging that are discussed in this thesis, have the potential of providing important information concerning the mechanisms of cerebral vascular diseases (CVDs). Diffusion images are sensitive to the translational motion of water protons that can be affected by changes in ionic homeostasis due to impairments in blood flow. The level of cerebral perfusion is an important indicator of tissue viability and function, and perfusion imaging attempts to directly quantify regional blood flow in the brain. The work in this thesis was undertaken in order to investigate the implementation of diffusion and perfusion MR imaging in the study of experimental cerebral ischaemia. The ischaemic insult triggers a wide variety of pathophysiological and biochemical processes that augment and evolve in a complex fashion and these MRI methods offer the opportunity to gain an insight into certain

crucial aspects of this complicated system. In order to achieve this aim, the underlying theory of these imaging techniques had to be investigated and the MRI pulse sequences required further development and optimisation.

The principal sections of the thesis are arranged in the following manner:

Chapter 1: The theory behind MRI is introduced and discussed with special regard to techniques that are later applied in this work such as magnetisation transfer contrast.

Chapter 2: The concepts of diffusion and perfusion are introduced and placed in the clinical settings of stroke and the cerebral circulation. Pathomechanisms of blood flow in the brain such as ischaemia are considered. Current methods of blood flow measurement are described.

Chapter 3: The implementation of MRI methods of arterial spin labelling for perfusion imaging is described. Techniques such as FAIR and continuous spin labelling are introduced and attendant issues regarding accurate quantification are discussed. Theoretical work relating to optimisation of RF pulses used in FAIR perfusion imaging is discussed with special regard to the development of an optimal adiabatic inversion pulses. An experimental study was performed in order to demonstrate the potential benefits of using these optimised RF pulses. A preliminary validation study for FAIR using the technique of hydrogen clearance is discussed. The implementation of the continuous labelling technique during a multi-parametric MRI study of an animal focal stroke model is described.

Chapter 4: A novel modification of the FAIR technique is described that allows high time course resolution perfusion mapping without compromising the quantitative accuracy. A theoretical analysis is followed by experimental validation.

Chapter 5: The chapter commences with a description of the ischaemic cascade and excitotoxicity. The modified FAIR technique is applied to an important study of the recirculation in the brain after a period of ischaemia in a gerbil model. Previous studies of the resulting reperfusion injury have been achieved using a variety of other blood flow measurement techniques. The advantages of the non-invasive MRI technique are demonstrated.

Chapter 6: The implementation of rapid, quantitative diffusion imaging on two MRI systems is described. In both cases, system-specific challenges had to be surmounted.

In particular, a novel modification of a standard TurboFLASH sequence was required in order to obtain quantitative maps of the diffusion coefficient. On the other system, the rapidly repeated collection of a rotationally invariant measure of the diffusion coefficient (the trace(D)) was optimised for improved accuracy of the measurement.

Chapter 7: The application of the rapid trace(D) sequence to an important animal study of repeated ischaemic events is described. The implications of the results of the investigation are discussed in relation to previous studies of the cumulative, deleterious effects of repeated ischaemia.

Chapter 8: Conclusions and discussion of further work

Appendices A-C: Additional information relating to Chapters 4 and 7 is provided in Appendices A and B respectively. Appendix C describes an MRI study of the absorptive mechanisms of water in superabsorbent polymers and wood-based fluff-pulp. The materials form the absorption layer in incontinence pads and a time course study of water movement in these pads is presented.

I INTRODUCTION TO NUCLEAR MAGNETIC RESONANCE

This chapter introduces the basic theory behind nuclear magnetic resonance (NMR), otherwise known as MRI, and explains the process of image acquisition. Pulse sequences can be used to sensitise the acquired image to various NMR biophysical parameters. Several basic sequences are briefly described and the concept of diffusion imaging is explained in greater detail.

1.1 Historical background

The phenomenon of nuclear spin was proposed by Wolfgang Pauli in 1924 (Pauli, 1924). The concept of NMR was first mentioned in the literature more than 50 years ago. In 1946, two research groups independently described an attribute of the magnetic properties of certain nuclei. They found that when these nuclei were placed in a magnetic field, they absorbed and emitted energy at radio frequency (RF) frequencies. The two principal scientists, Felix Bloch (Bloch, 1946) at Stanford and Edward Purcell (Purcell, 1946) at Harvard, were jointly awarded the Nobel Prize in 1952.

1.2 Nuclear Spin

The physical phenomenon that forms the basis of magnetic resonance imaging is nuclear magnetic resonance (NMR). NMR in turn is a result of the interaction of a spinning nucleus with a magnetic field. The property of nuclear spin is quantised and characterised by the nuclear spin quantum number, I. This quantum number can take either half-integer or integer values and it defines the total nuclear angular momentum, P, in the following manner

$$P = \sqrt{I(I+1)}\,\frac{h}{2\pi} \qquad [1.1]$$

A nucleus has spin because each of its fundamental components, the proton and the neutron, possess this property. The concept of nuclear spin is equivalent to that of electron spin. An electron spin is characterised by the spin quantum number, s = ½, and, therefore, the electron can exist in two spin states; spin up and spin down. The phenomenon of electron spin resonance (ESR) is a result of electrons flipping between these states. Nuclear magnetic resonance is a result of a comparable phenomenon. The simplest nucleus, hydrogen, consists of a single proton, has a spin quantum number I = ½, and, therefore,

similarly exists in two equivalent nuclear spin states, also denoted spin up and spin down. These spin states reflect the quantised nature of the angular momentum that the body can possess. The energy of these states are degenerate and, therefore, there is no observable difference between them. However, in the presence of a magnetic field, each spin state is characterised by a unique energy. The proton can flip between these two energy states by emission and absorption of quantised units of energy. Since the energy of absorption is equal to the energy of emission and the proton flips occur at certain quantised energies, this is a resonance phenomenon.

A spinning, positively charged nucleus gives rise to a magnetic dipole moment μ in the same way that an electric current circulating in a loop produces a magnetic field. The vector of the magnetic moment lies in a direction either parallel or anti-parallel to the angular momentum and the two quantities are related to each other by the relationship

$$\mu = \gamma P \qquad [1.2]$$

where γ is the gyromagnetic ratio, which is a constant for a particular nucleus.

If a nucleus with non-zero spin is placed within an external magnetic field B_0, it will tend to align itself with this field. However, due to the combination of the angular momentum and the magnetic moment, the nucleus can only precess around the direction of the external magnetic field. The angular frequency of the precession ω_0 known as the Larmor frequency, is related to the magnitude of the external magnetic field B_0, by the relationship

$$\omega = -\gamma B_0 \qquad [1.3]$$

This Larmor equation is fundamental to nuclear magnetic resonance.

The magnetic moment of a nucleus in the presence of a magnetic field B_0 determines the energy according to the following equation

$$E = -\mu B_0 \qquad [1.4]$$

Therefore, the energy of each individual spin is quantised in the same way as the magnetic moment. In an ensemble of nuclear spins, the energy states will be unequally populated. For the hydrogen proton, the most common naturally occurring nucleus in the body, the spins will distribute themselves amongst the two spin states ($I = ½$) until a

state of thermal equilibrium with the lattice - the molecular framework - is reached in which the spin down state is more populated than the spin up state. The resulting distribution known as the Boltzmann distribution, takes the following form

$$n\uparrow = n\downarrow \exp\left(-\frac{kT}{\Delta E}\right) \qquad [1.5]$$

where $n\uparrow$ and $n\downarrow$ are the number of spins in the spin up and spin down state respectively, k is the Boltzmann constant and T is the absolute temperature of the sample. The population differences between the two spin states for protons at the typical magnetic field strengths used in MRI are relatively small and this is responsible for the poor inherent sensitivity of NMR. The standard unit of magnetic field strength is the tesla (T) (also the gauss (G) where 1 T = 10^4 G). The earth's magnetic field is approximately 0.05 mT, which can be contrasted with the field strengths, 2.35T and 8.5T, of the MRI systems used in the work presented in this thesis. For a sample that comprises many nuclei, the population difference results in an equilibrium bulk magnetisation, M_0. With the use of vectors this bulk magnetisation, **M** [1], can be visualised in the manner shown in Fig. 1.1.

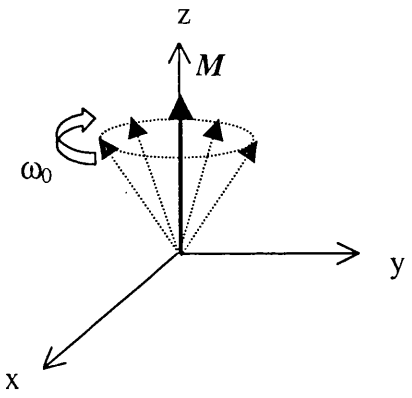

Fig. 1.1 The vector representation of the magnetisation. The bulk magnetisation **M** vector is the resultant vector of an ensemble of precessing spins. In the laboratory frame, these spins interact with the magnetic flux density B_0 that lies along the z-axis. The magnetic moment thereby experiences a torque which results in precession with angular velocity ω_0 about B_0.

[1] Vectors are displayed in bold script.

Under conditions of thermal equilibrium, the net magnetisation **M** is aligned with the direction of the static magnetic field, B_0 and no signal can be detected. If **M** can be tipped away from this position, B_0 will exert a torque on **M**, and a component M_{xy} in the xy-plane will be produced. This results in a precession of **M** around B_0 that will induce an oscillating current in a coil placed perpendicular to the direction of B_0. This is the principle of Pulsed or Fourier transform NMR that forms the basis of conventional MRI. In practice, the displacement of the magnetisation from the equilibrium position is achieved by the application of a magnetic field, B_1 that is rotating at an angular frequency ω_1 in a direction perpendicular to B_0. This results in a torque on **M**, which tend to rotate the magnetisation into the xy-plane. This displacement of **M** from its equilibrium position depends crucially on the magnitude and rotational frequency of the B_1 field.

1.3 The Bloch Equations

In 1946, Felix Bloch *et al.* (Bloch, 1946) proposed a series of equations that describe the magnetic field properties of an ensemble of nuclei in external magnetic fields. These phenomenologically derived equations have proved successful in describing the behaviour of minimally interacting spins such as exist in liquid samples. A heuristic argument for the derivation of these equations is presented here.

1.3.1 Equation of motion

In an arbitrary, homogenous magnetic field **B**, the equation of motion of the bulk magnetisation **M** is as described in Section 1.4 and is given by

$$\frac{dM}{dt} = \gamma \mathbf{M} \times \mathbf{B} \qquad [1.6]$$

The field can be fixed (B_0) or oscillating (B_1). Eq. [1.6] can be expanded in terms of the individual components in the x, y and z directions

$$\frac{dM_x}{dt} = \gamma(M_y B_z - M_z B_y) \qquad \text{(a)}$$

$$\frac{dM_y}{dt} = \gamma(- M_x B_z + M_z B_x) \qquad \text{(b)}$$

$$\frac{dM_z}{dt} = \gamma(M_x B_y - M_y B_x) \qquad \text{(c)}$$

[1.7]

1.3.2 Equations in the presence of relaxation effects

In a static field, the relaxation of the magnetisation towards its equilibrium value M_0 can be described by

$$\frac{dM_z}{dt} = - \frac{(M_z - M_0)}{T_1}$$

[1.8]

where T_1 is the longitudinal relaxation time (see Section 1.6). If the magnetisation is given a component at right-angles to **B** as a result of a stimulus such as a pulse of RF (radio frequency) irradiation, this transverse magnetisation will decay with a rate of change that can be represented in the following manner

$$\frac{dM_x}{dt} = - \frac{M_x}{T_2} \qquad (a)$$

$$\frac{dM_y}{dt} = - \frac{M_y}{T_2} \qquad (b)$$

[1.9]

where T_2 is the spin-spin relaxation time and the motion terms described in Eq. [1.7] are ignored. Bloch in deriving these equations, then proposed that in the presence of an applied field and a much smaller RF B_1 field, the motion due to relaxation can be superimposed on the motion of the spins. The equations then become

$$\frac{dM_x}{dt} = \gamma(M_y B_z - M_z B_y) - \frac{M_x}{T_2} \qquad \text{(a)}$$

$$\frac{dM_y}{dt} = \gamma(- M_x B_z + M_z B_x) - \frac{M_y}{T_2} \qquad \text{(b)}$$

$$\frac{dM_z}{dt} = \gamma(M_x B_y - M_y B_x) - \frac{(M_z - M_0)}{T_1} \qquad \text{(c)}$$

[1.10]

or the general result

$$\frac{d\mathbf{M}}{dt} = (\gamma \mathbf{M} \times \mathbf{B}) - \frac{(M_x + M_y)}{T_2} - \frac{(M_z - M_0)}{T_1}$$

[1.11]

1.3.3 Rotating reference frame – a simplification of the Bloch equations

The behaviour of **M** in the presence of static and oscillating magnetic fields can often be simplified by defining a co-ordinate system (x´, y´, z´), which rotates about B_0 at the same rate as B_1. In this frame of reference, B_1 is fixed along the x´ axis, and in the absence of B_1, **M** will remain stationary and aligned along the z-axis.

The effective magnetic field, $\mathbf{B}_{eff}$, acting on the magnetisation **M** in the rotating frame is therefore

$$\boldsymbol{B}_{eff} = (B_0 - \frac{\omega_i}{\gamma}) \hat{\mathbf{z}}' + B_1 \hat{\mathbf{x}}'$$

[1.12]

where the unit vectors are indicated in the z' and x' directions and ω_i is the oscillating frequency of the applied RF field (which is normally equal to or offset from ω_0). The effective magnetic field and its components are depicted in Fig. 1.2.

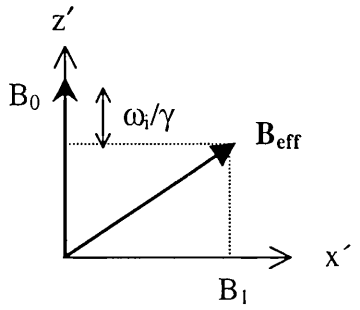

Fig. 1.2 The effective magnetic field, $\mathbf{B}_{eff}$, and its components in the vector representation.

If B_1 is applied at exactly the Larmor frequency ω_0, it can be seen from Eq. [1.12] that B_{eff} will equal B_1. Therefore, the magnetisation precesses around B_1. This has the effect of rotating **M** around the direction of B_1 (the x′ direction) with frequency ω_1 where

$$\omega_1 = -\gamma B_1 \qquad [1.13]$$

The B_1 field is typically considerably smaller than the static magnetic field, B_0 (B_1 is usually in the order of mT whereas a typical system field strength is 1-4T). The frequency of precession around this field in the rotating frame is therefore orders of magnitude smaller than the precessional frequency around B_0 (typically approximately 100 Hz compared to 100 MHz). If B_1 is removed after a period T_p, the angle α known as the flip angle, through which the magnetisation is rotated or nutated from the z-axis is defined by the relationship

$$\alpha = \gamma B_1 T_p \qquad [1.14]$$

Therefore, a 90° pulse ($\alpha = \pi/2$, so also known as a $\pi/2$ pulse) brings **M** totally into the (x′, y′) plane whereas a 180° (π) pulse inverts the magnetisation vector and leaves it antiparallel to its equilibrium position M_0.

1.4 Adiabatic pulses

Adiabatic pulses are a special category of RF pulses that are not affected by the possible inhomogeneities in the B_1 field that can otherwise have a deleterious effect on the image quality. Application of a time varying RF pulse results in the rotation of the

magnetisation vector through the angle α defined by Eq. [1.14]. Inhomogeneities in the B_1 field will, therefore, lead to a non-uniformity in the resulting magnetisation that will complicate interpretation of the image. Adiabatic pulses are relatively insensitive to the B_1 field. If the movement of the effective magnetic field, $\mathbf{B}_{eff}$, away from the initial equilibrium position of alignment with B_0, is slow enough in relation to the rate of change of the B_1 field, the magnetisation vector can follow the $\mathbf{B}_{eff}$ as the RF frequency is swept from one side of resonance to the other. This state is analogous to the adiabatic compression or expansion of a system in thermodynamics, which will cause no overall energy change if carried out in a slow enough manner. Across the spectral bandwidth of interest, spins with different precessional frequencies are sequentially rotated as the frequency of the sweeping B_1 field approaches the resonant frequency of the different spins. Rotation of the magnetisation vector into the xy-plane (adiabatic half passage) or full inversion (adiabatic full passage) can be achieved even when the B_1 field is extremely inhomogeneous. The adiabatic condition spells out the relationship between the changing B_1 field and the sweeping direction of the B_{eff} that defines the limits of adiabatic behaviour. This conditions can be shown to be defined in the following manner

$$\frac{1}{T_1}, \frac{1}{T_2} << \frac{d\alpha}{dt} << \gamma B_1 \qquad [1.15]$$

where the right inequality relates to the aforementioned condition and is equivalent to $(1/B_1)dB_{eff}/dt << dB_1/dt$ where α is the angle of magnetisation rotation. The left inequality states that the rate of change of the $\mathbf{B}_{eff}$ vector must be greater than the competing rate of decay of the magnetisation vector due to the NMR relaxation processes, T_1 and T_2, in order for adiabatic behaviour to be exhibited (see Section 1.6).

1.4.1 Detection of flow with adiabatic fast passage

The simplest use of adiabatic pulses is in the technique known as adiabatic fast passage (AFP) that utilises the sweeping of the RF frequency at a constant rate. If the value of the frequency offset from resonance, $\Delta\omega$ ($= \omega_i - \omega_0$; ω_0 will be a function of position in the presence of a gradient) is initially dominant with respect to B_1, the magnetisation will then lie in the direction of the B_0 field. As the value of $\Delta\omega$ declines and the significance of B1 increases (e.g. by sweeping the RF frequency through resonance) in a sufficiently slow manner such that the adiabatic condition is satisfied, the magnetisation will follow B_{eff} as it moves down the surface of a cone onto the transverse plane. As $\Delta\omega$ subsequently

increases, the magnetisation will reach a final value that is of opposite sign to the initial value. This translates into an inversion of the magnetisation.

The technique of adiabatic fast passage has found an application in the inversion of flowing spins, for example in blood water (Dixon, 1986). In this case, the natural flow of spins is employed in order to create the conditions necessary for the inversion. A field gradient is applied in the direction of the flow of blood. As the water spins in the flowing blood move through the linearly changing B_0 field, this has the same effect as the sweep of the RF frequency described in the previous section. If the adiabatic conditions are satisfied, the moving spins will follow the consequent change in the direction of B_{eff}, and inversion results as the field sweeps through resonance (see Fig. 1.3). The adiabatic conditions for this technique of spin inversion becomes

$$\frac{1}{T_1}, \frac{1}{T_2} << \frac{1}{B_1} \boldsymbol{G}.v << \gamma B_1 \qquad [1.16]$$

where T_1 and T_2 are the longitudinal and transverse relaxation times (see Section 1.6) and B_1 is the strength of the RF field; **G** is the magnetic field gradient strength, **v** is the linear velocity of the flowing spins and γ is the gyromagnetic ratio (Williams, 1992). The inequality on the right hand side in the above expression is equivalent to the adiabatic condition described previously (Eq. [1.15]) where the **G.v** term reflects the changing direction of the B_{eff}. The continuous arterial spin labelling techniques for perfusion measurement that are described in Section 3.3, make use of this technique of AFP in order to actively label the flowing spins in the blood.

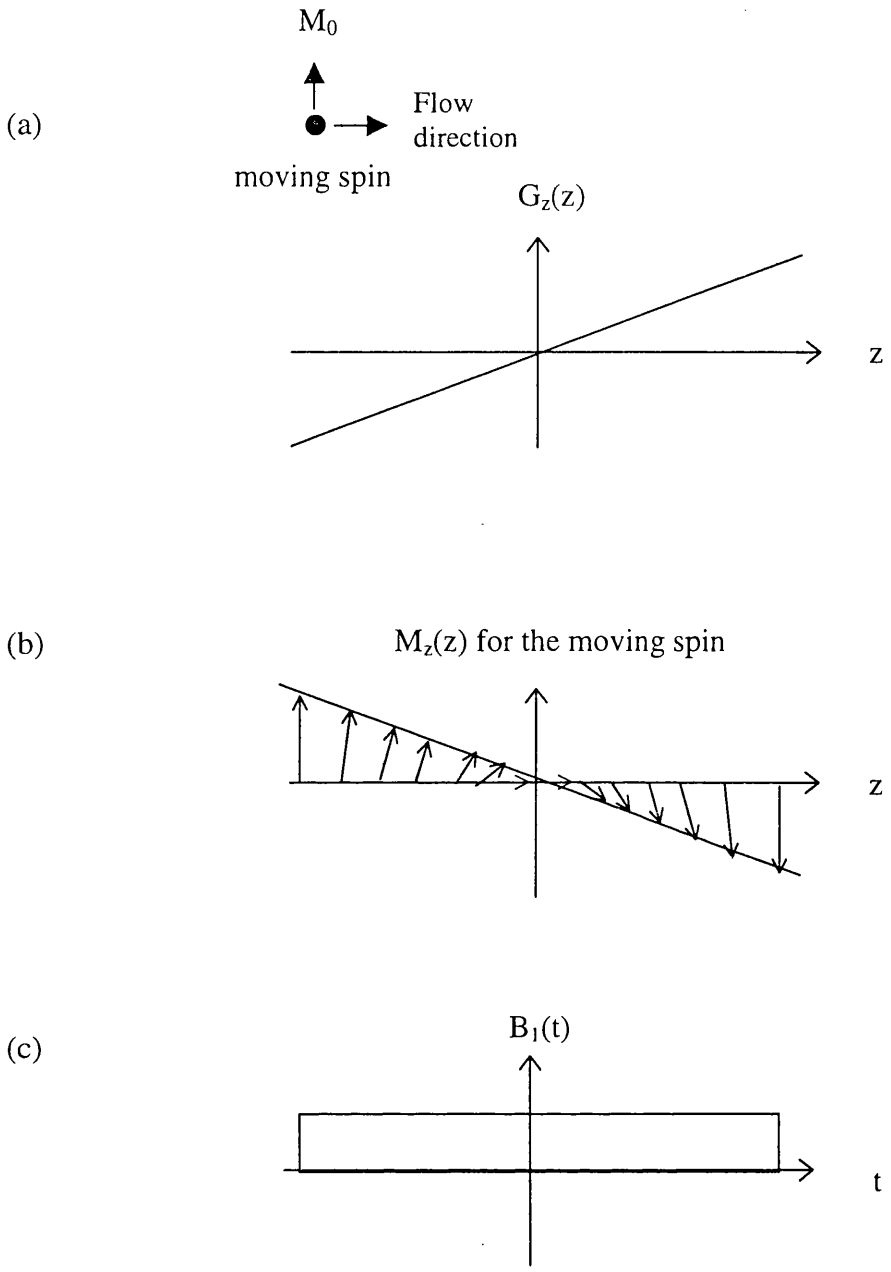

Fig. 1.3 The effect of adiabatic fast passage on a moving spin showing (a) magnetic field gradient applied along z-axis and (b) the changing direction of the z-direction magnetisation vector (M_z) of a spin as it moves into this gradient in the presence of (c) a constant RF B_1 field applied along x´. The sweep of M_z follows the sweeping frequency offset, $\Delta\omega(t)$, where $\Delta\omega(t) = \gamma G_z z = \gamma G_z vt$. The M_z vector becomes zero at the centre of the gradient field as the magnetisation is swept into the x´y´ plane and precesses in that plane.

1.5 Imaging

Conventional MR imaging makes use of the linear relationship of the angular frequency of precession with the applied magnetic field (Eq. [1.3]). In the early 1970s, Paul Lauterbur (Lauterbur, 1973) suggested the use of a controlled magnetic field gradient so that the magnetic field B_0 is a function of position. The decaying signal obtained after application of a $\pi/2$ pulse is known as an FID or free induction decay. If the FID is detected in the presence of a magnetic field gradient applied in the z-direction, then the spatial position along this axis will have been encoded onto the signal. Application of a Fourier transform on the FID produces the frequency distribution. The resulting spectrum can be considered as a one-dimensional (1D) projection of the spin density of the object onto the z-axis with the frequency axis corresponding to the z-displacement. By altering the direction of the applied field gradient and obtaining the frequency spectrum, projections of the object in different orientations can be collected. These can be reconstructed in order to produce an image by making use of a procedure similar to the methods of backprojection used in conventional X-ray CT scanning. This technique known an Projection Reconstruction has been superseded by the Fourier transform (FT) group of imaging methods developed by Kumar *et al.* (Kumar, 1975). These techniques utilise the evolution of the NMR signal in the presence of a combination of varying orthogonal field gradients. In the a similar way that the FT of a signal obtained by application of a single gradient results in a 1D projection in that direction, the application of a further orthogonal gradient together with a 2D-FT, enables a 2D image to be acquired.

1.5.1 Imaging gradients

In order to obtain the signal from one slice in the object, use is made of the technique of slice selection. The sample is irradiated with a B_1 field containing a narrow band of frequencies and in the presence of a gradient, known as the slice-selective gradient. The frequencies in the pulse determine the position of the slice along the object that is selectively excited by the pulse. In order to acquire a 2D image of the selected slice, methods such as Fourier zeugmatography (Kumar, 1975) and spin-warp imaging (Edelstein, 1980) have been developed. The FID is obtained in the presence of a frequency encoding gradient known as the read gradient. The third dimension is obtained by phase-encoding in which the FID is allowed to evolve in the presence of a perpendicular gradient applied with varying duration or more commonly a varying amplitude. Therefore, a 128×256 image would be acquired by sampling the FID on 256 occasions for each value of the

phase-encoding gradient and by varying this gradient in 128 steps. The dimension of the image in the phase-encoding direction must be equal to 2^x where x is an integer number in order to allow application of the Fast Fourier Transform algorithms (Edelstein, 1980). In order to distinguish N regions, it is necessary to acquire N signals with n = -N/2, -(N/2)+1, ..., -1,0,1, ..., (N/2)-1. A 2D-FT of the NMR signal can be used to reconstruct the image of the slice.

1.6 Principal contrast mechanisms

The spatial distribution of the spins is encoded in the image by the applied magnetic field gradients. The resulting image is then related to the density of contributing water protons, ρ, in each imaging voxel. In order to create additional contrast image, the time constants associated with the properties of the spinning protons can be manipulated and measured. The principal relaxation time constants are described in this section. An additional contrast mechanism, known as magnetisation transfer contrast (MTC) is also introduced.

1.6.1 Relaxation times : Longitudinal, T_1 relaxation

As has already been described, in the presence of a static B_0 field and under conditions of thermal equilibrium, the magnetisation will align itself along B_0 in the z-direction. The resulting equilibrium magnetisation M_0 is a consequence of the population differences between the various nuclear spin states. In fact, it is this population difference that causes the z-component of the magnetisation and a change in one affects the other. The B_1 field effectively alters the magnetisation in the z-direction, M_z, by manipulation of the total energy of the spin system that is the result of a change in the population difference. However, the system tends to return to the state of thermal equilibrium in a process known as spin-lattice or T_1 relaxation. In order for the spin system to return to this state, there must be an interaction of the spins with the surrounding lattice. In fact, it is the magnetic field variations in the xy-plane, B_{xy}, that oscillate at the Larmor frequency that provide the stimulus for this interaction. The most likely source for these magnetic field fluctuations are the dipole-dipole interactions of the spins themselves. The static field interaction between the magnetic moments will vary due to the tumbling nature of the spins, which is dependent on their size and environment. The correlation time, τ_c, reflects this process and is related to the minimum time for a molecule to rotate one radian ($\pi/2$ of a complete circle) or, alternatively, the time between "jumps" in the orientation of the magnetic

field (Fullerton, 1992). Thus time is therefore is an important parameter in the process of longitudinal relaxation and defines the frequency distribution, $J(\omega)$. A correlation time, $\tau_c=1/\omega_0$, is most efficient for T_1 relaxation.

1.6.2 Relaxation times : Transverse, T_2 relaxation

Once the magnetisation has been nutated from its equilibrium position, it will have a component in the xy-plane, M_{xy}. Spin-spin or T_2 relaxation is the process by which the magnetisation in the xy-plane decays away. This occurs, not only as a result of longitudinal relaxation, but also due to a loss of phase coherence in the xy-plane that causes the magnetisation to fan out in this plane.

Fluctuations in the magnetic and electric fields that occur, both at the Larmor frequency ω_0 due to a B_{xy} component, and at zero frequency ($\omega=0$) due to a varying B_z component, induce T_2 relaxation. Therefore, T_2 relaxation times cannot be longer than T_1 relaxation times. The two components of T_2 relaxation can be seen in the Bloch equations (Section 1.3.1). For example, the expression for dM_x/dt (Eq. [1.7(a)]) contains both a B_y term and a B_z term The factors that lead to the decay of M_{xy} can be intrinsic to the spin system or extrinsic, such as a result of magnetic field inhomogeneities. These separate processes of relaxation are both incorporated into the spin-spin relaxation time by the following relationship

$$\frac{1}{T_2^*}=\frac{1}{T_2}+\frac{1}{T_2'} \qquad [1.17]$$

where T_2^* is the total relaxation time, T_2 is the intrinsic relaxation time and T_2' is the extrinsic relaxation time. The reciprocal of the relaxation time is known as the relaxation rate. The resonance linewidth is directly proportional to the rate constant R_2^*.

$$\Delta\nu_{1/2}=\frac{R_2^*}{\pi} \text{ where } R_2^*=\frac{1}{T_2^*} \qquad [1.18]$$

where $\Delta\nu_{1/2}$ is the full width half maximum (FWHM) of the peak height in the frequency spectrum. Typical T_1 and T_2 values for human brain tissue are shown in Table 1.1. Approximate values for another important parameter, the density of water protons denoted ρ, are also displayed.

	T_1 [ms]		T_2 [ms]		approximate ρ
	2.35T	8T	2.35T	8T	[% H_2O]
Grey matter	1300	1850	65	35	97%
White matter	800	1200	35	15	80%
CSF	2250	3000	300	N/A	99%

Table 1.1 Approximate values of T_1, T_2 and ρ for brain tissue components from in-vivo data collected in our laboratory in the rat at two magnetic field strengths. The T_2 is measured with a multi-echo 2DFT sequence on the 8T machine (see Section 3.7). It is susceptible to the effects of diffusion-induced dephasing and this may explain the reduced T_2 value at the higher field strength. The parameter values vary over approximately ±5% due to natural variation. N/A indicates non-acquired data.

1.6.3 Magnetisation transfer contrast (MTC)

The natural state of protons in biological tissue can be simplistically divided into two classifications. The free proton pool (H_f) represents mobile water protons whilst the restricted proton pool (H_r) represents the bound, macromolecular protons incorporated within membranes and proteins. The resonance linewidths of free protons are relatively narrow and of the order of 100 Hz or less. This can be contrasted with the bound protons found in tissue principally in the form of macromolecules, whose mobility is limited. Therefore, the resonance linewidths are broad – 10 kHz or greater - and consequently, this proton state cannot be directly observed with conventional MRI. Figure 1.4 shows the absorption spectra form the two tissue components. However, the indirect influences of the bound protons on the H_f pool can be investigated by application of the technique known as magnetisation transfer contrast (MTC) developed by Wolff and Balaban (Wolff, 1989). The free and bound proton pools are constantly exchanging magnetisation by a process of cross-relaxation (magnetisation transfer by dipole coupling between different spin systems) and chemical exchange (mediation of the transfer by equilibrium exchange processes). For this reason, any perturbation of the magnetisation state of one pool will affect the magnetisation state in the other pool. The

technique of MTC makes use of this by utilising low power RF irradiation that is applied off-resonance in order to selectively saturate the broadline protons in the bound H_r pool. An indirect loss of signal from the H_f pool is observed due to cross-relaxation with the broadline H_r pool. A relatively long RF saturation pulse is usually employed in order to saturate the macromolecular protons, and care has to be taken that the direct effect of the pulse on the H_f pool is minimal.

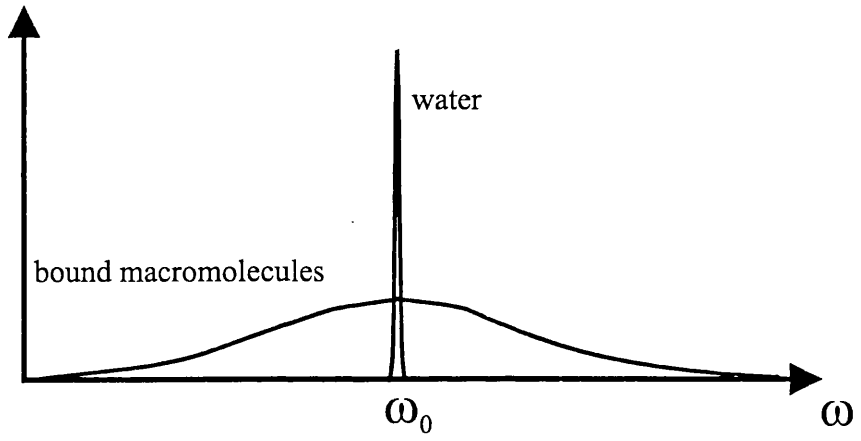

Fig. 1.4 A schematic representation of the free and bound proton pools.

By varying the offset frequency of the saturation pulse and observing the changes in signal intensity, the process of magnetisation transfer can be investigated. An important parameter in the description of the MTC effect is the magnetisation exchange rate k_F between the two proton pools (usual units : [sec^{-1}]). This rate constant is a function of the frequency offset and is defined by the following expression

$$k_F = \frac{1}{T_{1sat}}\left[1 - \left(\frac{M_s}{M_0}\right)_{ON}\right] \qquad [1.19]$$

where T_{1sat} is the spin-lattice relaxation time of free water protons in the presence of saturation, M_s, is the observed magnetisation and M_0 is the equilibrium magnetisation observed in a standard image. The term $(M_s/M_0)_{ON}$ represents the on-resonance intercept of the saturation curve. It is, however, not practically possible to acquire M_s signal at the resonance frequency of free water since its direct saturation will eliminate all of the NMR signal. The ratio $(M_s/M_0)_{ON}$ is therefore acquired at an offset frequency, Δf. The T_1 in the presence of saturation effects, T_{1sat}, is usually determined by utilisation of an

IR based pulse sequence. In order to aid comparison of the results obtained from different samples and spectrometers, the saturation pulse is normally set to correspond to a particular fixed angular frequency of nutation.

Images acquired with MTC display a unique contrast, which is specific to the magnetisation exchange between the free and bound proton pools. Although clinical work with MTC is in a relatively early stage of development, its use in research has given an indication of its potential. For example, MTC has been employed to track ischaemic damage and its correlations with changes in other important NMR parameters (Ordidge, 1991).

1.7 Pulse sequences

There are a number of combinations of RF pulses and gradients utilised in MR imaging that contribute to the contrast in the resulting image. These pulse sequences manipulate the magnetisation in order to obtain the NMR signal. This section will describe the simplest sequences, spin-echo and gradient-echo. Some of the other sequences used in this project are also discussed.

1.7.1 Spin-echo and gradient-echo

After application of a $\pi/2$ RF pulse, an FID is obtained. T_1 and T_2 relaxation subsequently induce the return of the magnetisation to the static field (B_0) direction. Similarly, T_2^* effects due to inhomogeneities in this field result in a variation of the precessional frequency of the spins at different positions in the sample. Therefore, the magnetisation appears to fan out in the xy-plane. In order to rephase these spins and thereby produce a secondary echo, a π pulse is applied at a time TE/2 after the 90° ($\pi/2$) pulse, where TE is known as the echo time. This pulse refocuses the xy magnetisation producing a spin-echo centred a time TE after the $\pi/2$ pulse (see Fig. 1.5(a)). Field inhomogeneities are rephased by the 180° (π) pulse and, therefore, the signal decays with time constant T_2. The pulse sequence repeats after a time TR known as the repetition time, during which time the magnetisation can recover.

Another technique that is commonly incorporated into pulse sequences to rephase the spins in the xy-plane is achieved without the need for another RF pulse. A dephasing gradient pulse -G is instead applied along the read-out direction, which is followed by a rephasing

gradient +G of the opposite polarity. Figure 1.5(a) shows the sequence. Reversing the sign of the gradient, reverses the direction of the precession of the spins in the xy-plane. Therefore, the spins begin to rephase and an echo known as a gradient-echo forms at a time TE after the $\pi/2$ pulse. The echo forms when the relative phase ϕ of all the spins in the excited slice becomes zero. In other words, when the following equation becomes true for all spins

$$\phi = \int_{t'=0}^{t} \gamma x G_x(t) dt' = 0 \qquad [1.20]$$

where G_x is the read-gradient.

For this reason, the echo appears when the areas under the gradients shown in Fig. 1.5(b) cancel. Field inhomogeneities are not rephased by the gradient pulse and, therefore, the signal decays with time constant T_2^*.

1.7.2 Inversion recovery

Sequences that utilise a spin-echo can be employed to acquire images that depend strongly on T_2 relaxation time values (T_2-weighted images). T_1-weighted images can be obtained by application of the inversion recovery (IR) pulse sequence. A π pulse is used at the start of the sequence. The equilibrium magnetisation M_0 is thus inverted with respect to the direction of the static field and tends to relax to its equilibrium position with time constant T_1. In order to interrogate the magnetisation, it has to be brought into the xy-plane by means of a $\pi/2$ pulse applied at a time TI after the $\pi/2$ pulse, where TI is known as the inversion time. A longer repetition time TR is required between each sequence of pulses since the z-magnetisation has to pass through zero before relaxing back to its equilibrium value. The detected signal can be positive or negative depending on the inversion time TI employed in the sequence and the T_1 of the sample. An expression for M(TI), the signal in an IR image after interval time, TI, is given by

$$M(TI) = M_0 \left[1 - 2\alpha_0 \exp\left(\frac{-TI}{T_1} \right) \right] \qquad [1.21]$$

where M_0 represents the equilibrium magnetisation per unit mass of the tissue and α_0 describes the efficiency of the inversion (and takes a value of, for example, 1.0 for ideal

inversion and 0.5 for saturation). This equation assumes that the repetition time TR is long and, therefore, the magnetisation has relaxed before application of the next sequence. This following expression predicts the point at which the IR signal disappears - the null point - which occurs when the magnetisation recovers to the extent that the z-component disappears [i.e. M(TI) = 0)].

$$TI = T_1 \ln 2 \qquad [1.22]$$

1.7.3 Rapid, low-angle techniques

The long duration of conventional MRI scans and the high cost of the machines, have led to the development of more sophisticated scanning techniques. Clinical efficiency is thereby increased and reduction of motion related image artefacts can be achieved. The scan time, T_s, to acquire the data for one image can be expressed as follows

$$T_s = TR \times N_y \times NEX \qquad [1.23]$$

where TR is the repetition time, N_y is the number of phase-encoding steps and NEX is the number of averages. Therefore, the scan time can be shortened by reduction of any one of these three parameters. One approach to rapid scanning is derived from sequences that employ a combination of low angle RF excitations and gradient-echo acquisitions. The first sequence that utilised this approach, developed by Haase *et al.* (Haase, 1986), was dubbed FLASH (fast low angle shot sequence). Variations of this sequence include GRASS, FISP, SSFP and SNAPSHOT. FLASH is a sequence with a short TR (< 200 ms) and a low flip angle ($< \pi/2$). Typical measuring times for a single 2D-FT are in the order of seconds. Application of a $\pi/2$ pulse results in the conversion of all the longitudinal magnetisation to the transverse direction in the xy-plane. An RF pulse with a flip angle less than $\pi/2$, leaves a longitudinal component of the magnetisation. An RF pulse with a flip angle of $\alpha=10^{\circ}$ for example, will rotate the magnetisation resulting in a transverse component of $M_z.\sin\alpha$ or 17.4% of M_z. A component $M_z.\cos\alpha$ or 98.5% of M_z is left in the direction of the static field. Therefore, the subsequent repetitions almost immediately restart after each gradient-echo acquisition without the need for waiting a significant TR for the longitudinal magnetisation to recover from the transverse plane. The value of α that optimises the signal-to-noise-with-respect-to-time obtained from a sample with spin-lattice relaxation time T_1, is known as the Ernst angle (Ernst, 1966).

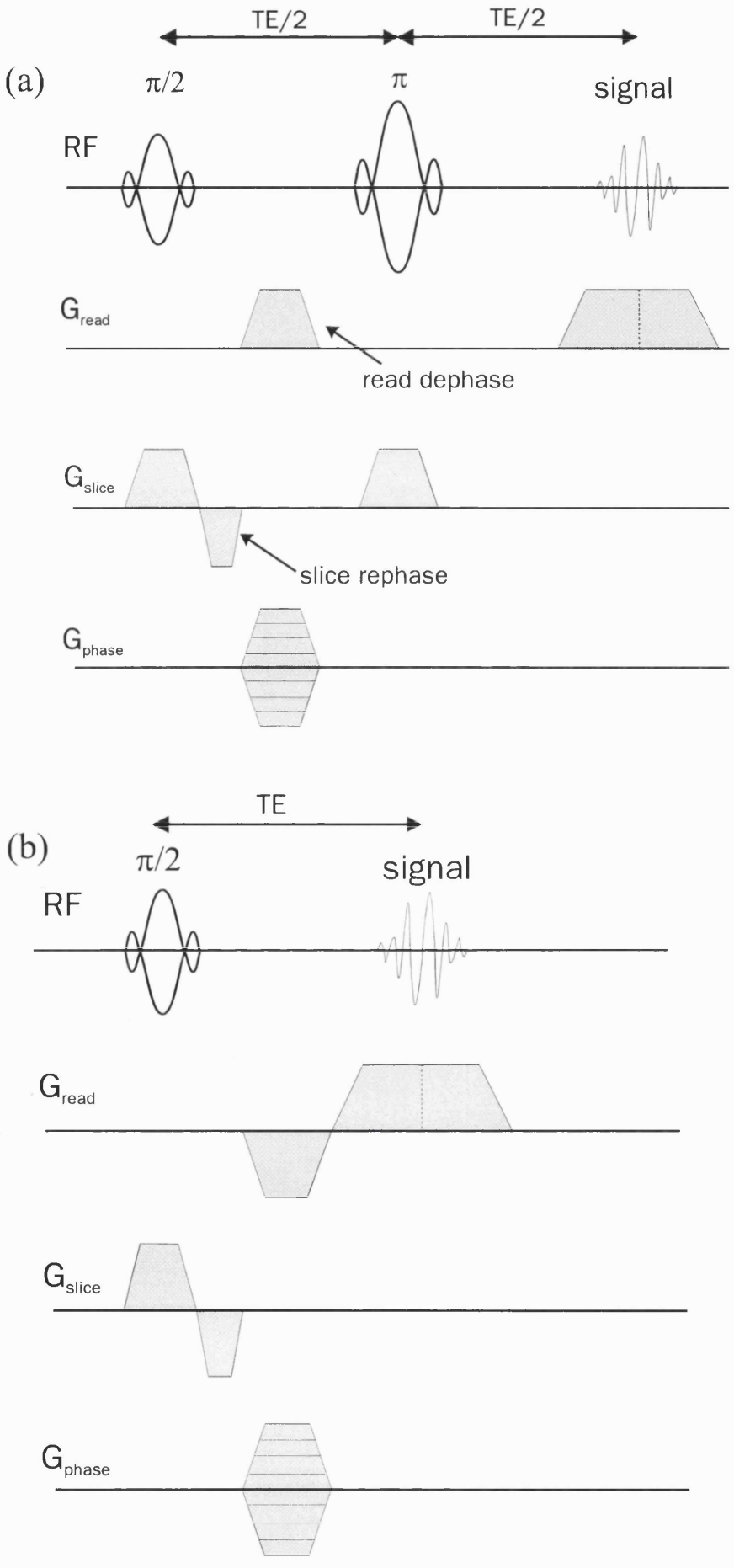

Fig. 1.5 Pulse sequence diagrams of basic 2D-FT (a) spin-echo and (b) gradient- echo sequences.

It can be calculated by use of the following expression

$$\alpha = \cos^{-1}\left[\exp\left(\frac{-TR}{T_1}\right)\right] \qquad [1.24]$$

In a variation of the FLASH imaging technique, known as TurboFLASH or SNAPSHOT, imaging times of approximately 200 ms for a 128 × 64 image can be obtained (see Section 6.2). This pulse sequence makes use of rapid gradient switching in order to obtain short repetition and echo times. A series of TurboFLASH imaging acquisitions is often used after an inversion pulse in order follow the changing longitudinal magnetisation as it relaxes back towards equilibrium. In this manner, a rapid measure of T_1 can be obtained (see Fig. 1.6) (Haase, 1986).

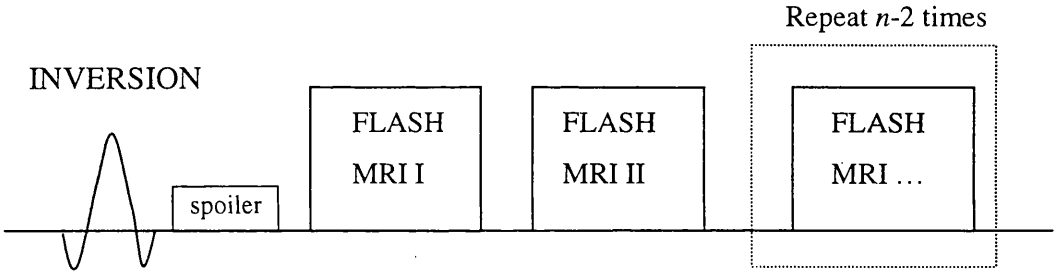

Fig. 1.6 Schematic representation of SNAPSHOT (TurboFLASH) method of T_1 measurement with *n* points acquired along the inversion recovery curve.

1.8 The k-space formulation

In order to develop an understanding of the encoding process in MRI, the correspondence between the time-domain signal and the frequency-domain spatial projections has to be appreciated. This is not always an intuitive task and it is often difficult to relate this methodology to certain imaging techniques. However, an alternative formulation exists that can be more readily used in order to describe the unique control that the MR imaging operator has over the acquisitions of the data. This alternative viewpoint is known as k-trajectory formulation. The abstract concept of k-space (Twieg, 1983) acts as the template upon which the image is acquired and then manipulated.

1.8.1 Mathematical formulation

For an ensemble of nuclei in a volume of tissue subjected to an imaging pulse that results in a transverse component of magnetisation and in the presence of constant gradients, G_x (read) and G_y (phase), the signal at time t, S(t) can be described by the expression for the 2D experiment

$$S(t_x,t_y) = M_0 \int_x \int_y \rho(x,y) \exp\left(\frac{-t_{x,y}}{T_2^*}\right) \exp[-i\gamma(G_x x t_x + G_y y t_y)]dxdy \qquad [1.26]$$

where $\rho(x,y)$ is the proton density at each co-ordinate position and t_x and t_y are the application times of the read and phase gradients respectively. The effects of the slice selection gradient do not need to be incorporated into the formulation since slice selection is carried out prior to phase-encoding and read-out. The non-spatially dependent components of the above expression can be combined in a constant **A** and for constant gradients, this expression becomes

$$S(t_x,t_y) = A \int_x \int_y \rho(x,y) \exp[-i\gamma(G_x x t_x + G_y y t_y)]dxdy \qquad [1.27]$$

The spin density $\rho(x,y)$ can be expressed in terms of its Fourier components $F(k_x,k_y)$

$$\rho(x,y) = \int_x \int_y F(k_x,k_y) \exp[i(k_x x + k_y y)]dk_x dk_y \qquad [1.28]$$

By carrying out a Fourier transform on the above expression, the Fourier components can be determined

$$F(k_x,k_y) = \int_x \int_y \rho(x,y) \exp[-i(k_x x + k_y y)]dxdy \qquad [1.29]$$

The similarity between this expression and Eq. [1.26], suggests that the time varying signal represents the 2D Fourier components of the spin density $\rho(x,y)$. The Fourier coefficients for time varying gradients are, therefore, given by the expressions

$$k_x = \gamma \int_t G_x dt \qquad \text{(a)}$$

$$k_y = \gamma \int_y G_y dt \qquad \text{(b)} \qquad [1.30]$$

These are the components with units of spatial frequency that in combination with k_z, define 3D k-space. This formulation mirrors the familiar wave equation for a travelling

wave propagating in the x-direction that can be described by

$$A(x,t) = A_0 \exp[i(kx - \omega t)] \qquad [1.31]$$

where $k = 2\pi/\lambda$, λ is the wavelength, A(x,t) is the amplitude at position, x, and at time, t, and ω is the angular frequency.

1.8.2 Image formulation in k-space

The formation of an image in MRI can be seen as the filling of the k-space domain in such a way as to satisfy the requirements of the imaging operator. Once the data have been placed in k-space, use of a FT reconstructs the image. The placement of data in k-space is controlled by the time integral of the gradient as described by Eq. [1.29]. A small gradient for example, will place the image data near the centre of k-space. For this reason, gradients are the principal causes of displacement within k-space. The displacement is in the corresponding direction in the k-domain and, therefore, the spacing between points in, for example, the phase-encoding direction, is determined by the increment in the phase-encoding gradient G_y. A $\pi/2$ pulse at the start of a pulse sequence can be seen as simply creating the conditions required for movement within k-space by the formation of a transverse component of magnetisation. A π pulse on the other hand, reflects the current k-space position through the x and y axes so that (k_x, k_y) is transformed to $(-k_x, -k_y)$. The spacing between lines in k-space (Δk) is related to the FOV and the extent of coverage in k-space (k_{max}) is related to the spatial resolution in the image.

1.8.3 The spin-echo sequence in k-space

The pulse sequence controls the way in which k-space is filled. The common spin-warp sequences can be used as an illustration of this process and the sequence and its effect on the k-space domain are shown in Fig. 1.7. The $\pi/2$ pulse brings the data into the centre of k-space. In terms of the steps shown in the above diagram, the process can be described in the following manner:

Stage (1) The combination of the two simultaneous gradients on the x and y directions, lead to a diagonal shift position to the edge of k-space

Stage (2) The π pulse reflects the point reached through the origin of k-space

Stage (3) Application of the read gradient starts the traversal through the horizontal line

in k-space when the signal is usually sampled by the analogue-to-digital-converter (ADC). When the dephasing effects of the gradient before and after the π pulse cancel each other out and the shaded areas in Fig. 1.7 are equal, a spin-echo results. In k-space, an echo can be seen as forming when a k-trajectory crosses one of the k-space axes. As the phase-encoding is stepped up and down, the process repeats itself at different positions along the k_y axes until the entire k-space domain has been filled.

1.8.4 The gradient-echo sequence in k-space

A typical gradient-echo acquisition is shown in Fig. 1.8.

Stage (1) The k-trajectory moves diagonally to the edge of k-space.

Stage (2) The horizontal line in k-space is traversed. The gradient-echo forms as the k_y axis is crossed and this occurs when the shaded areas in Fig. 1.8 are equal. As the phase-encoding gradient is stepped up and down, the process repeats itself at different positions along the k_y axis until the entire k-space domain has been filled.

1.8.5 The EPI sequence in k-space

An alternative method for filling k-space is achieved by the pulse sequence shown below in Fig. 1.9 together with its k-space trajectory. This pulse sequence is known as EPI (echo-planar imaging) – or more precisely by the acronym MBEST - and can be used to acquire images in less than 50 ms by filling the whole of k-space in a single-shot (Mansfield, 1977). It is currently the fastest acquisition technique in standard implementation on commercial systems. It is based on the principle of a single RF excitation of the spin system, followed by rapid switching of the read gradient to form gradient-echoes. In the standard implementation, each of these echoes is given a different degree of phase encoding by a series of small gradient blips that moves k-space through one line in the phase-encode direction. The EPI readout is usually incorporated within a standard spin-echo RF excitation in order to reduce the T_2^* dephasing of the signal. The sequence places great demands on the gradient amplifiers, which need to be rapidly switched at a high level of gradient strength in order to achieve the large bandwidths required for acquisition. The sequence is very sensitive to susceptibility-related artefacts due to its inherent T_2^* weighting and therefore, its implementation at high magnetic field strengths is problematic. Recent studies have reported animal images at 9.4T (Kim, 1998) with EPI.

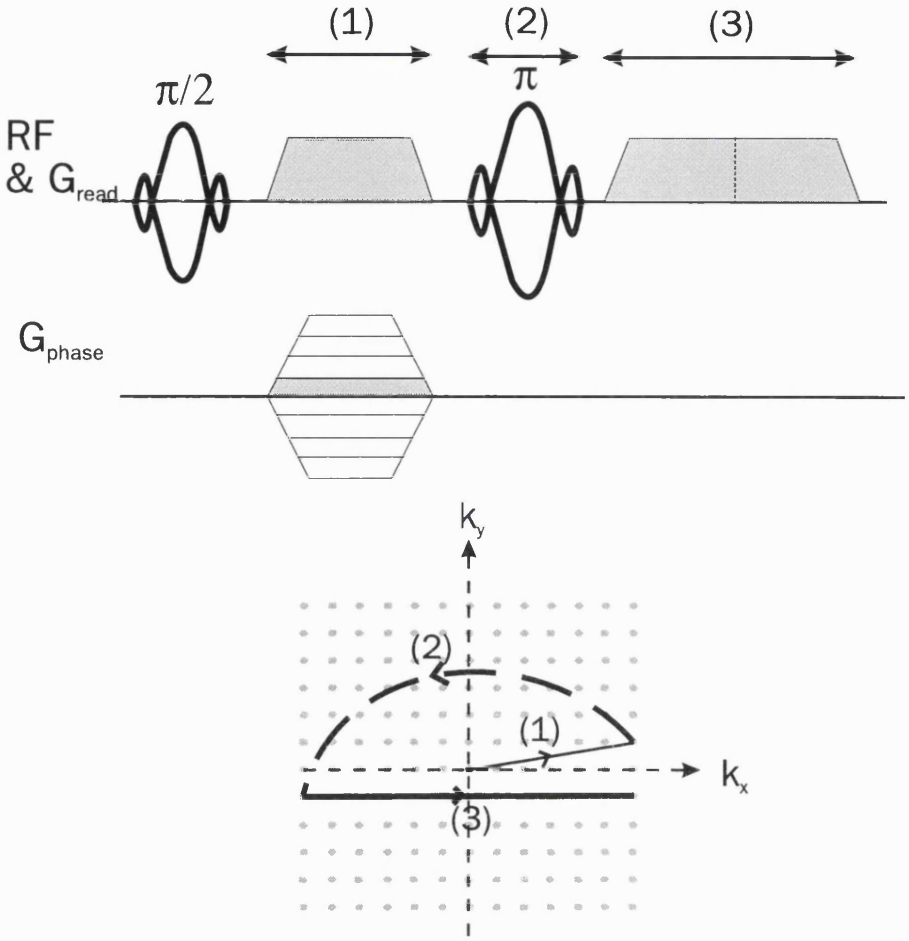

Fig. 1.7 k-space representation of spin-echo pulse sequence

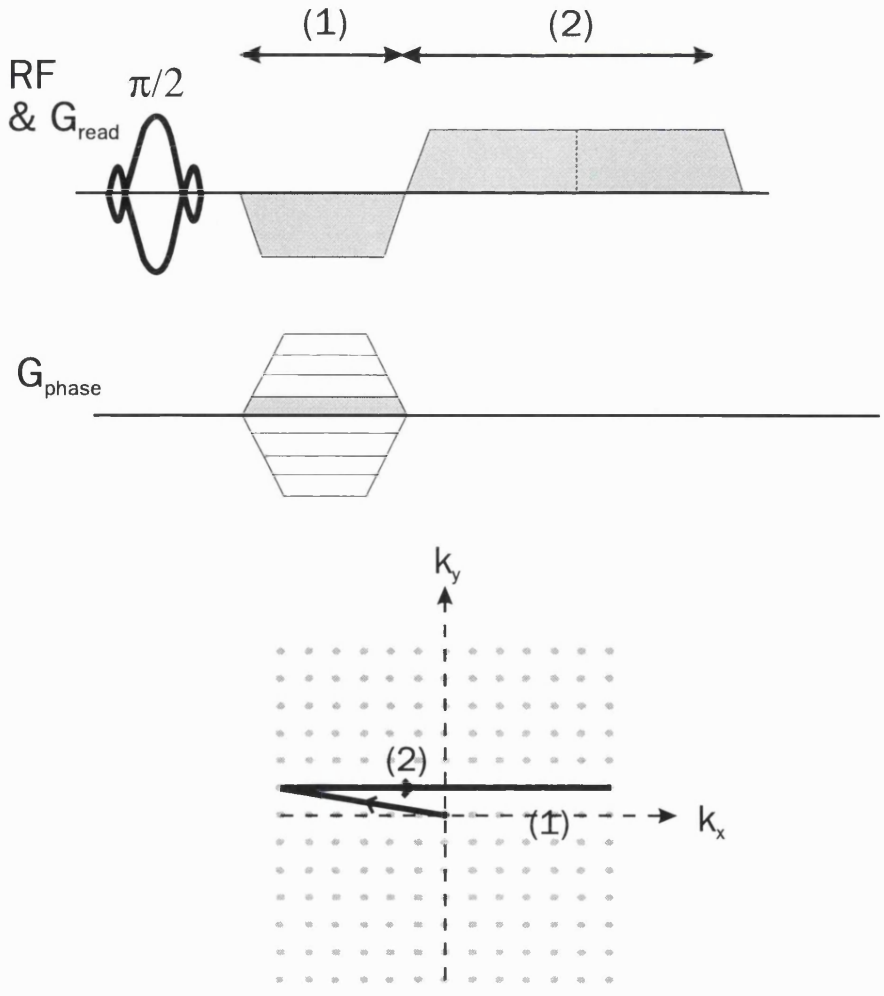

Fig. 1.8 k-space representation of gradient-echo pulse sequence

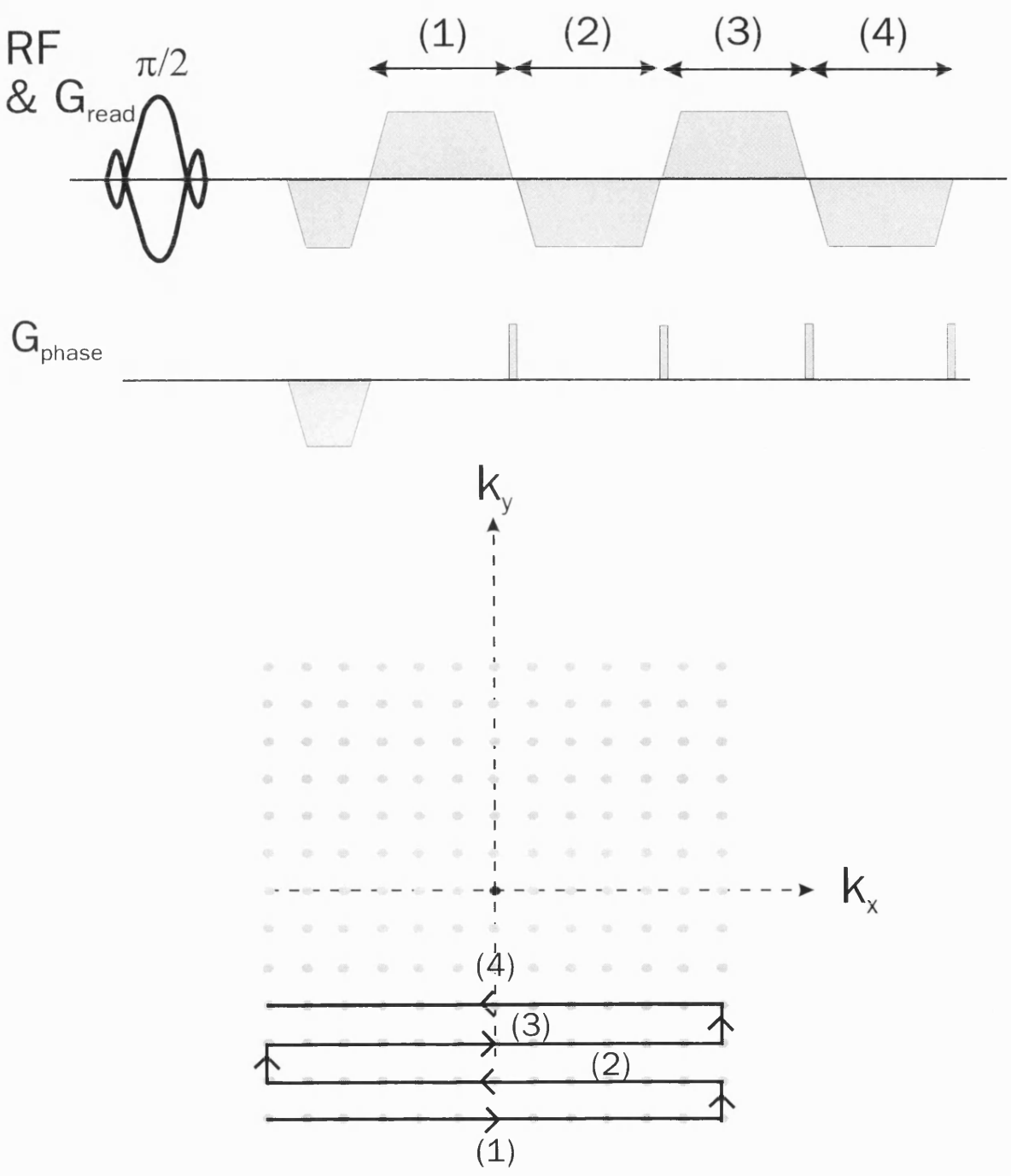

Fig. 1.9 k-space representation of the EPI pulse sequence.

II THE CONCEPTS OF DIFFUSION AND PERFUSION

This thesis concentrates on the MRI sensitivities provided by perfusion and diffusion imaging. The following chapter relates the concepts of perfusion and diffusion to their clinical contexts. The theory of diffusion-weighted imaging is explained and its sensitivity in detecting acute stroke is introduced. The concept of perfusion is discussed in relation to the clinical understanding of cerebral blood flow. Perfusion measurements are by no mains solely in the domain of MRI and methods for blood flow determination have been in use for many years. The range of techniques for perfusion quantification are tabulated so that their relative merits can be compared.

2.1 Diffusion

The diffusive nature of water molecules within tissue has been introduced as an additional NMR contrast parameter. The process of diffusion describes the mainly random, microscopic translational movement of water molecules. For an ensemble collection of water spins, this process results in a net displacement r in time t that is distributed in the form of a Gaussian function with a mean of zero. The variance of the distribution of r is given by Einstein's equation

$$\langle r^2 \rangle = 2D\,t \qquad [2.1]$$

D, known as the diffusion coefficient, which is the proportionality constant in the above equation, is therefore related to the mean displacement over a certain period of time. For the diffusion of water molecules within tissue, this displacement will be affected by phenomena such as restricted diffusion in which molecules are confined within borders, and the permeability of the cell membranes through which the water molecules diffuse. For this reason, the measured tissue diffusion coefficient known as an apparent diffusion coefficient (ADC), is closely related to the biophysical environment of the tissue water and can be used to describe cell function and structure. It is termed an apparent measure since the motion of water molecules in tissue is modulated by a number of factors other than Brownian motion including chemical exchange, cell membrane permeability and structural restriction.

2.1.1 Measurement of diffusion

In order to sensitise a pulse sequence to diffusion, gradient pulses are utilised. Spins moving through a magnetic field gradient experience a phase shift since the gradient defines the associated resonant frequency at each point. An expression for the phase shift, ϕ, is

$$\phi = \gamma \int_{t'=0}^{t} \boldsymbol{r}.\boldsymbol{G}(t)\, dt' \qquad [2.2]$$

where γ is the gyromagnetic ratio, G(t) is the gradient at time t, and r is the distance moved by the spin during this time. For an imaging voxel whose spins diffuse through such a gradient, the distribution of phases will be of a gaussian form around a mean of zero and a variance displacement given by Eq. [2.1]. In order to rephase these spins, a gradient can be applied with opposite polarity or alternatively, with the same polarity in combination with a π pulse. For static spins, perfect rephasing then occurs. However, if the spin has moved during the application of these gradients, the phase shift accumulated during the first gradient is not reversed by the phase dispersion caused by the second gradient pulse since the spin's position and, therefore, phase will have altered. A net attenuation of the signal results due to incomplete rephasing of diffusing spins that can be described by

$$S = S_0 \exp(-bD) \qquad [2.3]$$

where S and S_0 are the signal levels before and after application of the gradients respectively; D is the diffusion coefficient (usual units : [mm^2/sec]) and the b-value is a factor that is dependent on the dephasing power of the diffusion gradients (usual units : [sec/mm^2]). Figure 2.1 depicts the effects of diffusion gradients on a spin in the rotating reference frame.

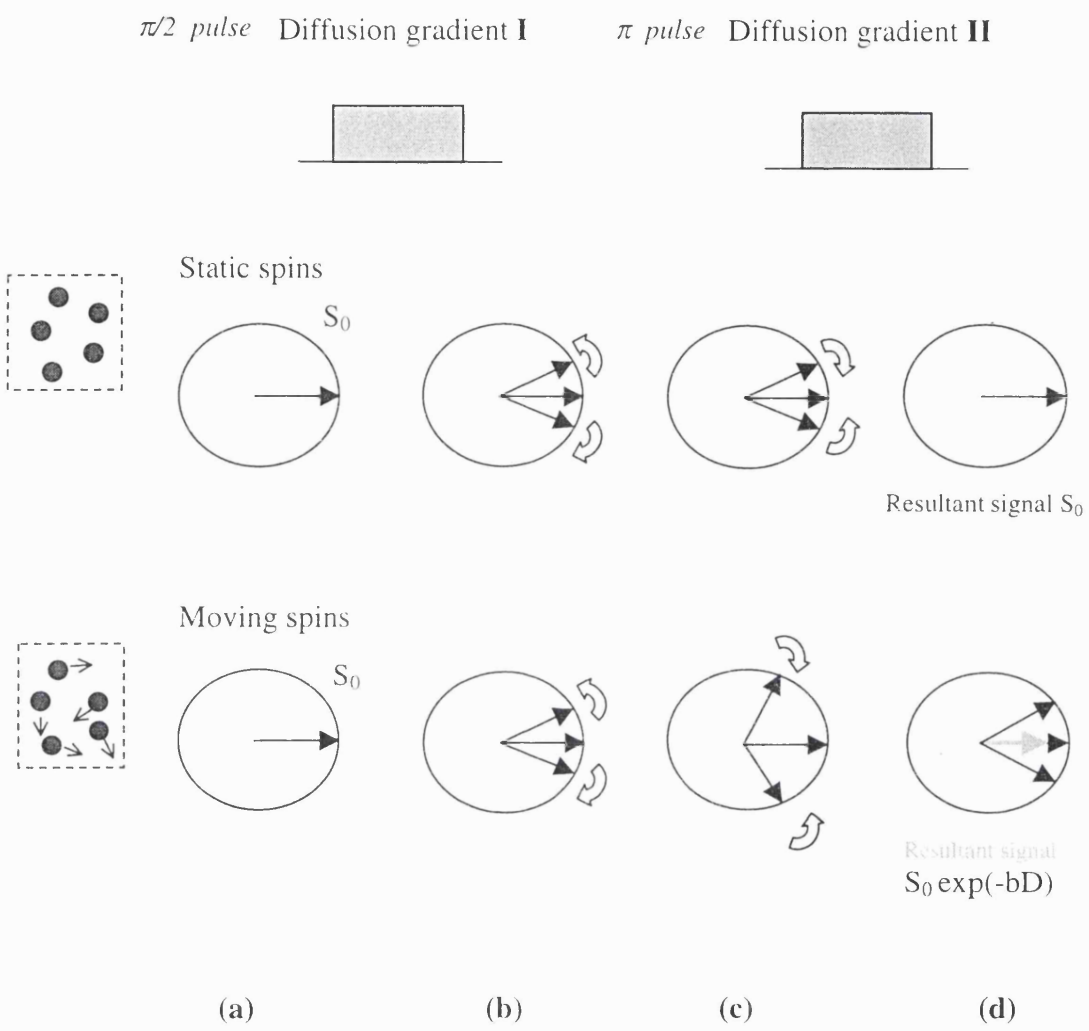

Fig 2.1 The effect of diffusion gradients on a simple 3-spin system in the rotating reference frame during a spin-echo combination of pulses. The diffusion gradients are separated by a π pulse and the magnetisation state of a set of three spins is shown at the end of the two diffusion gradients (b,c). The initial and final magnetisation states of these spins are depicted (a,d).

In this manner, a value for D can be obtained by measuring the signal attenuation obtained at a number of different diffusion gradient strengths (i.e. at a number of b-values) and fitting to Eq. [2.3]. Maps of the diffusion coefficient can be obtained by fitting each pixel in the series of differently diffusion-weighted images. The classic pulse sequence for ADC measurement was devised by Stejskal and Tanner (Stejskal, 1965) and is based upon a spin-echo 2D-FT sequence. It consists of a pair of diffusion gradients placed around the π pulse (see Fig. 2.2).

The b-value for this combination of gradient pulses is approximately equal to

$$b = \gamma^2 G^2 \delta^2 \left(\Delta - \frac{\delta}{3} \right) \qquad [2.4]$$

where δ and Δ are as shown in Fig. 2.2 and the effects of the gradient ramps have not been taken into account. The b-value can be calculated for any combination of gradients applied along any combination of directions, with the generalised formula (see ref. (Basser, 1992)) given by

$$b = \int_{t'=0}^{t} \left| k(t) \right|^2 dt'$$

$$\text{with } k(t) = \gamma \int_{t'=0}^{t} G(t') \, dt' \qquad [2.5]$$

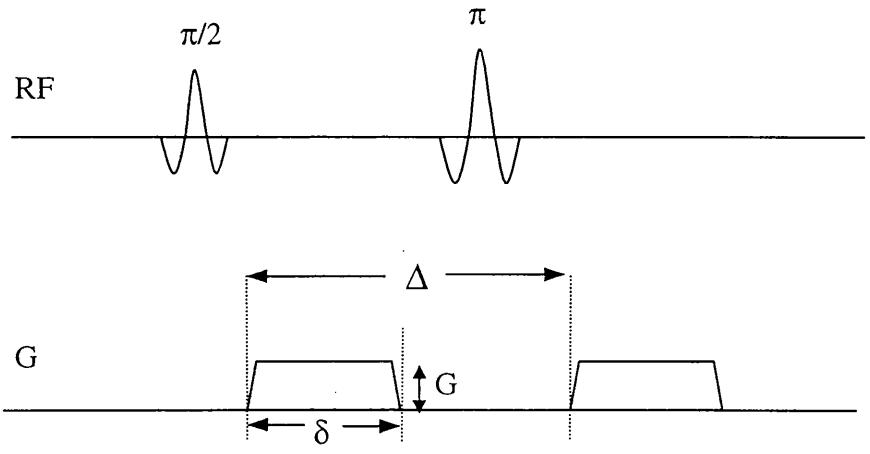

Fig 2.2 Stejskal-Tanner diffusion-weighted sequence (Stejskal, 1965) showing diffusion gradients applied along one axis.

Diffusion gradients can be incorporated into a large variety of NMR pulse sequences such as EPI (Turner, 1990), steady state free precession (SSFP) (Le Bihan, 1989) and stimulated echo sequences (Merboldt, 1992). Motion artefacts are a serious problem in diffusion imaging since the sequence is sensitised to small-scale motion. As faster imaging sequences have become more widespread on conventional MRI scanners, much work has been carried out to optimise the application of diffusion sensitisation to these sequences. Chapter 6 discusses the suitability of the TurboFLASH and EPI pulse sequences for rapid, quantitative diffusion imaging.

2.1.2 Diffusion anisotropy and the diffusion trace

Diffusion is a three-dimensional process and water mobility may be favoured along one axis of a structure. The measured ADC along this orientation will be larger than other directions. The directional dependence of diffusion is known as diffusion anisotropy and is especially apparent in brain white matter in which diffusion mobility is greater along the nerve axon fibres. Along other directions, diffusion is considered as being *restricted*. Studies have also indicated that even grey matter displays a certain degree of anisotropy (Lythgoe, 1997). The diffusion coefficient is therefore better represented within brain tissue by a rank-3, 2D tensor, **D**, that takes into account molecular displacements in the x, y and z directions (diagonal terms) and also their possible coupling terms (non-diagonal terms). The elements of the tensor are denoted by the notation D_{ij} where the elements i and j can take any of the three gradient directions x, y and z (Basser, 1994).

Cerebral ischaemia is reflected in an acute reduction of the diffusive property of tissue water. Important investigations of the pathophysiology of ischaemia have been undertaken using the contrast created by diffusion-weighted imaging. The effects of diffusion anisotropy complicate the interpretation of diffusion-weighted images. Variations in intensity across the image may reflect the geometric relationship between the acting diffusion encoding gradients and the alignment of the structural organisation of the tissue rather than the inherent mobility of water molecules in an environment that has no directional-dependence. Contrast between ischaemic and normal tissue can hence be impaired. Direction-insensitive and, therefore, more generalised ADC measurements are provided by scalar invariants of the tensor. One of these parameters is provided by the mathematical trace of the diffusion tensor that essentially represents the directionally averaged ADC. The effects of adverse anisotropic contrast are hence

avoided. The trace of a matrix is mathematically invariant under rotations (Mori, 1995), and in the context of the diffusion tensor **D**, is denoted Trace(**D**) = $3.D_{av}$ and is described by the relationship

$$Trace(\mathbf{D}') = D_{xx}' + D_{yy}' + D_{zz}' = D_{xx} + D_{yy} + D_{zz} = Trace(\mathbf{D}) = 3D_{av} \quad [2.6]$$

where D_{xx}' is the ADC along the principal axis, x' (given by the eigenvector space of the diffusion tensor); D' is the diffusion matrix of the system within the space described by the principal axes; D_{xx} is the ADC along the laboratory x-axis; **D** is the diffusion matrix in the laboratory frame. The matrices **D** and **D'** are related by a rotation matrix (Basser, 1994).

A third of the trace of the diffusion tensor, 1/3.Trace(**D**) [2] (also denoted D_{av}), can be most easily determined by obtaining separate diffusion-weighted measurements with the diffusion encoding gradients placed along orthogonal directions and by averaging the result (van Gelderen, 1994). However, the effects of *cross-talk* from the imaging and background gradients (see Section 6.1) complicate the acquisition of the purely unidirectional diffusion-weighted images that represent the diagonal elements of the diffusion tensor (Basser, 1995). Cross-terms of the diffusion tensor result from interactions of gradients in orthogonal directions. In addition, this method does not represent a time efficient use of the gradient power. Single-shot sequences have therefore been developed that employ a set of gradient pulses applied along multiple directions in order to obtain the trace(D) within one scan. Mori *et al.* have proposed a gradients scheme in the three gradient axes to cancel the off-diagonal elements of the diffusion tensor (Mori, 1995). Cross-terms are avoided by the immediate refocusing of the diffusion gradients, which are arranged as a combination of bipolar pairs. However, the gradient efficiency of these sequences is sub-optimal and numerical optimisation methods have been employed to improve the relative efficiency of such pulse sequences (Wong, 1995). This provides a scheme of tetrahedral diffusion encoding gradient waveforms. This technique was implemented as part of the investigations described in this thesis and is further described in Section 6.3.

[2] The parameter described by a third of Trace(**D**) is here-on simply denoted trace(D)

2.1.3 Oedema and acute stroke

An early suggestion for a use of diffusion imaging was as a means of measuring tissue perfusion. However, this has been largely superseded by the discovery in 1990 that diffusion imaging can provide an indication of the early stages of reversible and irreversible cerebral ischaemia (Moseley, 1990). Ischaemia is a state of reduced blood flow in tissue and is usually implicated in the manifestation of a stroke (see Section 2.2.1). The sensitivity of diffusion imaging to this state is significant because conventional MRI with its use of spin-density and T_2-weighted imaging, displays little contrast and is only able to detect the delayed effects of the development of vasogenic oedema (Knight, 1991). This process occurs when the integrity of the blood-brain-barrier (BBB) (Section 2.2.4) is compromised and the necrosis of endothelial cells and the separation of tight junctions results in the extravasation of macromolecules. The *leaky* BBB can no longer withstand the hydrostatic pressure from the vasculature and water, therefore, accumulates in the extracellular space (Tominaga, 1995). The observation of an increased signal on the onset of ischaemia in a diffusion-weighted image corresponds to a decrease in the ADC and occurs at an earlier stage while the BBB is still intact. The physical basis for this contrast in diffusion-weighted imaging is the change in the biophysical environment of cellular water in the state of ischaemia. The precise mechanism for this process has not been completely understood. Explanations have been proposed that relate to the effects of changing brain temperature on ADC and to a decrease in cellular membrane permeability (Helpern, 1992). However, the main body of opinion explains changes in diffusion characteristics during ischaemia as being a direct result of the breakdown in ionic homeostasis within the affected cells. The normal intra- and extracellular concentration of sodium and potassium is disrupted due to depletion of energy stores during ischaemia. Table 2.1 shows the concentrations of these ions inside and outside of cells under normal conditions. Extracellular sodium, Na^+, and calcium, and other ions (such as Ca^{2+} and Cl^-) move into the cell, with an efflux of potassium ions, K^+, and the resulting increase in osmolality causes a redistribution of tissue water from the extracellular into the intracellular compartment. This process is known as cytotoxic oedema and is illustrated schematically in Fig. 2.3.

	[Intra-cellular]	[Extra-cellular]
Na^+	15 mM	150 mM
K^+	150 mM	5.5 mM

Table 2.1 Normal intra- and extra-cellular concentrations of sodium and potassium ions. Data from (Mommaerts, 1978).

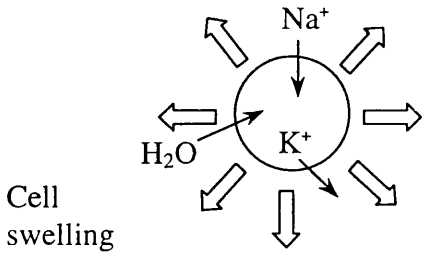

Fig. 2.3 Ion movements in cytotoxic brain oedema

Most explanations for the subsequent drop in ADC are based upon either the increased contribution of signal from the intracellular compartment where tissue water is more restricted (Moseley, 1990; Mintorovitch, 1991; Benveniste, 1992), or an increase in the tortuosity of the extracellular compartment (Hossmann, 1994; Latour, 1994; Norris 1994; Verheul 1994). The latter theory is, however, controversial due to the small ratio of extracellular to intracellular water (approximately 1:20) The relationship between the changes observed in diffusion-weighted images and the development of ischaemic injury is intrinsically related to the physiological and metabolic processes that occur. The use of diffusion-weighted imaging (DWI) in understanding these mechanisms has proved invaluable especially in studies in which this technique is combined with other imaging methodologies that provide complementary information concerning such processes as energy metabolism and cellular acidosis (Back, 1994). Care must however be taken when comparing ADC data from different laboratories since anisotropy-related effects related to the directions along which the diffusion gradients are applied, need to be considered. The amount of time that is allowed for diffusion-induced dephasing,

known as the diffusion time (Δ-δ/3 in Fig. 2.2), is also significant in the analysis of situations of restricted diffusion. This imaging method has been used in a number of the studies discussed in this thesis in combination with the acquisition of other information such as perfusion and T_1 values.

2.2 Perfusion

2.2.1 Cerebrovascular diseases and the importance of measuring blood flow

Cerebral vascular diseases such as acute strokes are one of the most common causes of death and disease in the Western World. There are approximately 250,000 cases of stroke in the UK each year and it is the third largest killer after cancer and heart attacks (1990 statistics). A stroke is a neurological accident in the brain than can result due to interference with the cerebral blood flow (CBF). A general definition of stroke is that used by The National Survey of Stroke in the USA that is paraphrased and expanded upon here. It is a clinical syndrome consisting of a large number of neurological findings, sudden in onset, which persist for more than 24 hours, and whose vascular origins are limited to the following circumstances (with approximate frequencies given in parentheses):

(a) Thrombotic (60%) or embolic (20%) occlusion of a cerebral artery, resulting in infarction (tissue death, necrosis). A cerebral thrombosis occurs when a blood clot (thrombus) forms in a blood vessel in the brain. A cerebral embolism occurs when a wandering clot or some other particle forms in a blood vessel away from the brain, usually in the heart. The clot is carried in the bloodstream until it lodges in a the cerebral vasculature.

(b) Spontaneous rupture of a vessel resulting in intracerebral (10%) or subarachnoid haemorrhage (10%). The former condition occurs when a defective cerebral artery bursts and floods the surrounding area with blood. A subarachnoid haemorrhage occurs when a blood vessel on the surface of the brain ruptures and bleeds into the space between the brain and the skull.

Signs and symptoms vary according to the extent, duration and the area of brain damage. Cerebral ischaemia describes an inadequate flow of blood in the brain. Symptoms of stroke can range from a passing inability to move a limb, to speech deficiency, limb paralysis, coma and death. Research into the aetiology of stroke with the view to disease prevention and treatment, is therefore of great importance. A non-

invasive means of assessing the blood flow in the brain such as MRI, would contribute much to such studies. The following sections describe the structure and the regulation of cerebral circulation and discuss the development of methods to measure the cerebral blood flow.

2.2.2 Perfusion and the cerebral circulation

The vascular system of the brain can be considered as the most important circuit supplied by the heart within the body. The blood delivers to tissue the substrates such as oxygen and glucose that are necessary for energy metabolism, and extracts the waste products of this process. The human brain weighs approximately 1.4 kg and receives 50-60 ml/100g/min during rest or approximately 750 ml/min in total. Thus nearly 15% of the cardiac output is directed to an organ that makes up only 2% of total body weight. Similarly the oxygen utilisation of the brain is nearly 20% of total oxygen usage. The brain's circulation is supplied via an extensive system of branches that issue from two groups of vessels, the internal carotid arteries and the vertebral arteries. The basilar artery is formed at the junction of the vertebral arteries. These vessels enter the brain at the circle of Willis (Fig. 2.4) and divide to form a dense network of smaller arteries and arterioles before reaching the capillary bed. The diameter of the microcirculation at this stage is less than 100 μm. Anastomoses are the interconnections between the blood vessels that are numerous; the vascular network resembles a meshwork of fine steel wool. At the capillary level, blood flow can be thought of as irrigating or perfusing a volume of tissue. Since flow at the level of the microcirculation is not a vector quantity, the scalar unit of cerebral blood flow (CBF) is described in terms of the volume of blood perfusing a unit volume of tissue per unit time. The most common units are ml/100g/min. The CBF of brain grey matter in man is approximately 60 ml/100g/min (Quarles, 1990).

2.2.3 Circle of Willis

The four principal vessels that enter the brain meet at its base in the circle that was first described by Willis in 1664 (Willis, 1664). Blockage of the middle cerebral artery is a common cause of clinical stroke and can be reproduced in animal models of focal ischaemia (see Section 3.7).

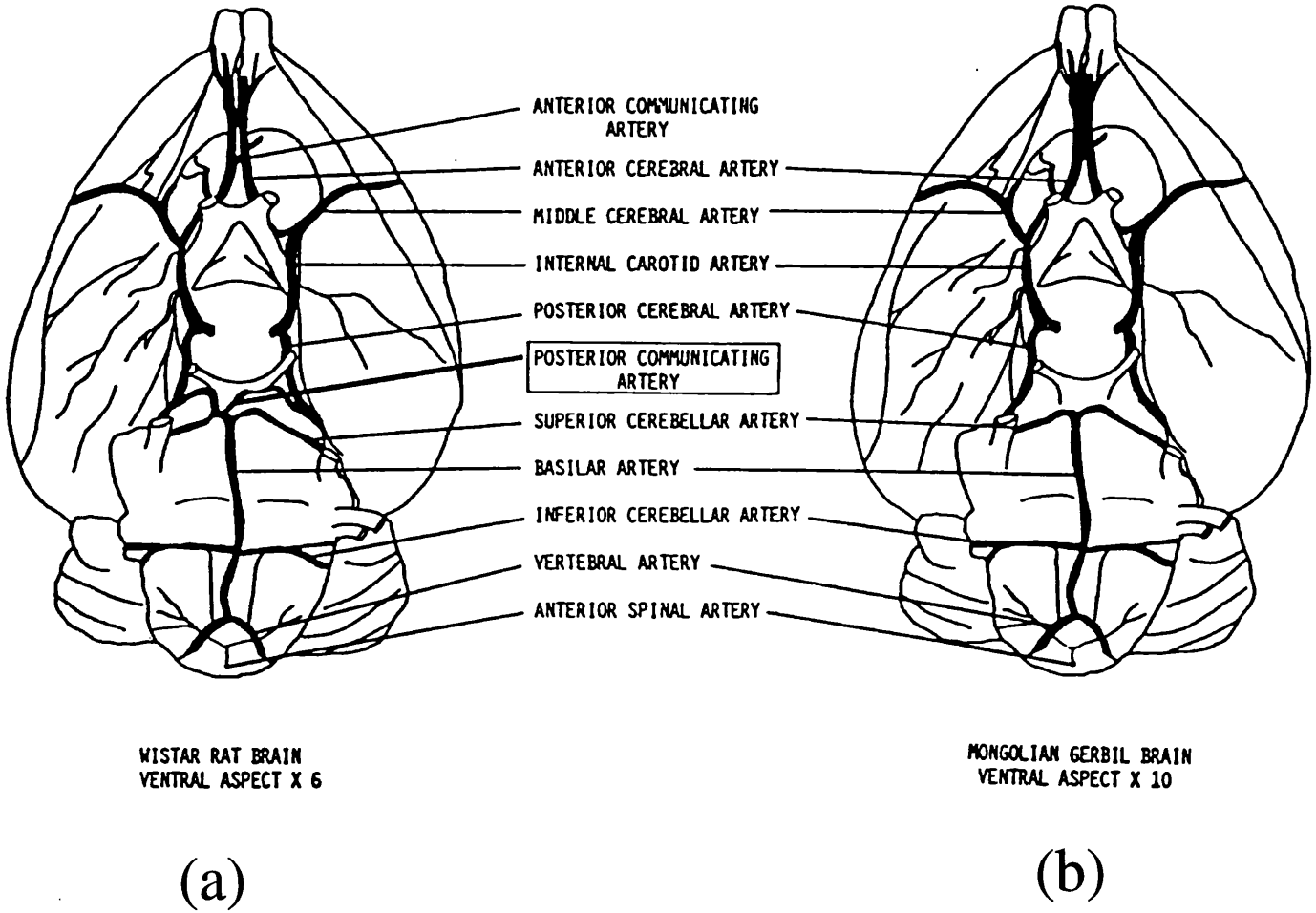

Fig. 2.4 Comparison of the blood system in the circle of Willis in (a) the rat and (b) the gerbil (figure provided by K.L. Allen).

A unique characteristic of the circle of Willis in a gerbil is that there are no significant interconnections between the carotid and the vertebral arterial systems. For this reason, bilateral occlusion of the common carotid arteries induces almost total forebrain ischaemia. Gerbil models are therefore, often used in studies of global ischaemia (see Chapters 4-7). Figure 2.4 shows a comparison of the circulation in the circle of Willis in the gerbil and the more typical circulation of the rat.

2.2.4 Blood brain barrier

The membranes between the circulating blood and the brain possess unique permeability characteristics. The concept of a blood brain barrier (BBB) first described by Ehrlich in 1885 provides the brain with its own mechanism of allowing passage of certain substrates while preventing others. Water and lipid soluble substances readily diffuse across the concentration gradient while other substrates rely on mechanisms of facilitated diffusion (for example, glucose) and active transport (for example, sodium and potassium ions).

2.2.5 Autoregulation

The remarkable power of autoregulation by the blood vessels in the brain maintains the blood flow at a constant level over a wide range of arterial blood pressures. An increase in this pressure or in partial pressures of oxygen and carbon dioxide, results in a decrease in perfusion as a result of mechanisms such as vasoconstriction. Similarly, an increase in cerebral metabolism or a decrease in cerebral blood flow owing to conditions such as hypoxia and hypercapnia, results in vasodilatation. However, below a certain threshold of decreasing arterial blood pressure, the CBF begins to fall because the driving pressure of the blood is insufficient to maintain adequate perfusion. Although autoregulation is usually discussed in terms of the mean arterial blood pressure (MABP), the cerebral perfusion pressure (CPP) is a more precise parameter and is defined as the difference between the mean arterial blood pressure (MABP) and the intracranial pressure (ICP). The ICP has components of pressure due to cerebral venous blood and cerebrospinal fluid (CSF); it increases due to conditions such as reperfusion after cerebral ischaemia. The underlying mechanisms that drive autoregulation have not yet been fully understood.

2.2.6 Techniques for perfusion measurement

A quantitative method for the evaluation cerebral perfusion has obvious experimental and clinical utility. A large number of techniques have been developed most of which rely upon the introduction of an exogenously administered tracer that enters the bloodstream. Knowledge of how the tracer is partitioned between the blood and the brain tissue enables a time dependent change in tracer concentration to be directly related to cerebral perfusion.

An ideal method for CBF quantification would provide accurate measurements in a non-invasive manner with both a high temporal and a high spatial resolution. Most current techniques are compromises between these various factors.

2.2.6.1 Historical background

One of the first attempts to categorise means of perfusion measurement was made by von Schulten in 1885 (von Schulten, 1885). He described the use of direct observations in the pia mater, brain volume recordings and measurements of flow velocity in cerebral vessels. Hill and Bayliss (Hill, 1896) employed a complicated and invasive mechanical set-up in their studies of cerebral circulation in 1887, and Gärtner and Wagner (Gärtner, 1887) investigated venous outflow from the lateral sinus in animals. Thermal clearance techniques (1929) rely on flow dependent changes in the thermal capacitance of a probe inserted into the brain tissue (Rein, 1929; Betz, 1966). Electromagnetic flowmeters placed directly into the blood supply were developed in the late 1930s (Katz, 1938). Lennox and Gibbs measured CBF in humans by sampling venous blood from the jugular vein and measuring differences in arteriovenous glucose and carbon dioxide concentrations.

2.2.6.2 Current techniques

Most of today's methods for CBF measurement are based upon the pioneering work of Kety in the late 1940s (Kety, 1948; Kety, 1951). He based his theoretical work on Fick's Principle of Material Conservation, described by Adolf Fick in 1870, which related the total oxygen absorbed per minute and the arteriovenous oxygen difference to the total blood flow in the lungs. Kety restated this principle in order to calculate the cerebral blood flow by recording the uptake of an inert gas (nitrous oxide) in brain tissue and the arteriovenous difference of oxygen. His interpretation of Fick's Principle

expresses the simple result that the quantity $Q_b(t)$ of any tracer substance extracted from the blood per unit time by an organ is equal to the inflowing amount $Q_a(t)$ of the substance minus the amount $Q_v(t)$ extracted by the venous system and therefore

$$\frac{dQ_b(t)}{dt} = \frac{dQ_a(t)}{dt} - \frac{dQ_v(t)}{dt} = F\left(C_a(t) - C_v(t)\right) \qquad [2.7]$$

where $C_a(t)$ is the instantaneous arterial concentration of the substance (units : [mass/volume]), $C_v(t)$ is the corresponding venous concentration and F is the total cerebral blood flow (units : [volume/time]). If tracer diffusion is not significantly limiting, the tracer in the capillary blood that enters the tissue compartment can be considered to have reached equilibrium with the surrounding tissue at the time of its exit. The venous concentration can then be related directly to the tissue concentration in the region (C(t); units [quantity/mass]) and formulated as

$$C_v(t) = \frac{C(t)}{\lambda} \qquad [2.8]$$

where λ is the tissue:blood partition coefficient. Hence one can obtain an expression for the differential change in the indicator concentration

$$\frac{dC(t)}{dt} = f\left(C_a(t) - \frac{C(t)}{\lambda}\right) \qquad [2.9]$$

where f is the cerebral blood flow (units : [volume/mass/time]). In order to determine flow, the progressive wash-in (saturation) or wash-out (desaturation) of a tracer can be monitored. Alternatively, one can wait for the steady state to appear when the brain and the tracer reach a virtual equilibrium. An integrated form of Eq. [2.9] will then provide a measure of the flow.

2.2.6.3 Global measurements

The previous theory was used by Kety to obtain a global measurement of the blood flow in the human brain by means of inhalation of nitrous oxide (N_2O) (Kety, 1948). The differential rates of change in the arteriovenous concentrations of N_2O can be directly measured. In following the uptake rather than the wash-out of the tracer, the method differed from later clearance techniques. The amount of tracer taken up by the brain $Q_b(t)$ can be determined by allowing inhalation until a steady state has been established

with brain tissue and blood in equilibrium. At this point in time, the following relationship applies where W is the weight of the brain.

$$Q_b(t) = C_v \lambda W$$

[2.10]

The inhalational method was employed in order to obtain a global CBF measurement in humans of 54±12 ml/100g/min (± standard deviation [SD]).

2.2.6.4 Regional measurements

The brain being such a heterogeneous and complex organ is susceptible to a great variety of localised pathologies. A means of assessing CBF on a regional rather than a global basis is therefore optimal. Eq. [2.10] can be modified for the concentration of a tracer in a homogeneously perfused tissue region to provide the following expression

$$\frac{dC_i(t)}{dt} = \frac{f_i}{\lambda_i}\left(C_a(t) - C_v(t)\right)$$

[2.11]

where the subscript *i* denotes the region of interest. The Kety equations described previously can be used to provide an expression for the concentration of the tracer in a small tissue region at time, T, at the end of the experiment in terms of the indicator arterial concentration. (Kety, 1951)

$$C_i(T) = f_i \int_0^T C_a(t) \exp\left(\frac{(-(T-t)f_i}{\lambda_i}\right) dt$$

[2.12]

The so-called tissue equilibration techniques make use of this theory for perfusion quantification. Rapidly exchangeable tracers that are completely extracted in a single capillary passage are employed. An alternative but closely related class of methods are the indicator fractionation techniques (Sapirstein, 1958) in which the measurement of the tracer concentration takes place before equilibrium with the venous outflow has been reached.

The regional tissue concentration of the tracer, $C_i(t)$, can be obtained by use of a detector that is sensitive to its passage, for example with the use of a radioisotope in conjunction with the single photon emission computerised tomography (SPECT) imaging technique. Beginning with the initial N_2O studies of Kety, a whole host of alternative tracer and detector set-ups have been employed. Ingvar and Lassen *et al*

(Ingvar, 1961) pioneered measurements with injection or inhalation of radioactive tracers such as ^{85}Krypton and ^{133}Xenon. Lassen's method was employed to provide the first quantitative measurement of blood flow in humans in 1961, with the β-emission of ^{85}Kr counted from the surface of the brain exposed by craniotomy. The stable isotope of xenon in conjunction with computerised tomography (CT) is now a common clinical clearance technique for perfusion measurement.

2.2.6.5 Table of techniques for CBF quantification

The following table summarises the methods of perfusion quantification in animals and humans that have been devised and implemented during the past half a century. The relative advantages and disadvantages of each method are described. The NMR methods discussed in the succeeding chapters are included. A review detailing our historical awareness to the cerebral circulation and describing earlier methods of perfusion measurement can be found in ref. (Bell, 1984).

Technique	Details	Detector	Advantages	Disadvantages	Reference
Nitrous oxide (N_2O) inhalation	inhalation of the highly diffusable gas until steady state reached; sample arterial and venous blood; provides global flow measurement	blood sampling of carotid artery or femoral vein	freely diffusable gas, simple, repeatable technique	requires catheterisation of blood vessels; does not provide regional measurement; need to estimate brain weight	Kety, 1948
^{42}Kr, ^{86}Ra, ^{133}Xe techniques (for example, ^{133}Xe-clearance)	intra-carotid injection or inhalation; follow dynamic changes or wait for steady state; indicator fractionation equations employed for analysis; first method to provide 2D measurements of flow	scintillation detectors or gamma camera	technique was first to provide regional measurements. If sample dynamic clearance, no need to sample arterial blood for input function since tracer is immediately washed out [$C_a(t)=0$].	use of radioactive tracers; limited temporal and spatial resolution; blood sampling required; gases can have anaesthetic effect and some are not freely diffusable. Possibility of unwanted sampling of extracerebral tissue	Ingvar, 1961
Autoradiography	^{14}C or ^{3}H tracers (e.g. ^{14}C-iodoantipyrine); injection, arterial blood sampling, then animal killed; brain sectioned and analysed on radiographic plates; tissue equilibration equations used for analysis (Kety, 1951)	film densitometry or scintillation counters	*gold* standard technique; high spatial resolution (<1 mm^3). Derivative method allows regional glucose utilisation mapping; inexpensive	limited to animal studies; highly invasive; does not allow longitudinal measurements on one animal; tracer is diffusion limited at high flow rates; blood sampling required	Sakurada, 1978
Radiolabelled Microspheres	carbonised or plastic microspheres (outer diameter ≈15μm); injection; spheres lodge in capillaries; arterial blood sampling, then animal killed; brain sectioned; indicator dilution theory used for analysis (Meier, 1954)	film densitometry, scintillation counter or gamma camera	*gold* standard technique; high spatial resolution (<1mm^3); technique averts problems of backflux and recirculation so can delay after injection; allows multiple measurements with use of different labels; inexpensive	limited to animal studies; highly invasive;perfusional changes can alter microsphere distribution; microspheres are diffusion limited at high flow rates; blood sampling required	Warner, 1987
Xe-CT (Computerised Tomography)	technique adapted from ^{133}Xe-clearance; inhalation or injection and tissue saturation, desaturation (washout) or steady state is followed	CT (Computerised Tomography)	freely diffusable; relatively inexpensive for sophisticated imaging; maps of λ (partition coefficient) can also be obtained; used widely in clinical settings; co-registration with anatomical CT images	xenon has mild anaesthetic effect; blood sampling required; poor SNR (approx. 7:1); bone artefact; sensitivity to motion; inability to acquire multiple slices	Drayer, 1978

Table 2.2 Methods of cerebral blood flow measurement I

Technique	Details	Detector	Advantages	Disadvantages	Reference
PET (Positron Emission Tomography)	injection or inhalation of positron-emitting, short-lived isotopes such as ^{15}O-labelled water or butanol; coincidence counting of annihilation photons from these positron-emitting tracers. Kety equilibration equations used for analysis	gamma camera arrays (paired opposing detectors); modern scanners employ rotating arrays of paired barium fluoride detectors	simultaneous measurements of perfusion and also cerebral metabolism (e.g. oxygen and glucose utilisation)	relatively invasive; most quantification techniques still rely on arterial blood sampling; poor spatial resolution (16-500 mm^3) compared to NMR; expensive; requires co-ordinated multidisciplinary effort; diffusion-limitations of water (incomplete extraction at high flows)	Powers, 1985
Hydrogen (H_2) clearance	polarised platinum electrodes inserted into exposed animal dura tissue; air and H_2 mixture inspired until saturation; switch to room air and follow tissue desaturation; electric current related to H_2 that reaches the electrode. Kety tissue equilibration equations used for analysis.	reference electrodes (Ag/AgCl) set up voltage (≈500 mV) that oxidises H_2; H^+ ions diffuse through the tissue to the platinum cathode	H_2 is a freely diffusable tracer; permits multiple, repeated measurements at approx.10 minute intervals; small volume of tissue sampled (<3mm^3) so highly localised measurement	limited to animal studies; electrode sensitive only to cortical depths; electrode insertion is invasive procedure; variation between flows measured with this technique and other methods perhaps due to partial volume effects (see Chp. 5)	Aukland, 1964
Laser Doppler Flowmetry (LDF) [An older implementation of this technique is Trans-cranial Doppler (TCD)]	flow-induced frequency shift between transmitted and reflected beams of low-power laser light; either tissue implantation or cranial windows; method relies on Doppler Shift due to movement of red blood cells (RBCs) in microcirculation; final signal is related to RBC velocity and RBC concentration	small scale fibre optics to illuminate and sample reflected laser light	samples changes in microcirculatory flow; highly localised measurement (<1 mm^3); method could be used clinically on neonates; measurement is proportional to flow	limited at the moment to animal studies; invasive insertion of optics; very motion sensitive; only qualitative changes in CBF can be determined; correlation with other techniques therefore not easy	Kaneko, 1986

Table 2.2 Methods of cerebral blood flow measurement II

Technique	Details	Detector	Advantages	Disadvantages	Reference
Near-Infra-red Specroscopy (NIRS)	Level of blood oxygenation affects NIR absorption-characteristics of haemoglobin; transmitting and receiving optodes placed on skull	infra-red CCDs (charge-couple-devices)	non-invasive method; used clinically on neonates; high spatial resolution ($\approx 1mm^3$); simultaneous measurement of blood volume, oxygenation and flow; potential for tomographic imaging	relative CBF changes only; a number of assumptions to quantify flow; currently, technique provides measurements that are localised to cortical areas	Edwards, 1993
SPECT methods (single photon emission CT)	intravenous injection of diffusable, γ-ray-emitting short-lived tracers such as ^{123}I-labelled amines and ^{99}Tc-HMPAO; arterial blood sampled for input function; indicator fractionation equations employed	arrays of fixed sensors or rotating gamma camera	highly diffusable tracers; technique is used clinically; advantage over Xe-CT that is can be used to acquire multiple slices; co-registration with anatomical CT images	poor spatial resolution ($2\text{-}6cm^3$); some tracers require high doses; blood sampling required; expensive technology; kinetics in the brain of e.g. ^{99}Tc-HMPAO remain to be completely determined	Holman, 1987
NMR methods I: non-diffusable intravascular, paramagnetic agents (known as dynamic susceptibility contrast imaging (DSCI))	intravenous bolus injection of MRI-visible tracers such as $(Gd\text{-}TPA)^{-2}$; tracers affect relaxation and susceptibility; T_1/T_2 weighted pulse sequences track dynamic tissue concentration of the tracer; arterial blood sampled for input function; quantification by determination of mean transit time (MTT) and blood volume (CBV) . Steady state methods (using iron based tracers) can also be used to provide values of rCBV.	MRI scanner; T_1/T_2-weighted rapid pulse sequences such as EPI, FLASH	high temporal and spatial resolution of proton MRI; provides CBV and MTT information; can obtain non-quantitative rCBV information by injection, then imaging; co-registration with anatomical MRI images	tracers are not freely diffusable so a non-ideal measure of local tissue perfusion; in order to quantify flow, require MTT and accurate measurement of arterial input function is crucial; toxicity places limits on administered doses; indicator recirculation needs to be taken into account	Rosen, 1990

Table 2.2 Methods of cerebral blood flow measurement III

Technique	Details	Detector	Advantages	Disadvantages	Reference
NMR methods II: diffusable agents	injection or inhalation of MRI visible diffusable tracers such as ^{19}F and D_2O; follow dynamic tissue tracer concentrations	MRI scanner; rapid pulse sequences	freely diffusable tracers therefore potentially provides a measure of local tissue perfusion; co-registration with other MRI images	toxicity places limits on administered doses; indicator recirculation needs to be taken into account; SNR is low so resolution is limited (normally spectroscopy is employed); currently, limited to animal studies	Bolas, 1985; Detre, 1990
NMR methods III: arterial spin labelling methods (*pulsed* and *continuous*). These techniques are discussed in detail in Chp. 3, 4 and 5 Techniques include *continuous* spin tagging and the *pulsed* techniques, FAIR, UNFAIR, EPISTAR, PICORE	inflowing arterial blood water spins labelled with respect to static tissue water; modified Bloch equations predict resulting changes in tissue magnetisation; either continuously invert flowing spins and measure steady state (*continuous*) or dynamically label blood, wait for inflow, then image (*pulsed*); must eliminate signal from bulk arterial spins and only detect tissue magnetisation; subtraction of flow sensitive image and flow-insensitive image.	MRI scanner; rapid pulse sequences (EPI, FLASH) modified to include arterial spin labelling pulses;	tracer is endogenous, freely diffusable tissue- water therefore non-invasive; high temporal and spatial resolution; can be used clinically; *continuous techniques* - perfusion contrast-to-noise increased with respect to pulsed methods; *pulsed techniques* – low RF power deposition; MTC effects less significant; transit time effects less significant; co-registration with other MRI techniques such as DWI, NMR spectroscopy, functional MRI etc.	diffusion limitation of water at high flow rates; assumptions involved with quantification; flow signal is only 1-4% of original signal so require good SNR continuous techniques – high RF power deposition; MTC effects significant; transit time effects of blood flowing from labelling site; *pulsed techniques* - perfusion contrast-to-noise reduced with respect to *continuous* techniques	Detre, 1992; Edelman, 1994; Wong, 1997

Table 2.2 Methods of cerebral blood flow measurement IV

III PERFUSION

As Chapter 2 has discussed, perfusion yields important information regarding tissue status and function. Many of the methods of CBF measurement listed in Table 2.2 are invasive and are subject to various limitations. This chapter describes the theory and implementation of the non-invasive spin-tagging methods of CBF quantification that offer the benefits of the improved spatial and temporal resolution of MRI.

This chapter is arranged in the following manner. The methodology of the spin-tagging approach is described and the principal variations of these techniques are then introduced together with examples of their experimental implementation. The major systematic errors that need to be taken into consideration for accurate quantification are discussed and the effect of their incorporation into the perfusion model is demonstrated with experimental data. Finally, three studies are described that aim to address the implementation, validation and optimisation of the spin tagging techniques.

3.1 Introduction

Perfusion is a fundamental physiological process that is sensitive to tissue viability and function, and provides important information regarding a broad range of pathologies. Traditionally, techniques of blood flow measurement have made use of the wash-in and wash-out kinetics of perfusion tracers. MRI in combination with intravascular tracers such as Gd-DTPA can be used in a similar way to these techniques (see Table 2.2) to obtain information concerning the cerebral vasculature (dynamic susceptibility contrast imaging (DSC-MRI)) (Rosen, 1989; Rosen, 1990; Rosen, 1991). Measurements of cerebral blood volume (CBV) and the mean transit time (MTT) of the tracer through the capillary network are possible if the arterial input function (AIF) can be accurately determined. Direct quantification of flow is, however, difficult with these non-diffusable tracers due to factors such as tracer dispersion and recirculation (Østergaard, 1996). A model of the vascular topology may be necessary for the measurement of the MTT that is a prerequisite for the determination of CBF (Weiskoff, 1993). Deconvolution of the signal-time relationship with the arterial input function is required and although studies have reported absolute CBF values using such methods (Rempp, 1994; Schreiber, 1998), relative or cross-calibrated flows may prove to be the only realistic measurement with DSC-MRI (Weiskoff, 1993; Østergaard, 1998). The technique is also hampered by its invasive and dynamic, character that necessitates a

trade-off between temporal resolution and SNR. The first pass of the tracer in the tissue volume of interest (VOI) and the dynamic changes associated with the AIF both require accurate characterisation with rapid sequential imaging during the wash-in and wash-out of the tracer.

The past 10 years has seen the development of alternative, non-invasive NMR techniques for quantitative measurements of cerebral perfusion that use tissue water as an endogenous, freely diffusable tracer. The techniques are based on the differentiation of flowing arterial water spins and static tissue spins by the magnetic labelling of one compartment with respect to the other. The blood water spins are delivered to the brain voxel where they are extracted from the capillary bed and join the larger pool of tissue water. The exchange between the magnetically differentiated water in blood and tissue leads to a change in tissue magnetisation that can be detected by MRI. The goal of the so-called arterial spin-labelling (ASL) methods is to extract and analyse the flow-related magnetisation change. The *tagged* images are alternated with *control* images in which the flow label is not applied. The signal difference between these two images directly reflects local quantitative perfusion since the static tissue signal is eliminated. The sensitivity of the ASL method is an order of magnitude smaller than for DSC-MRI (signal changes of approximately 1-5% and 30-40% for ASL and DSC imaging respectively).

There are two distinct classifications of the ASL techniques: continuous and pulsed. Continuous arterial spin labelling (CASL) methods utilise the tagging of arterial blood water at the level of the feeding arteries by continuous saturation (Detre, 1992) or, more commonly, by inversion using adiabatic fast passage (AFP) (see Section 1.4.1; Dixon, 1986). The blood arriving at the imaging plane in the brain contributes to a steady state level of tissue magnetisation that is lower than the equilibrium level by an amount that is proportional to perfusion.

Pulsed arterial spin labelling (PASL) techniques utilise a single, relatively short RF pulse to create the magnetic label. Variants of this non-steady-state classification of techniques have been developed that invert a thick slab of tissue proximal to the imaging slice so that the inflowing arterial blood is inverted with respect to the static tissue. During the subsequent delay period denoted the TI interval, the tagged blood flows into the imaging plane and the resultant, dynamic change in magnetisation is

related to the delay and to the level of perfusion. The PASL techniques of EPISTAR (Edelman, 1994), PICORE (Wong, 1997) and UNFAIR (Helpern, 1997) are based upon this approach and differ with respect to the spatial localisation of the inverted slab and the combination of RF and gradient strength employed in the control image. A conceptually similar approach to these PASL techniques is the variant proposed by Kwong *et al.* and later, Kim who denoted it the flow-sensitive alternating inversion recovery (FAIR) technique (Kwong, 1992; Kwong, 1995; Kim, 1995), in which the tissue is inverted with respect to the blood during the tagging experiment and the signal detection takes place within that zone of inverted tissue. The flow-weighted signal is obtained by the acquisition of an inversion recovery (IR) image with a *slice selective* inversion that creates the magnetic label. This image is subtracted from a *non-selective* IR image in which both the blood and tissue pools are inverted so that the difference signal reflects the magnetisation delivered by flow to the tissue voxel during the TI interval.

The flow-induced signal is only a small proportion of the overall signal (approximately 1-5%) and the isolation of this signal places great demands on the MRI system. Both continuous and pulsed ASL techniques potentially suffer from a variety of systematic errors. These will be described in this chapter as they became apparent upon implementation of the techniques. The sources of error differ in their significance between the various methods and include transit time effects, MTC and vascular contamination.

3.2 The flow models

The quantification of perfusion using the methods of ASL is dependent on the formulation of a realistic model that describes the combined effects of kinetics and relaxation during the experiment. Two approaches have been devised to model this situation, the T_1 model and the General Kinetic Model. These will be described in turn.

3.2.1 The T_1 model

In the original study of continuous labelling, Detre *et al.* described the experiment in terms of the differential, longitudinal Bloch equations (Detre, 1992). The fundamental relaxation-magnetisation relationships were modified to include the effects of flow and magnetisation transfer. The principal assumption of this model is that of single

compartment kinetics. A *well-mixed compartment* is, thereby, predicted in which the equilibrium ratio of water concentration in the tissue and venous pools remains constant as the freely diffusable tracer (water) is undergoing rapid exchange even though the total tissue concentration is changing as a function of time (the *fast exchange* limit). The concentration ratio of water at equilibrium is defined as the blood:brain partition coefficient, λ, and is defined as (ml of water/g of brain tissue)/(ml of water/ml of blood) and possesses units [ml/g]. This parameter is assumed in this work to have a uniform value of 0.9 ml/g (Herscovitch, 1985). Figure 3.1 displays a schematic representation of the tissue and blood compartments and their description according to the T_1 model. The effects of magnetic transfer contrast are also depicted with rate constants describing the transfer between the tissue and macromolecular pools.

The flow-modified Bloch equations with consideration of the MTC effect, are described by the following relationship (see legend of Fig. 3.1)

$$\frac{dM}{dt} = \frac{M_0 - M(t)}{T_1} + fM_a(t) - \frac{fM(t)}{\lambda} - k_f M(t) + k_r M_m(t) \qquad [3.1]$$

where M_0 in the equilibrium longitudinal (z) magnetisation of tissue water per unit weight of tissue, T_1 is the longitudinal relaxation time of tissue water and f is the blood flow [ml/100g/min]; $M_a(t)$ is the longitudinal magnetisation per unit volume of arterial blood. $M_m(t)$ is the longitudinal magnetisation of the macromolecules per unit weight of brain tissue; k_f and k_r are the magnetisation transfer rates between tissue water and macromolecules (units [sec^{-1}]).

The experimental scheme used for spin tagging defines the initial conditions and the expressions that describe the relaxation of the arterial and tissue pools. The time-dependent expressions for the tissue magnetisation in the tag and control states can, thereby, be determined by integration of Eq. [3.1]. For example, on consideration of the scheme of label creation by inversion of the tissue slice of interest with respect to the inflowing blood, Eq. [3.1] can be rewritten as

$$\frac{dM}{dt} = \frac{M_0 - M(t)}{T_1} + \frac{f}{\lambda}\left(M_0 - M(t)\right) = \left(M_0 - M(t)\right)\left(\frac{1}{T_1} + \frac{f}{\lambda}\right) \qquad [3.2]$$

in the absence of the MTC effect.

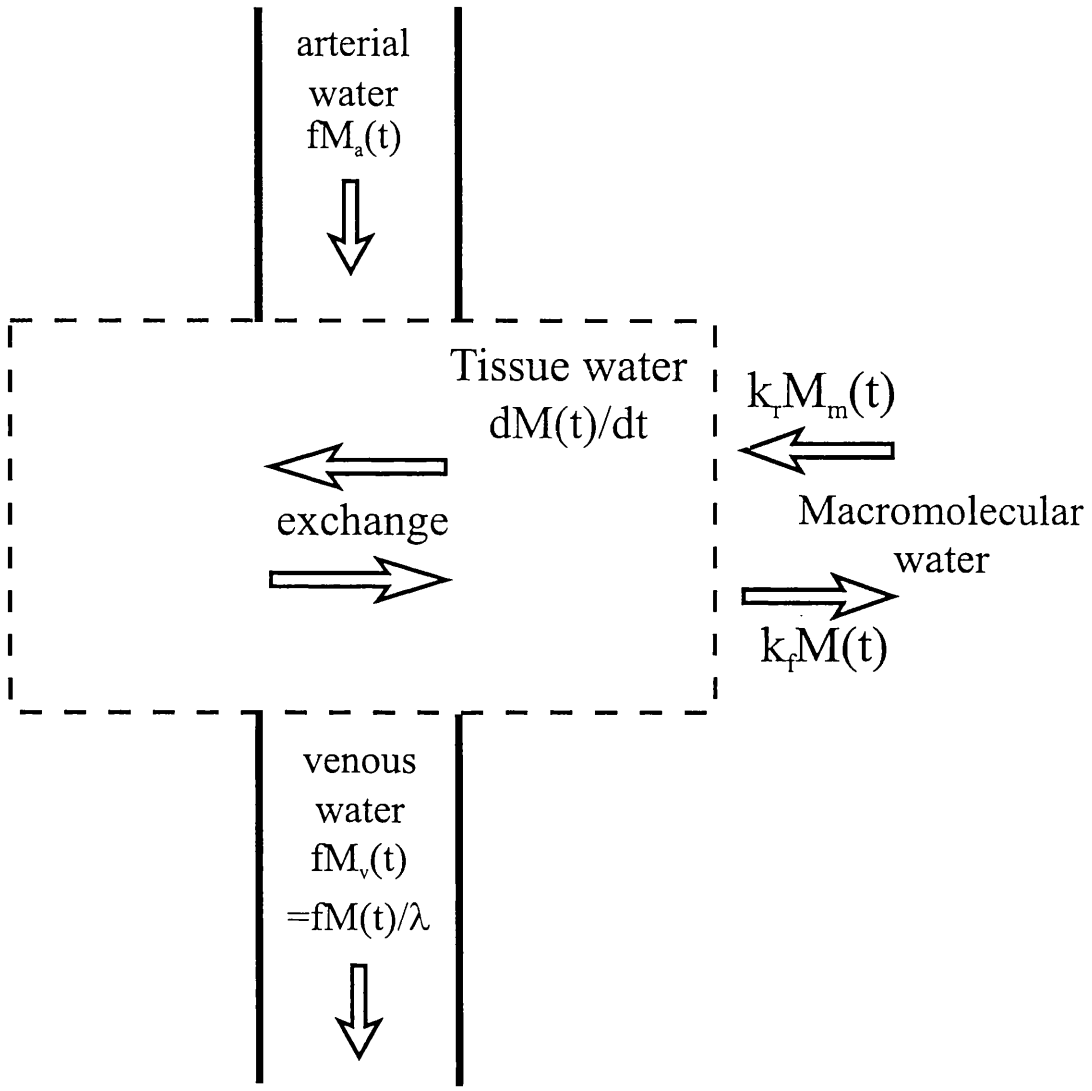

Fig. 3.1 Schematic representation of the inflow and outflow of blood into the idealised tissue compartment (the dashed box). The flow model enables the calculation of the resultant, rate of change of the tissue magnetisation, M(t). The arterial inflow delivers oxygen and nutrients to the tissue compartment, while the venous supply carries away the waste products of metabolism such as carbon dioxide.

It can be easily seen that an apparent tissue relaxation time in the presence of flow, T_{1app}, can be defined in the following manner

$$\frac{1}{T_{1app}} = \frac{1}{T_1} + \frac{f}{\lambda} \qquad [3.3]$$

This is the underlying principle of the ASL methodology and all these techniques essentially manipulate the difference in the relaxation rates in the presence and absence of flow in order to isolate the flow signal.

3.2.2 The General Kinetic Model

The T_1 model has been successfully implemented in describing the various continuous and pulsed labelling strategies (for example, Detre, 1992; Zhang, 1992; Kwong, 1995). Buxton *et al.* have recently described a more general kinetic model that reproduces these analyses with the use of appropriate assumptions (Buxton, 1998). The methodology of the model is framed within the context of the Central Volume Principle (Stewart, 1894) and the associated indicator-dilution theory that has been principally applied to intravascular tracers (Meier, 1954; Østergaard, 1996). The signal difference is considered as a quantity of magnetisation that is carried to the voxel by arterial blood and cleared by venous outflow. To these fundamental kinetic processes considered by previous indicator-dilution treatments, is added the magnetisation decay due to tracer relaxation and the extraction of the tracer from blood to tissue. The magnetisation difference can be mathematically described as a convolution of the arterial input function, denoted in this treatment as c(t), and the clearance terms combining relaxation, extraction and venous outflow so that the following relationship applies

$$\Delta M(t) = 2M_0^a f\left(c(t) \otimes [r(t)m(t)]\right) \qquad [3.4]$$

where r(t) is the residue function that describes the fraction of the delivered magnetisation that is present in the voxel at time *t*, m(t) is the magnetisation relaxation term and M_0^a is the normalised equilibrium magnetisation of the arterial component. By splitting the delivery and clearance terms in this manner, the kinetic approach gains an advantage over the T_1 model in that it facilitates the manipulation of the central assumptions of the ASL methods by substituting the terms in Eq. [3.4] with more realistic expressions. The general kinetic model places a stronger emphasis on the

perfusion signal's blood related origin than the T_1 model, which concentrates on its final state within the tissue. This is due to the general model's consideration of the overall history of the evolution of the magnetisation difference, and the majority of the lifetime of the water spins before imaging are spent in the blood compartment. The units of the measured perfusion rate using the kinetic model are, therefore, more correctly defined as ml/100g/ml-of-blood (Buxton, 1998). These units can be readily converted to the standard form by normalisation to the tissue mass by using tissue density.

For the remainder of this work, the T_1 model will be principally used to consider the analysis and implementation of the continuous and pulsed techniques. These techniques are described in turn in the following sections.

3.3 The continuous technique

3.3.1 Theory

Table 3.1 summarises the different arterial spin labelling methods. The steady state technique is most commonly implemented with continuous adiabatic inversion by AFP. The tagging pulse selectively inverts the arterial water spins in the neck if the B_1 RF irradiation is applied in the presence of a slice gradient and at a frequency offset, $\Delta\omega$, which is much larger than the water bandwidth. The pulse duration is in the order of seconds in order to reach the steady state; a significant magnetisation transfer effect develops as the coupled macromolecular pool becomes saturated. The resultant reduction in signal can be an order of magnitude greater than any flow-induced change. CBF quantification is not affected by the MTC-related signal change if a proper control experiment is performed with the RF irradiation applied at the symmetrically opposite plane with respect to the imaging slice (Zhang, 1992). The effects of cross-relaxation must, however, be included in the analysis of the Bloch equations (Eq. [3.1]). If complete saturation of the macromolecular pool (i.e. $M_m = 0$) is achieved, subtraction of the tagged image from the control image provides a magnetisation difference, $\Delta M(t)$, during the application of the pulse that is given by the following expression

$$\Delta M(t) = M^1(t) - M^2(t) = \frac{2\alpha_0 f}{\lambda} M_0 T_{1sat}\left(1 - e^{-t/T_{1sat}}\right) \qquad [3.5]$$

where $M^1(t)$ and $M^2(t)$ are the magnetisation values in the control and tagged images respectively, $t = 0$ at the start of the application of the inversion pulse and α_0 is the

labelling efficiency or degree of inversion and takes a value of 1.0 for ideal inversion and 0.5 for saturation; T_{1sat} (or more exactly, $T_{1sat}(\omega_1,\Delta\omega)$) is the longitudinal relaxation in the presence of off-resonance irradiation applied at frequency offset $\Delta\omega$ and a B_1 magnetic field strength defined by the associated angular frequency of nutation, ω_1, for proton spins. The relationship between this relaxation time and T_{1app} is

$$\frac{1}{T_{1sat}} = \frac{1}{T_{1app}} + k_f \qquad [3.6]$$

It can be shown that $T_{1sat} \approx M^1(t)T_{1app}/M_0$ (Zhang, 1995; McLaughlin, 1997) and this treatment allows the magnetisation difference to be expressed in terms of the observed longitudinal relaxation rate.

The expression described in Eq. [3.5] as a function of time is plotted in Fig. 3.2 and it can be seen that for $t >> T_{1sat}$, a steady state is reached and the exponential term is eliminated. In the steady state, the flow can then be expressed in three ways:

$$f \begin{cases} = \dfrac{\lambda \Delta M(t)}{T_{1t}\left(M^2_{ss} + (2\alpha_0 - 1)M^1_{ss}\right)} & (a) \\ = \dfrac{\lambda \Delta M(t)}{2\alpha_0 M_0 T_{1sat}} & (b) \\ \approx \dfrac{\lambda \Delta M(t)}{2\alpha_0 M^1_{ss} T_{1app}} & (c) \end{cases} \qquad [3.7]$$

where M_{ss}^1 and M_{ss}^2 are the steady state levels in the control and tagged images respectively (so that $M^1(t) \rightarrow M^1_{ss}$ and $M^2(t) \rightarrow M^2_{ss}$) and T_{1t} is the intrinsic T_1 of the tissue in the absence of cross-relaxation with the macromolecular compartment (see Section 3.5.3.1).

Technique	CASL or PASL	Tagged experiment	Control experiment	Tagged experiment (schematic)	Control experiment (schematic)	Notes
Steady-state / continuous	CASL	proximal AFP inversion at level of feeding arteries	distal AFP inversion	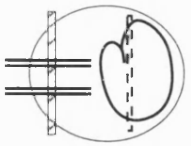	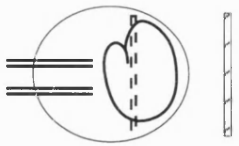	post-labeling (w) delay reduces δ-sensitivity; AM control or 2-coil technique allows multi-slice acquisition
FAIR	PASL	slice-selective inversion	non-slice-selective inversion		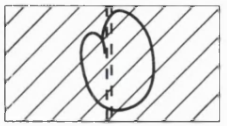	amenable to multi-slicing; susceptible to slice profile imperfections
UNFAIR	PASL	non-selective followed by a selective inversion	dual non-selective inversion (360°)	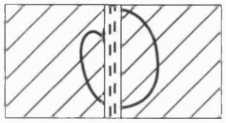		see FAIR
EPISTAR	PASL	proximal slab inversion	distal slab inversion or double inversion	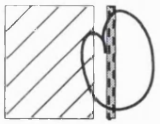	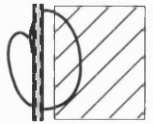	see FAIR
PICORE	PASL	proximal slab inversion	inversion pulse applied without selective gradient	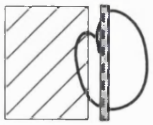		see FAIR
QUIPSS / QUIPSS II	PASL	bolus time-width defined by saturation pulse in the imaging (QUIPSS) or tagging region (QUIPSS II) of the above pulse sequences		see Fig. 1 in (Wong, 1998a)		generic means of reducing δ-sensitivity of the PASL techniques

Table 3.1. Principal classifications of the arterial spin labeling techniques. δ denotes the transit time. The schematic representations of the experiments are shown relative to a sagittal view of the brain. The dashed lines represents the area of the imaging slice; ▨ depicts the inverted area and ▬ denotes the pre-saturation of the imaging slice. The schematic representation of the CASL tagging experiment displays a labeling plane that intersects the carotid arteries.

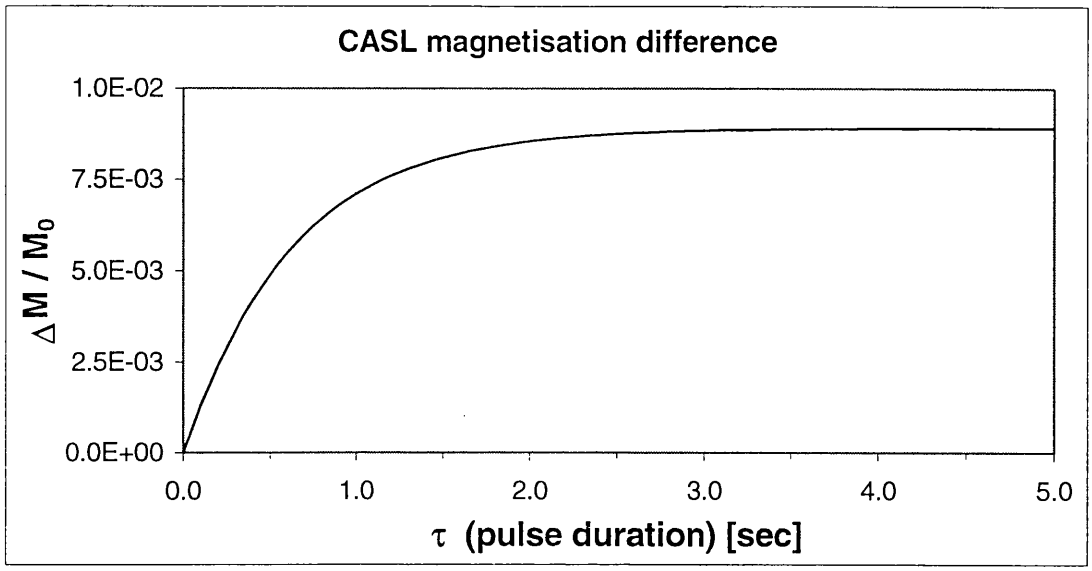

Fig. 3.2 Relationship of the normalised CASL magnetisation difference, $\Delta M(t)$, with the increasing pulse duration, τ, according to Eq. [3.5], showing the build-up of the steady-state for $\tau >> T_{1sat}$ (T_{1app} = 1.7 sec, k_f = 1.0 sec-1; T_{1sat} = 0.63 sec from Eq. [3.6]).

3.3.2 Implementation

The CASL sequence was implemented on the vertical bore 8.5T system in our laboratory (SMIS console, Guilford, UK) with the use of constant 5 sec AFP pulse in the presence of a gradient of approximately 680 Hz/mm (1.6 G/cm). The pulse was applied at a frequency offset of approximately 9 kHz in order to tag at the level of the carotid arteries in the neck of the animal. The power of the tagging pulse at this frequency offset was varied on a rat until the MTC-related signal reduction reached a plateau level. A RF irradiation level of approximately 320 Hz (75 mG) was thereby obtained in order to achieve complete saturation of the macromolecules. The switch between the tagged and control images was mediated by alternating positive and negative application of the longitudinal 5 sec inversion gradient. Experiments on a static water phantom indicated the absence of a significant eddy current effect as a result of this gradient. The degree of inversion, α_0, was determined in the rat according to the method of Zhang *et al.* (Zhang, 1993) that uses images of the carotid arteries at various tagging amplitudes. A labelling efficiency of α_0=0.71 was thereby determined (data not shown).

A perfusion quantification experiment was performed (Male Wistar rats, weighing approximately 130-150 g; n=5). A TurboFLASH sequence was used for image acquisition (echo time, TE = 2 ms; repetition time, TR = 5 ms) (see Section 3.7 for further pulse sequence details). A transverse pilot scan aided the positioning of the labelling plane in the neck. In order to obtain absolute flow values, the T_{1app} relaxation rate was acquired with a TurboFLASH IR sequence (see Section 1.7.3 and Section 3.7). A representative pair of control and tagged images and the accompanying maps of T_{1app} and CBF, are shown in Fig. 3.3. The CSF ventricles are visible in these maps but the CBF map is relatively noisy. High artefactual areas of signal were also observed in the flow map and a cortical flow of approximately 200 ml/100g/min was measured. The apparent overestimation of perfusion was due to the systematic errors that are associated with the spin tagging methods (see Section 3.5).

3.4 The pulsed techniques

3.4.1 Theory

PASL techniques are characterised by a dynamic labelling procedure that is followed by a time delay - the TI time - during which tracer deliverance, exchange and clearance occur. The short inversion pulses (duration 5–15 ms) considerably reduces RF deposition in tissue. MTC effects are minimal but may require consideration especially if longer 360° adiabatic pulses are implemented (Edelman, 1998). The PASL techniques are comparable to the kinetic perfusion methods of wash-in and wash-out (see Section 2.2). The time dependent components of the magnetisation of the tissue and the arterial supply, must be considered in contrast to the continuous techniques that rely on the steady state. Analysis of the T_1 model in this case provides a biexponential expression for the magnetisation difference since both the tissue and the arterial pools are inverted during a stage of the experiment. These compartments will thus relax with their characteristic T_1 values. The same expression for $\Delta M(t)$ is obtained whether the tagged experiment inverts the blood with respect to the tissue (EPISTAR (Edelman, 1994), PICORE (Wong, 1997), UNFAIR (Helpern, 1997)) or vice versa (FAIR (Kim, 1995)). Table 3.1 summarises the different methods of arterial spin labelling.

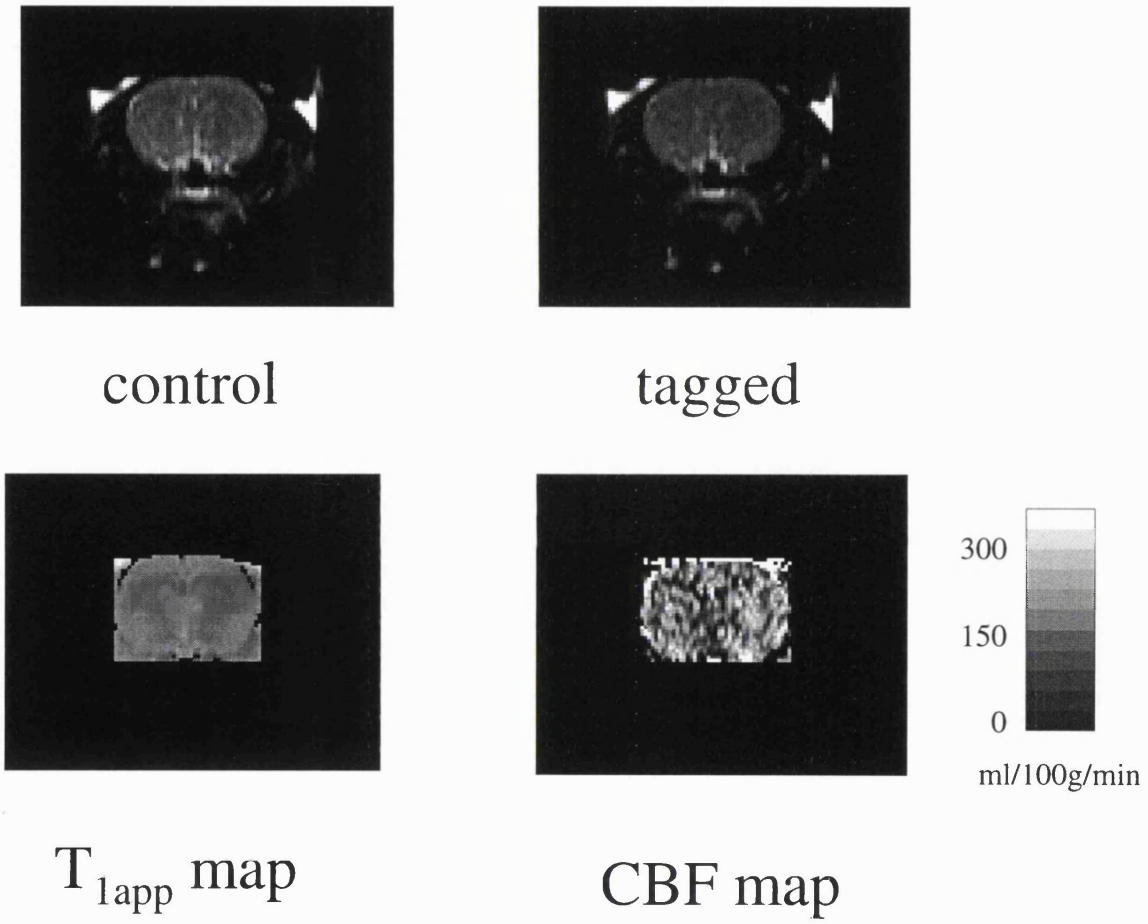

Fig. 3.3 Continuous arterial spin tagging experiment in a rat, showing the control and tagged images and the corresponding CBF map. The T_{1app} map is also displayed which is used in the calculation of the CBF (Eq.[3.6]).

This expression is described by

$$\Delta M(t) = 2M_0\alpha_0 \frac{f}{\lambda}\left[\frac{\exp(-t/T_{1app}) - \exp(-t/T_{1a})}{\frac{1}{T_{1a}} - \frac{1}{T_{1app}}}\right] \qquad [3.8]$$

where T_{1a} is the T_1 value of blood, t = 0 at the start of the inversion and ΔM(t=TI) is the relevant magnetisation difference where TI represents the delay between the label creation and the image acquisition. Chapter 4 and the accompanying Appendix A further describes the analysis of the T_1 model in the case of the PASL techniques. In order to obtain a quantitative flow measurement, it is necessary to acquire the tagged and control images over a range of different TI delays so that the data can be fitted to the biexponential expression.

3.4.2 Implementation

The PASL techniques of FAIR, UNFAIR and EPISTAR were implemented on the horizontal bore 2.35T scanner in our laboratory (SMIS console). UNFAIR is similar to the FAIR technique and makes use of an additional non-selective inversion pulse applied immediately before the selective and non-selective pulses (Helpern, 1997). The inflowing blood spins instead of the static tissue in the slice, are alternately inverted (tagged image) and non-inverted (control image) and, in this sense, the technique is more similar to EPISTAR than to FAIR.

3.4.2.1 Flow Phantom I

The flow sensitivities of the PASL techniques were validated with use of a simple flow phantom consisting of 3 mm diameter plastic tubing wrapped around a water phantom. Water was pumped through the tube with a syringe pump (IVAC, USA) at a rate of approximately 2 mm/sec. A spin-echo EPI sequence was used for image acquisition (TE=37.5 ms) and tagged and control images were collected at a range of 6 TI times between 500-6000 ms (imaging slice thickness (slth) in all experiments = 2 mm; FAIR/UNFAIR: selective inversion slth = 5 mm; EPISTAR: inversion slab thickness = 100 mm; Δω = 2 kHz; alternating sign of the tagging gradient). The continuous spin tagging approach was also implemented (tagging offset = 5 mm, Δω = 5 kHz, alternating sign of the tagging gradient). Representative pairs of tagged and control

images acquired at TI = 2000 ms are displayed in Fig. 3.4. The difference between the FAIR and UNFAIR techniques with regard to the labelled compartment can be observed. The disappearance of the signal from the static phantom in the FAIR images and of the flow signal in the other images is on account of the recovery from inversion in the imaging plane that leaves the magnetisation at the null point for TI = 2000 ms (Section 1.7.2). The flow signal in the tagged image is hyperintense due to the subsequent wash-in of uninverted, "fresh" spins. In the UNFAIR images, the magnetisation undergoes a dual inversion (360°) and it is the in-flowing and out-flowing water that is tagged by the inversion pulse. The flow signal in the tagged image is hypointense due to the wash-in of inverted spins into the 360° rotated slice. The different sensitivities of the various techniques to directional flow is visible in the images in Fig. 3.4. The FAIR and UNFAIR images are equally sensitised to both directions of inflow since all the spins outside the imaging slice are inverted. By way of contrast, the EPISTAR technique and the continuous method, employ a unilateral labelling scheme and are, therefore, differently sensitised to directional flow. In both cases, wash-in of labelled spins leads to hypointense signal in the tube due to inversion.

3.4.2.2 Flow phantom II

The characteristics of the FAIR sequence was further investigated on the 8.5T system by varying the flow rate of the syringe pump with the use of the same flow phantom as described previously (slth = 4 mm; inversion slth = 10 mm; TI = 2500 ms; FLASH imaging sequence with TE = 6 ms and TR = 10ms). Subtraction images (selective – non-selective) were obtained at a range of flow velocities.

Regions of interest (ROIs) were drawn around the static phantom and the tube, and a smaller ROI was drawn around the centre of the tube where the distribution of laminar flow velocities will be greatest. The regional data were plotted against a measure of the linear flow velocity calculated using the displayed flow rate of the pump and with the assumption of plug flow (Fig. 3.5). The principal issues of the pulsed techniques are apparent in the data and this aids the understanding of the use of these methods to quantify CBF. An initial delay is apparent in Fig. 3.5 before the magnetisation difference starts to increase with flow velocity. This interval is a manifestation of the transit time effect (Section 3.5).

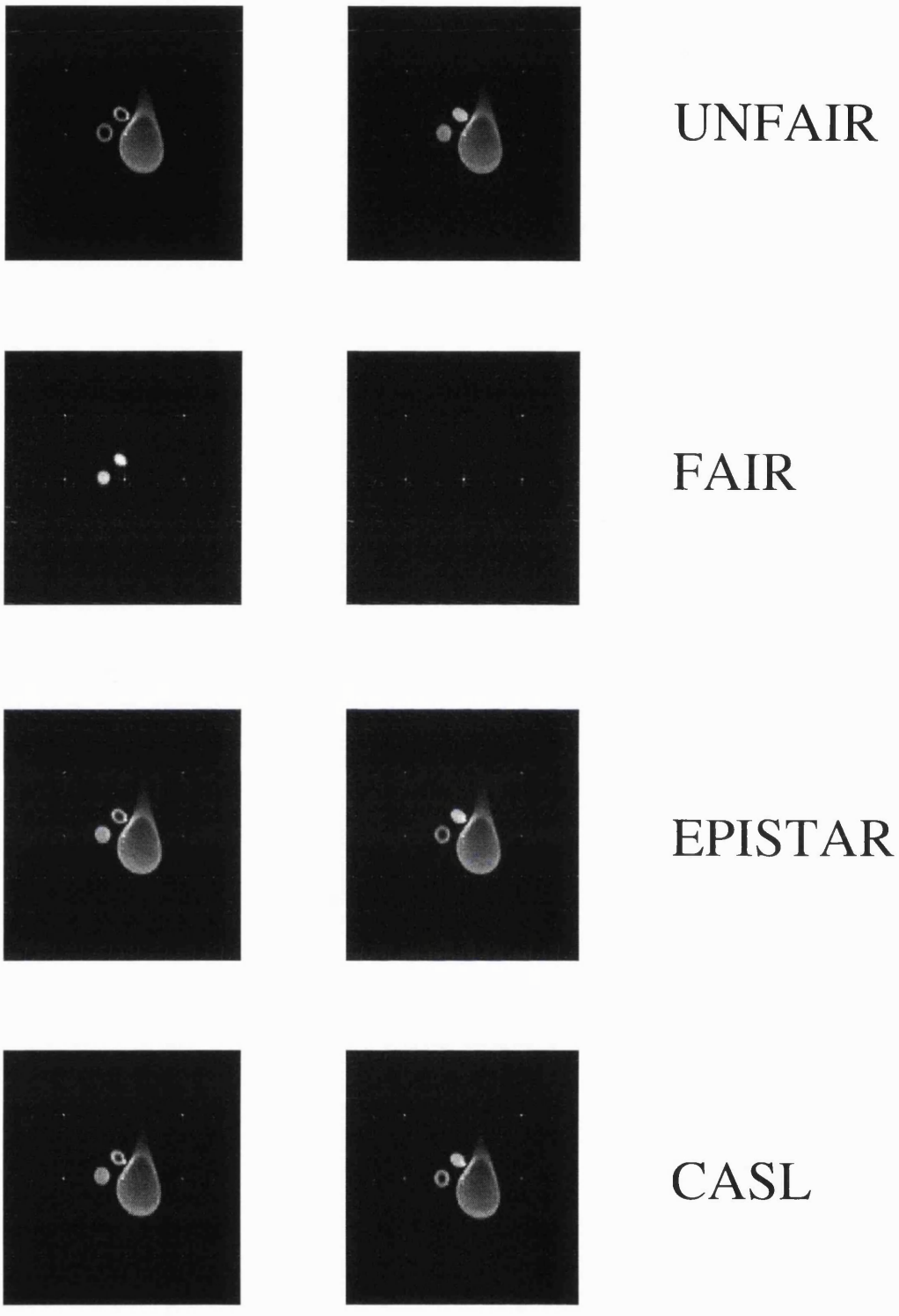

Fig. 3.4 Flow phantom experiment using PASL and CASL techniques with images acquired for TI = 2 sec (T_1[water] ≈ 2.7 sec). Tagged and control images are shown. The tube was wrapped around the central static water phantom so that both flow directions are represented. The signal *ring* sometimes observed around the flow tubes is due to the slower velocities close to the surface of the tube. The static phantom is misshapen due to a susceptibility artefact from an air bubble. The small, regular spaced dots in the EPI images are harmonic frequencies of the leaking clock frequency.

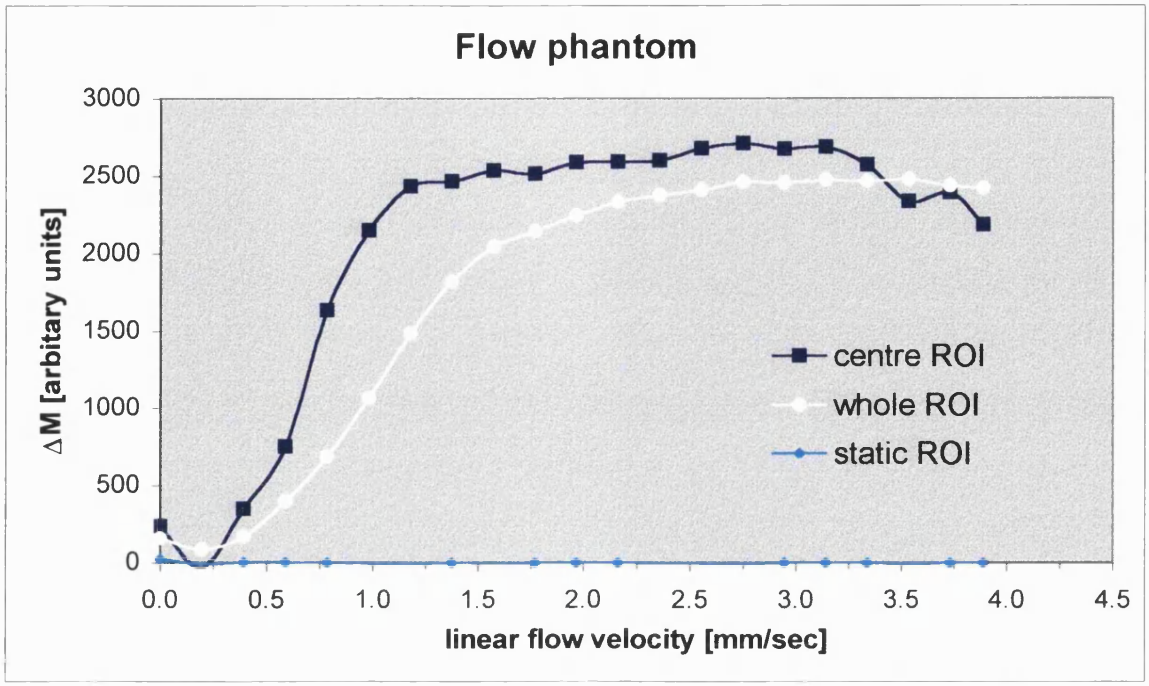

Fig. 3.5 Test of the flow-sensitivity of FAIR using a linear flow phantom. The magnetisation difference (ΔM) is plotted against the linear velocity. Regions of interest were drawn in the centre and around the entire area of the flow tube. It can be seen that the flow-weighted signal rises and reaches a plateau level earlier in the cente ROI than in the whole tube ROI. The latter region will contain a wider variation of laminar flow velocities and the signal behaviour will overemphasise the effect of slower velocities. For CASL techniques, in order to determine of the degree of inversion, α_0, in the carotid artery, this effect must be taken into consideration (Maccotta, 1997). A region in the static water phantom is also shown for comparison.

The difference between the imaging and inversion slice thicknesses (see Section 3.6.1) defines an initial linear velocity, v_i, when flow sensitisation begins is given by

$$v_i = \frac{inv\_slth - slth}{2TI} \qquad [3.9]$$

where slth represents the imaging slice thickness and inv_slth denotes the inversion slice thickness, for the experimental parameters. An approximately linear relationship of the signal with velocity is then subsequently observed. Complete wash-in of fresh spins defines the point when the profile appears to reach a plateau level. This should occur at a velocity, v_f, defined by the following relationship

$$v_f = \frac{inv\_slth + slth}{2TI} \qquad [3.10]$$

For the parameters used in the experiment, v_i=1.2 mm/sec and v_f = 2.8 mm/sec. As the flow rate is further increased, a drop in the signal is observed in the central ROI that contains a greater proportion of the faster moving spins. This is a result of the finite width of the *tag* in the control image (i.e. the non-selective inversion width), which in the case of FAIR, is defined by the B_1 profile of the RF transmitter coil. Fresh spins will, therefore, reach the imaging plane for a sufficient TI interval or spin velocity. This so-called *inflow* effect is discussed in detail in Section 4.2.3 and must be incorporated into the perfusion model.

3.4.2.3 In-vivo study

The FAIR technique has been implemented for the in-vivo perfusion studies described in Chapters 4 and 5, and detailed experimental descriptions are provided in these later chapters. An example of a control data set obtained with a gerbil is provided in this section. Experiments were carried out on the 2.35T system. A series of non-selective/selective image pairs were acquired and fitted to Eq. [3.8]. Image sequence parameters and a description of the data analysis are detailed in Section 4.4. Figure 3.6 displays a representative series of these image pairs. Individual plots of the biexponential fit are also shown for a cortical and striatal region.

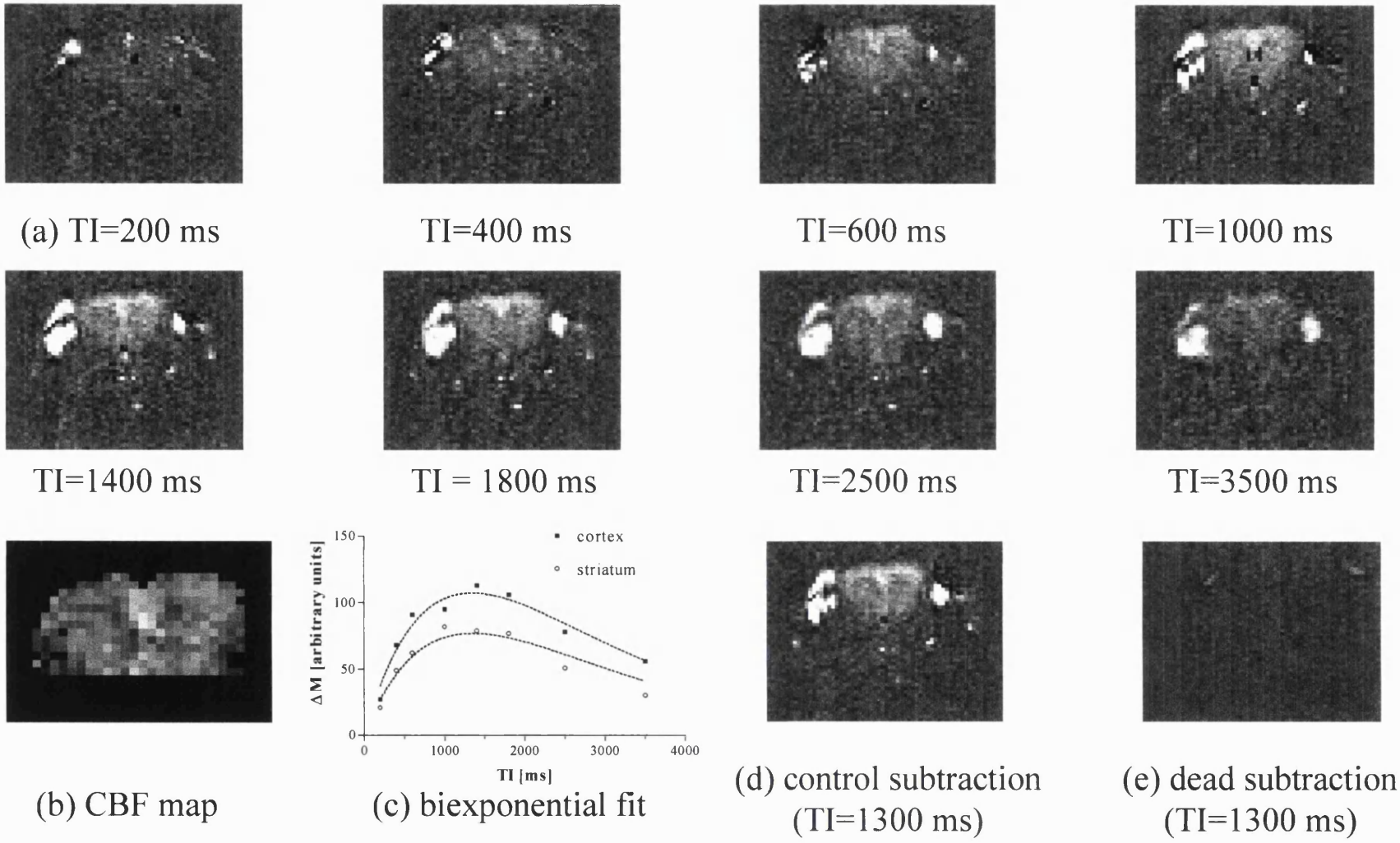

Fig. 3.6 (a) A series of FAIR (modulus) subtractions in a control gerbil obtained at a number of TI delays fitted to Eq. [3.8] (see Section 3.4.2.3). In (b), the corresponding CBF map is displayed and (c) shows the individual biexponential fits for two regions drawn in the TI series of images. In (d) and (e), control and dead subtraction images (ss - ns) are shown for a single TI delay. The bright signal areas in the TI series of images indicate the presence of arteries and possibly, fat and muscle tissue.

3.5 Issues related to perfusion quantification

In this section, the principal systematic errors that are associated with flow determination using the ASL techniques are described. Experimental methods of correction are also presented.

3.5.1 The transit time

The transit time effect essentially describes a loss of the magnetic label due to the physical extent of the tagging procedure. The transit time, δ, representing the delay between the creation of the tag and its arrival at the imaging slice, is expected to be especially significant for the CASL techniques since the tagging plane is normally placed in the neck in order to intersect a major artery. By way of contrast, in the case of the pulsed techniques such as EPISTAR, the inversion slab is positioned close to the imaging slice. Nevertheless, the degree of proximity is still limited by the introduction of systematic errors due to the imperfect slice profiles. In an analogous manner, for practical implementations of the FAIR technique, the width of the inversion slice must be increased with respect to the imaging slice in order to eliminate effects from imperfect edges of the inversion profiles. During the resultant δ time, inflowing blood moves into the imaging plane but will not contribute to the flow signal since these spins are within the inversion slice. The transit time effect reduces the intrinsic sensitivity of the ASL techniques especially to lower levels of flow. Errors will be introduced into the CBF measurements if the effect is not considered in the analysis of the perfusion model (see Section 4.6). Furthermore, it is likely that the transit time will vary significantly across the imaging plane, resulting in a variable attenuation of the ASL signal and this will exacerbate the errors in the quantification process.

3.5.1.1 Reduced transit time modifications

Analogous modifications of the continuous and pulsed methods have been proposed in order to decrease the transit time sensitivity of the techniques. A post-labelling delay is employed that has a dual effect; the delay allows the tagged blood water to reach the tissue compartment and, thereby, reduces the significance of the vascular signal (see the next section) and minimises the effects of variable transit delays. It also allows time for the tagged blood that is flowing through the imaging voxel without exchange, to do so before the time of image acquisition. These blood spins should only contribute to the signal in the distal voxels which contain the capillary exchange sites that are their

eventual destination. This corrective scheme is implemented in the CASL method by simply delaying the image acquisition after the continuous RF irradiation (Alsop, 1996). In the case of the pulsed methods, a delay (the TI time) after the inversion pulse is inherent to the procedure of these techniques but the tagged bolus possesses an undefined width due to the geometric spread and the dispersion of the transit times from the distal end of the inversion slab to the tissue. A slightly different approach is, therefore, needed to reduce the transit time sensitivity for the PASL methods. The modification is known as Quantitative Imaging of Perfusion Using a Single Subtraction (QUIPSS II) and creates a slab of known time width by saturating the tagging region at a time TI_1 after the inversion pulse. An additional delay, TI_2, before the image acquisition then reduces the sensitivity of the method to the transit time in the same manner as the modified continuous technique (Wong, 1997).

3.5.2 Intravascular contamination

The significance of the vascular signal to the magnetisation difference is closely related to the discussion of the previous section since the transit delay determines the time spent by the water spins in the vasculature before entering the tissue compartment at the capillary exchange sites. Two principal sources of intravascular contamination need to be considered; the blood in the major arteries, and the component that is in closer contact with the tissue bed within the arterioles and capillaries.

3.5.2.1 Arterial signal

The most obvious illustration of the *vascular artefact* is the observation of bright focal anomalies in the perfusion images (see Fig. 3.3). The macroscopic blood flow violates the assumption of a well-mixed compartment (Section 3.2.1) and should, therefore, be eliminated from the measured signal. A minimal amount of diffusion weighting ($b < 2$ sec/mm^2) such as that provided by the EPI imaging gradients, should dephase the majority of this signal component.

3.5.2.2 The vascular signal in the smaller vessels

The initial descriptions of the perfusion T_1 model (for example Zhang, 1992) assumed that only the tissue compartment is contributing to the observed signal difference. The combination of imaging and diffusion gradients and the inherently small volume of the vascular compartment (approximately 5% in the rat (Sandor, 1986)) was expected to

reduce the contribution of the blood signal to an insignificant level. The observed tissue-based magnetisation difference then provides a direct measurement of the irrigating blood flow after *back-correction* with the partition coefficient (i.e. $M_v=M(t)/\lambda$). In this sense, the ASL methods measure perfusion as the biologically relevant – *useful* - blood delivered to the voxel since only the exchanged blood water should be considered in the analysis. With the further development of these techniques, the systematic errors associated with the vascular signal have become better understood and characterised. It has become clear that the empirical adjustment of diffusion gradients within the perfusion sequence to dephase the vascular signal (Ye, 1997a), is a sub-optimal procedure. It is also probable that a substantial fraction of the blood spins may not be dephased by these gradients (Henkelman, 1994). It must, therefore, be accepted that the ASL signal is principally sensitised to the exchanged tissue water but will also contain a contribution from the vascular compartment. It can be argued that the blood spins may be justifiably included in the measurement of tissue perfusion as long as they will exchange or have already exchanged across the capillary bed in that voxel (Buxton, 1998). The vascular signal at the capillary level is, thereby, considered as biologically relevant blood signal and should be incorporated in the overall measurement of perfusion in the imaging voxel. The inclusion of this component of the ASL signal must, however, be reflected in a modified analysis of the perfusion model. This is discussed in the next sub-section.

The nature of a particular water spin will be characterised by the NMR parameters that are associated with its environment. The different longitudinal relaxation times of the tissue and vascular compartments can be incorporated into the perfusion model and analysis. The general model has demonstrated that the perfusion measurement is especially sensitive to the time spent by a water spin in the different environments (Buxton, 1998). The differing transverse relaxation rates of the two compartments must also be considered since the relatively long echo times of the commonly used EPI method of image acquisition, will weight the signal towards the blood component (T_2[blood] $\approx$ 200 ms; T_2[tissue] $\approx$ 80 ms at 1.5T (Wong, 1998a)). Moreover, when collecting data at a number of TI delays, the deleterious effect of this resultant bias will be intensified with increasing TI as the influence of the vascular component becomes less significant due to exchange and outflow. This T_2 effect has not been considered in the existing treatments of the ASL methods but will require analysis as the SNR and, hence, the precision of the techniques improve.

3.5.2.3 Quantification of the vascular component

Several authors have attempted to incorporate the blood signal into their analysis of the T_1 model (St. Lawrence, 1997). Alsop *et al.* described the vascular compartment in its role as the arterial input to the tissue exchange sites (Alsop, 1996). However, this treatment neglects the blood water associated with the vascular output of the tissue compartment that does not exchange in the voxel and the tissue water that diffuses back into the vascular pool. Silva *et al.* have attempted to include this signal contribution in their analysis of the continuous technique (Silva, 1997a). The existence of unexchanged blood spins in the outflow of the vascular compartment is intrinsically related to the assumption of a freely diffusable tracer. The extraction fraction, E(f), describes the flow-dependent competitive partition of water spins between the vascular and tissue compartments after equilibrium has been reached. The common assumption of E(f)=1 in the perfusion model has been shown to be invalid for higher flow rates using both tracer kinetics and MRI approaches (Eichling, 1974; Go, 1981; Silva, 1997a; Silva 1997b; Zaharchuk, 1998).

In the following theoretical analysis, an original combined approach was taken in order to model the contribution of both the arterial/tissue interface (input) and tissue/venous interface (output) components of the vascular signal in the smaller blood vessels within the tissue volume. Figure 3.7 depicts a schematic representation of the modified model that can be compared with the standard form shown in Fig. 3.1. This treatment was carried out for the FAIR experiment assuming the following form for the total signal, $S_{TOT}(t)$, from an imaging voxel with a unit volume

$$S_{TOT}(t) = S_{Tissue}(t) + S_{ai}(t) + S_{vo}(t)$$

$$S_{TOT}(t) = M(t)(1-V)\rho_t + M_{ai}(t)V + \left[(1-E(f))M_a(t) + \frac{E(f)}{\lambda}M(t)\right]V \qquad [3.11]$$

where V is the fractional volume occupied by the vasculature (approximately 5%), E(f) is the extraction fraction, and ρ_t is the density of brain tissue in g/cm^3; $S_{tissue}(t)$, $S_{ai}(t)$ and $S_{vo}(t)$ are the signal levels within the unitary voxel from the tissue, arterial-tissue-input and tissue-venous-output compartments respectively (see Fig. 3.7); $M_a(t)$ represents the total normalised magnetisation in the arterial compartment (Section 3.2.1), and $M_{ai}(t)$ is the corresponding magnetisation in the arterial-tissue-input compartment. The expression within the square brackets in the above equation

represents the magnetisation from the vascular output compartment, $M_{vo}(t)$ and contains contributions from the fraction of arterial water that does not exchange ($[1-E(f)]M_a$) and from the tissue water that diffuses back into the vasculature ($E(f)M/\lambda$) (see Fig. 3.7). MTC effects are neglected for the pulsed experiment.

The overall signal difference, $\Delta S_{TOT}(t)$, between the selective and non-selective FAIR images, is provided by the combined signal from the three components, so that

$$\Delta S_{TOT}(t) = \Delta S_{Tissue}(t) + \Delta S_{ai}(t) + \Delta S_{vo}(t) \qquad [3.12]$$

where $\Delta S_{tissue}(t)$ is equal to the normalised FAIR subtraction signal (Eq. [3.8]). The total signal can be calculated for FAIR by following the analyis described in ref. (Alsop, 1996) and (Silva, 1997a) for the two components of the vascular signal. In this way, the following expression was obtained

$$\Delta S_{TOT}(t) = \frac{2\alpha_0 M_0 E(f)}{\left(\frac{1}{T_{1app}} - \frac{1}{T_{1a}}\right)} \frac{f}{\lambda}\left(e^{-t/T_{1a}} - e^{-t/T_{1app}}\right)\left(\rho_t(1-V) + \frac{E(f)}{\lambda}V\right) + 2\alpha_0 e^{-t/T_{1a}} \frac{M_0}{\lambda} V(1-E(f)) \qquad [3.13]$$

It can be seen that under the dual assumptions, E(f)=1 and V=0 (i.e. for complete extraction and elimination of the vascular component), Eq. [3.13] reduces to the standard FAIR expression (Eq. [3.8]) with normalisation to the volume of the voxel. Figure 3.8 displays graphs of the theoretical error in the FAIR CBF measurement if E(f) and V differ from their normal assumed values. It can be seen that the sensitivity to these assumptions is considerably more significant for a change in E(f) than for a changing blood volume.

The analysis that is presented here offers the opportunity to measure the extraction fraction or the relative cerebral blood volume (rCBV=V) by combining two subtraction pairs, $\Delta S_{d\_off}(t)$ and $\Delta S_{d\_on}(t)$, acquired in the presence and in the absence of the vascular signal respectively (so that $\Delta S_{d\_off}(t)=\Delta S_{TOT}(t)$ in Eq. [3.13]). The obvious way to attempt the acquisition of a solely tissue-based subtraction image is with the use of diffusion gradients, although, as has been stated earlier, this is not an optimal procedure.

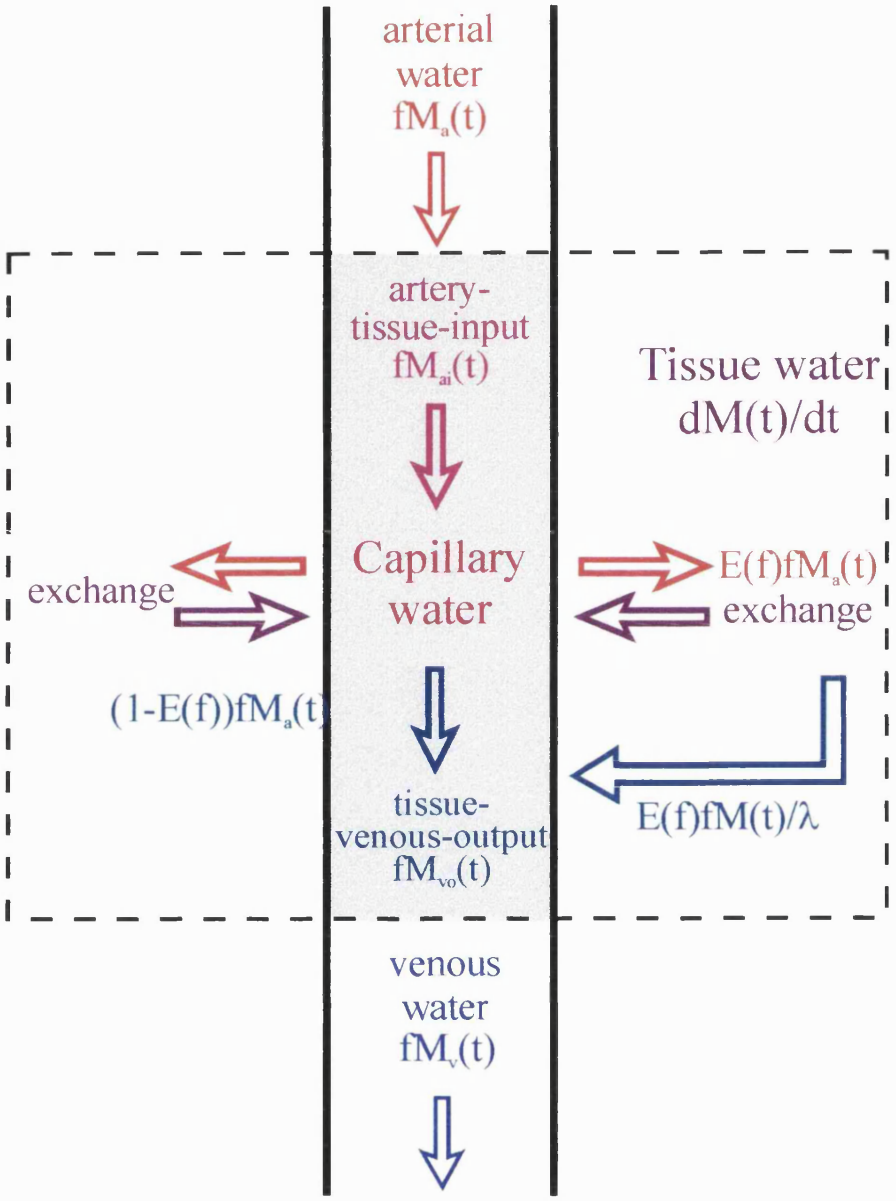

Fig. 3.7 Schematic representation of the modified model for the measurement of perfusion with inclusion of the relevant vascular component (area shaded in grey). The macromolecular pool is not considered (cf. Fig. 3.1). The total signal (tissue and vascular signal) is obtained from the area defined by the dotted box and includes an input and output component of vascular signal. The signal from the arterial and venous compartments in the larger arteries is assumed to be principally crushed by the diffusion and imaging gradients. If bulk vessel signal remains, the definition of E(f) can be modified to describe the proportion of the blood in all the vessel types that reaches the tissue compartment. E(f) will then be dependent on the geometrical distribution of the vasculature within the system.

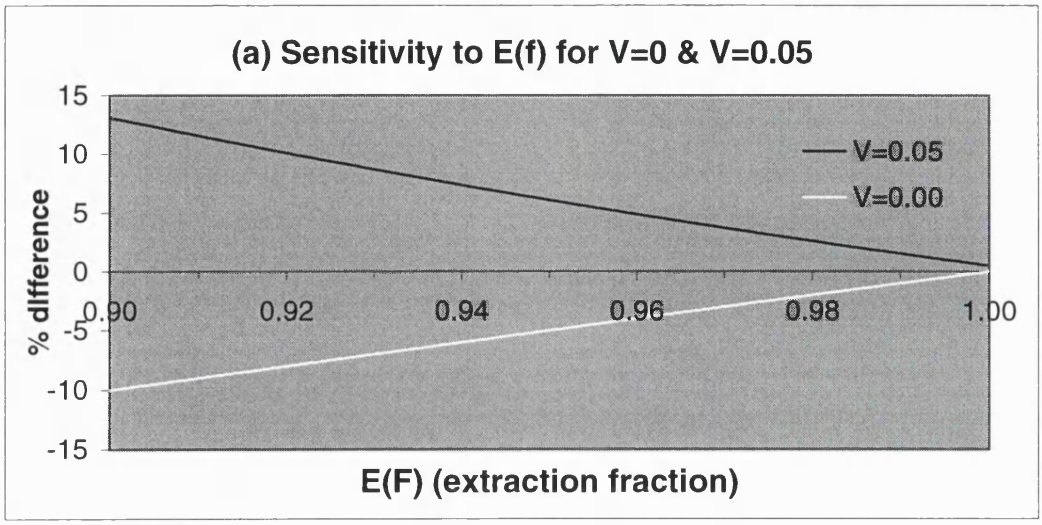

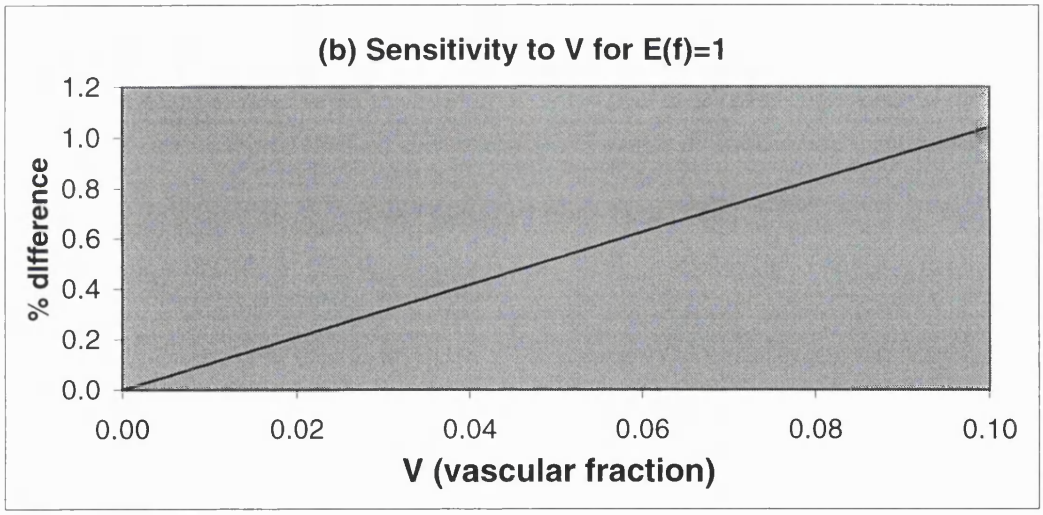

Fig. 3.8 Sensitivity of the FAIR flow measurement to (a) E(F) for two fixed values of V, and (b) V for a fixed E(f)=1. A positive value of the % difference, for example, implies that the standard quantification procedure (Eq. [3.8]) overestimates the *true* value (Eq. [3.13]). It can be seen that, in the absence of the blood signal, a non-unitary value of E(f) results in an underestimation of the flow. A fixed value of ΔM is assumed in this analysis which provides a flow value of approximately 110 ml/100g/min.

For example, it can be shown that the expression for the rCBV is given by

$$V = \frac{\Delta S_{d\_off} - \Delta S_{d\_on}}{\left(2\alpha_0 \frac{M_0}{\lambda} e^{-t/T_{1a}} - \Delta S_{d\_on}\right) + E(f)\left[\frac{\Delta S_{d\_on}}{\lambda \rho_t} - 2\alpha_0 \frac{M_0}{\lambda} e^{-t/T_{1a}}\left(1 - \frac{f\rho_t}{\lambda}\right)\right]} \quad [3.14]$$

The implementation of this method to measure V or E(f) is hindered by the limited SNR and time efficiency of the ASL techniques (see Chapter 4) and the problems associated with acquiring a purely tissue-based subtraction image. The majority of previously reported studies have not considered the vascular contribution and commonly attempt to reduce its effect by the use of diffusion gradients.

3.5.3 The MTC effect

As previously mentioned in the chapter, in the case of the CASL techniques, magnetisation transfer contrast acts as a competing mechanism of signal decrease and its effect must be eliminated by the acquisition of a control image. MTC has a strong, enhancing influence on the process of longitudinal relaxation. In the presence of the off-resonance irradiation of the AFP pulse, the relevant relaxation time becomes T_{1sat} which is a function of the frequency offset and the pulse power. Two MTC–related complications arise during flow quantification using the CASL method, and these will be discussed in turn.

3.5.3.1 The relevant T_1 relaxation time

The magnetisation difference can be formulated with various approaches (Eq. [3.7]). In one approach, Eq. [3.7(b)], $\Delta M(t)$ is normalised to M_0 and T_{1sat}, but initial perfusion studies have utilised a different approach, Eq. [3.7(c)], which associates $\Delta M(t)$ with T_{1app} (the apparent T_1 relaxation time) and the control signal intensity. Rigorous analysis of a four-compartment model of magnetisation transfer has demonstrated that the use of the *observed* T_1 relaxation time in the presence of flow, T_{1app}, is an oversimplification (McLaughlin, 1997). The anomaly arises since any standard measurement of the longitudinal relaxation time will contain an additional contribution due to cross-relaxation between the tissue and macromolecular pools (k_f and k_r). The relevant T_1 relaxation time in the flow analysis is, however, related to the intrinsic T_1 of the tissue, T_{1t}, (related to the relationship described in Eq. [3.7(a)]). The equality of the two times is clearly dependent on the chosen frequency offset and the RF amplitude used for the

tagging experiment. The two relaxation times are only equivalent if this combination of parameters produces a negligible degree of saturation of the macromolecules. This is likely to be the case in clinical studies which have employed non-saturating levels of RF irradiation in order to limit the power deposition. However, experimental implementations of the continuous techniques such as those carried out in our laboratory (Sections 3.3 and 3.7), have utilised direct saturation of the macromolecules in order to aid the quantification procedure (Zhang, 1992). In this case, a systematic error in the measurement can be avoided if the correct relaxation rate, denoted $\Re_1(\omega_1, \Delta\omega)$, is measured by analysis of the steady state level of the signal during the RF irradiation and the rate constant for the decrease to this level (McLaughlin, 1997). Comparative measurements of this relaxation time and of T_{1app} in our laboratory at a field strength of 8.5T have shown that T_{1app} can underestimate the correct value by approximately 15%. This would lead to a systematic bias in the perfusion measurements and will contribute to the overestimated flow values described previously (Section 3.3).

3.5.3.2 The treatment of MTC during the post-labelling delay

The other principal cause of the artefactually high flow measurements (Section 3.3) is the inclusion of vascular signal (see Section 3.5.2). A post-labelling delay should largely eliminate this effect if the delay is of sufficient duration. This delay modifies the steady state level of the magnetisation difference since the relaxation rate switches from T_{1sat} to T_{1app} once the continuous AFP pulse has terminated. This change will not be instantaneous since the bound component remains saturated for a period of time determined by the T_1 of the bound component, T_{1b}. If $w > \delta$ where w is the post-labelling delay, it can shown that the expression for $\Delta M(t)$ becomes (Alsop, 1996)

$$\Delta M(t) = 2\alpha_0 e^{-\delta/T_{1a}} \frac{f}{\lambda} M_0 \left[T_{1sat} e^{-w/T_{1app}} + T_{1app}\left(e^{-(w-\delta)/T_{1app}} - e^{-w/T_{1app}}\right)\right] \quad [3.15]$$

where the time dependence follows the changing value of w. The analysis formulated in ref. (Alsop, 1996) defined another transit time, δa, which describes the time for the arterial side of the vascular compartment to be filled (so that $\delta a < \delta$). However, for $w > \delta$, this component does not contribute to the overall signal difference since the vascular compartment is filled to an equal extent with untagged blood in both experiments. Modified profiles of $\Delta M(t)$ are shown in Fig. 3.9(a) and (b) for four values of the δ time (0.5-1.1 sec) and for two values of the MTC forward rate constant, k_f.

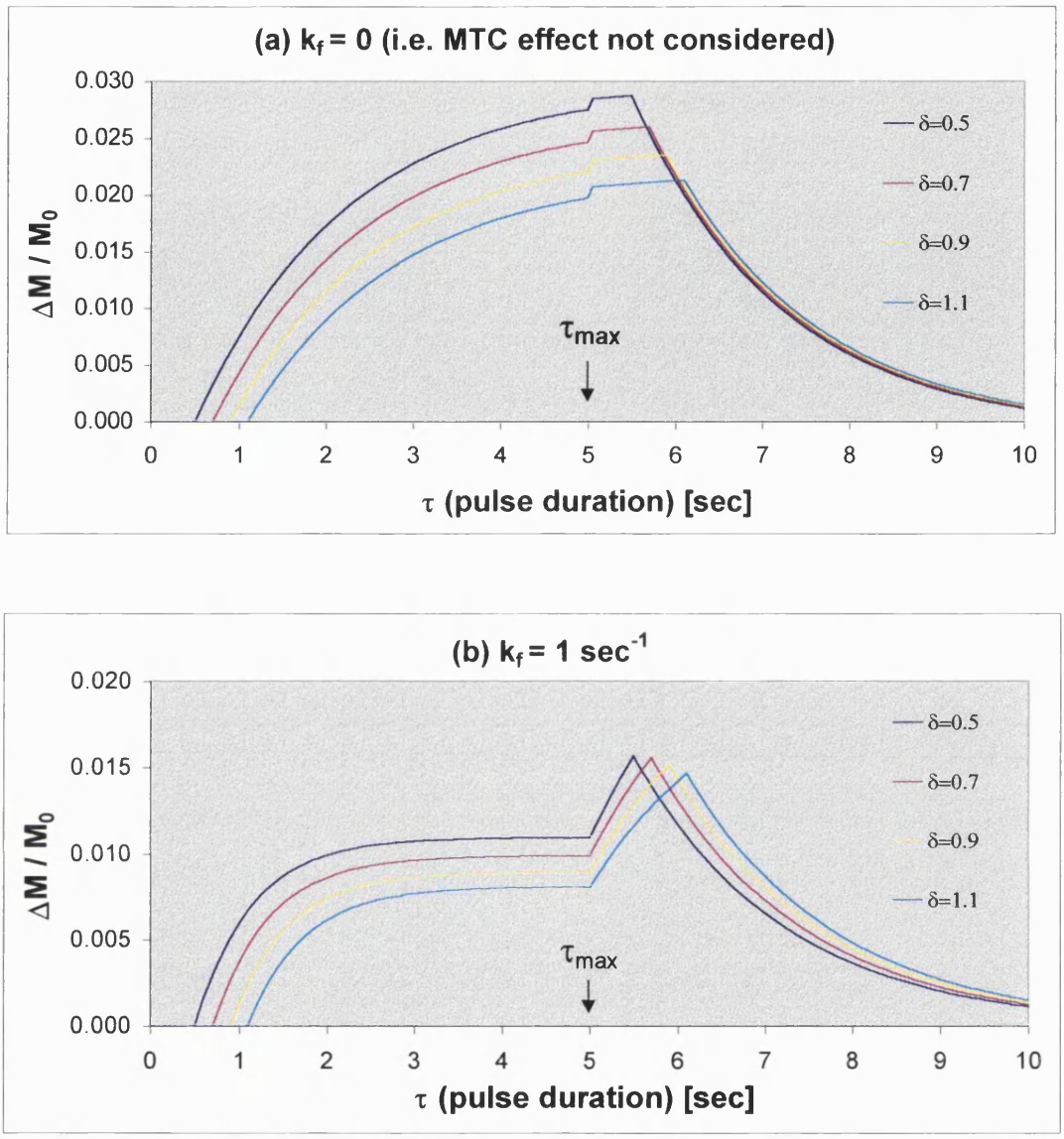

Fig. 3.9 Profiles of ΔM(t) (normalised to M_0) during and subsequent to the CASL pulse application for a range of transit times. Profiles (a) and (b) differ with regard to the treatment of the MTC effect. Simulation parameters are typical values for grey matter tissue at a field strength of 8.5T (intrinsic T_1=1.75 sec, f=60 ml/100g/min, T_{1app} = 1.72 sec, T_{1a} = 2 sec, δa = 0.4 sec [with δa defined in Section 3.5.3.1]). T_{1sat} is derived from T_{1app} and k_f (Eq. [3.6]) so that in (a), T_{1sat} = T_{1app} and in (b), T_{1sat} = 0.63 sec. A maximum pulse duration, τ_{max}=5 sec, is assumed such that for $t > \tau_{max}$, the post-labelling delay (w) is being applied The sharp rise in (b) at this point is due to the change in the relevent T_1 time from T_{1sat} to T_{1app} since the RF pulse has been terminated while the flow of inverted spins into the slice in the tagged image continues until w=δa. The T_1 of the bound component, T_{1b}, which will dampen the sudden rise, is not considered here. An exponential decay of ΔM(t) then occurs as fresh blood reaches the slice in both experiments.

An instantaneous change from T_{1sat} to T_{1app} is assumed when the pulse is terminated since the measurement of T_{1b} is currently not possible; its consideration will reduce the sudden change in $\Delta M(t)$ that is observed in Fig. 3.9(b). NMR parameters are typical tissue values for the high field, 8.5T system. It can be seen that if MTC effects are not considered (Fig. 3.9(a) with $k_f = 0$), the magnetisation difference and, therefore, the measured flow, will be relatively insensitive to δ as long as the post-labelling delay is chosen with a greater duration than the longest expected transit delay. This has obvious benefits but the post-labelling delay reduces the signal amplitude, and the SNR of the experiment must be balanced against the reduced sensitivity to δ (precision vs. accuracy). Furthermore, Fig. 3.9(b) shows that if MTC effects are considered ($k_f = 1$ sec^{-1}), the sensitivity to the transit time remains to a certain extent. The increased rate of change of $\Delta M(t)$ for $t > \tau$ (i.e. after the pulse has been terminated) apparent in Fig. 3.9(b) is a result of the different magnitudes of T_{1sat} and T_{1app} since the relevant relaxation time switches from one to the other at this point. This difference is magnified at higher field strengths.

The effectiveness of the post-labelling strategy for the CASL methods is closely related to the significance of the MTC effect. This will depend upon the proportion of the total time spent by the labelled spin in the vascular compartment (in which $k_f = 0$ and $T_{1a} > T_{1t}$) relative to the time spent in the tissue compartment (in which $k_f \approx 1.0$ sec^{-1}). For typical continuous pulse durations (3-6 sec), the influence of the tissue compartment will be dominant (since $\delta \approx 1$ sec) and the MTC effect will reduce the effectiveness of the post-labelling delay. The PASL techniques are not influenced by MTC to a significant degree (Frank, 1997) and the QUIPSS methods for transit time insensitivity may, therefore, prove to be more robust.

In order to demonstrate the practical importance of a reduced sensitivity to transit times and the incorporation of the correct T_1 relaxation time, CBF maps from the same animal are compared in Fig. 3.10. One map (Fig. 3.10(a)) was obtained without a post-labelling delay and quantification performed with Eq. [3.7]; the other map (Fig.3.10(b)) was obtained with w = 800 ms and quantified using Eq. [3.15]. The T_{1sat} data for the latter calculation were acquired using the following method; the intensity of the signal was measured after eight periods of off-resonance irradiation (200-3500 ms) applied at the same offset and power as for the tagging and control experiments. A mono-exponential

fit to this data provided the T_{1sat} value, and the intercept on the ordinate axis provides a measure of M_0. Values of the transit times, δa = 200 ms and δ = 600 ms, were chosen from the results of experiments carried out in our laboratory (according to the procedure described in ref. (Alsop, 1996)) and by analysis of previously reported studies. Cortical and striatal ROIs were drawn on these maps and provided values of 183 ml/100g/min and 207 ml/100g/min in Fig. 3.10(a) and of 114 ml/100g/min and 111 ml/100g/min in Fig. 3.10(b). The latter values correspond well with measurements obtained in the rat obtained using other flow techniques such as autoradiography (Ginsburg, 1986) and hydrogen clearance (Todd, 1986a).

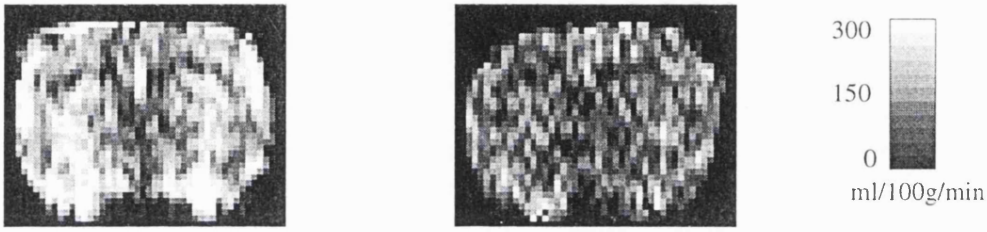

(a) (b)

Fig. 3.10 Comparison of CBF maps (CASL technique) from a rat obtained (a) without a post-labelling delay and (b) with w = 800 ms. The experiment was carried out on the 8.5T system using the procedure described in Section 3.3 and 3.7. The ventricles are visible in both images. The bright areas of signal evident in (a) represent the vascular artefact that is almost eliminated by the post-tagging delay employed in (b)

3.5.4 Discussion of the errors of the ASL methods

This section has described the principal, interrelated systematic errors that can have a significant impact on the accuracy of the flow measurement – the transit time, intravascular contamination and the MTC effect. An original means of incorporating the vascular compartment within the capillaries, arterioles and venules into the T_1 model in the case of the PASL techniques was presented since this had not been thoroughly analysed in previous studies. This treatment offers the potential of quantifying the extraction fraction and the relative CBV using pairs of subtraction images. It was suggested that the vascular component of the signal should be quantified and included

in the analysis since it is likely that even diffusion gradients will not completely eliminate the blood signal. However, the SNR of the ASL techniques will need to improve before this can be achieved with a sufficient degree of precision.

3.5.4.1 Summary of ASL quantification issues

Accurate quantification of perfusion in animals and humans with the ASL techniques requires consideration of a number of additional factors. Under- or over-estimation of the CBF will often result if these issues are not taken into account in the analysis of the perfusion model and the design of the experiment. These factors are summarised here:

(1) **Transit time effects, intravascular contamination and MTC effects** which have been discussed in Section 3.5. In addition to the transit time, the spatial extent of the tagged region defines an *inflow time* that must be considered (see Section 4.2.3) unless a modification such as QUIPSS is implemented.

(2) **Implementation of the CASL method on clinical scanners**: This is hampered by the increased magnitude of the transit times from the tagged proximal arteries in humans. Loss of the label is also intensified by the shorter longitudinal relaxation times at the typically lower field strengths.

(3) **RF deposition**: The limits on the duty cycle of RF amplifiers and the specific absorption rate (SAR) of the sequence often restrict the application of a totally continuous pulse over the required duration that is in the order of seconds ($>>T_{1sat}$). Instead, a pulse train is applied consisting of repeated rectangular pulses with a duty cycle of approximately 75-90% (Roberts, 1994; Ye, 1997a). CBF quantification with the procedure described in the initial analyses of the CASL experiment (Zhang, 1992) assumed the complete saturation of the macromolecular compartment (i.e. $M_m=0$) (Eq. [3.7(b)]). This is difficult to achieve on clinical systems and the measured flow will be underestimated if this is not taken into consideration (Lei, 1997). The alternative approach described in later treatments (McLaughlin, 1997), normalised the signal difference to T_{1sat} (the T_1 in the presence of off-resonance relaxation) and the spin density, M_0 (Eq. [3.7(c)]). This procedure does not require complete macromolecular saturation and is hence, advantageous.

(4) **The degree of inversion, α_0**: An accurate measurement of α_0 is necessary for both continuous and pulsed methods. The method of α_0 determination employed in our investigation (Section 3.3.2) described in ref. (Zhang, 1993) has been criticised over the measurement location and the measurements's bias towards the lower range of laminar flow velocities present in the carotid artery (Maccotta, 1997). The degree of inversion is considerably more velocity-dependent for the CASL technique than for the pulsed techniques (Wong, 1998b) since the fulfilment of the adiabatic condition in the case of the continuous AFP pulse (Eq. [1.16]) is intrinsically related to the velocity of spin passage through the tagging gradient. Individual calibration of the value of α_0 may, therefore, be necessary for the CASL technique.

(5) **The blood:brain partition coefficient, λ**: A uniform value of λ is often assumed in previous studies of CBF quantification but this may represent an unrealistic assumption. Different values of the partition coefficient have been reported for GM and WM and for varying haematocrit levels (Herscovitch, 1985). It is also possible that the regional values of λ will vary as a consequence of evolving pathophysiology. An imaging method for λ determination on a pixel-by-pixel basis has been described (Roberts, 1996).

(6) **The assumption of a freely diffusable tracer**: As previously discussed, the extraction fraction, E(f), is intrinsically related to the validity of this assumption and describes the partition between the vascular and tissue compartments during the passage of the blood through the vasculature in the tissue (Section 3.5.2.3). This parameter has been measured using MRI methods and it has been shown to decrease from 1.0 to approximately 0.5 at very high flow rates (~500 ml/100g/min). However, E(f) should be approximately unity for the normal range of physiological flows in humans and animals. The inclusion of the vascular compartment into the FAIR model that is discussed in Section 3.5.2.3, has described a method of E(f) determination using a pair of subtraction images.

(7) **Multi-slice data acquisition**: The standard continuous technique (Section 3.3) is only amenable to implementation on a single slice due to the necessity of acquiring a control image for MTC correction. A two-coil modification of this technique largely eliminates the MTC contribution and, thereby, enables multi-slice acquisition (Zhang, 1995). Alternatively, use of an amplitude modulated RF pulse in order to obtain the

control image has been recently proposed to allow multiple slice data collection, but the resultant overall degree of inversion is impaired (Alsop, 1998a). The PASL techniques are immediately amenable to multi-slice acquisitions but the pulsed methods are especially susceptible to slice-order-related signal contamination (Wong, 1997; Kim, 1997a) and to slice profile imperfections (Frank, 1997; Wong, 1998b). The variable transit times to the multiple slices must be considered for both continuous and pulsed methods. Implementation of the modified sequences with reduced transit time sensitivity or with use of a means of simultaneous slice acquisition (Kao, 1998), is recommended.

(8) **Image orientation**: A tagging plane that is perpendicular to the direction of the main feeding carotid arteries is the natural choice for the tagging experiment. The standard implementation of both classification of methods complicates the acquisition of non-axial scans since the imaging plane has to be parallel to the tagging plane in order to reduce the transit time and to eliminate the static signal with an effective distal control. However, the multi-slice implementation of CASL (Alsop, 1998a) allows the simple acquisition of non-axial images due to the coincidence of the labelling plane in both the tagged and control experiments. The tagging and imaging planes are consequently independent of each other.

(9) **BOLD contrast**: Simultaneous flow and T_2*-contrast information can be extracted from a gradient-echo based ASL experiment. Several groups have, thereby, employed FAIR (Kim, 1997b; Kim, 1997c, Zhu, 1998) and QUIPSS (Wong, 1997) techniques in studies of the combined flow and blood oxygenation level dependent (BOLD) responses to functional activation paradigms. For flow quantification studies using gradient-echo or spin-echo image acquisition, the respective T_2*- and T_2-weighting of the signal (that is incorporated within the measured spin density, M_0 in for example, Eq. [3.8]) must be extracted (see Section 3.5.2.2), and this procedure is usually based upon baseline measurements (Kim, 1995).

(10) **CSF contamination**: The partial volume effect of CSF, which is exacerbated with the larger voxel sizes used in clinical imaging, can result in significant underestimation of the flow measurements. Kwong *et al.* predicted an underestimation of approximately 30% for a GM:CSF volume fraction of 50%:50% (Kwong, 1995). A perfusion measurement given in the standard units normalised to the tissue mass are, therefore, unrealistic in this context unless a means of determining the volume fractions can be

implemented. This error can be reduced with the use of increased resolution and CSF suppression.

(11) **The T_1 of blood, T_{1a}**: Quantitative PASL techniques are based on a biexponential expression containing both the T_1 values of tissue and blood (Eq. [3.8]). The corresponding CASL measurement is a monoexponential fit to the tissue T_1 but relaxation during the transit time follows T_{1a}. The measurement of flow with both classifications of techniques, therefore, requires a determination of T_{1a}. The majority of previous reports have obtained a value of this parameter by extrapolation from published in-vitro data. The dependence of T_{1a} on factors such as oxygenation, haematocrit and vessel size and environment may be significant and requires further study.

(12) **Venous contamination**: The blood in the venous circulation during the experiment may have been labelled by the control or tagging experiments. This will largely depend upon the treatment of the distal area relative to the imaging slice which differs between the ASL techniques. This effect may, therefore, provide an unwanted contribution to the subtraction signal although if the blood had been tagged while in the arterial circulation, the label should have decayed by a significant extent by the time it reaches the venous circulation.

(13) **Geometrical layout of the tagged vasculature**: The CASL technique assumes a tagging plane that is perpendicular to the direction of the feeding artery, and the inversion efficiency will be compromised of this is not the case. For both pulsed and continuous techniques, the less direct path of the blood to the imaging slice in this situation will be reflected as a longer transit time. The techniques are not sensitised to blood that remains in vessels running parallel to the imaging plane during the course of the experiment.

(14) **Alternative causes of signal variation**: The inherent, theoretical flow sensitivity of the standard CASL technique is greater than that of the PASL methods by a factor of $e \approx 2.718$. However, it has been shown that on implementation of the equivalent sequences with reduced transit time sensitivity, the SNR-per-unit-time of the two classifications of methods are approximately equal (Wong, 1998b). The techniques produce a flow-induced magnetisation difference of approximately 1-5% at standard field strengths and this places significant demands on the detection procedure. Any

alternative origin for the signal difference such as imperfections in the RF pulse profile (Frank, 1997; see Section 3.6), eddy currents (Pekar, 1996), radiation damping (Zhou, 1998), or the quality of the shim, may result in a systematic offset in the subtraction image. Therefore, attempts must be made to eliminate these effects. In addition, the interleaving of control and tagged experiments is recommended in order to minimise errors resulting from hardware instability and temperature variations. The CASL techniques operate under steady state conditions, and cannot, therefore, be implemented in this way in a time efficient manner.

(15) **Sensitivity to low flows**: The ASL techniques are especially susceptible to inaccuracies in the quantification procedure at lower flow values due to the limited SNR and the sensitivity to the transit time effect. This may severely hamper the clinical implementation of the spin tagging methods since the need to measure CBF is of greatest importance in such conditions. The wider variation of transit and outflow times across the brain and a general increase in the transit time to the affected area combine to complicate the implementation of the modified AST methods that have been designed to reduce the transit time sensitivity (Section 3.5.1). The delay times of these techniques that *create* the insensitivity can be increased in order to cover the variability in the expected transit times. However, this will be accompanied by a corresponding loss of perfusion signal. Instead, sufficient subtraction images can be acquired such that the transit time may be obtained from the data by fitting to the theoretical expressions derived by analysis of the perfusion models discussed in Section 3.2. Experimental determinations of the transit time have thus been obtained for CASL (Ye, 1997a) and PASL (Wong, 1997) techniques. Other authors have reported further modifications to the ASL techniques that allow similar transit time fitting (Barbier, 1998; Branch, 1998). Buxton *et al.* have suggested the use of a two-point scheme for the PASL methods with subtraction images acquired at two TI delays (Buxton, 1998). The early part of the $\Delta M(t)$ relationship provides an approximately linear expression for flow with the intercept on the time axis of the profile representing the transit delay (see Fig. 3.9). The acquisition of multiple time points are, however, beneficial since the 2-point method relies on a chosen initial TI delay that is greater then the longest expected transit time.

Detre *et al.* have recently suggested a novel use of the intrinsic transit time sensitivity of the standard ASL methods to provide useful pathological information (Detre, 1998, Alsop, 1998b). Bright, artefactual areas of signal were observed in the CBF maps

obtained from patients with regions of impaired flow using the CASL delay-modified sequence. These regions appeared amongst areas of damaged vascularity and seemed to reflect the presence of intraluminal spins with an excessive transit time.

The optimal experimental scheme for accurate quantification of impaired perfusion is expected to be provided by a combined approach of transit time quantification with the previously mentioned procedure, and with slice profile optimisation to minimise the magnitude and the variation of the transit times. The limited temporal resolution of such measurements restricts the implementation of the scheme but will be ameliorated by improved pulse (see Section 3.3) and coil design, and by optimised sequence time efficiency (see Section 4.2).

A number of studies were undertaken relating to the methodology and implementation of the ASL techniques. These are now described in the following three sections.

3.6 Pulse profile optimisation

As has been previously discussed, transit time sensitivity is one of the principal systematic errors that affects the accuracy of CBF measurements with ASL techniques. Efforts must, therefore, be made to reduce the intrinsic sensitivity to the transit delay in order to provide accurate quantification at lower levels of flow. In addition, a related consideration is the susceptibility of the pulsed techniques to imperfections in the RF tagging and imaging slice profiles due to off-resonance and relaxation effects. The resultant variation in the static signal between the control and tagged images may be in the order of magnitude of the flow signal and limits the extension of the PASL techniques to multi-slice implementations (Frank, 1997). Of all the pulsed methods, FAIR should suffer least from transit time effects due to its method of in-slice labelling. However, the quality of inversion and imaging pulse profiles has, thus far, not allowed this inherent advantage of the technique to be fully realised. This section describes an investigation of profile optimisation for the FAIR experiment.

3.6.1 FAIR and the pulse profile

In the case of the FAIR technique, the quality of the inversion pulse profile plays a further, crucial role in the effectiveness of the method. The slice-selective inversion is meant to label the tissue relative to the flowing blood so that any movement of blood

into the imaging plane creates a magnetisation difference. This aim necessitates the use of an inversion slab that has exactly the same width as the imaging slice. However, in practical implementations of the technique, the width of the inversion slab must be wider than the imaging slice in order to eliminate effects from imperfect edges of both the inversion and the imaging pulse profiles. A typical inversion/imaging slice thickness ratio (STR) used is 3:1 (Kim, 1995). The magnitude of the resultant transit time is related to the velocity of the inflowing arterial blood and simplistically, to the distance between the edges of the imaging slice and the slice selective inversion slab.

3.6.2 The inversion pulse

Adiabatic inversion pulses are largely insensitive to B_1 inhomogeneities and are, therefore, attractive for use in ASL experiments in which uniformly tagged regions are required. The quality of the inversion profile is also significantly improved relative to a standard, *sinc* (sinx/x) 180° inversion pulse. Deviations from the ideal, *square* profile, however, remain in the transition regions at the edges of the inversion band (see Sections 3.6.2.2 and 3.6.2.3 and the accompanying Fig. 3.13). The influence of the relaxation times on the profile imperfections has been investigated and transverse relaxation was shown to be especially significant in defining the transition band (Frank, 1997). The application of shorter pulse durations with reduced RF amplitude was recommended. However, the transition region imperfections were not completely eliminated by this strategy and the slope at the edges of the profile was largely unaffected. In order to further improve the inversion profile, a modified adiabatic inversion pulse has been proposed (Ordidge, 1997). The frequency offset correction inversion (FOCI) pulse makes use of a magnified gradient to increase the degree of spatial localisation. The frequency sweep of the adiabatic pulse brings successive spins across the plane of the slice into resonance and subsequent inversion. The leading and trailing edges of the pulse profile are thus defined at the beginning and end of the pulse application. The FOCI pulse localisation gradient is increased and temporally shaped during these phases of the pulse and the spatial definition of the profile edges is thereby improved. In general, the waveforms describing the gradient, RF amplitude and frequency sweep, $G(t)$, $B_1(t)$ and $\Delta\omega(t)$ respectively, are derived from the standard hyperbolic secant (HS) pulse, multiplied by a shaping function, $A(t)$, so that, for example, the following relationship applies for the B_1 field

$$B_{FOCI}(t) = A(t)B_{HS}(t) = A(t)B_0\text{sech}(\beta t)^{(1+i\mu)} \qquad [3.16]$$

where B_0 is the maximum intensity and β and μ are the adiabatic pulse parameters that define the truncation and the bandwidth of the pulse (truncation level = $\text{sech}(\beta T_p/2)$ where T_p is the pulse duration; bandwidth[Hz] = $\beta\mu/\pi$). The effective magnetic field, B_{eff}, is multiplied by the same A(t) function and the adiabatic condition (Eq. [1.16]) is, thereby, satisfied to a greater extent than the standard HS pulse. The threshold RF amplitude is unchanged but the total power deposition is increased (Payne, 1997). In order to theoretically analyse the inversion profile of the modified pulses, a computer simulation program was devised to numerically solve the Bloch equations that the adiabatic inversion describes. Several different forms for the A(t) function have been considered, and the so-called T-shape and C-shape pulse designs (Ordidge, 1997) have been implemented (Payne, 1997; Pell, 1998; Yongbi, 1998). No significant difference was found between the simulation profiles of these two designs and the T-shape pulse with a tetrahedral gradient waveform was implemented for investigation in our laboratory (Fig. 3.11).

3.6.2.1 The optimisation procedure

The optimal design of the FOCI pulse with parameters described by Eq. [3.16], requires the appropriate choice of a number of the often interrelated parameters: β; μ; pulse bandwidth; pulse duration, T_p; maximum B_1 intensity; maximum of the A(t) function, denoted max[A(t)]; the fraction of A(t) over which the waveform ramps down, denoted ramp[A(t)]. The simulation computer program was employed in order to decide upon the optimal combination of these parameters.

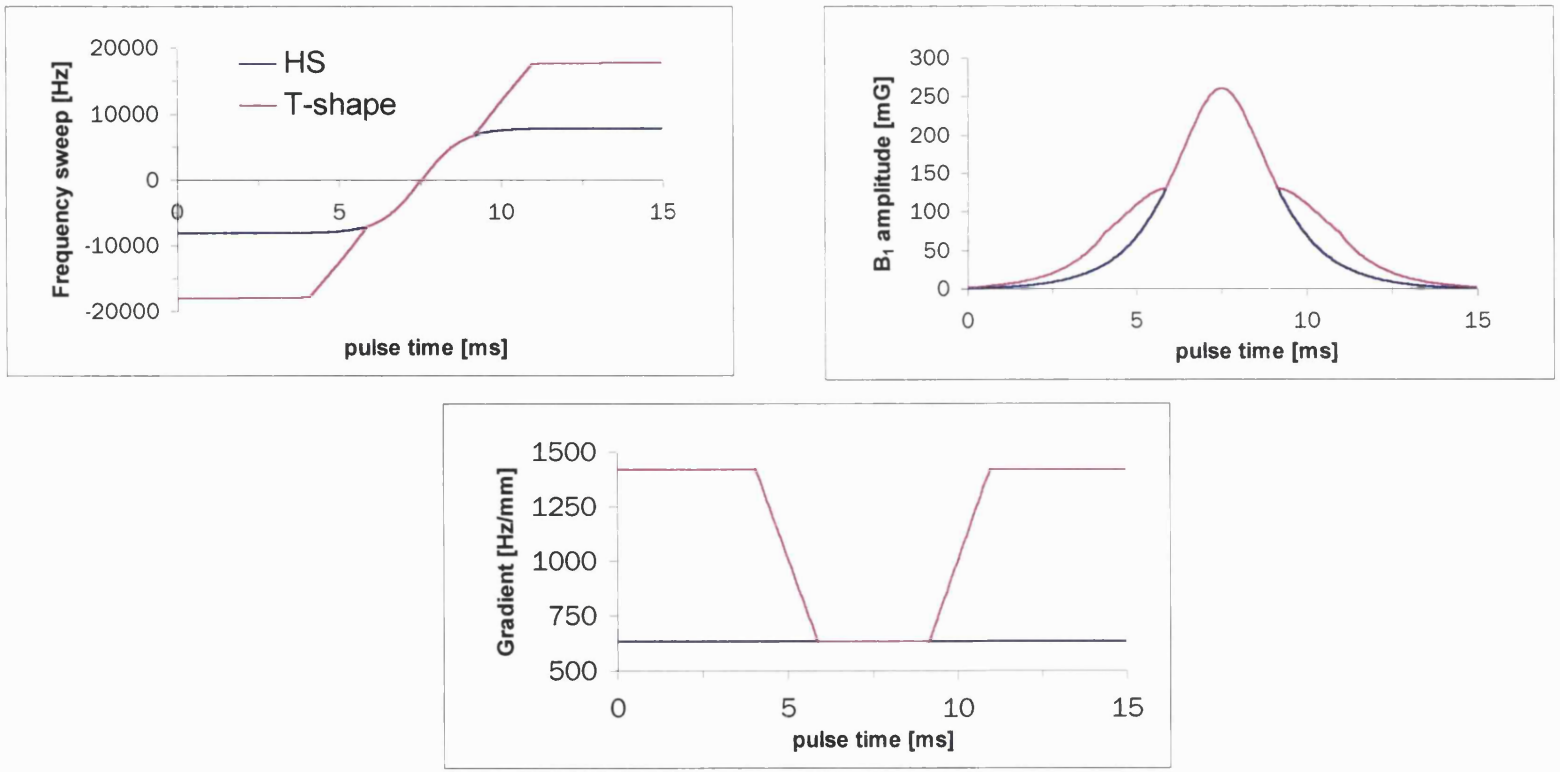

Fig. 3.11 Comparison of frequency sweep, B_1 amplitude and gradient waveforms for the FOCI and standard HS pulses. Overlap of the profiles is apparent in the central region where A(t)=1. Adiabatic pulse parameters were: $\beta = 800s^{-1}$, $\mu = 10$, pbw = 2546 Hz, $T_p = 15$ ms, max[A(t)] = 5, ramp[A(t)] = 40%. The maximum gradient of our system is 1421 Hz/mm and, therefore, a plateau in the A(t) function is evident in these waveforms where the gradient output would otherwise exceed this limit.

The following conclusions were reached:

(1) A higher value of μ improves the pulse profile (Payne, 1992) but, for a constant bandwidth, is accompanied by an increased level of pulse truncation (i.e. decreased β). Shorter bandwidths, therefore, limit the maximal value of μ that can be used.

(2) A larger bandwidth (increased β or μ) reduces the number of spins in the transition region of the pulse profile and is therefore beneficial. However, this is limited by gradient strength and eddy current considerations. An associated increase in the RF intensity is also required and this may conflict with the limits of the RF amplifier.

(3) The relaxation times, T_1 and T_2, have a significant effect on the inversion profile. T_1 relaxation results in a variation in the degree of inversion across the slice as the spins reach inversion; T_2 relaxation reduces the quality of the inversion band (see later in this section). These effects encourage the use of a shorter pulse duration (reduced time for T_1 relaxation) and minimal inversion power (reduced time for T_2 relaxation as spins spend less time in transverse plane) (Frank, 1997).

(4) The overall sharpness of the FOCI pulse profile is improved in the transition regions with an increase of either max[A(t)] or ramp[A(t)]. However, this is accompanied by an increase in the size of the *ripples* in the z-magnetisation evident in this region and across the inverted area.

Based on these considerations, optimal pulses were designed for a minimum desired inversion slice thickness. In order to investigate the sensitivity of the FOCI pulse to the relaxation time and off-resonance effects described by Frank *et al.* (Frank, 1997), simulations were produced under a variety of conditions (Fig. 3.12).

The difference in the longitudinal magnetisation, ΔM_z, between the inversion profiles in the presence and absence of relaxation (defined by $\Delta M_z = M_z(\textit{ideal}) - M_z(\textit{non-ideal})$) is displayed for the inversion pulses shown in Fig. 3.11. An exaggerated scale is employed in Fig. 3.12 in order to display the effects of (a) T_2 relaxation, (b) T_1 relaxation and (c) B_1 amplitude. It can be seen that the relaxation-dependent characteristics of the FOCI and standard HS pulses are very similar. The similar threshold B_1 characteristics required for inversion (indicated by Fig. 3.12(c)), are discussed in ref. (Payne, 1997).

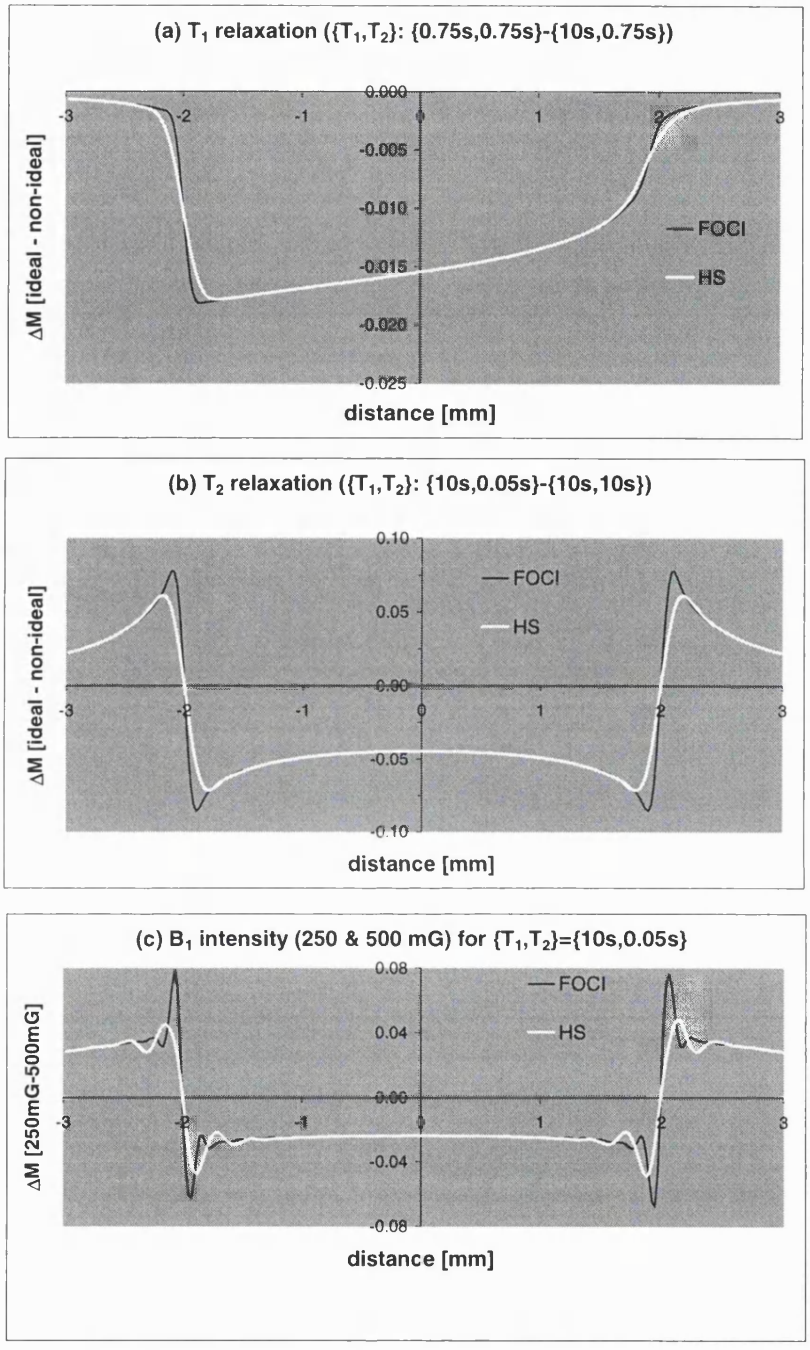

Fig. 3.12 Comparison of relaxation time and RF amplitude effects on the pulse profiles of the HS and FOCI pulses. An exaggerated ordinate scale is employed and the subtracted values (ΔM) are relative to the starting magnetisation, M_z, of +1. The simulated pulses parameters are as in Fig. 3.12 with an inversion slice thickness of 4 mm. The *ideal* relaxation time parameters are T_1=T_2=10 sec. For (a) the relaxation times are {T_1,T_2}= {0.75sec,0.75sec} and {10sec,0.75sec}; for (b), the corresponding times are {10sec,0.05sec} and {10sec,10sec}; for (c), the corresponding values are {10sec,0.05sec} in both, and B_1=250 mG or 500 mG.

3.6.2.2 Experimental demonstration I : Pulse profile

In order to demonstrate the benefits of the FOCI over the standard HS pulse, computer simulations were obtained and compared to experimental profiles collected using an agar phantom on the 2.35T system The pulse parameters are described in the figure legend. The acquisition sequence was a standard spin-echo 1D-FT with the readout gradient applied along the slice-selection axis. Results are displayed in Fig. 3.13 and compared to the simulated profiles. A significant improvement in the pulse profile is apparent.

3.6.2.3 Experimental demonstration II : FAIR subtractions

The effect of the improved inversion profile on the quality of the FAIR subtractions of static tissue was demonstrated on the 2.35T system by acquiring selective and non-selective images at a number of inversion slice thicknesses and a uniform, cylindrical agar phantom. The pulse parameters were identical to those described for the previous experiment and the nominal slice thickness was 4 mm. The FAIR spin-echo EPI imaging sequence was employed as described in Section 4.4. The results are displayed in Fig. 3.14(a). It can be seen that the improved pulse profile of the FOCI pulse is reflected by the absence of a systematic offset at shorter values of the inversion slice thickness.

3.6.2.3 Experimental demonstration III : Degree of inversion, α_0

The combined effect of the inversion and imaging pulses in FAIR is a convolution of the individual pulse profiles. The degree of inversion in the case of the slice selective inversion recovery technique reflects the interaction of the profiles and was obtained by a 3-parameter fit at 12 inversion slice thicknesses between 4-10 mm (Fig. 3.14(b)). The data demonstrate that for a tighter slice thickness ratio (STR), the FOCI pulse maintains its value while the degree of inversion of the HS pulse decreases resulting in the systematic signal offset in the FAIR subtractions indicated in Fig. 3.14(a).

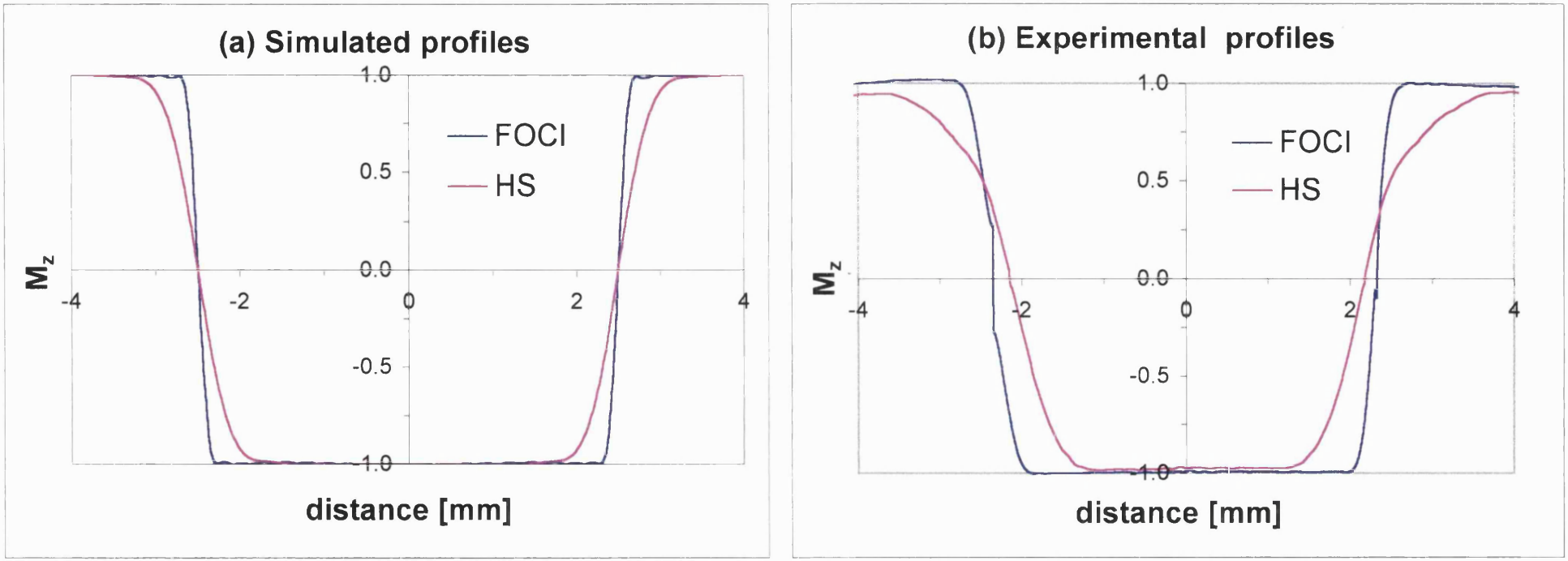

Fig. 3.13 Comparison of (a) simulated and (b) experimental pulse profiles of the z-magnetisation, M_z, for the FOCI and standard HS pulses. The imaging slice thickness is 5 mm. Pulse parameters were $\beta = 800\text{sec}^{-1}$, $\mu = 4.5$, pbw = 1137 Hz, $T_p = 15$ ms, max[A(t)] = 5, ramp[A(t)] = 40%.

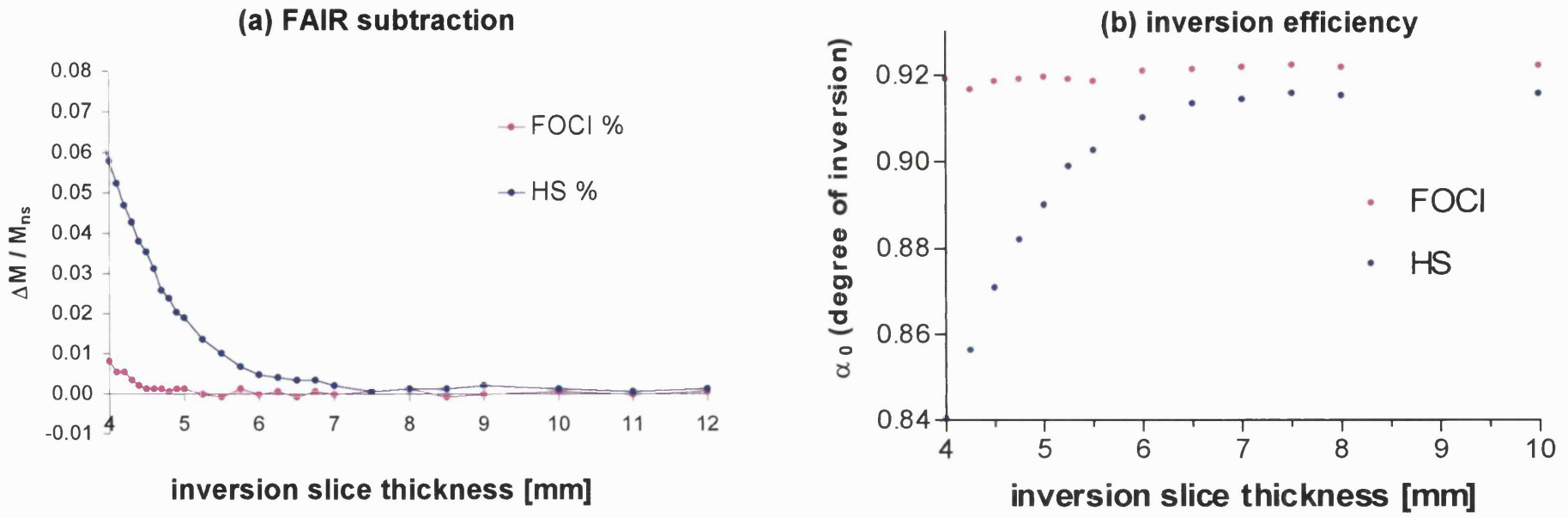

Fig. 3.14 Relationships of (a) the magnetisation difference, ΔM, (selective - non-selective) normalised to the image signal intensity, and (b) the degree of inversion, α_0, with the inversion slice thickness. The imaging slice thickness in both cases was 4 mm. The inversion pulse parameters for graph (a) were as employed for the data shown in Fig. 3.14, while the parameters for graph (b) were $\beta = 800\ sec^{-1}$, $\mu = 6.7$, bandwidth = 1706 Hz, $T_p = 12$ ms, max[A(t)] = 5, ramp[A(t)] = 40%. The ΔM profile indicates the benefit of the tighter FOCI pulse. The initial positive offset is exaggerated in the case of the HS pulse due to the greater degree of overlap of the pulse profiles.

3.6.3 The imaging pulse

The superior inversion profile of the FOCI pulse allows a tighter STR and should, therefore, be beneficial in reducing the transit time sensitivity of the FAIR sequence. However, the standard sinc imaging pulse profile is also imperfect and may negate the positive benefits of the modified inversion. The data in Fig. 3.14(a) and (b) indicates that the inversion pulse requires an inversion slice thickness that is only slightly wider than the imaging slice in order to eliminate the static tissue artefacts (STR $\approx$ 1:1). This conclusion is, however, tempered by the practical, relative coverage of the inversion and imaging profiles.

The 90°-180° imaging pulse combination used in the previous experiments (T_p = 4 ms; bandwidth = 3 kHz) with equivalent slice-selective gradients for both pulses, results in a slice with approximately 75% of the nominal slice thickness. This is due to inefficient refocusing and inhomogeneity-induced flip angles of less than 180° (Frahm, 1984). Experimental and theoretical profiles are compared in Fig. 3.15(a) and (b) and the phase distortions are especially apparent in (a). A non-selective 180° pulse would be beneficial in this respect but does not allow the possibility of multi-slice acquisitions. Further experiments in our laboratory have demonstrated that the FOCI inversion / 90°-180° imaging pulse combination allows a minimum STR of approximately 1.85:1 with consideration of the *true* imaging slice thickness. This can be contrasted to the corresponding minimum ratio in the case of the HS pulse of approximately 3:1 (data not shown). A non-unitary ratio of slice thicknesses is, therefore, necessary even for the FOCI pulse combination and this is due to the imperfections that are apparent in the imaging pulse profiles as through-slice oscillations and side lobes (Fig. 3.15).

In order to improve the quality of the imaging pulses, a modification to a previously reported adiabatic refocusing pulse scheme was implemented. A single adiabatic pulse cannot be used for efficient refocusing across a plane of spins since the pulse acts progressively across the slice (see Section 3.6.2) and an off-resonance spin will be dephased by the residual gradient. A non-linear phase remains across the slice which is symmetrical about the central position. An additional adiabatic pulse can, however, be used to compensate for the non-linear phase across the slice since the sign of the phase evolution is reversed (Conolly, 1991).

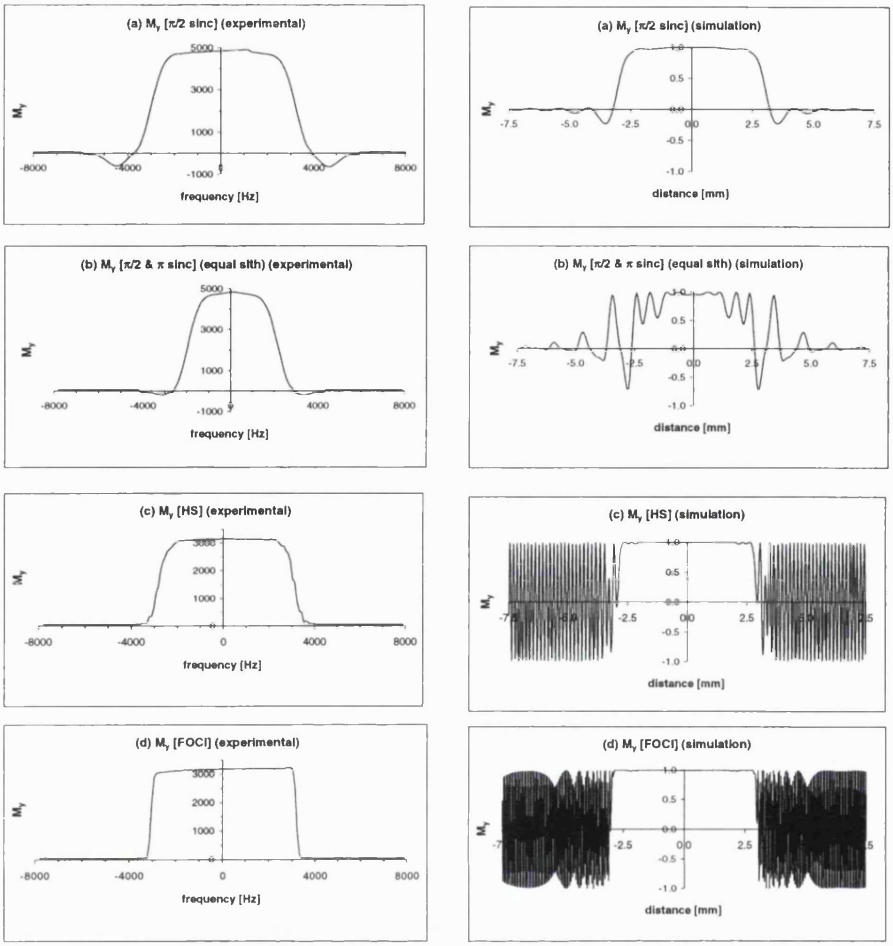

Fig. 3.15 Comparison of experimental and simulated profiles of various imaging pulse acquisition schemes. The π/2 pulse profile was acquired with a slice selective sinc π/2 pulse and a non-selective sinc π pulse; the π/2 & π combination pulse was implemented with the same slice-selective gradient. It should be noted that the simulation of the latter combination of pulses is an oversimplification since the effect of gradient crushers has not been considered. Magnetisation, therefore, is apparent outside the main slice profile that has *seen* the π pulse but not the π/2 pulse and vice versa; this magnetisation had been eliminated by the crushers in the experimental profile. The FOCI and HS pulses have pulse parameters as follows: $\beta = 800\ sec^{-1}$; $\mu = 6.7$; bandwidth = 1706 Hz; $T_p = 12$ ms; max[A(t)] = 5, ramp[A(t)] = 40%. The 5-lobed sinc pulses have a bandwidth of 5000 Hz ($T_p = 2$ ms). The ordinate axis represents a measure of the amplitude of the magnetisation in arbitrary units. Experimental profiles were collected on the 2.35T system using an agar phantom (see Section 3.6.2.2). In the case of the double-adiabatic refocusing scheme, the transverse magnetisation exhibits the phase wrapping outside the slice that is characteristic of gradient-induced dephasing after a non-selective π/2 pulse. This makes no net signal contribution due to its vanishing integral across the sample.

The imaging pulse scheme consists of a set of two adiabatic pulses following a non-selective 90° pulse and, thereby, acts as a slice-selective *pancake flipper* with the magnetisation constantly perpendicular to the rotating B_{eff}. The pulse combination should produce inhomogeneity-independent refocusing with the superior spatial definition of the standard HS pulse. This scheme was implemented on the 2.35T system with the modification of substituting FOCI pulses for the HS pulses in order to further improve the pulse profile. A potential drawback of this method of refocusing is the extended minimum echo time in comparison with the standard spin-echo combination due to the longer duration of the adiabatic pulses and the additional pulse. This can be mitigated to a certain extent by application of the first selective adiabatic pulse immediately after the initial 90° pulse since the echo from this pulse is not needed (Conolly, 1991).

The $90°_{ns}$-$FOCI_{ss}$-$FOCI_{ss}$ refocusing scheme was simulated and the components of the transverse magnetisation subsequent to the first and second adiabatic pulses are displayed in Fig. 3.16. The pulse scheme was experimentally validated on an agar phantom, and the profiles are shown in Fig. 3.15(c) and (d) for the HS and FOCI implementations. It can be seen that the slice lobes are almost eliminated and in the latter case, the slice definition is further improved.

The combination of improved inversion and imaging pulses should enable implementation of FAIR with slice thickness ratios that are closer to the ideal situation (1:1) and, thereby, reduce the transit time sensitivity of the sequences. Initial experiments using the double-FOCI refocusing scheme have utilised the acquisition of FAIR subtractions at a number of TI delays in a bilaterally-occluded gerbil (n=1). These subtraction images were fitted to a modification of the FAIR biexponential expression which incorporates the transit time (see Appendix A, Eq. [A2]).

The transit delay determined in this manner by the optimal sequence (FOCI inversion and 90° / double FOCI imaging pulse) was compared to equivalent, experimental values obtained with a standard FAIR pulse combination (HS inversion and 90°-180° imaging pulse). Regional analysis, thereby, provided values of 506±71 ms (standard) and 109±110 ms (optimal combination) in the striatial region (data not shown). These data

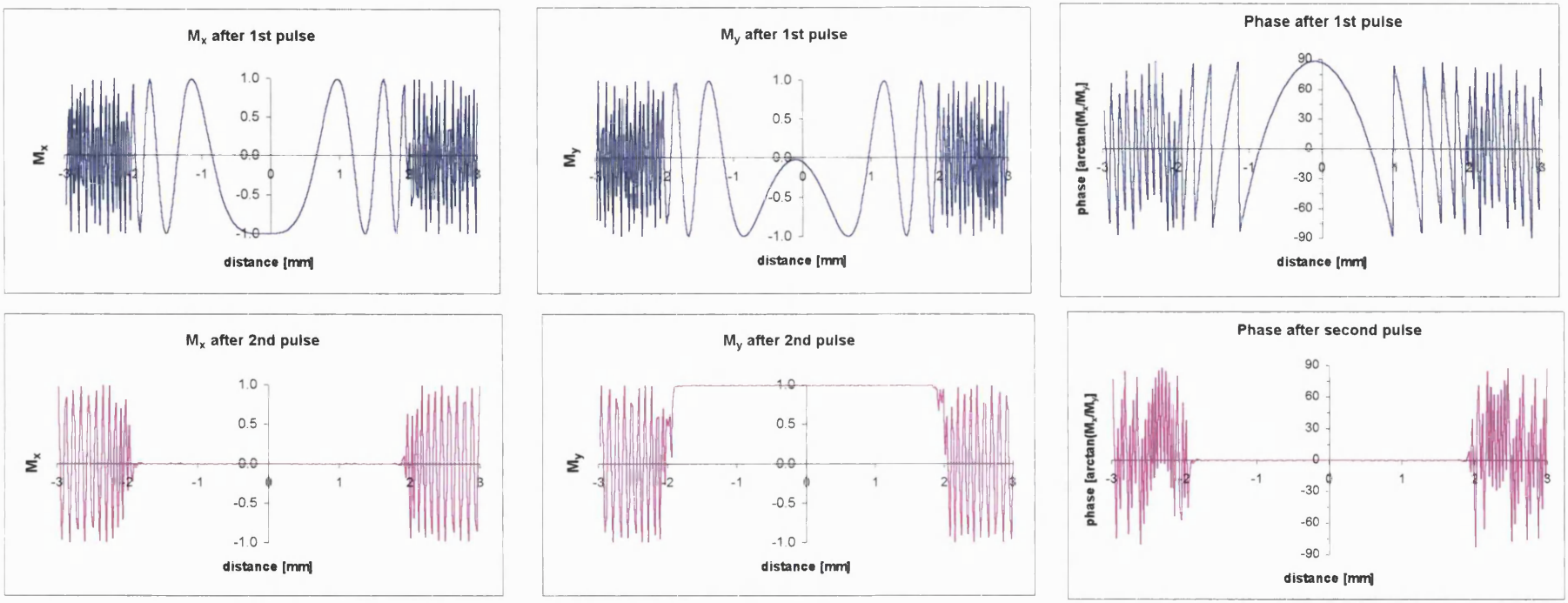

Fig. 3.16 Comparison of the simulated transverse components of the magnetisation, M_x and M_y, subsequent to the first and second adiabatic pulses of the double-FOCI refocusing scheme. The phase [in degrees], defined by $\arctan(M_x/M_y)$, at these stages is also shown. The adiabatic pulse parameters are as described in Fig. 3.12. It can be seen that a symmetrical, almost linear phase is left across the slice after the first pulse which is eliminated by the second pulse. Outside the slice, the transverse magnetisation exhibits the phase wrapping that is characteristic of gradient-induced dephasing and which makes no net signal contribution.

suggest the utility of the optimised pulses but further work with more animals is required in order to confirm these suggestions.

3.7 Measurement of perfusion using CASL in a model of focal ischaemia

The ASL techniques are expected to be especially useful for the study of experimental and clinical stroke (Detre, 1998; Siewert, 1997). A high field study was undertaken that employed multi-parametric quantitative MRI in order to follow the time evolution of focal ischaemia induced by permanent middle cerebral artery occlusion (MCAO) in the rat. Two such models were investigated in which the degree of ischaemia was varied by changing the size of the occluding device. It was desired to use the combined perfusion and diffusion information as a tool to delineate regions with different degree of ischaemic damage and to thus examine the changes of the other parameters in these areas. A basic outline of this study emphasising the perfusion data is described here and the details of the investigation are described in refs. (Calamante, 1999; Lythgoe, 1999).

3.7.1 Methods

3.7.1.1 NMR Methods

Measurements were carried out on the 8.5T vertical bore system with a 50 mm internal diameter, a 38 mm diameter birdcage coil as transmitter/receiver and a maximal gradient strength of 16 G/cm. The chosen coronal slice was 2 mm wide and positioned approximately 7 mm from the interaural line. NMR measurements of the diffusion trace (trace(D) defined in Section 2.1.2), T_2, T_1 and CBF were obtained throughout the course of the experiment using a combination of spin-echo 2D-FT (trace(D) and T_2) and high time-resolution FLASH techniques (T_1 and perfusion). Each sequence used a 128×64 acquisition matrix size, which was then zero filled to 128×128 points before the FT. Sequence parameters were as follows:

T_1 measurement: Series of 20 SNAPSHOT-FLASH IR images ($TE/TR/T_{image}$ = 2.0/3.6/231 ms; inter-FLASH delay = 2 ms; flip angle = 5°; number of averages (NEX) = 20). For efficient spin inversion, a slice-selective FOCI pulse was used.

T_2 measurement: Four echo multi-spin-echo sequence ($TE_{\{n=1,4\}}$ = 35,70,105,140 ms; TR = 1000 ms; NEX = 4).

Measurement of the trace of trace(D): Trace(D)-weighted 2D-FT imaging sequence using the diffusion gradient patterns reported by Mori *et al.* (Pattern III in Mori, 1995) (δ/Δ = 5/5.4 ms; b-values = 30,800,1700 sec/mm^2; TE/TR = 80/1000 ms; NEX = 4).

Perfusion measurement: The CASL method was employed without the implementation of a pre-labelling delay or T_{1sat} acquisition since the importance of these modifications had not yet been appreciated. A continuous 5 second RF pulse was applied at a 9 kHz offset and in the presence of a field gradient (1.6 G/cm). The tagging pulse was immediately followed by FLASH imaging acquisition (see Section 6.2) (centre-out phase encoding; TE/TR/T_{image} = 2/5/320 ms; flip angle = 14°; NEX = 25; alternating sign of tagging gradient).

3.7.1.2 Animal methods

Male Wistar rats (130-150 g) were prepared for remote MCA occlusion (n=15). Anaesthesia was induced with a 3% halothane/O_2 mixture and maintained via a nose cone at 1.25% halothane for the duration of the surgery. Once the animal was inside the magnet, the halothane concentration was reduced to 0.8% in a gas mixture of 70% N_2O and 30% O_2. Rectal temperature was recorded and maintained at 37-38°C. Animals were allowed to breathe spontaneously throughout the experiment.

Occlusion was induced by an intraluminal suture method based on a modified Zea-Longa approach (Zea-Longa, 1989). The remote occluding device was either a blunted 0.2 mm diameter (n=10) or 0.24 mm diameter (n=5) length of nylon monofilament (Perlon, Bayer, Germany). It was expected that varying degrees of ischaemia would be induced by the different sizes of thread.

3.7.1.3 Experimental protocol

After a period of control imaging, occlusion was initiated and cycles of multi-parametric imaging were continued for 4-6 hours. The time interval between successive measurements of the parameters were approximately 70 min (trace(D)) and 30 min (T_1, T_2, CBF).

3.7.1.4 Image and data analysis

Diffusion, T_1 and T_2 maps were generated on a pixel-by-pixel basis. Two parameter non-linear regression was employed for the T_2 and trace(D) data, and a 3-parameter fit was used for the T_1 data. Perfusion values were obtained by fitting the CASL data to Eq. [3.7(c)]. Regional analysis was carried out on the basis of the severity of the focal ischaemia that was indicated by the trace(D) data. If an area became evident that displayed ischaemic damage, three region were drawn in the maps as shown in Fig. 3.17(a)), in (1) the ischaemic core determined using the terminal trace(D) maps at 4-6 hours post-occlusion, (2) a region in the contralateral, normal cerebral hemisphere, and (3) a region in the *border* area of moderate ischaemia. This latter region was positioned anterior to the core of the ischaemic lesion, between the area supplied by the middle and anterior cerebral arteries. The border represents an area of moderately reduced blood flow with no change in the trace(D) value. If an ischaemic area did not become apparent, regions were drawn in the cortex and basal ganglia in both the ipsilateral and the contralateral hemispheres (see Fig. 3.17(b)). Data are presented as mean ± SEM (standard error in the mean). The statistical significance of comparisons was analysed with t-tests. Significance was set at P-values less than 0.05.

3.7.2 Results

The post-occlusion diffusion changes were crucially dependent on the size of the occluding device. The larger filament size (0.24 mm) induced an ischaemic lesion that was clearly identifiable in the diffusion and perfusion maps. Therefore, the regional data from three regions in the core, border and normal areas were analysed. The smaller occluding device (0.2 mm) induced a noticeable change in the CBF but not in the trace(D) value of the ipsilateral hemisphere (Fig. 3.17). It was clear that the two MCAO models were distinct and the results of each type are described in turn. The time courses are described in ref. (Calamante, 1999; Lythgoe, submitted). In the following sections, a review of the flow and accompanying diffusion measurements are principally described.

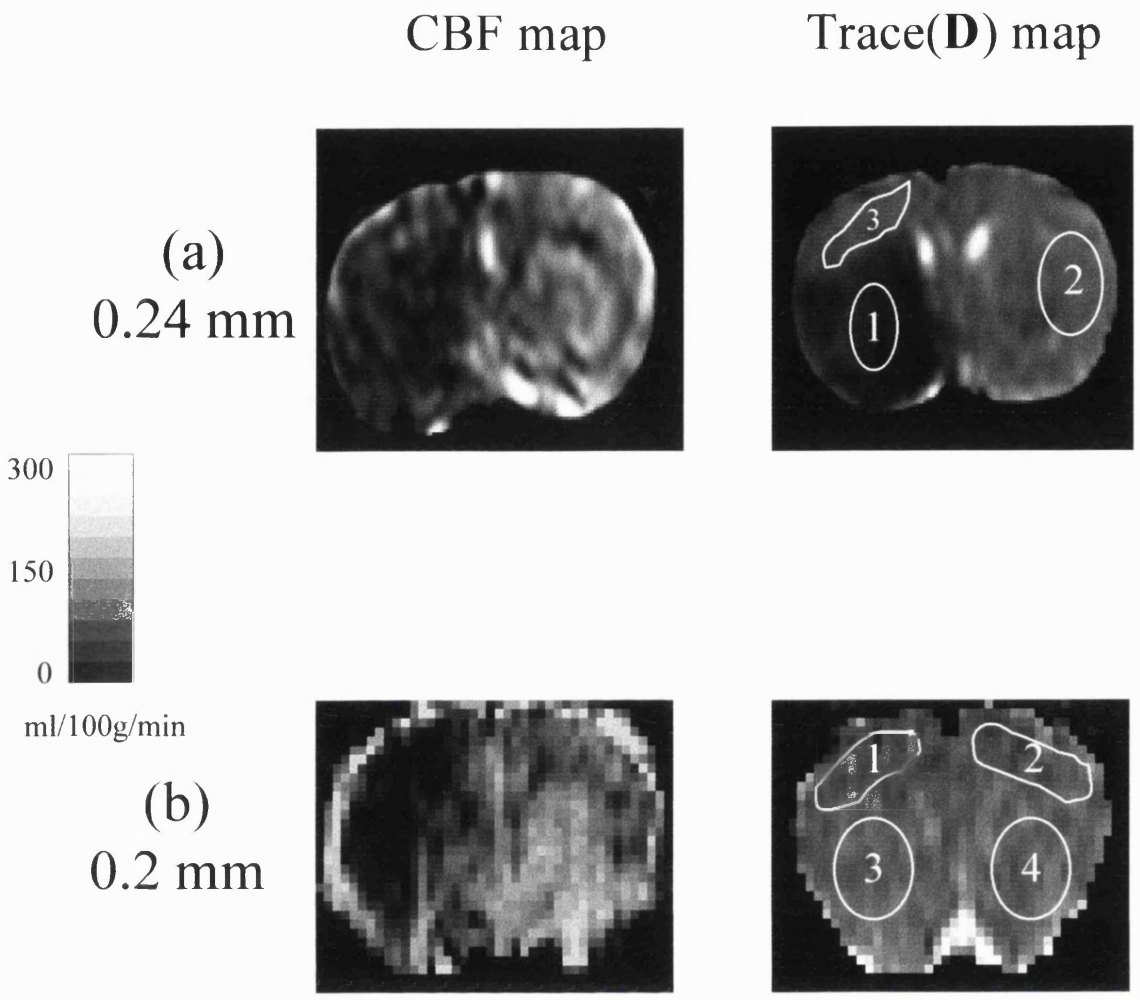

Fig. 3.17 Typical maps obtained from the occluded rat for (a) the standard MCAO (0.24 mm occluding thread) and (b) the misery perfusion (0.2 mm) models. In each case, a perfusion map (left image) with reduced flow in the occluded side (acquired with $t \geq 4$ hr) and a corresponding trace(D) map (right image) is shown. The position of the ROIs used in the analysis of the two model are displayed on the trace(D) maps. Note that the degree of smoothing observed in the two CBF maps is not identical due to differences in the fitting procedure. Bright areas of signal in the CBF maps are evidence of vascular artefacts (see Section 3.5.2).

3.7.2.1 Occluding device (0.24 mm)

(1) **Core**

Diffusion: The pre-occluded trace(D) value was 0.83±0.02 $\times 10^{-3}$ mm^2/sec and was reduced by approximately 23% by the first time point post-occlusion (acquisition time, t ≈ 50 min). The value of the diffusion coefficient gradually decreased and reached an asymptotic value of 0.51±0.02 $\times 10^{-3}$ mm^2/sec.

Perfusion: The pre-occluded value was 186±11 ml/100g/min and permanently dropped on occlusion by approximately 160 ml/100g/min to a range that was almost within the noise level of the measurement.

(2) **Border**

Diffusion: The pre-occluded value was 0.81±0.01 $\times 10^{-3}$ mm^2/sec and displayed no apparent post-occlusion change.

Perfusion: On occlusion, the CBF decreased from the control value of 146±8 ml/100g/min by approximately 83 ml/100g/min. This signal drop was significantly less than the corresponding decrease in the core region (paired t-test, $p<0.0001$).

(3) **Normal**

Diffusion: Pre-occluded value was 0.83±0.01 $\times 10^{-3}$ mm^2/sec and displayed no apparent post-occlusion change.

Perfusion: The pre-occlusion value was 205±14 ml/100g/min on occlusion. This initial decrease was significantly different from zero ($p=0.01$) and the flow then gradually returned to the control level.

Summary of T_1 and T_2 data

T_2: The initial post-occlusion T_2 map (t ≈ 1 min) indicated a significant decrease in the core and border regions. The relaxation time subsequently increased during the course of the observation period. In the core region, the T_2 reached a value that was considerably higher than the pre-occlusion level. No changes were observed in the contralateral hemisphere.

T_1: A rapid T_1 rise was immediately observed in the core and border regions (first data point acquired at t ≈ 5 min). The time evolution after this early increase was different in the two regions, progressively increasing at a slow rate in the core, while remaining approximately constant in the border region. No changes were observed in the normal hemisphere.

3.7.2.2 Occluding device (0.2 mm)

Diffusion: Pre-occlusion values were 0.80±0.02 $\times 10^{-3}$ mm^2/sec and 0.81±0.02 $\times 10^{-3}$ mm^2/sec in the basal ganglia and cortex respectively. No post-occlusion changes in the trace(D) were observed.

Perfusion: The control values were 198±19 ml/100g/min and 177±17 ml/100g/min in the basal ganglia and cortex respectively. On occlusion, the behaviour of the CBF was markedly different in the ipsilateral and contralateral hemispheres. In the ipsilateral regions, the CBF displayed an immediate decrease of approximately 192 ml/100g/min and 105 ml/100g/min in the basal ganglia and in the cortical region. After 40 min of occlusion, the perfusion values began to gradually rise. In the contralateral hemisphere, smaller decreases of 23 ml/100g/min and 26 ml/100g/min in the two regions were observed but the terminal values were not significantly different from zero.

Summary of T_1 and T_2 data

T_2 : An initial rapid decrease was apparent in the ipislateral regions and, by approximately 60 min post-occlusion, the T_2 had recovered to the control level.

T_1 : A rapid initial rise in T_1 was observed that had levelled off at a level that became significantly higher than the control value by approximately 50 min post-occlusion.

3.7.3 Discussion

Two models of MCA occlusion have been demonstrated in which the size of the occluding device has appeared to determine the severity of the response to permanent occlusion. The combination of diffusion and perfusion imaging in this study has enabled the delineation of regions that corresponded to known states of compromised tissue. The spatial registration of the accompanying time data has offered further insights into the vascular and cellular response to focal ischaemia (Calamante, 1999). The border region (0.24 mm occluding device) and the ipsilateral regions (0.2 mm occluding device) were characterised by a decrease in the CBF by approximately 50% of the control level, without an accompanying change in the diffusion coefficient. These observations may reflect the development of oligaemic misery perfusion in these regions which is a state of ischaemia in which a constant level of oxygen metabolism is maintained despite an impaired degree of flow (see Section 7.4.2 and Appendix B). This can be contrasted with the core region (0.24 mm occluding device) in which the tissue status is compromised by a combination of reduced CBF and oxygen metabolism (ischaemic

misery perfusion). Areas of oligaemic misery perfusion reflect tissue in a compromised state that does not necessarily proceed to infarction and may correspond to the potentially salvageable penumbral zone (Hossmann, 1994a). Standard models of MCAO have tended to induce large regions of severely reduced CBF and this has given rise to difficulties in investigating the state of oligaemic misery perfusion. The model employed in this study using the smaller 0.2 mm occluding device presumably allows a residual blood flow through the MCA and, thereby, produces a hemisphere-wide zone of misery perfusion. The model, thereby, offers considerable potential in the investigation of this important tissue state which must represent the focus of post-hoc stoke therapy.

The measured values of perfusion were high and displayed considerable inter- and intra-animal variability due to the factors discussed in Sections 3.3 and 3.5. The post-occlusion values are expected to be underestimated especially in the ischaemic core as a result of a heterogeneous distribution of extended transit times. Further investigations of the MCAO models using the modified CASL technique of Alsop *et al.* (Alsop, 1996) are required in order to better understand and follow the state of compromised flows in the occluded area.

3.8 Validation of the ASL techniques

The validation of regional perfusion values with corresponding values obtained using other flow measurement techniques in the same subject, has only been performed to a limited degree and solely for the continuous labelling technique (Walsh, 1994; Ye, 1997b; Hernandez, 1998). The attempted validation of any perfusion technique is complicated by the absence of an accepted, *gold standard* method. The different methods listed in Table 2.2, may not all measure exactly the same quantity by virtue of their differing theoretical foundations and methodologies. Nevertheless, useful information can be gained by comparing the values obtained from different techniques. This section describes two such comparative investigations.

3.8.1 FAIR and CASL

3.8.1.1 Methods

The continuous and pulsed (FAIR) variants of the ASL techniques were implemented in tandem on a coronal 2.3 mm slice in the rat (n=2). In one of the two animals, an MCA

occlusion had been induced by the conventional intraluminal suture method. All experiments were carried out on the 2.35T system with EPI-based sequences. Both FAIR and continuous pulse sequences incorporated bipolar gradients ($b \approx 10$ mm^2/sec) in order to reduce the effects of intravascular contamination.

FAIR: Selective and non-selective images were obtained at 8 TI delays (TI = 200-3500 ms, TR = 8 sec, NEX = 25, imaging slth = 2.3 mm, inversion slth = 6 mm, spin-echo EPI acquisition). Other details of the sequence were as described in Section 4.4.2. The transit time was taken into consideration by assuming a constant value of 100 ms for the pulsed experiment, and the modified biexponential expression (Eq. [A2]) was employed for quantification.

CASL technique: The T_1 in the presence of off-resonance irradiation, T_{1sat}, was measured using the method described in Section 3.5.3.2. The off-resonance pulse length, τ, was varied in 8 steps (τ = 200-3500 ms, $\Delta\omega$ = 5 kHz, TR = 10 sec, spin-echo EPI acquisition). The spin-tagging control and tagged experiments employed the same spin-echo EPI acquisition sequence (τ = 6 sec, tagging RF amplitude = 70 mG, tagging gradient = ±140 Hz/mm, $\Delta\omega$ = 5 kHz, post-labelling delay(w)=100 ms, NEX = 64, TR = 10 sec). The frequency offset corresponded to a tagging plane in the neck that was 18 mm from the imaging slice. The transit times are, therefore, expected to be significant and must be included in the analysis (Eq. [3.15]). Values of δa = 200 ms and δ = 600 ms were chosen (see Section 3.5.3.2) from the results of previous experiments and reported data (Alsop, 1996; Ye, 1997a).

3.8.1.2 Image and data analysis

CBF maps were created on a pixel-by-pixel basis. Regions were drawn in the cortical and striatal regions in each cerebral hemisphere. In the occluded animal, an ROI was placed in the ischaemic area (as determined from a pilot diffusion-weighted scan) and the analysis of this region was treated separately. Regions contained approximately 200 pixels; statistical analysis could not be performed on this data due to the limited number of experiments carried out thus-far.

3.8.1.3 Results and Discussion

The average non-occluded perfusion values were as follows (with SDs within the individual regions not quoted):

FAIR:

101 ml/100g/min and 141 ml/100g/min in cortex and striatum respectively (Animal 1)

144 ml/100g/min and 151 ml/100g/min in cortex and striatum respectively (Animal 2)

CASL:

101 ml/100g/min and 151 ml/100g/min in cortex and striatum respectively (Animal 1)

118 ml/100g/min and 150 ml/100g/min in cortex and striatum respectively (Animal 2)

In the occluded cortical region, the CBF was 19 ml/100g/min (FAIR) and 4 ml/100g/min (CASL).

The CBF values in the unoccluded regions as measured by the two techniques were in good agreement. The CASL measurements in the occluded area appear to underestimate the corresponding FAIR values (values approximately 80% lower than the FAIR measurements) and this may reflect the greater transit time sensitivity of the former technique. The transit time insensitivity of the continuous technique had not been optimised since the chosen post-labelling delay (w=100 ms) was considerably smaller than the tissue transit time. The CBF measurements were, therefore, sensitive to the chosen values of δa and δ. Further experiments are required in order to confirm this observed underestimation.

3.8.2 FAIR and Hydrogen (H_2) clearance

Hydrogen clearance is a commonly used polarographic technique for the measurement of blood flow under a wide variety of experimental conditions (see Table 2.2; Young, 1980). Positively polarised electrodes inserted into tissue oxidise inhaled hydrogen and provide an acceptor surface for the electrons. The subsequent flow of current is normally in the order of nanoamperes (nA) and is detected by an electrode impedance measuring system. The relatively inexpensive technique allows multiple flow measurements over long periods of time unlike autoradiography or microsphere methods. In this study, FAIR and H_2 clearance measurements were compared in the gerbil. This work was carried out in conjunction with Dr. E. Proctor of the Royal College of Surgeons, London.

3.8.2.1 Methods

FAIR: The FAIR technique was implemented on the 2.35T system in the manner described previously in this chapter and in Section 4.4.2. Both the long TR (biexponential fit) and the short TR single subtraction implementations of FAIR were employed in various combinations (see Section 4.4). The coronal slice (slth=2.3 mm) was positioned between the frontal and parietal electrode positions. The electrode positions were slightly visible in the spin-echo EPI images as partial volume and through-slice susceptibility effects but the placement of the ROIs avoided this area.

H_2 clearance: In order to simultaneously obtain H_2 clearance and MRI readings, the standard clearance set-up required modifications including in-line filtering of the electrode circuitry, lengthening of the anaesthetic gas lines and a redesign of the NMR probe. The implementation of the H_2 clearance technique has been thoroughly covered in a previous paper (Gadian, 1987). Briefly, up to four platinum electrodes (125 μm diameter) were inserted into the cortex to a depth of 1 mm through burr holes in the skull. The electrodes were positioned in the frontal and parietal lobes of the cerebral hemispheres (2 mm anterior [frontal], posterior [parietal] and lateral [both] to the bregma). The electrodes were polarised to +400 mV with respect to a reference Ag/AgCl electrode that was placed subcutaneously in the flank. In order to measure the CBF, hydrogen was added to the anaesthetic gases to a fixed concentration of approximately 5%. The electrode currents were then monitored and the hydrogen inhalation discontinued at the point of tissue saturation. Output from the electrodes was sampled, digitised and processed every 15 sec using a computer-controlled detection system. Auckland *et al.* demonstrated that clearance curves in the gerbil display principally monoexponential characteristics (Avery, 1984) and multiple clearance compartments were not considered. Blood flow was calculated by either a *manual* time constant procedure or an *on-line* computer-controlled method (Busza, 1992; Allen, 1992; Allen, 1993).

The manual method utilises a monoexponential fit of the electrode currents obtained during the washout period, according to the following expression

$$I(t) = I(0)e^{-kt} \qquad [3.17]$$

The fitted time constant, k, corresponds to f/λ_H where λ_H is the blood:brain partition coefficient of hydrogen ($\lambda_H \approx 1.0$ ml/g). Figure 3.18(a) shows a representative data set.

The on-line method provided a flow reading for every 15 sec interval that was immediately displayed on the computer terminal and calculated according to the expression

$$\frac{I(t)-I(t+\Delta t)}{I(t)}\times\frac{1}{\Delta t}\times 100 \qquad \text{[ml/100g/min]} \qquad [3.18]$$

where I(t) and I(t+Δt) are the successive current readings at times t and t+Δt respectively (Δt = 0.25 min) (Allen, 1992). As long as the electrode currents decay in a monoexponential fashion, the blood flow calculated in this manner remains constant and the display of CBF as a function of washout time will have a zero slope. In order to calculate the mean CBF, the data points were averaged over this flat portion of the plot of CBF vs. washout time. Figure 3.18(b) displays representative data output from the flow program. Comparison of the on-line and manual methods have demonstrated a high degree of agreement for flow values below approximately 50 ml/100g/min (Allen, 1992). The accuracy of the on-line method is limited at higher flows by the time resolution of current measurements (Δt).

Animal methods: Mongolian, gerbils (60-70 g) were anaesthetised with halothane/oxygen (n=10). Three of the animals were prepared for unilateral occlusion using a modified, remote snare procedure (E. Proctor, unpublished).

3.8.2.2 Image and data analysis

The on-line clearance flow calculation method was usually used for CBF determination but for higher flows, the manual procedure was employed in order to improve the accuracy of these measurements. The MRI and hydrogen clearance readings were temporally correlated by combining the simultaneous measurements, or if concurrent readings had not been obtained, by comparing measurements that were acquired within the closest time interval. Four ROIs were drawn in the FAIR CBF maps in the cortical and striatal regions of the left and right hemispheres. Regional correlation between the techniques were carried out on a *hemisphere-basis* by averaging the cortical and striatal measurements in the CBF maps. These values were compared to the averaged H_2 clearance readings obtained from the frontal and parietal electrodes in the hemisphere.

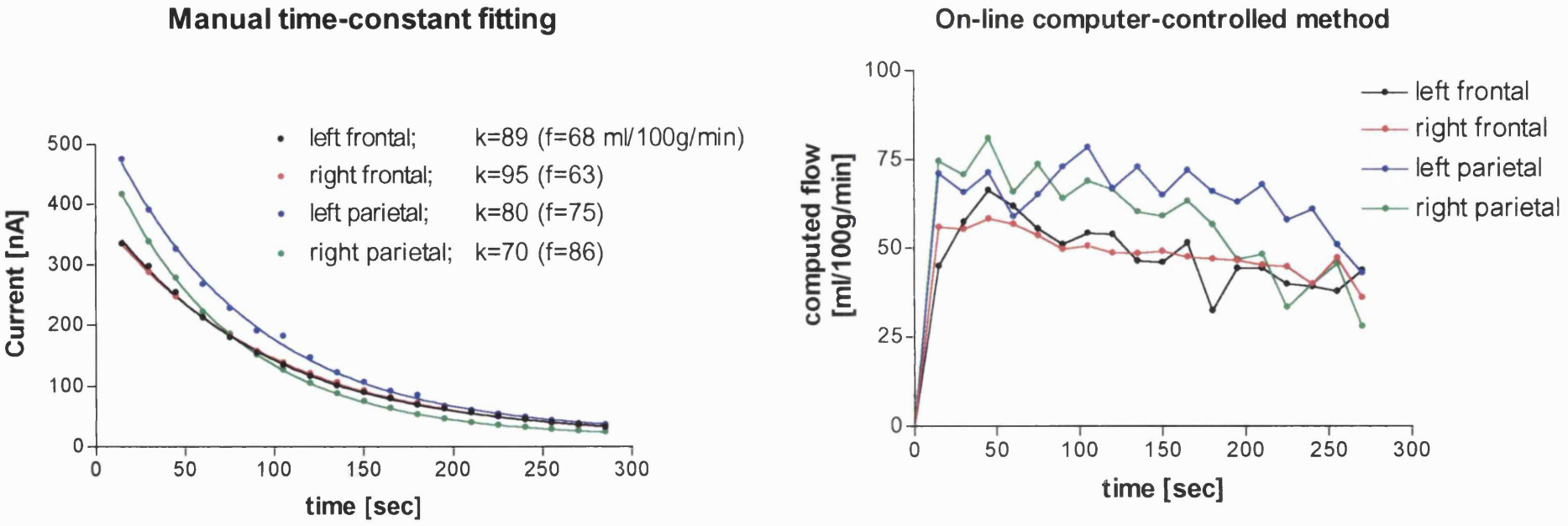

Fig. 3.18 Representative data output produced from the two methods of flow determination for H_2 clearance, (a) the manual procedure (with the slope, k, and the flow, f, indicated), and (b) the on-line method (see Methods). Four electrodes positions in the frontal and parietal cortical lobes were utilised in both cases. The two data sets are not from the same animal.

Comparisons were not made between the readings if only one electrode had been placed in the cerebral hemisphere. Previous experiments in our laboratory had demonstrated that electrode implantation induces a heterogeneous reduction in flow in the hemisphere (also Verhaegen, 1992). However, a more homogeneous distribution of flows in the hemisphere is obtained with the insertion of two electrodes. Flows in the left and right hemispheres were treated independently in the analysis for the same reason. A number of MRI readings were rejected from the analysis due to the presence of artefactually high signal as a result of electrode-related susceptibility effects, in which event the slice position was moved or the shims adjusted.

3.8.2.3 Results

The FAIR measurements are plotted against the corresponding H_2 clearance readings in Fig. 3.19. The line of identity (y=x) is shown for comparison. The generally lower control CBF values observed in this study reflect tissue injury due to the insertion of the electrodes (Tomida, 1989). The flow has been found to recover to the normal range of values by approximately six hours after electrode insertion. Concordance analysis (Lin, 1989) was carried out on the data from seven (out of the ten) animals since flows were obtained over a wide range of values in these experiments. The concordance correlation coefficient, ρ_c, was not significantly different to its ideal value of ρ_c=1.0 in six of these animals and this indicates a significant general degree of concordance. The lower range of flows (10-80 ml/100g/min) display a good level of agreement between the two techniques. For higher flows (>80 ml/100g/min), the hydrogen clearance values generally appear to be lower than the FAIR measurements. This may reflect interference with the assumption of diffusion limitation as the flow rises may occur since the ability of the electrode to reduce the adjacent hydrogen concentration to zero is reduced and the effect of the diffusion barrier becomes more significant (Young, 1980). In addition, an intensified level of intravascular contamination of the FAIR images would result in an artificial increase in the measured MRI flow values.

3.8.2.4 Discussion

A reasonable degree of correspondence between the two techniques of blood flow quantification was demonstrated by this study. The two methods are fundamentally similar in their reliance on the measurement of the free diffusion of either tissue water or inhaled hydrogen. Precise regional correlation was, however, complicated by the need to displace the position of the MRI imaging slice from the plane of the inserted electrodes and by the averaging of the cortical and striatal regions. Hydrogen clearance can provide measurements with a high time resolution and from multiple locations, but is limited by factors such as the necessary delay between measurements, undetermined spatial localisation and the significance of the diffusion barrier and the baseline current (Young, 1980). The injurious effect of electrode placement is indicated by the immediate alteration in the measured flow, and the overall CBF values obtained in this study are significantly lower than measurements from a standard control experiment (see Section 4.5.3). The MRI technique provides a measurement with an improved temporal resolution and its ability to map the flow within a single slice can be enhanced by extension to multi-slice acquisition. The accuracy of measurements with the ASL technique at low flows is compromised by the transit time effect and, if this is not taken into account, the accuracy of hydrogen clearance readings in this range is theoretically superior. However, for the flows measured in this steady, the correspondence between the two techniques is encouraging.

3.9 Conclusion

This chapter has described the ASL techniques that allow the non-invasive quantification of CBF. The methods have been implemented in a number of animal studies and attempts have been made to optimise their performance with the use of pulse profile optimisation.

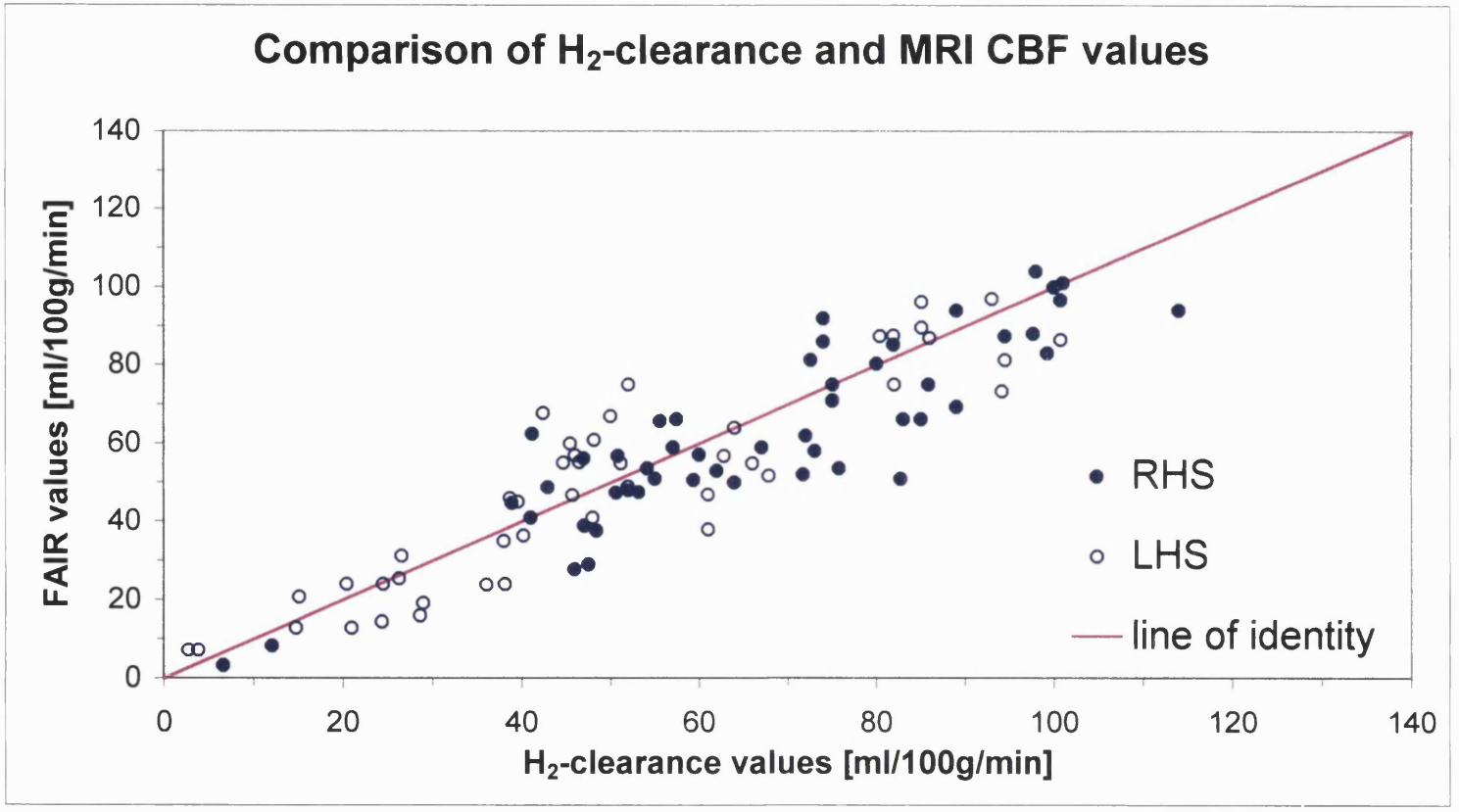

Fig. 3.19 Comparison of H_2 clearance and FAIR measurements of flow. The line of incidence is shown. FAIR values were obtained in each cerebral hemisphere (RHS and LHS).

IV THE IMPLEMENTATION OF QUANTITATIVE FAIR PERFUSION IMAGING WITH A SHORT REPETITION TIME IN TIME-COURSE STUDIES

MRI techniques that can provide quantitative and non-invasive measurements of cerebral perfusion have shown great potential over recent years. Arterial spin labelling techniques for quantitative perfusion measurements were introduced in Sections 3.3 and 3.4. These non-invasive MR techniques offer significant advantages over exisitng methods that are in standard use for CBF quantification. In particular, they have the potential to provide a good degree of spatial and temporal resolution. The latter aim has had to be somewhat compromised in recent quantification studies since the existing theoretical treatment of the FAIR technique requires full longitudinal relaxation between averaged acquisitions. This chapter describes a modification of FAIR with use of pre-saturation pulses that allows significant improvements in the SNR-per-unit-time but maintains the ability to accurately quantify perfusion. The investigation is described in ref. (Pell, in Press).

4.1 Introduction

One of the pulsed arterial spin labelling technique described in the previous chapter, is that of FAIR which utilises a combination of slice-selective and non-slice-selective inversion pulses in order to create a flow sensitive image. In time-course investigations of a system with potentially changing levels of flow, it is necessary to be able to quantify CBF with a high degree of temporal resolution. An ideal study of such a system would follow the time-course of these changes in a single subject and would offer good regional differentiation since a heterogeneous distribution of flows may be expected. Perfusion quantification with FAIR offers the benefits of MR imaging. However, the technique in its standard implementation for quantification with full relaxation between averaged acquisitions does not provide measurements of flow with optimum time efficiency. A means of extending the quantification model to incorporate the effects of more time efficient implementations of the sequence is therefore desirable.

The purpose of this study was to develop high time resolution CBF mapping with FAIR for subsequent implementation in time course investigations. This was achieved in two stages. First, a modification of the FAIR technique was investigated and implemented that would enable a time-course study of cerebral perfusion with improved time

efficiency. Second, the accuracy of the modified technique was demonstrated by experimental comparison with data acquired using the standard, slower version of the ASL sequence. Implementation of FAIR in this study has brought to attention various issues involved with the quantification of perfusion using this technique, and these are discussed. The theoretical aspects of this time-course study of quantitative perfusion imaging are described in this chapter. In Chapter 5, the modified sequence was employed in a time course investigation of the effects of reperfusion.

4.2 Theory

The normalised tissue magnetisation, M(t), in the presence of inflowing spins can be described by the extended Bloch equation (the T_1 model, see Section 3.2.1). This model can be used to provide values for the non-selective and selective magnetisation states, $M_{ns}(t)$ and $M_{ss}(t)$. In the original analyses using the model (Detre, 1992; Kim, 1995), the analysis was simplified by assuming that the longitudinal relaxation time of blood, T_{1a}, is equal to that of tissue, T_1. However, T_{1a} is longer than the tissue T_1, and it has been shown that the model's assumptions of equal T_1 values introduces errors into the quantification that can be significant (Calamante, 1996). If the differing T_1 values of blood and tissue are incorporated into the model, the expression for the magnetisation difference at time TI, $\Delta M(TI)$, takes on a biexponential form (Kwong, 1995; Calamante, 1996) given by Eq. [3.8]. In order to obtain an accurate flow measurement, it is necessary to acquire selective and non-selective images over a range of different TI times.

4.2.1 FAIR with a short TR

The model has thus far assumed full longitudinal relaxation between the averaged acquisitions. However, this does not optimise the perfusion signal-to-noise (SNR) with respect to time (SNR-per-unit-time), and acquisitions with a reduced repetition time would increase the time efficiency of the sequence (Tsekos, 1996). An approximate expression for the subtracted signal intensity has been obtained for such a situation (Eq. [8] in ref. (Kim, 1997a)) and is given by

$$\Delta M(TI) \approx \frac{f}{\lambda} M_0 \, TI \exp(-TI / T_1) \left[2 - \exp(-\tau / T_1)\right] \qquad [4.1]$$

where τ is the recovery time between the image acquisition and the subsequent inversion, so that the total repetition time, TR, is equal to (TI + τ). In addition to the assumptions of equal blood and tissue T_1 values and of $(f/\lambda)TI << 1$, an extra assumption is made in order to arrive at this expression; that relaxation during the recovery time following the non-selective image. This assumption, however, is not completely realistic since T_{1app} recovery only occurs when the inflowing blood is fully relaxed. During the inversion time and recovery time intervals that follow the non-selective inversion, the inflowing spins will still be relaxing. Similarly, in the case of interleaved selective and non-selective acquisitions, the inflowing spins will not have fully relaxed by the time of the subsequent selective inversion if $\tau << 5T_{1a}$. In fact, relaxation during these two phases is governed by biexponential characteristics. It can be shown (see Appendix A) that once the steady state has been reached, the expression then takes on a more complicated form

$$X(TR) = \sum_{n=0}^{N} (1-2\alpha_0)^n \exp(-2nTR/T_{1a}) \qquad [4.2]$$

where *X(TR)* is a factor that describes the steady state level of the inflowing blood

$$\Delta M(TI) = \frac{2M_0\alpha_0 \frac{f}{\lambda} X(TR)}{\frac{1}{T_{1app}} - \frac{1}{T_{1a}}} \left(1-e^{-TR/T_{1a}}\right)\left[\left(e^{-TI/T_{1a}} - e^{-TI/T_{1app}}\right) - (1-2\alpha_0)e^{-TI\,(1/T_{1a}-1/T_{1app})}\left(e^{-\tau/T_{1a}} - e^{-\tau/T_{1app}}\right)\right] \qquad [4.3]$$

magnetisation, which is caused by the application of a series of non-selective inversions with a short repetition time. An expression for *X(TR)* is given by

where *N* is the total number of non-selective inversions and the factor of *2n* is needed since there is a period of *2TR* between each interleaved non-selective acquisition when the blood is again inverted. For typical experimental parameters, terms in this series become less significant with increasing *N* so that for $N \geq 4$, a constant value of *X(TR)* can be assumed. Figure 4.1 shows the form of the steady state factor for two TR times. Equation [4.2] reduces to Eq. [3.8] for $\tau \geq 5T_1$. In order to fit experimental data to Eq. [4.2], a series of dummy acquisitions would be required so that the system would reach a steady state. The error in using the simplified equation (Eq. [4.1]) instead of Eq. [4.2] can be significant, representing an underestimation of approximately 20% for typical parameter values of grey matter (GM) at 1.2T (TI = 1.2 sec, T_1 = 0.9 sec, T_{1a} = 1.2 sec, τ = 1.5 sec).

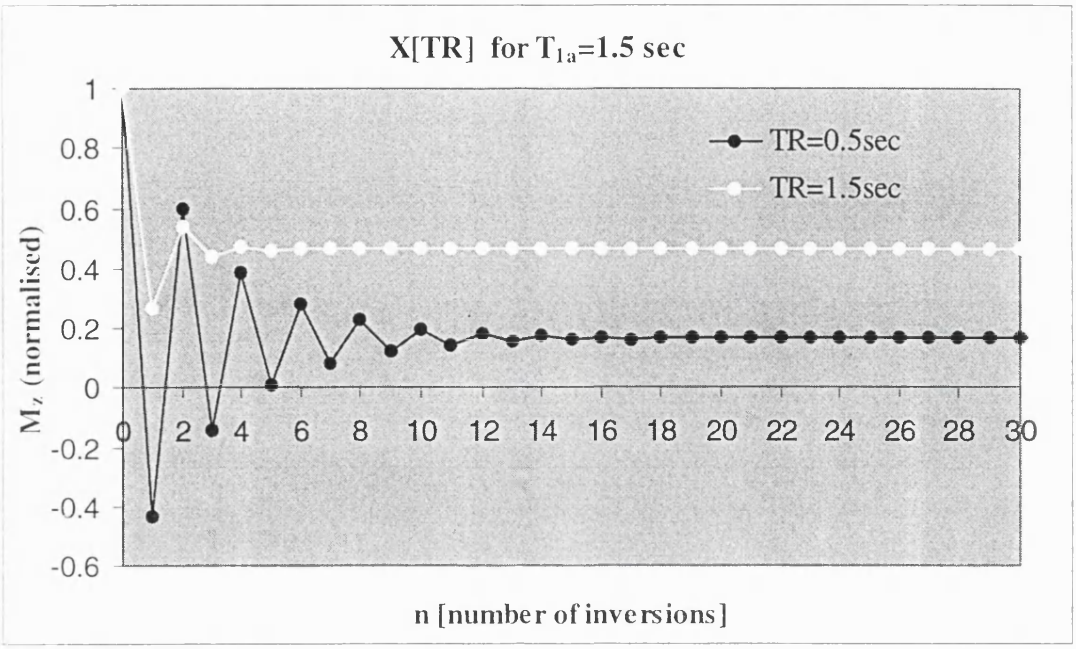

Fig. 4.1 Form of the steady-state factor, X[TR], for T_{1a} = 1.5 sec and the repetition time (between subsequent inversions) of 0.5 and 1.5 sec. It can be seen that for these interval times, approximately 10 cycles (TR = 0.5 sec) or 4 cycles (TR = 1.5 sec) are required for the steady state to be reached.

4.2.2 FAIR with a short TR : the use of pre-saturation

As an alternative to waiting for the steady state, if the longitudinal magnetisation of both the blood and the tissue is forced to start at the same point for both selective and non-selective acquisitions, the quantification will become significantly simplified. This can be achieved if global pre-saturation pulses are applied at the start of each τ period. The pre-saturation sets up the initial conditions from which the Bloch equations can be solved to give the following, simpler expression for the magnetisation difference, ΔM(TI)

$$\Delta M(TI) = 2M_0\alpha_0 \frac{f}{\lambda}\left[\frac{\exp(-TI/T_{1app}) - \exp(-TI/T_{1a})}{\frac{1}{T_{1a}} - \frac{1}{T_{1app}}}\right]\left[1 - \exp(-\tau/T_{1a})\right] \qquad [4.4]$$

where the modification to Eq. [3.8] is a term related to the blood relaxation during the τ delay. In addition to simplifying the quantification procedure, it can be seen that this method also offers the opportunity to measure the T_1 of blood by acquiring magnetisation subtractions at different τ delays and a constant TI time, and fitting to the mono-exponential recovery predicted by Eq. [4.4].

Practical implementation of the FAIR model is limited by the validity of two further assumptions concerning the nature of the selective and the non-selective acquisitions that have not yet been considered in this treatment. These assumptions underlie the intrinsic flow sensitivity of the selective image on the one hand, and the flow insensitivity of the non-selective acquisition on the other. The first limitation relates to the selective image that is assumed to be sensitised to all levels of flow for any value of the TI time. As Section 3.5.1 discusses, this premise is fallible in practical implementations of the technique due to the effect of the transit time delay, δ. The blood magnetisation then fulfils the following condition

$$M_a(t) = \begin{cases} \frac{M_0}{\lambda}\left(1 - 2\alpha_0 \exp(-t/T_{1a})\right) & t < \delta \\ \frac{M_0}{\lambda} & t \geq \delta \end{cases} \qquad [4.5]$$

where M_0/λ represents the blood equilibrium magnetisation with the assumption of a well-mixed compartment. The degree of inversion, α_0 is more realistically described by a spatially variant parameter whose form depends on the inversion profile.

The second limitation is related to the non-selective image and is discussed in the following section.

4.2.3 Coil inflow time effects

The non-selective image is assumed to possess only a negligible flow component. The validity of this assumption is dependent on the difference between T_{1a} and T_1. This situation is however, only realistic for the truly global inversion that a RF transmitter body coil would provide. If a transmitter coil is used that does not provide complete coverage of the subject, the non-selective inversion will have a finite slab width. Therefore, there will exist a coil inflow time, Δ, after which fresh blood spins begin to reach the excitation slice (Kim, 1995; Kim, 1997a). Once this occurs, the inflowing

blood will be in the same state in both the selective and non-selective acquisitions. This places an upper limit on the measurable flow rate for a given TI time. The blood magnetisation is given by

$$M_a(t) = \begin{cases} \frac{M_0}{\lambda}\left(1 - 2\alpha_0 \exp(-t/T_{1a})\right) & t < \Delta \\ \frac{M_0}{\lambda} & t \geq \Delta \end{cases} \qquad [4.6]$$

This set of conditions can be compared to those defining the transit time (Eq. [4.5]). Flow values will be underestimated if coil inflow during the TI time is not included in the FAIR model since the fresh spins will reduce the magnetisation difference between the non-selective and the selective images. If FAIR is implemented with a reduced repetition time – and, as in our study, in conjunction with global pre-saturation pulses applied at the start of each recovery time – coil inflow during τ as well as during TI must be considered. The effect of inflow during the recovery period is complicated in the particular situation of $\tau < \Delta$; fresh blood spins will then move into the transmitter coil volume during the recovery time but do not reach the imaging slice until a time (Δ - τ) after the subsequent inversion pulse. This sets up two 'zones' of arterial inflowing blood spins within the transmitter coil at the end of the τ delay with spins closer to the excitation slab relaxing from the global saturation and an outer volume of fresh blood spins (Fig. 4.2). The state of the tissue and blood magnetisation at the end of the recovery period becomes the initial state of the magnetisation during the inversion time. The magnetisation in both the non-selective and the selective acquisitions is thereby modified and depends on the magnitude of τ and TI relative to the coil inflow time, Δ. If $\tau > \Delta$, no inner volume of recovering spins will exist since uninverted blood spins will have reached the imaging slice during the recovery time. In the resulting analysis of the FAIR experiment, a number of possible situations will need to be considered which depend on the value of the inflow time and the choice of imaging parameters (Table 4.1). For example, Case (ii) utilises a choice of recovery and inversion times that are both greater than the inflow time, Δ. Appendix A details the resulting equations.

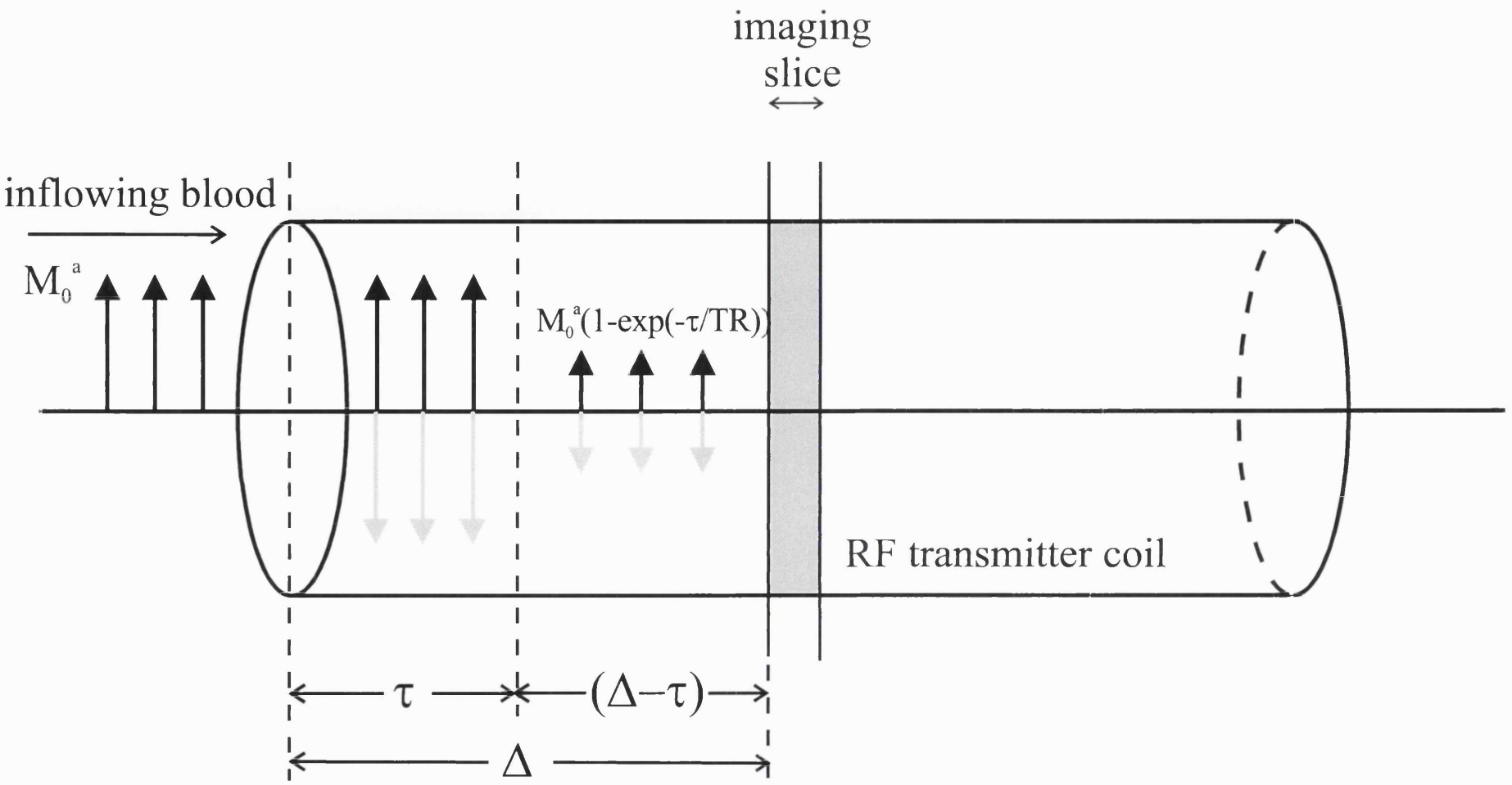

Fig. 4.2 The state of the blood magnetisation inside and outside the transmitter coil immediately after the recovery time, τ. The case shown is valid for $\tau < \Delta$ and for flow into the coil in one direction. Distances are expressed in time intervals. Global pre-saturation pulses had been applied at the start of the τ period. If a non-selective inversion instead of a selective inversion follows, the grey arrows indicate the state of the blood magnetisation.

	Recovery time (τ)		Inversion time (TI)		
	$\tau < \Delta$	$\tau > \Delta$	$TI < (\Delta-\tau)$	$(\Delta-\tau) < TI < \Delta$	$TI > \Delta$
Case (i)		✓	**N/A**	✓	
Case (ii)		✓	**N/A**		✓
Case (iii)	✓		✓		
Case (iv)	✓			✓	
Case (v)	✓				✓

Table 4.1 The set of conditions that need to be considered in order to extend the perfusion model to include the effects of the coil inflow time. A ✓ mark indicates a condition that has been satisfied while **N/A** indicates that the condition is not applicable. For example, Case (ii) utilises a choice of recovery (τ) and inversion times (TI) that are both greater than the coil inflow time (Δ). See Appendix A for the derivation of the equations that describe these cases.

4.3 Computer simulation

In the case of short TR FAIR without the use of pre-saturation, the error of using the approximate expression for the magnetisation difference (Eq. [4.1]) instead of the more complete theoretical expression (Eq. [4.2]) is demonstrated in Fig. 4.4 for typical parameter values.

In order to compare the SNR-per-unit-time for the various implementations of FAIR, theoretical normalised signal differences, $\Delta M(t)/(TR)^{1/2}$, were calculated using the previously described equations and heuristically optimised parameter values (see figure legend of Fig. 4.5). The denominator of this expression corresponds to the relationship between the number of averages and the SNR. This was carried out for four cases; (i) full relaxation between acquisitions (Eq. [3.8]); (ii) reduced repetition time without pre-saturation (Eq. [4.2]); (iii) reduced repetition time with pre-saturation (Eq. [4.4]) and (iv) reduced repetition time with pre-saturation and with inclusion of coil inflow effects (see equations derived in Appendix A).

4.4 Material and Methods

4.4.1 Animal Experiments

Mongolian, adult male gerbils, weighing between 60-70 g, were used in this investigation (n=8). These animals were subsequently employed for the reperfusion experiments described in Chapter 5.

4.4.2 NMR Methods

MRI measurements were performed on a 2.35T horizontal bore magnet (Oxford Instruments, Oxford, UK) interfaced to a SMIS console. Home-made gradient coils (12cm internal diameter (i.d.), non-shielded) were used which were capable of producing gradients of up to 4 G/cm in the phase-encode (y) and slice-select directions (z), and 13.5 G/cm along the read direction (x). Images were acquired using a slotted-tube, volume transmitter coil with a length of 6 cm, and a separate 3 cm diameter surface coil as the receiver, decoupled as described in (Bendall, 1986; Styles, 1988). A 2D-FT spin-echo sequence was employed for reproducible positioning of the animal within the magnet. The coronal slice was positioned approximately 1.8 mm from the bregma.

4.4.2.1 Perfusion MRI

The FAIR sequence implemented in this study is shown in Fig. 4.3. A FOCI (frequency offset corrected inversion) inversion pulse with a T-shape (Ordidge, 1997) was employed in order to produce efficient spin inversion and improved selective slice definition (with parameters: μ=5; β=628; pulse length=12 ms; maximum of the T-shape multiplication factor, A(t)=5) (see Section 3.6 for a more detailed description of these pulses). The inversion pulse was followed by a gradient spoiler (10 ms, 2 G/cm) to dephase residual transverse magnetisation and to reduce the effects of radiation damping (Zhou, 1998). The choice of inversion/imaging slice thickness ratio was made that gave subtractions that were within the noise level for an agar gel phantom (data not shown). Bipolar gradient pulses (b = 5 sec/mm^2), applied simultaneously along each gradient direction were necessary in order to eliminate signal contamination from fast moving arterial spins that would otherwise result in overestimation of flow values (Wong, 1996). The required gradient strength was determined empirically by increasing the b-value until the fitted CBF did not decrease further.

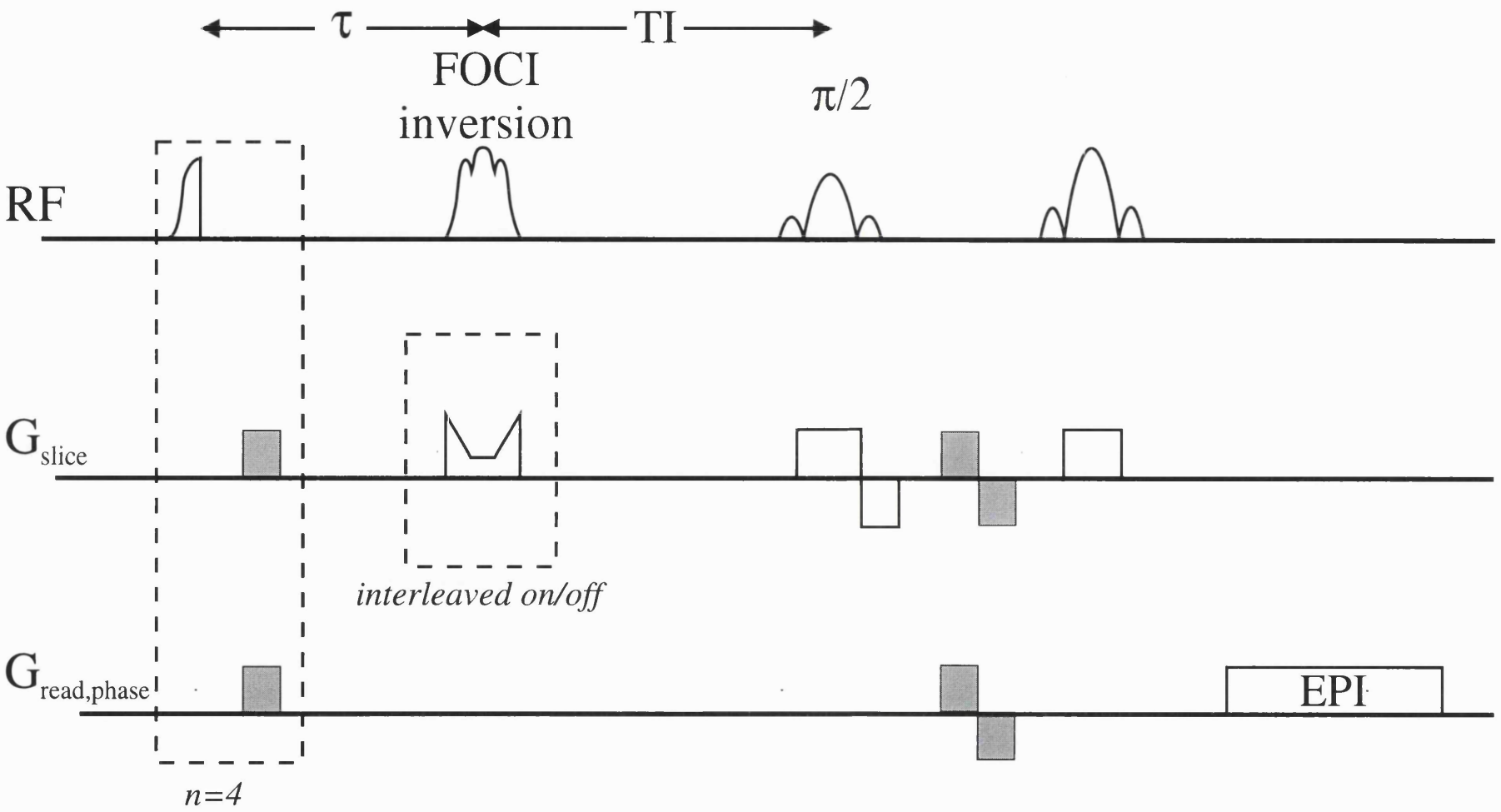

Fig. 4.3 Pulse sequence diagram for the modified FAIR sequence. The preceding global saturation pulses were employed for the reduced TR implementation of FAIR. The biexponential (long TR) pre-occlusion fitting procedure did not utilise the saturation pulses. Spoiler and crusher gradients are shown shaded in grey. The recovery time between the end of one acquisition and the next inversion, τ, begins after the application of the last saturation pulse.

The FAIR sequence was implemented with a spin-echo EPI sequence. Imaging parameters were TE = 35 ms; imaging slice thickness (slth) = 2.3 mm; inversion slth = 6 mm; image matrix size = 64×128; field of view (FOV) = 27.5×55 mm. Slice-selective and non-slice-selective acquisitions were interleaved.

4.4.2.2 Coil inflow effects

The transmitter coil used in this study did not provide global coverage of the animal's body; coil inflow effects therefore had to be taken into consideration. As discussed previously, the implementation of FAIR in conjunction with global pre-saturation offers a non-invasive means for the determination of the T_{1a} by following the variation of the magnetisation difference, ΔM, with the recovery time, τ (according to (Eq. [4.4]). However, if coil inflow effects are significant, ΔM will instead follow a piecewise, continuous behaviour with transition points that depend on the relationship between τ, TI and the inflow time (see Section 4.2.3). In order to determine the significance of the inflow time, Δ, the following experiment was carried out on a control animal. A large number of data points at different values of τ were used in order to characterise the form of the relationship with ΔM. The recovery time was varied in twenty steps between 100 ms and 6000 ms and the selective and non-selective images acquired using the FAIR sequence with the preceding global saturation. The inversion time, TI, was fixed at 1300 ms. Two methods were employed to estimate the inflow time from this data. First, the data were fitted to the composite, piecewise behaviour predicted by the theoretical equations. The confidence intervals of such a fit are expected to be considerable and, therefore, a second method was used in which a mono-exponential saturation recovery curve was fitted to the experimental data as an approximation. The relaxation time constant from this procedure was compared to values obtained by similar fits on simulated recovery curves obtained using the theoretical equations for the experimental parameter values. The choice of the inflow time in these curves was varied until the fitted relaxation times of the experimental and the theoretical data coincided. An estimation of the coil inflow time was thereby made and used in the subsequent analysis.

4.4.2.3 Pre-occlusion biexponential (long TR) data

During the control pre-ischaemic phase of the experiment, time was available to acquire enough data to fit to the biexponential curve described by Eq. [3.8]. Selective and non-

selective images were acquired at seven TI values [200,400,600,1000,1400,1800,2500 ms], with full relaxation between acquisitions (τ = 6500 ms so that $\tau \approx 5.T_1$ [grey matter]). For twenty averages, this procedure lasted approximately 45 min. Analysis of the data involved fitting the selective image set for T_{1app}, M_0 and α_0. The values obtained were used in the subsequent biexponential fitting of the subtracted data with flow, *f*, as the free parameter assuming a constant value for T_{1a} (Kwong, 1996). The biexponential data were also used to obtain a value for T_1 using the fitted values of flow and T_{1app} (Eq. [3.3]). The T_1 of blood is required for accurate perfusion quantification. By extrapolation of data obtained at other field strengths (Schwarzbauer, 1996; Tadamura, 1997), a value for T_{1a} of 1500 ms was estimated and used for subsequent quantification.

The effects of a transit time can be accounted for in the FAIR model (see Section 3.5.1 and Appendix A). The resulting biexponential relationship is modified by the transit time with a characteristic shift along the time axis (Eq. [A2]). In order to assess the significance of the transit time during this phase of the study, the biexponential data were examined for this effect.

4.4.2.4 Time-course single subtraction (short TR) data

For the time-course measurements of CBF, the reduced repetition time implementation of FAIR was employed. In order to demonstrate the validity of this method, this technique was also used to acquire pre-occlusion data that could be compared to the biexponential-fitted values. In our study, four half-passage hyperbolic secant pulses were utilised in order to produce efficient global saturation (Fig. 4.3) (pulse parameters : μ = 5; β = 628; pulse length = 6 ms). Profile data obtained with a phantom demonstrated that this combination of pulses reduced the global signal by approximately 99% (data not shown). A recovery time of 1500 ms and a TI time of 1300 ms were chosen in order to provide improved time efficiency. 100 (n=3) or 30 (n=5) interleaved averages for each pair of selective and non-selective images, provided a time resolution of 9.3 min or 2.8 min respectively. The values of M_0, T_1 and α_0 obtained during the biexponential scanning procedure were used to obtain perfusion measurements directly from each short repetition time, subtraction image.

4.4.3 Image and data analysis

For regional analysis of the perfusion time-courses, the data were imported into IDL (Floating Points Systems, Boulder, Colorado, USA). By rewriting T_{1app} in terms of T_1 and flow, the relevant reduced repetition time equation provides a non-linear expression for the blood flow. CBF maps were produced for each subtraction by solution of the equation using an iterative root-finding routine (*fx_root*). Four regions-of-interest (ROIs) were drawn on these perfusion maps in the left and right hemispheres of the slice, in the cortex and the corpus striatum of each hemisphere (see Fig. 4.7). Data are presented as mean ± SEM (standard error in the mean). The statistical significance of comparisons was analysed with t-tests. Significance was set at P-values less than 0.05.

4.5 Results

4.5.1 Computer simulation

Figure 4.4 shows the error associated with using the approximate expression for short TR FAIR derived in ref. (Kim, 1997a). For a typical TI time of 1300 ms, the error is approximately 13%. Figure 4.5 displays the relationship of SNR-per-unit-time with TI in the different situations. The short TR implementations of FAIR, with and without pre-saturation, display an improved time efficiency when compared to the sequence with full relaxation between acquisitions. The saturation pulse at the start of each acquisition reduces the SNR-per-unit-time but the steady state factor does not need to be considered. When coil inflow effects are significant, application of the saturation pulse is especially advantageous since the alternative analysis of the build-up of the steady state would be complex. In this situation, the magnetisation difference and therefore the time efficiency curve displays the piecewise, continuous characteristics of the theoretical equations (curve [iv]).

4.5.2 Coil inflow time determination

The variation of the magnetisation difference, ΔM, with the recovery time at a fixed value of TI was examined in order to estimate the coil inflow time, Δ. The piecewise fit is shown in Fig. 4.6(a) with Δ, T_{1a} and the multiplying coefficient related to M_0, as three free parameters. The fit provided a value for Δ of 1702±237 ms. In order to confirm this determination, a second method was employed. The mono-exponential saturation recovery curve predicted by Eq. [4.4] was fitted to the experimental data as an approximation (Fig. 4.6(b[i])).

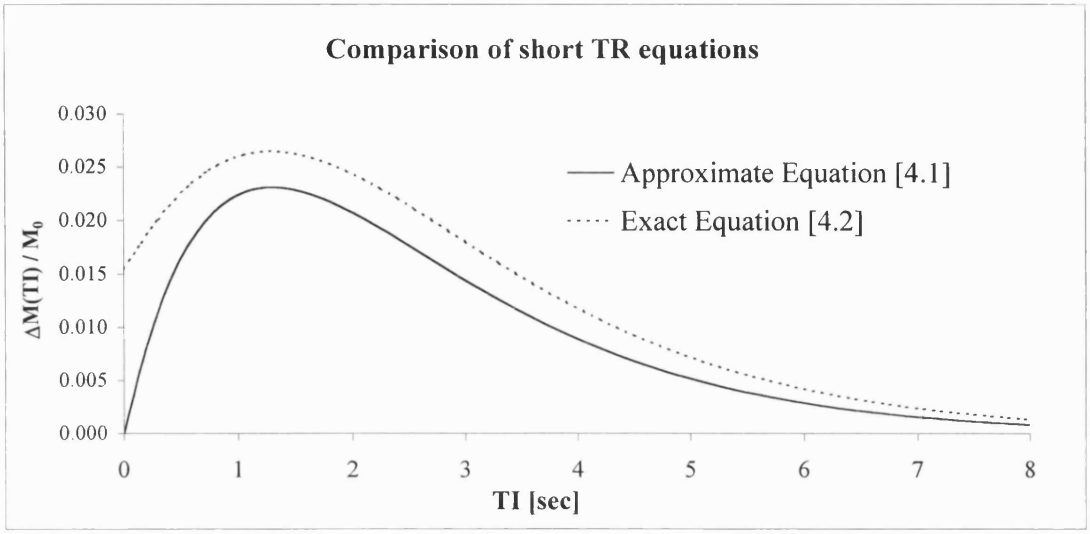

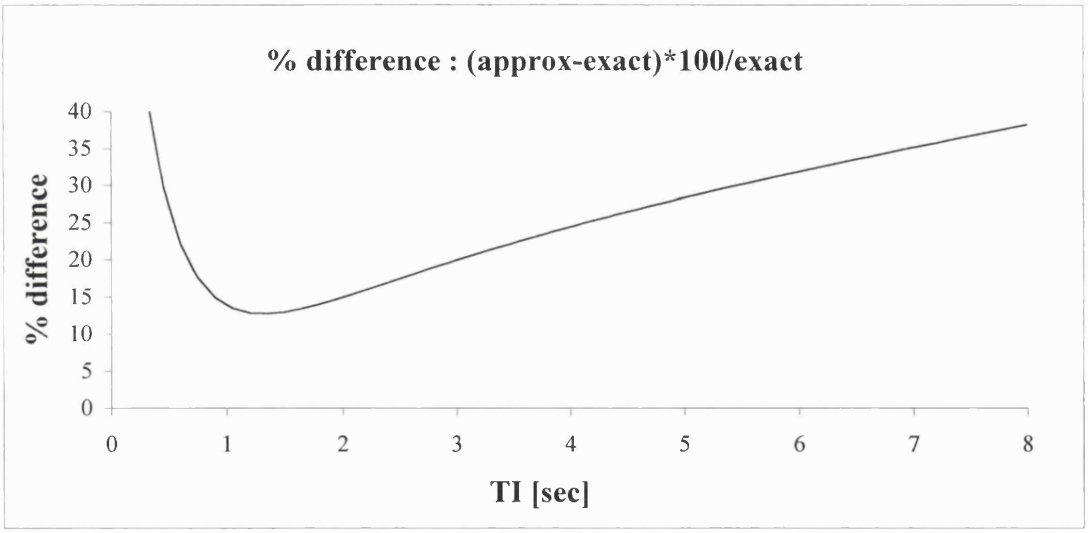

Fig. 4.4 Comparison of the *approximate* (Eq. [4.1]) and *exact* [Eq. [4.2]) expressions for FAIR with a short TR (with T_1 = 1300 ms; T_{1a} = 1500 ms; flow = 150 ml/100g/min). The figures depict (a) the magnetisation difference and (b) the percentage error in the magnetisation difference

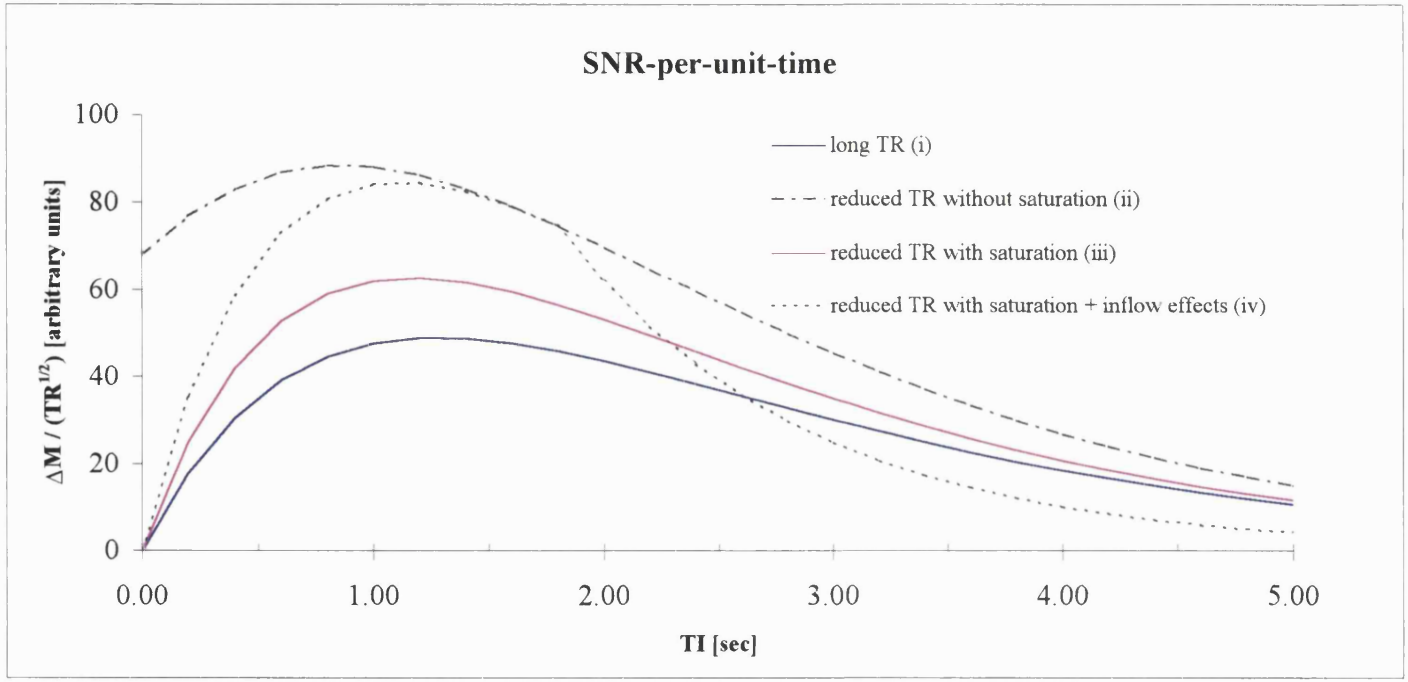

Fig. 4.5 Normalised SNR-per-unit-time for the following heuristically optimised values of the recovery time and equations for ΔM predicted by :
((i) τ = 8000 ms, Eq. [3.8]; (ii) τ = 1500 ms, no coil inflow (Δ=infinite) and no pre-saturation, Eq. [4.2];
(iii) τ = 2740 ms, no coil inflow, with pre-saturation, Eq. [4.4];
(iv) τ = 1900 ms with coil inflow and pre-saturation (Δ = 1800 ms), Eq. [A6] (for TI < Δ) and Eq. [A7] (for TI > Δ)
In the situation described by (iii), it is assumed that the steady state has been reached. ΔM at TI = 0 is non-zero since flow effects evolve during the recovery time.

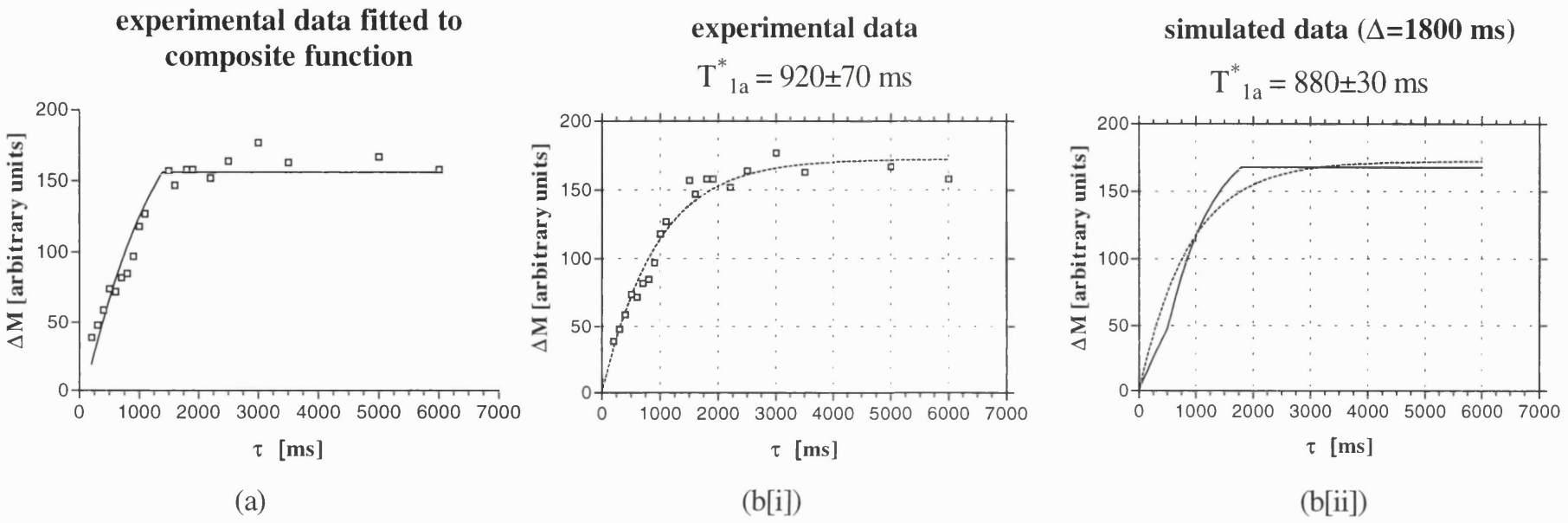

Fig. 4.6 Determination of the inflow time, Δ, by following the variation of ΔM with τ at a fixed TI = 1300 ms, showing (a) the first approach, a single, piecewise fit to the three equations described below. Parameters obtained from the fit were: $\Delta = 1700\pm240$ ms; $M_0 = 1320\pm5340$; $T_{1a} = 1500\pm1080$ ms. T1 and α_0 were fixed parameters in the fit and obtained from the ssIR data set.

The second approach made use of both (b[i]) the experimental data and the (b[ii]) simulated data for Δ = 1800 ms. The simulated curve is made up of three piecewise components that describe the ranges:

(i) $\tau < (\Delta\text{-TI})$, (ii) $(\Delta\text{-TI}) \leq \tau < \Delta$ and (iii) $\tau \geq \Delta$.

These correspond to the following cases in Table 4.1 and equations in Appendix A:

(i) Case (iii), Eq. [A10], (ii) Case (iv), Eq. [A11] and (iii) Case (i), Eq. [A6].

The curves were fitted to the exponential recovery curve ($\Delta M = M_0^* [1\text{-}\exp(-\tau/T^*_{1a}]$) that is predicted by Equation [4.4]. The resulting fit is displayed on the graphs by the dotted line. T^*_{1a} is the apparent relaxation time obtained from the fit and is shown above the graphs.

The resulting fit is displayed on the graphs by the dotted line. This fit was compared to curves fitted to simulated data sets obtained from the theoretical equations for different choices of the inflow time and for our experimental parameters (Eq. [A6-A12]). If the inflow effect had been negligible, the fitted relaxation time for the experimental data would have provided a value that was equal to the T_1 of blood (approximately 1500 ms), but this was clearly not the case. The value of Δ used to generate the simulated data curves was varied in steps of 100 ms until the fit provided equivalent values of the apparent relaxation time constant, T^*_{1a}. For example, with a choice of Δ=1500 ms, T^*_{1a} was found to be 670±20 ms; for Δ=1700 ms, T^*_{1a}=810±25 ms; for Δ=1900 ms, T^*_{1a}=1000±35 ms; and for Δ=2400 ms, T^*_{1a}=1220±40 ms. Figure 4.6(b[ii]) displays theoretical data obtained by setting the coil inflow time to a value of 1800 ms. The equivalent fitted relaxation time constants in this case (920±70 ms and 880±30 ms for experimental and simulated data respectively) indicate that the value of Δ is in the order of 1800 ms. The experimental data follow a piecewise form that is qualitatively similar to that predicted by the model. Furthermore, observation of the start of the plateau level of the curve at approximately 1800 ms confirmed our evaluation. Therefore, this value was used in subsequent fitting of the perfusion time-course data. Since a recovery time of 1500 ms ($\tau < \Delta$) and an inversion time of 1300 ms ($TI < \Delta$) were utilised in the time-course study, the perfusion subtractions were solved for flow according to the following equation that fulfils the conditions of Case (iv) described in Table 4.1

$$\Delta M(TI) = \frac{2M_0\alpha_0 \frac{f}{\lambda}}{\left(\frac{1}{T_{1app}} - \frac{1}{T_{1a}}\right)} \left[e^{-\tau/T_{1a}} e^{-TI/T_{1app}} \left(1 - e^{-(\Delta-\tau)(1/T_{1a}-1/T_{1app})}\right) + \left(e^{-TI/T_{1a}} - e^{-TI/T_{1app}}\right)\right] \quad [4.7]$$

4.5.3 Pre-occlusion CBF data : biexponential and single subtraction methods

For the biexponential fitting of the pre-occlusion data, the longest TI time of 2500 ms was found to be greater than the inflow time of the transmitter coil. Changes of ΔM with TI follow a T_1-based mono-exponential decay by this stage since the inflowing arterial blood consists solely of fresh spins. The first six data points should lie on the biexponential predicted by Eq. [3.8] but the last point requires fitting to a different curve described by Eq. [A8]. Fitting data to such a composite function is difficult since only one data point had been acquired during the second phase. However, by simulating data using these equations and for our combination of parameters, the biexponential fit of Eq. [3.8] that included this time point was found to lead to an underestimation of

approximately 4% in the perfusion values (data not shown). This systematic error is within the noise level of the perfusion values. Inclusion of the extra data point improved the confidence level of the fit since it is the only point acquired during the $\Delta M(TI)$ decay that occurs after the peak in the biexponential curve. The full data sets were therefore fitted to the single equation (Eq. [3.8]). Ideally, however, more data points would have been collected that lay on the second curve so that a composite fit to the two curves would have been possible.

The data acquired during the pre-ischaemic phase displayed no evidence of a significant transit time (all data from the first TI time point at 200 ms were positive). Transit time effects were, therefore, neglected in the subsequent analysis.

The pre-ischaemic blood flows were measured using both the long TR biexponential fitting procedure and the short TR, single subtraction modification. Representative perfusion maps from one gerbil are displayed in Fig. 4.7. The former procedure also provided values of tissue T_1 and the degree of inversion, α_0. The values obtained using these methods for the four ROIs are shown in Table 4.2. Cortical and striatal control flows were found to be statistically different (P=0.001, paired t-test) using both quantification procedures. There was no significant difference between the control CBF values in each hemisphere measured with the two implementations of FAIR (paired t-test, either cortical or striatal regions).

	right hemisphere		left hemisphere	
	cortex	**striatum**	**left cortex**	**left striatum**
(i) Control CBF [biexponential]	139±7	134±9	153±7	125±8
(ii) Control CBF [single subtraction]	155±9	132±5	161±8	129±9
T_1 [ms]	1219±13	1207±10	1229±7	1226±5
α_0	0.945±0.003	0.945±0.002	0.942±0.001	0.945±0.001

Table 4.2 Parameters from the selective inversion recovery fit and comparison of control perfusion measurements. Flows quoted in units of ml/100g/min. CBF values are obtained (i) by the biexponential curve fitting procedure (Eq. [3.8]) and by (ii) solving the subtractions (selective - non-selective) for flow using Eq. [A11] assuming $\delta = 0$. Values for T_1 and α_0 were obtained by fitting the selective inversion recovery data to the standard mono-exponential curve. Data are averaged over all the animals studied (n=8).

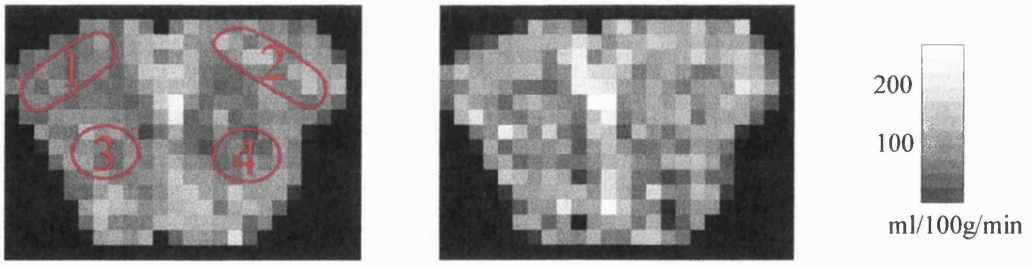

(a) (b)

Fig. 4.7 Representative CBF maps (one animal). The CBF maps are acquired using (a) the long TR biexponential fitting procedure and (b) the short TR implementations and the flows in these maps can be seen to be very similar. The biexponential CBF map is acquired in 50 min; the control, single subtraction map is acquired in 3 min. In the biexponential map, the approximate position of the cortical and striatal regions in both cerebral hemispheres is depicted.

4.6 Discussion

This study has demonstrated the use of quantitative, short repetition time FAIR imaging in following the time-course of post-ischaemic disturbances. An implementation of FAIR was developed that employs saturation pulses in order to enable quantification even in the presence of complicating inflow effects. Perfusion values thus obtained were in good agreement with the flows obtained using the more time-consuming biexponential fitting procedure. Perfusion subtractions were acquired with a time resolution of approximately 3 min. CBF maps were obtained with this time resolution using the previously determined inversion recovery parameters.

The implementation of short repetition time FAIR has necessitated the consideration of the coil inflow effect which was found to be significant with our set-up. If this effect has not been considered and the data fitted to Eq. [4.4], the value of the control flow would have been overestimated by approximately 50%. Without pre-saturation, this situation is further complicated by the need to consider the build-up of the steady state magnetisation of the arterial blood that arises on application of a series of non-selective inversion pulses. Inflow of fresh blood spins, first into the internal volume of the transmitter coil and then into the imaging slice will be occurring at all stages of each experiment (each inversion followed by a recovery time), and this process will evolve during the build-up of the steady state. The quantification of such a situation is significantly simplified with use of global pre-saturation pulses applied at the start of each experiment. This pulse destroys the residual magnetisation that remains from the previous scan so that analysis of each experiment can be considered in isolation. The pre-saturation does, however, reduce the flow-related signal, but the time efficiency is still significantly improved in comparison with the standard implementation of FAIR with a long repetition time (see Fig. 4.5). It should be noted that during the QUIPSS II experiment (Wong, 1997), the saturation of the tagging region has the indirect effect of eliminating the flow-related signal during the recovery time. In our study, analysis of the theoretical and experimental relationship between the perfusion signal and the recovery time provided a means to obtain an estimation of the coil inflow time that was necessary for quantification. By modelling the relationship between the flow and the inflow time using the theoretical equations, the sensitivity of the measurement to the coil inflow time was determined for our parameters. The systematic error in the measured flow was found to be within the noise level of the experimental data if the inflow time is approximately 300 ms above or below the measured value of 1800 ms. A

distribution of values across the slice is, however, likely on account of the spread of blood velocities and vascular geometry.

In the situation where coil inflow effects are significant, the improved time efficiency can be readily seen in the example shown in Fig. 4.5. Inflow of fresh spins washes out the relaxing blood spins during the recovery time so that the magnetisation difference created by the inversion pulse of the next experiment is magnified. However, quantification is complicated under certain regimes that are dictated by the choice of imaging parameters (Table 4.1). Ideally, a choice of coil size and imaging parameters would be made such that the conditions of Case (i) in Table 4.1 are fulfilled (Eq. [A6]) so that inflow only occurs during the recovery time. The benefits of improved time efficiency are then achieved without the penalty of requiring an accurate measure of the coil inflow time since the flow equation is dependent on the TI time but not on Δ. However, a reasonably accurate measurement of the inflow time must still be known in order to verify the fulfilment of these conditions. Therefore, one might argue that the only practicable means of attempting accurate CBF quantification with the FAIR technique would be to employ a full body coil as the RF transmitter. Inflow then does not occur, and the time efficiency can be optimised with short repetition time implementations. However, head coils are generally used to maximise SNR in brain imaging, thus making consideration of inflow effects necessary.

Even if a body coil is used, the transit time effect would be the complicating factor that still remains. Transit times were neglected in this study since no evidence was found of a significant effect during the control period (see Results). However, if the flow level is significantly impaired, the flow values will be underestimated if the transit time effects are not taken into consideration (see Section 5.4.2). Since the transit time, δ, is related to the distance between the edges of the inversion and imaging slabs, the sensitivity of FAIR to this effect would be considerably reduced if the profiles of the slice-selective inversion slab and the imaging slab were improved. This would allow thinner inversion slices and therefore an improved slice thickness ratio (STR). Preliminary investigations described in this thesis have demonstrated the potential benefits in CBF quantification when using the improved inversion profile of the FOCI pulse with a reduced STR (see Section 3.6). However, a slice thickness ratio of 1:1 would not necessarily eliminate the problem since a lower limit on δ might exist. This limit could be dictated either by (i) the redistribution time spent by the blood within the arterial microcirculation of the

imaging slab before reaching the capillary exchange sites (Ye, 1997) or (ii) by the residency time of the blood at these sites before exchange occurs with the tissue water (Eichling 1974, van Zijl, 1998). Approximate times suggested for both of these possible durations are 500 ms in humans. Therefore, transit time effects might always be significant, especially in human studies. This can be contrasted with continuous spin tagging studies on rats that have found total transit times from the tagging plane placed 20 mm proximal to the tissue and as a result, an upper limit for δ, of approximately 300 ms (Zhang, 1992). In this context, the pulsed arterial spin labelling technique of QUIPSS II (Wong, 1997) is attractive due to its theoretical insensitivity to transit time and its emphasis on measuring blood water before exchange occurs. This insensitivity to δ is, however, dependent upon the fulfilment of conditions concerning the delay times in the sequence and the magnitude of the transit time. The robustness of the insensitivity will therefore be adversely affected by depression of CBF in a similar way to FAIR.

In order to examine the sensitivity of the flow measurement with the short TR FAIR technique to the inflow and transit times and to T_{1a}, simulated profiles were calculated showing the percentage error in the flow measurement when assuming values for these parameters and thereby measuring a flow of 150 ml/100g/min (see Fig. 4.8). It can be seen that the flow measurement is more sensitive to variations in the transit time than the inflow time. For example, with an increase in the transit and inflow times and T_{1a} of 300 ms (from assumed values of δ=0 sec, Δ=1.8 sec and T_{1a}=1.5 sec), the *true* flow is underestimated by 15% , 9% and -7% respectively.

A time-efficient implementation of FAIR was employed in this investigation in order to accurately follow potential changes in the blood flow with a time resolution as low as 2.8 min. The mean global pre-ischaemic CBF value obtained with our modified implementation of FAIR was 144±7 ml/100g/min. A comparison of the FAIR technique with previous autoradiography data has been reported on normal rats (Tsekos, 1998). In the gerbil, investigations employing techniques such as [^{14}C]-iodoantipyrine autoradiography (Levy, 1979; Kato, 1990a; Nadasy, 1990), the similar [^{3}H]-nicotine and [^{14}C]-butanol methods (Suzuki, 1983; van Uitert, 1978) and H_2 clearance (Busza, 1992; Tomida, 1989; Osburne, 1975) have reported diverse levels of flow. On the whole, values determined by the first two techniques are in good agreement with our FAIR pre-ischaemic flows whereas values measured with the latter method are lower.

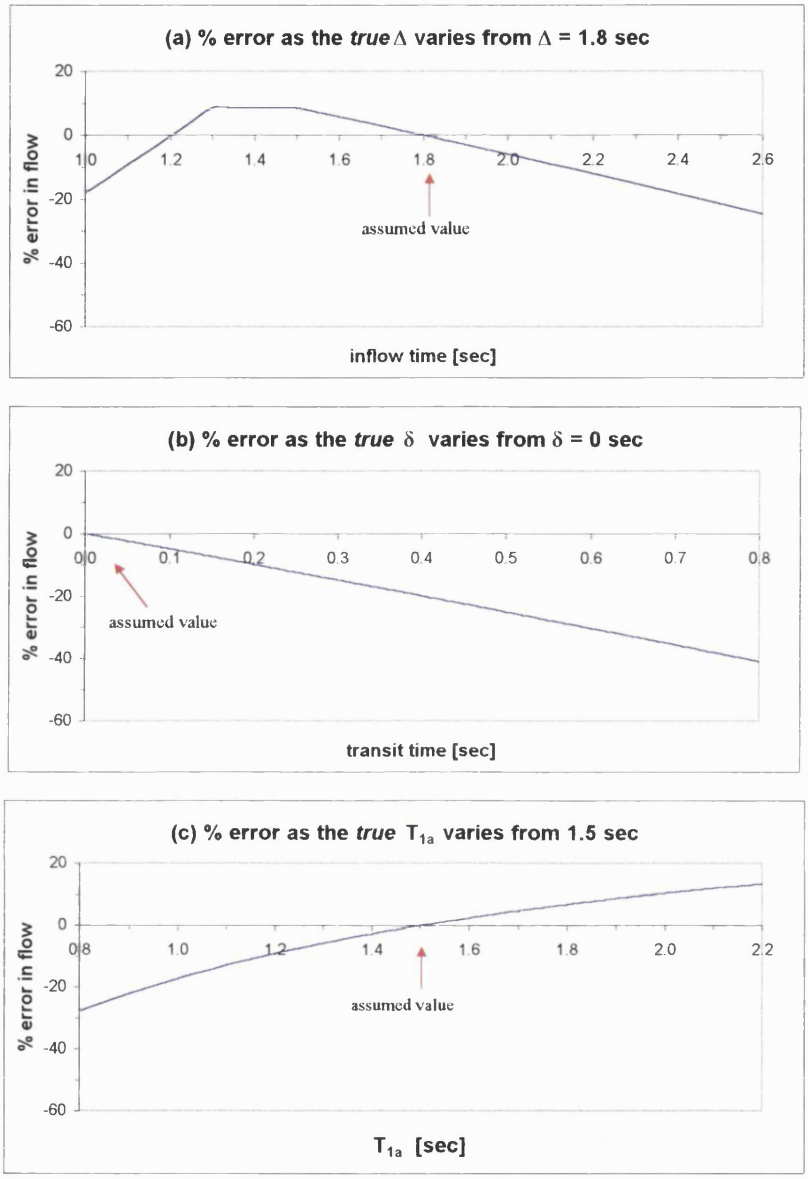

Fig. 4.8 Sensitivity of the flow measurement to (a) the inflow time, (b) the transit time, and (c) the T_1 of blood, as the *true* values of these parameters are varied from the assumed values that are indicated. The percentage flow error is calculated as [f(m)-f(t)].100/f(t) where f(m) and f(t) refer to the measured and *true* flows respectively. For example, a negative percentage implies that the flow will be underestimed if the change in the parameter is not accounted for in the perfusion model. Simulated parameters are a a fixed value of ΔM, and $\tau = T_{1a} = 1.5$ sec, and $TI = T_1 = 1.3$ sec. The assumed parameters (depending on the particular simulation case) are $\delta = 0$, $\Delta = 1.8$ sec and $T_{1a} = 1.5$ sec.

For the inflow time profile (a), the three piecewise components are (see Table 4.1) (1) $\Delta < 1.3$: case (ii) [since $TI > \Delta$]

(2) $\Delta = \{1.3\text{-}1.5\}$: case (i) [since $TI < \Delta$ and $\tau > \Delta$]

(3) $\Delta > 1.5$: case (iv) [since $\tau < \Delta$].

For example, Osburne *et al.* reported a mean flow of 54±8 ml/100g/min in the gerbil (Osburne, 1954). A comparative study has noted this disparity that is especially evident in smaller animals and has related it to partial volume effects (Rosenblum, 1977). Others have described the injurious consequences of electrode placement that include the stimulation of waves of spreading depression (SD) (Tomida, 1989). Verhaegen *et al.* reported that small electrodes (50 μm in diameter) inserted to a depth of 1 mm into the cortex provided control flow values in the gerbil of 155±18 ml/100g/min (Verhaegen, 1992). These values are in excellent agreement with flows measured with the [^{3}H]-nicotine indicator fractionation technique during that study and with the FAIR technique in our investigation. However, further cross-validation with these techniques in the same animal is required.

The ability to follow and characterise a time-course of events by quantitative mapping of cerebral perfusion has obvious potential in the investigation of conditions such as cerebral ischaemia and in studies of functional brain activation. Such non-invasive MRI studies offer a superior combination of time resolution and regional differentiation in comparison with methods that have previously been used. In combination with other MRI and MRS methods, it is possible to investigate changing relationships of flow and other physiological variables such as tissue energy status.

V A STUDY OF REPERFUSION IN A GERBIL MODEL OF FOREBRAIN ISCHAEMIA USING SERIAL MAGNETIC RESONANCE PERFUSION AND DIFFUSION IMAGING

This chapter uses the short repetition time implementation of FAIR described in the previous chapter in order to follow a fast changing time course of flow that develop upon recirculation. It has long been the aim of investigators to understand the pathomechanisms that are induced by reperfusion. In this study, the combination of perfusion and diffusion imaging allows the changing flow and its consequences on tissue cellular stasis to be investigated. This chapter introduces the biochemical and pathological background to the study of reperfusion. The gerbil experiment is then described and the results placed in the context of these previous investigations. This investigation is described in ref. (Pell, submitted).

5.1 Introduction

Following a stroke, reperfusion may occur spontaneously or via an interventional technique such as thrombolysis. Animal studies of global ischaemia have demonstrated that an impaired level of cerebral blood flow (CBF) may develop on recirculation and therefore reperfusion does not necessarily prevent further development of ischaemic injury (Hossmann, 1985a). Certain pathomechanisms that are initiated during the ischaemic phase develop and mature during the post-ischaemic period (Ito, 1975; Klatzo, 1975). In models of focal ischaemia, the picture is less clear and a varied range of flow levels have been observed on reperfusion (Hossmann, 1985a; Kaplan, 1991). Some studies have suggested that a period of compromised blood flow after recirculation may not be pathogenic (Michenfelder, 1991; Crumrine and LaManna, 1991). Clinical reports of the pathogenesis of CBF impairment after reperfusion are limited (for example, Beckstead, 1978; Fujioka, 1994) and this may reflect the time delay before most patients can be scanned. Since the use of thrombolytic (rtPA) therapy for the treatment of stroke is becoming more widespread, it is important to be able to understand any detrimental effects of recirculation. An aim of this study was to use the magnetic resonance imaging (MRI) techniques of perfusion and diffusion imaging to gain further insight into post-reperfusion vascular and tissue status.

Many studies have been carried out that have aimed to characterise and follow the post-ischaemic disturbances in circulation that occur after a period of transient global ischaemia. An ideal study of post-ischaemic reperfusion would track the time-course of

these changes in a single animal and would offer good regional differentiation since a non-uniform pattern of reperfusion may be expected. Previous investigations have employed methods of perfusion quantification such as autoradiography using [^{14}C]-iodoantipyrine (Pulsinelli, 1982), [^{3}H]-nicotine (Suzuki, 1983) or [^{14}C]-butanol (van Uitert and Levy, 1978), hydrogen clearance (Todd, 1986a), ^{133}Xenon clearance (Nemoto, 1981) and the technique of laser Doppler flowmetry (Kloiber, 1993). All of these methods suffer from limitations in their application to such studies. For example, hydrogen clearance relies on the invasive placement of electrodes and provides measurements which are localised to the cortical volume in their immediate vicinity. The technique of ^{133}Xenon clearance is limited in spatial resolution and is susceptible to errors due to partial volume effects and high volumetric flow rates (Rottenberg, 1982). Autoradiography, although displaying good spatial resolution, is invasive and does not permit longitudinal observations in a single animal. We have implemented a technique for perfusion quantification that offers the relatively high spatial and temporal resolution of MRI.

The principal use of MRI is to obtain structural images of brain tissue. Flow sensitive implementations of the technique have been reported that allow quantitative maps of cerebral perfusion to be obtained; these techniques have been discussed in Chapters 3 and 4. Perfusion MRI with the FAIR technique was combined in this study with diffusion imaging which provides measurements of the apparent diffusion coefficient (ADC) of tissue water. A reduction of the ADC is believed to be consistent with the development of cellular energy failure and the resultant cell swelling (see Section 2.1.3).

The purpose of this study was to employ a combination of quantitative perfusion and diffusion imaging in an investigation of the post-ischaemic circulation. A modification of the FAIR method had been developed that enabled a time-course study of cerebral perfusion with improved time efficiency (see previous chapter). These techniques were employed in an investigation of the reperfusion deficits that occur following a transient period of total forebrain ischaemia in a gerbil model. This chapter describes the results of this experiment and places them into the context of previous investigations of reperfusion. This study has brought to light the advantages and disadvantages of using MR perfusion imaging in such a study and these issues are discussed.

5.1.1 Background : Post-ischaemic circulation

Any impairments in post-ischaemic circulation can have a significant outcome in the recovery process and it is therefore important to define the factors that contribute to secondary perfusion deficits. Two major categories of defects in circulation that follow a period of transient global ischaemia have been characterised over the past thirty years. These are described in the following two sections.

5.1.1.1 The no-reflow phenomenon

The first of these is known as the no-reflow phenomenon (Ames, 1968) in which areas of the brain fail to reperfuse. This response is heterogeneous (Kågström, 1983a) and is dependent upon the type and the extent of the period of ischaemia. Incomplete and stagnant tourniquet-induced ischaemia of more than fifteen minutes duration was shown to result in impaired recirculation affecting approximately 95% of the total brain volume in a rabbit model (Ames, 1968). Putative mechanisms for this phenomenon are numerous and include obstruction of the capillary lumen by swollen astroglia (Ames, 1968; Miller, 1972), and leukocyte plugs (del Zoppo, 1991), endothelial bleb formation (Chiang, 1968; Dietrich, 1984), increased blood viscosity (Fischer, 1973), and blood aggregates and microthrombi formation (Cuypers, 1974). A mechanism related to an increase of extracellular potassium concentration in the brain and resulting vasoconstriction has also been proposed (Wade, 1975). No-reflow can be prevented by enabling measures that optimise the physiological conditions during the initiation of recirculation. The blood pressure requires suitable adjustment in order to counteract hypotension, blood osmolality must be artificially increased and the level of blood acidity needs to be carefully controlled (Hossmann, 1985a).

5.1.1.2 Hyperaemia followed by Hypoperfusion

The alternative pattern of post-ischaemic impairment that has been demonstrated is that of hyperaemia followed by hypoperfusion. On restoration of the circulation, an immediate return of the blood flow to a level over and above that of the pre-occlusion control value is observed (Haggendal, 1970, Kågström, 1983a). This reactive hyperaemic response correlates with the development of later morphological damage (Pulsinelli, 1982b) and with the duration and severity of the ischaemia (Kågström, 1983b).

Flow values reached during this phase can be as high as 400% of control in some areas of the brain (Miller, 1980). Kågström *et al.* have demonstrated that the hyperaemic response is heterogeneous and observed an increase in blood flow on recirculation but never a true hyperaemic overshoot (Kågström, 1983a). The mechanism for this transient increase in blood flow is vasodilatation of the capillaries caused by the accumulation during the ischaemic period of various vasoactive metabolic products such as lactic acid, carbon dioxide (Lowry, 1964) or an increase in extracellular potassium concentration (Cameron, 1971). Even though the potential benefits of hyperaemia are obvious in that substrate delivery to the tissue is immediately restored, possible detrimental effects of hyperperfusion have been described. Disruption of the blood brain barrier during this phase has been demonstrated (Klatzo, 1983) and this might contribute to the development of brain oedema and therefore become a limiting factor in the recovery process.

The hyperaemic phase is followed by a decrease in the cerebral blood flow which remains depressed for a variable period of time (Hossmann, 1973). This phase known as delayed hypoperfusion, displays distinct interstructural variability and levels of reduced flow between 20-60% have been observed (Kågström, 1983b). It is characterised by a dissociation between suppressed carbon dioxide and maintained autoregulation (Nemoto, 1975). Possible mechanisms for the phenomenon of hypoperfusion include blockage of capillaries by glial or endothelial swelling (Little, 1976). The most likely mechanism is an increase in vascular smooth muscle tone which is triggered by a neurogenic process and results in vasoconstriction (Miller, 1980; Tagaki, 1977). The state of cerebral metabolism during the period of post-ischaemic reflow has crucial significance since any mismatch between metabolic demands and cerebral blood flow would have a deleterious effect.

5.1.2 Post-ischaemic metabolism

Ischaemia rapidly depletes the energy store but it is possible that energy metabolism does not fully recover during the recirculation period and this may contribute to morphological damage. Even though some authors have not found evidence of any such a mismatch (Michenfelder, 1991; Crumrine and LaManna, 1991), a number of investigators have observed a period of post-ischaemic hypermetabolism that accompanies the deficiency in blood flow (Levy 1977; Diemar 1979; Hossmann, 1985a). The resulting combination of factors might contribute to an injurious period of

post-ischaemic tissue hypoxia as the demand of oxygen and substrates is not met by the available blood supply. The role that post-ischaemic disturbances plays in the pathophysiological mechanisms of cell injury and death is not certain. Some argue that the period of global ischaemia triggers a series of neurochemical events that culminate in delayed functional and morphological damage and that this process is totally independent of the level of recovered perfusion (Dirnajl, 1993). Others maintain that post-ischaemic reflow offers a significant opportunity for therapeutic intervention (Hossmann, 1985a); a homogeneous recirculation is critical, oedema must be resolved and no-reflow must be avoided.

5.1.3 Selective vulnerability

Investigations of transient global ischaemia have identified specific populations of brain neurones that are especially susceptible to cell damage and death (Brierly, 1976; Kirino 1982). These so-called selectively vulnerable areas include the CA1 zone in the hippocampus, layers in the cerebral neocortex and the Purkinje cells in the cerebellum. Kirino *et al.* found that five minutes of bilateral carotid occlusion in the gerbil resulted in a delayed process of neuronal death in the CA1 hippocampal subfield that became apparent two days post-ischaemia (Kirino, 1982). Similarly, twenty minutes of ischaemia was shown to result in delayed neuronal damage in 85% of rats that had undergone four-vessel global occlusion (Pulsinelli, 1982a). This so-called maturation phenomenon of the delayed neuronal damage (Ito, 1975) gave investigators the first indication of the possible deleterious effects of post-ischaemic circulation.

Much work has been carried out in order to determine the revival time of areas of the brain that are not selectively vulnerable (known as potentially resistant) . This defines the longest duration of ischaemia following which, full restoration of physiological and metabolic functions of the brain can be achieved. At one extreme of these findings, Hossmannn *et al.* found that recovery can follow up to sixty minutes of global ischaemia if no-reflow is prevented in a cat model (Hossmann, 1973).

5.1.3.1 Excitoxicity

A complex cascade of events is expected to contribute to ischaemic cell death. Neuronal damage occurs as a result of a multiple parallel injury mechanisms that are triggered simultaneously by the ischaemic insult.

Excitoxicity amino acids (EAAs) such as glutamate act as neurotransmitters in the transmission of action potentials. Microdialysis techniques have demonstrated the abnormal release of excessive amounts of glutamate during a period of ischaemia (Benvensite, 1988). The pathogenesis of this exposure is known as excitoxicity (Olney, 1986). This phenomenon is believed to be mediated by calcium ions (Ca^{2+}) and the trans-membrane influx of abnormal amounts of Ca^{2+} into the intracellular medium is triggered by glutamate exposure (Rothman, 1986). Calcium accumulation occurs via Ca^{2+}-sensitive channels that open upon only cell depolarisation, and via receptor-operated channels, that open upon activation by specific agonists such as N-methyl-D-aspartate (NMDA) and AMPA. It is believed that cell damage and ultimately, ischaemic cell death, is accelerated by calcium accumulation.

5.1.3.2 The role of calcium in selective vulnerability

In order to account for the phenomenon of selective vulnerability, a large amount of work has focused on the biochemical cascade of events that is initiated by transient ischaemia (for example, Siesjö, 1981; White, 1993; Cheung, 1984). Calcium ions are the mediators in these mechanisms. Under normal conditions, calcium plays an important role in the regulation of a large number of cellular processes. The intracellular concentration of Ca^{2+} is 10^{-7} M while extracellular concentration is 10^{-4} M. On the onset of ischaemia, excessive amounts of the neurotransmitter glutamate are released into the extracellular spaces. As a result of adenosine triphosphate (ATP) depletion, the glutamate cannot be removed as this process requires energy. The neurotransmitter binds to NMDA receptor site on neighbouring neurones and this triggers the influx of Ca^{2+} into the intracellular space and a loss of the normal transmembrane gradient. This sets off a cascade of complex events that begin with rapid hydrolysis (lipolysis) of the phospholipid constituents of cell membranes. As a result of this process, there is an accumulation of free fatty acids (FFA), the largest relative change occurring in the concentration of arachidonic acid (AA) (Bazán 1970). The synthesis of proteins is also inhibited (Siesjö, 1981). Recirculation results in the oxidative metabolism of the FFAs that were released during ischaemia, with consequent generation of free radical-containing compounds (Demopoulus, 1977; Siesjo, 1981); these are highly reactive molecules with unpaired electrons and therefore constitute powerful oxidising agents. Iron-containing compounds are also released. The damage caused by these free radicals is therefore related not only to the accumulation of compounds during ischaemia but

also to post-ischaemic events. These mechanisms have been linked to the empirical result that incomplete ischaemia seems to have a poorer prognosis than total global ischaemia; the trickle of blood that remains during ischaemia could contribute to the build-up of these compounds (Siesjö, 1993). In the selectively vulnerable neurones, the free radical damage is aggravated by their higher iron content (Zaleska, 1985) and in their greater susceptibility to membrane lipolysis which is perhaps due to a higher density of voltage dependent Ca^{2+} channels (Siesjö 1982). The mechanism of free radical damage remains unclear although it is likely that the microcirculation is the principal target.

5.2 Material and Methods

5.2.1 Animal methods

Mongolian, adult gerbils (n=8, 60-70 g) were used in this study. The animals were anaesthetised with 3% halothane. Anaesthesia was subsequently maintained with a mixture of 1.5% halothane and 0.4 l/min of oxygen that was supplied via a nose cone, and the gerbils were allowed to breathe spontaneously throughout the study. The common carotid arteries were visualised with an operating microscope and carefully dissected away from the vagus nerves. Nylon snares (Ethilon 2/0, Ethicon, Edinburgh, UK) were placed around both arteries and attached to individually controlled manual screw systems in order to allow remote bilateral occlusion with the animal in the magnet (Allen, 1993). Before the animal was placed inside the magnet bore, the mechanics of the occlusion procedure were verified. Body temperature was recorded with a rectal thermometer and maintained at between 37-38°C by blowing warm air into the magnet bore. Respiratory rate and ECG were also monitored.

The gerbil is a convenient model for such studies since bilateral occlusion of the common carotid arteries induces virtually complete forebrain ischaemia. There exists no significant connection between the basilar-vertebral system and the carotid system as the circle of Willis is incomplete (see Section 2.2.3, Fig. 2.4). Bilateral carotid occlusion therefore results in infarction of uniform inter-animal severity and in 100% mortality within four hours (Levine, 1966; Levine, 1969).

5.2.2 Experimental protocol

The experimental protocol commenced with a period of control imaging. Bilateral occlusion was then initiated by tightening the snares around the common carotid arteries. This state was maintained for four minutes. The snares were then opened to begin the recirculation phase. Perfusion and diffusion imaging were continued for at least three hours.

5.2.3 MRI Methods

MRI measurements were performed on the 2.35T horizontal bore magnet interfaced to a SMIS console.

5.2.3.1 FAIR perfusion imaging

The details of the perfusion sequence are described in Section 4.4. Briefly, perfusion maps were obtained with the FAIR technique that used an adiabatic FOCI T-shape inversion pulse. A bipolar gradient pulse (b = 5 sec/mm^2) applied simultaneously along each gradient direction eliminated signal contamination from fast moving arterial. FAIR was implemented with a spin-echo echo-planar-imaging (EPI) sequence (parameters given in Section 4.4.2.1). Images were obtained in the coronal plane.

During the control phase of the experiment, a combined selective/non-selective inversion recovery set was acquired (τ = 6500 ms) at seven TI values (see Section 4.4.2.3). The selective data were fitted for the parameters T_{1app}, M_0 and α_0 which are required for the quantification of perfusion (standard inversion recovery Eq. [1.22]). For the time-course measurements of CBF, the reduced repetition time implementation of FAIR with pre-saturation pulses was employed (TI = 1300 ms, τ = 1500 ms). During the acute phase of the experiment and during the majority of control imaging periods, perfusion maps were acquired with a time resolution of 2.8 min. At other times during the experiment the number of averages was increased in order to increase the signal-to-noise ratio of the images with a 9.3 min time resolution.

A series of repeated non-selective inversion recovery measurements, obtained during the entire reperfusion phase in a separate series of experiments, indicated that the parameters T_1, M_0 and α_0 did not change significantly during the course of the experiment at our field strength (n=2, data not shown). Therefore, the control values of

these parameters were used to provide perfusion measurements directly from the subtracted image obtained at each time point by solving the relevant reduced repetition time equation for flow.

The tissue T_2 value is expected to change due to changing levels of deoxyhaemoglobin during the course of the experiment. This will affect the M_0 term in the equations for the magnetisation difference (for example, in Eq. [3.8]) since this term represents $M_0.\exp(-TE/T_2)$ and is only measured during the control phase of the experiment. The measured magnetisation difference $\Delta M(TI)$ is also weighted by the same amount and the T_2-weighting terms should therefore cancel. However, the T_2 value is expected to vary during the course of the experiment over a range of up to approximately 8 ms due the effects of occlusion and recirculation (see Section 7.3.5). Flow values will be underestimated by less than 10% if, as in this study, the T_2 term is not taken into consideration.

A value for the transmitter coil inflow time, Δ, was experimentally determined in a control experiment as described in the previous chapter (see Section 4.4.2). The transit time was not included in the analysis since no evidence of a significant transit time effect was found in the control data (see Section 4.5.3).

5.2.3.2 Diffusion MRI

Measurements of a third of the trace of the diffusion tensor, denoted trace(D), were obtained in five of the animals during the control period and at approximately half-hour intervals during the post-reperfusion phase. A single-shot trace-weighted EPI sequence (Wong, 1995) was employed with parameters (TE = 110 ms; TR = 1000 ms; NEX = 30; b-values 0 and 1187 sec/mm^2). Section 6.3 provides a more complete description of the pulse sequence.

5.2.4 Image and Data Analysis

Perfusion values were calculated pixelwise by importing the data into IDL (Floating Points Systems, Boulder, Colorado, USA). The relevant reduced repetition time equation (Eq. [4.6]) for the magnetisation difference provides a non-linear expression for the CBF. Four regions of interest (ROIs) were drawn on these perfusion maps (see Fig. 4.7). All values are presented as mean ± SEM. Statistical analyses of the factorial

(region × group) within-subjects data were performed by mixed-model regression analysis using appropriate random effects models. In order to examine the significance of temporal trends in flow and trace(D) data during certain phases of the experiment, linear regression was performed on the data. A P-value of <0.05 was considered to indicate statistical significance.

In order to characterise certain features of the flow response during the acute phases of the reperfusion, a suitable random coefficients model was fitted to the first hour of the reperfusion data. Maximum likelihood non-linear mixed model regression was performed using a SAS macro (NLINMIX, supplied by R. Wolfinger, SAS Institute, Cary, North Carolina, USA) (Littell, 1996). A detailed models comparison study was not performed and the mean curve was analysed rather than the curve of the means (Crowder, 1981). Instead, an exponentially damped polynomial model was adopted with the following form

$$f(t) = \alpha + (\beta_0 + \beta_1 t^3)\exp(-\lambda t) \qquad [5.1]$$

where f represents the flow, t is the time since the occlusion and α, β_0, β_1 and λ are random coefficients (Crowder, 1981). This model was selected since it is economic in the number of coefficients and provides an adequate description of the zero-time and asymptotic behaviour [$f(0) \neq f(\infty)$].

5.3 Results

A value for the coil inflow time, Δ, of 1800 ms was experimentally derived and assumed to be constant throughout the experiment (see Section 4.5.2). CBF measurements were obtained with the reduced repetition time implementation of FAIR. Equation [4.6] was used to obtain CBF maps from each subtraction image since the conditions $\tau < \Delta$ and $TI < \Delta$ that define this equation were satisfied in our experiment (Table 4.1). The inversion recovery data set acquired during the control phase of the experiment provided values of tissue T_1 and the degree of inversion, α_0. The mean pre-occlusion blood flow measurements (over both hemispheres) were 158±8 ml/100g/min in the cortex and 130±6 ml/100g/min in the striatum respectively (n=8). Representative perfusion maps are displayed in Fig. 5.1. After recirculation had been initiated, a marked variability in the response to recirculation became obviously apparent on visual inspection.

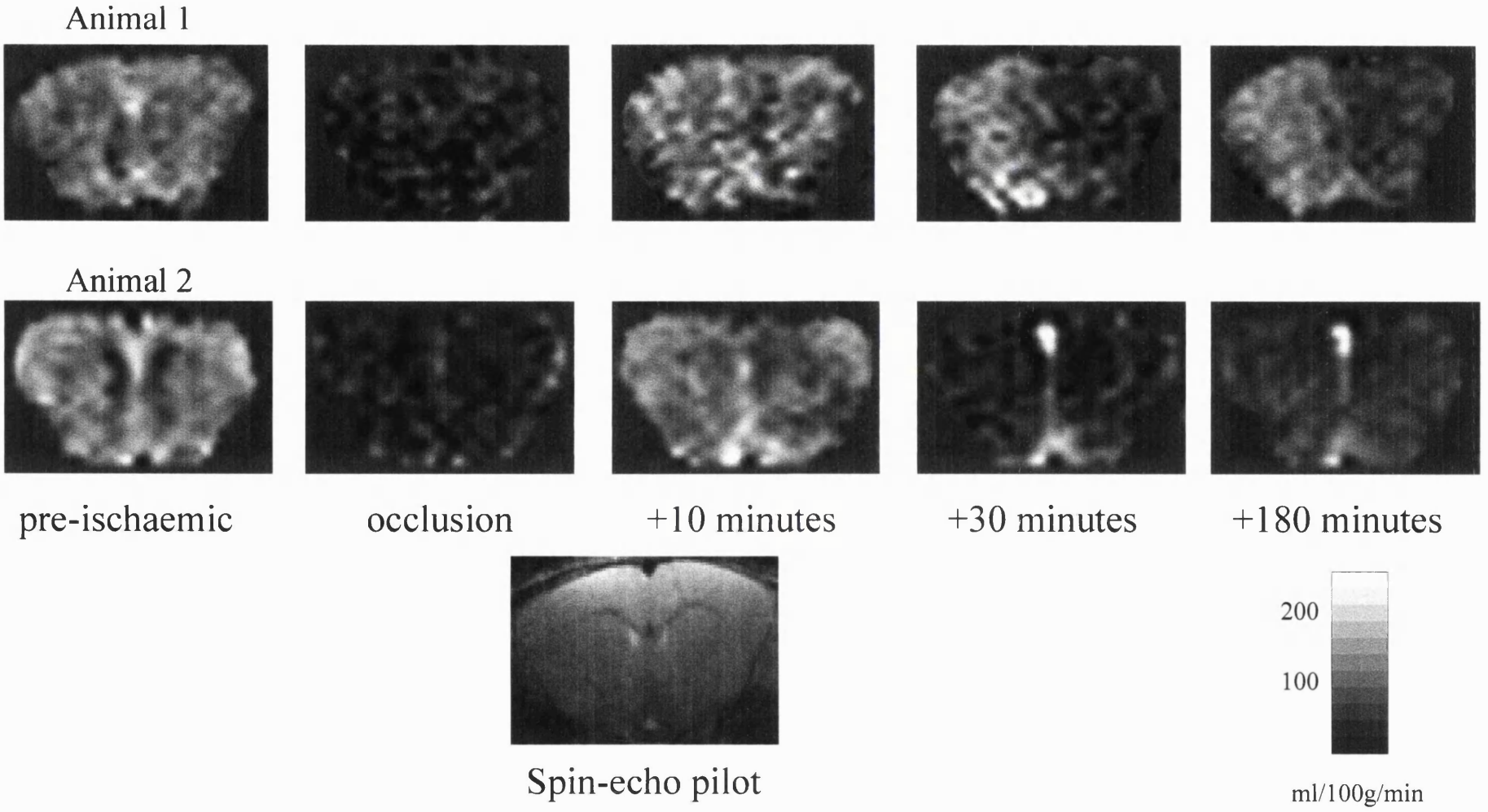

Fig. 5.1 Representative CBF maps obtained in two of the studies. Animal 1 displays a unilateral Group A / Group B response (n=4), while Animal 2 follows a bilateral Group B pattern (n=4). Times are denoted as minutes post-reperfusion. Pre-ischaemic, occlusion, +10 min and + 30 min CBF maps were acquired in 3 min; the +180 min maps were acquired in 10 min. A high-resolution spin-echo image of the imaging slice (1 mm slice thickness) is displayed for anatomical reference.

Representative perfusion maps are displayed in Figure 5.1. After recirculation had been initiated, a marked variability in the response to recirculation became obviously apparent on visual inspection. Based on these observations, the responses observed in the cerebral hemispheres of each animal were assigned to two groups (Groups A and B). The group response reflected the characterisation of the reperfusion time course in each hemisphere. In each of the 8 animals, at least one cerebral hemisphere displayed an early transient recovery of CBF that was followed by a period of hypoperfusion. Hemispheres that showed this response were assigned to Group B. In 4 of the 8 animals, a side-to-side difference became apparent and the Group B hemisphere was accompanied by the observation in the contralateral hemisphere of a permanent immediate renormalisation of the flow (Figure 1(a)); these hemispheres were assigned to Group A. Each of the 4 animals thereby provided one Group A and one Group B hemisphere. The other 4 animals displayed a bilateral Group B response (Figure 1(b)). The complete data set of 8 animals, therefore, provided 4 Group A hemispheres and 12 Group B hemispheres. Figure 5.2 shows the time-course of the CBF values for the data sets in each of the two groups.

For the subsequent analysis, the data from cortical and striatal regions were considered as independent measurements. If the same Group A or B response was observed bilaterally, the regional flows were determined by averaging over both cerebral hemispheres. If a different response was observed between the hemispheres, the regional data from each cerebral hemisphere was individually analysed.

Table 5.1 details the control and occlusion flows in Group A and Group B data. Mixed model regression analysis of the pre-occlusion data showed a significant regional (cortex versus striatum) difference ($P=0.01$) while the difference between the two groups (Group A versus Group B) was not significant. There was no significant regional or group differences in the flow values measured during the occlusion phase.

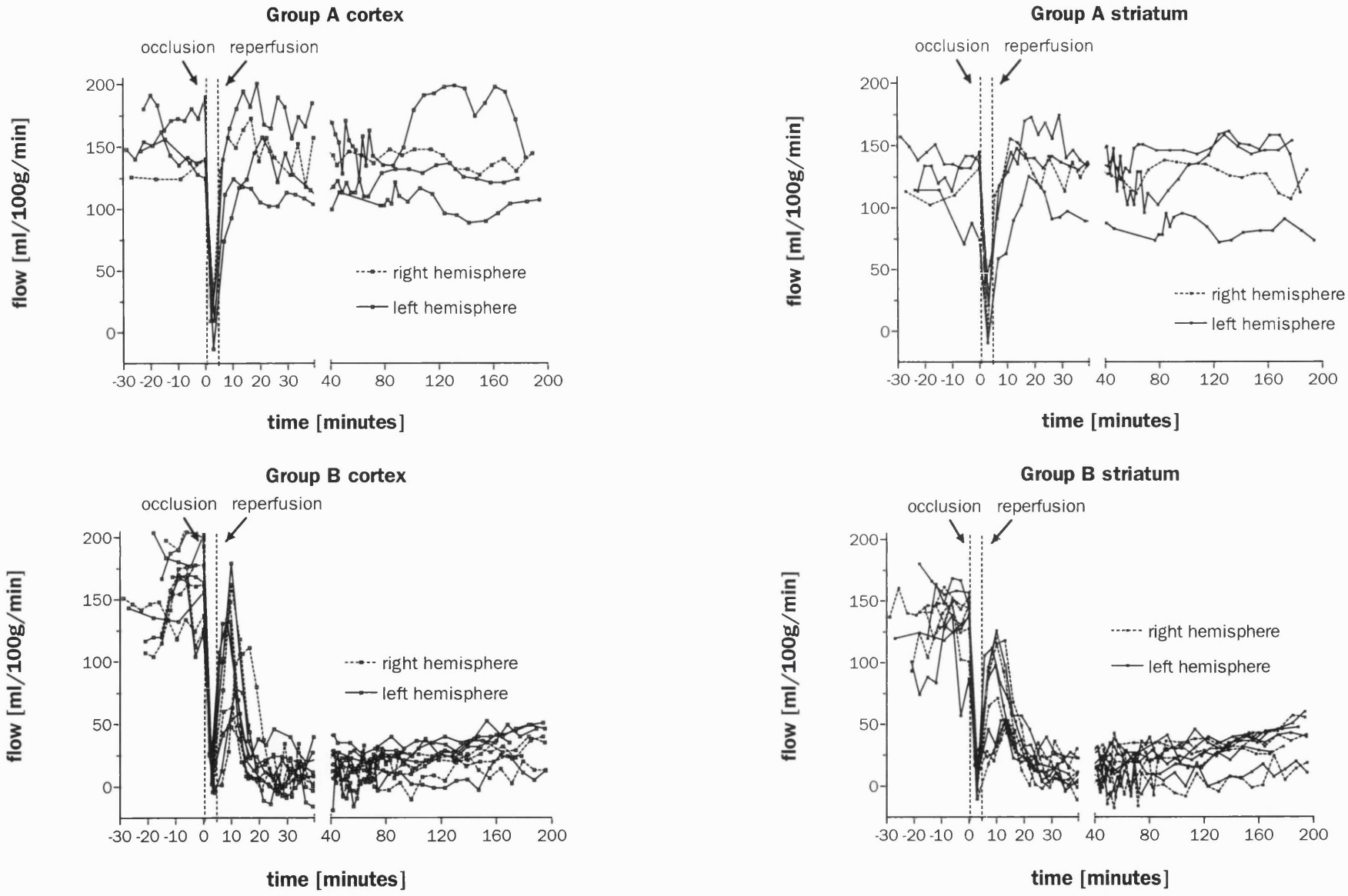

Fig. 5.2 Time courses of cortical and striatal regional data in both groups of data and in both hemispheres (see results in Section 5.3).

	Group A		Group B	
	cortex	**striatum**	**cortex**	**striatum**
Pre-occlusion	152±10	120±10	159±8	134±6
Occlusion	6±7	12±1	4±3	3±3

Table 5.1 Mean pre-occlusion and occlusion flows in the cortex and striatum. Cortical and striatal perfusion values in ml/100g/min (mean ± SEM). Values are shown for Group A (n=4 independent hemispheres) and Group B data (n=8 independent hemispheres)

5.3.1 Time-course CBF data : Group A (immediate renormalisation)

In 4 out of the 8 animals in this study, a unilateral Group A effect was observed. This response of immediate normalisation of the flow never occurred in both cerebral hemispheres of the same animal. Pre-occlusion and occlusion flows for this group of responses are listed in Table 5.1. On recirculation, the blood flow recovered to a value close to the pre-occlusion level. In order to characterise the initial recovery and the subsequent flow response, an exponentially damped polynomial was fitted to the first hour of the post-reperfusion data (Eq [5.1]). In order to test for regional differences, two such models were compared, one of which is a full model and consists of a separate set of coefficients for the cortical and striatal regions; the second model is a reduced model and assumes a common set of coefficients for the two regions. The difference between the models was not significant (log-likelihood ratio χ^2_4=5.42); the reduced, region independent model was therefore adopted. The common coefficients at the maximum likelihood solution of Eq [5.1] were: α = 126±7, β_0 = -226±23, β_1 = 0.29±0.07, λ = 0.24±0.02. The calculated mean time-dependent behaviour is shown in Fig. 5.3. The level of the initial recovery on reperfusion was provided by the peak of the fitted model. A value of 159 ml/100g/min at 11.7 min post-reperfusion (i.e. at 15.7 min post-occlusion) was thereby obtained. This maximal flow is 8% lower and 12% higher than the pre-occlusion levels in the cortex and striatum respectively. The mean response data are, therefore, suggestive of a period of *true* reactive hyperaemia in the striatum. At the end of the 1 hour period, the CBF reached an asymptotic level of 126 ml/100g/min.

By 3 hours post-reperfusion, the measured CBF values were 140±5 ml 100 g^{-1} min^{-1} and 122±6 ml 100 g^{-1} min^{-1} in the cortical and striatal regions respectively. These values are not significantly different from the pre-ischaemic CBF measurements (paired t-test). In order to characterise the behaviour of the flow subsequent to this initial period of reperfusion, linear regression was performed on the data collected from 1 hour post-reperfusion until the end of the experiment. In three out of the four animal data sets, the mean slope of this part of the time-course was not significantly different from zero in either the cortical or the striatal regions. The recovery of the CBF to the pre-occlusion level was not evident in the other animal during which there were uncontrollable temperature swings and therefore changes in tissue T_1 (Parker, 1983) and in the CBF.

5.3.2 Time-course CBF data : Group B (recovery followed by hypoperfusion)

This response occurred in 50% of the animals as a unilateral response and in the other animals as a bilateral response; in the latter situation, regional data were averaged over the two cerebral hemispheres. Pre-occlusion and occlusion flows for this group of responses are shown in Table 5.1. On initiation of recirculation, the blood flow recovered and, at approximately 5 min of reflow, reached a maximal level. A period of hypoperfusion then followed. In order to characterise the initial recovery and the decline in the flow response, an exponentially damped polynomial was fitted to the first hour of the post-reperfusion data (Equation [5.1]). The likelihood ratio test comparing a full, region-dependent coefficients model with the restricted common coefficients model was not significant (χ^2_4=0.3). Therefore, a common coefficients model (i.e. coefficients independent of region) was chosen to provide an adequate description of the data. The common coefficients at the maximum likelihood solution of Equation [5.1] were: α = 12.7±2, β_0 = -90±13, β_1 = 2.41±0.2, λ = 0.36±0.01. The mean time-dependent behaviour provided by the model is shown in Fig. 5.3. The maximal level of the initial recovery on reperfusion was provided by the peak of the fitted model. A value of 80 ml/100g/min at 4.9 min post-reperfusion (i.e. 8.9 min post-occlusion) was thereby obtained. This flow is 49% lower and 38% lower than the mean pre-occlusion levels in the cortex and striatum respectively and, therefore, the mean response is not suggestive of a period of *true* reactive hyperaemia. The calculated mean flow subsequently dropped to an asymptotic level during this 60 min period of 13 ml/100g/min. The rate of decline of the flow can be characterised by the time to reach a level that is 50% of the difference between this peak flow and the asymptotic flow level; this occurred 6.9 min after the peak.

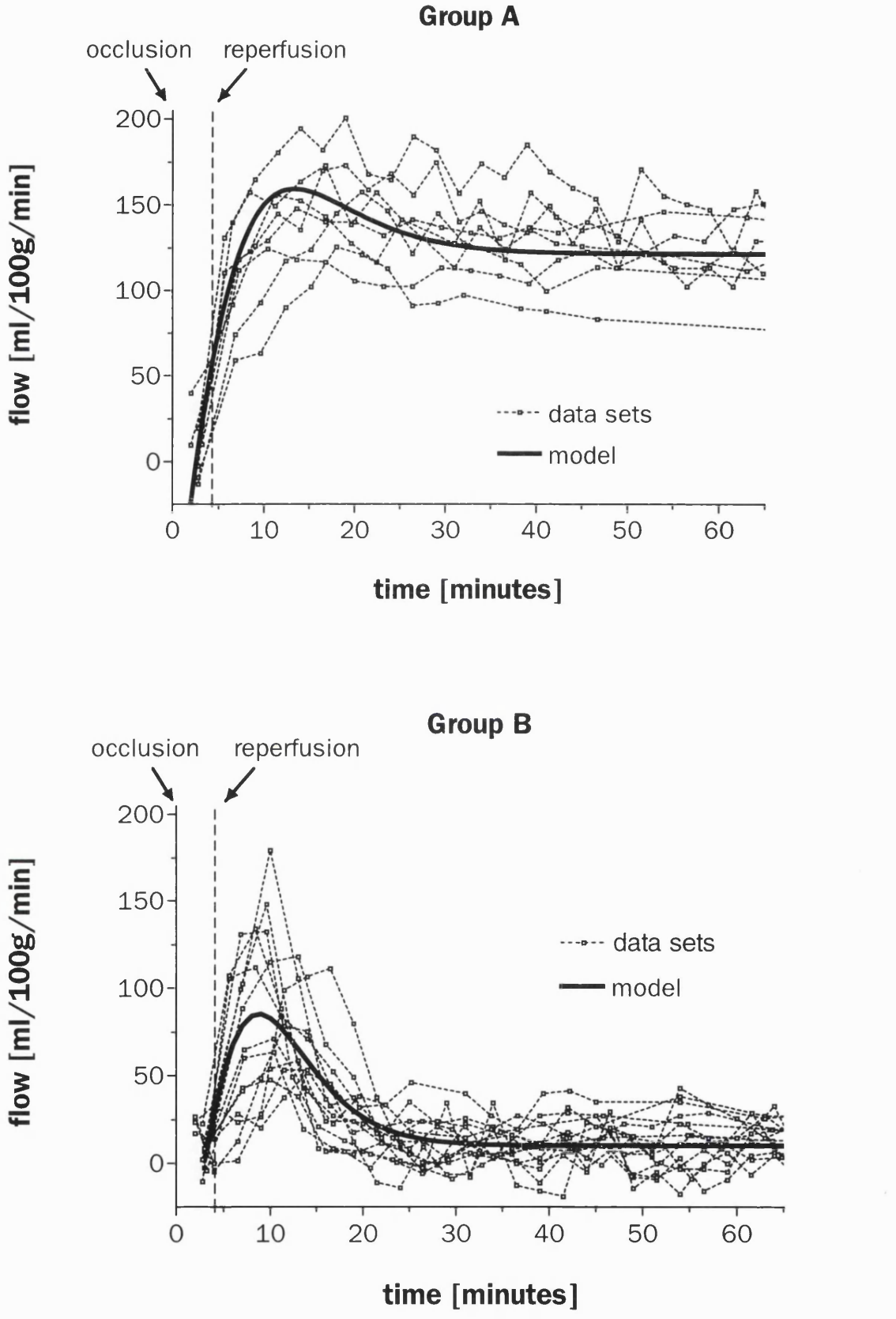

Fig. 5.3 The exponentially damped polynomial model that was fitted to the first 60 minutes of post-occlusion Group A and Group B data (see Image Data and Analysis section). All of the data sets are shown for Group A and a selection of data sets for Group B that include the extreme cases. Note that in Group B , there is considerable variation in the magnitude and the position of the maximal response and this affects the amplitude of the model.

At approximately 60 min post-reperfusion, the blood flow began to recover slowly. The mean slope of the recovery obtained by linear regression of data collected from 1hr post-reperfusion until the end of the experiment was significantly different from zero with values of 9.8±1.0 [ml/100g/min]/hour and 9.4±1.5 [ml/100g/min]/hour in the cortical and the striatal regions. By 3 hours post-reperfusion, the CBF had reached a level of 35±3 ml/100g/min and 37±4 ml/100g/min in the cortex and striatum respectively.

5.3.3 Diffusion trace(D) data : Group A (immediate renormalisation)

Trace(D) measurements were obtained in five animals, two of which displayed a side-to-side asymmetry on recirculation. Figure 5.4 displays the temporal profiles of the trace(D) data. The mean pre-occlusion trace(D) values were 0.77±0.04 and 0.78±0.02 ($\times 10^{-3}$) mm^2/sec in the cortex and striatum respectively. No occlusion data were acquired. The post-reperfusion trace(D) values in the cerebral hemispheres which displayed a Group A response, were very similar to the pre-ischaemic values and remained at a relatively constant level. However, a statistical comparison could not be performed due to the limited number of observations.

5.3.4 Diffusion trace(D) data : Group B (recovery followed by hypoperfusion)

Figure 5.4 displays the time courses of the trace(D) data. The five animals displayed the Group B response in one or both hemispheres. The mean pre-occlusion trace(D) values were 0.77±0.01 and 0.75±0.01 ($\times 10^{-3}$) mm^2/sec in the cortical and striatal regions respectively. No data were acquired during the occlusion. Linear regression of the post-reperfusion trace(D) values with time in each animal indicated a generally decreasing trend. In the cortex, four out of the five data sets exhibited a negative slope but the mean slope was not significantly different from zero (mean slope = -1.4±1.4 $\times 10^{-7}$ [mm^2/sec] min^{-1}). In the striatal region, a negative linear trend was obtained in all of the data sets and the mean slope was significantly different from zero (mean slope = -3.0±1.1 $\times 10^{-7}$ [mm^2/sec] min^{-1}; p=0.05). The values predicted by the regression lines of the trace(D) at the time of the first post-reperfusion measurement (35 min) were 0.75±0.03 and 0.79±0.02 ($\times 10^{-3}$) mm^2/sec in the two regions. These values are not statistically different from the pre-occlusion level (paired t-test). The regression slopes were used to obtain the mean change in the trace(D) values during the observation period, denoted $\Delta_{35\text{-}180}$.

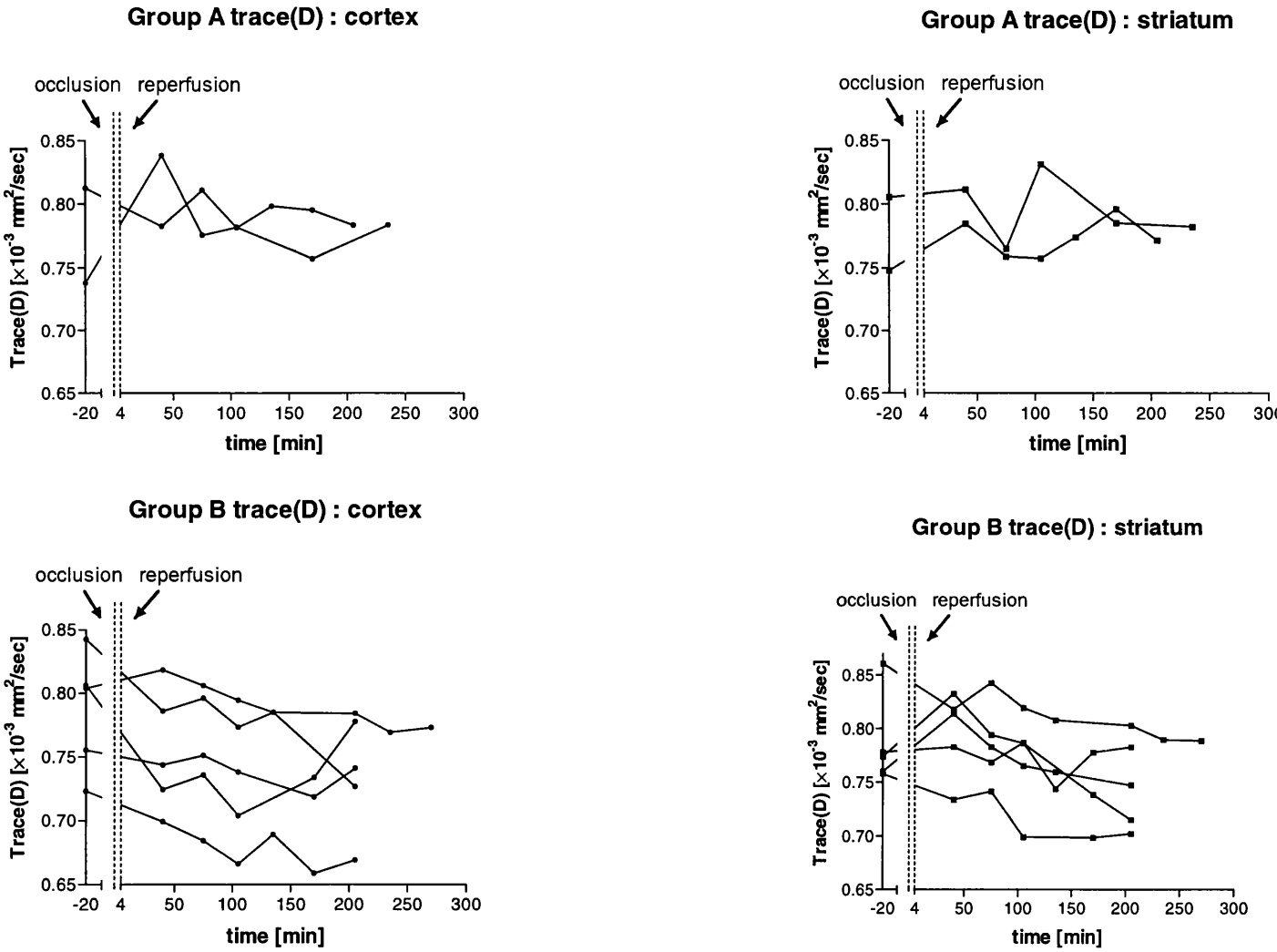

Fig. 5.4 Temporal evolution of the measurements of the trace of the diffusion tensor in both cortical and striatal regions in Group A and B animals. Group B data are averaged over the same regions in both hemispheres if a bilateral Group B response was observed. Trace(D) data were acquired in five animals.

The values of $\Delta_{35\text{-}180}$ were -0.021±0.008 (2.7% of control level) and -0.043±0.02 ($\times 10^{-3}$) mm^2/sec (5.7% of control level) in the cortical and striatal regions respectively. These values are not significantly different (paired t-test).

5.4 Discussion

The principal findings of this investigation were the demonstration of the benefits of using rapid FAIR imaging in a time course study of reperfusion, the observation of the two flow patterns of reperfusion (Group A and Group B responses) and the regional trends in the diffusion coefficient.

A time-efficient implementation of FAIR was employed in this investigation in order to accurately follow the changes in the blood flow with a time resolution of 2.8 min. This method has offered significant advantages over invasive techniques of perfusion measurement that do not permit longitudinal studies in the same animal. The serial measurements of flow have enabled distinct discrimination of the two group responses to reperfusion. This would not have been possible in a cross-sectional study. The increased power of the statistical analysis of longitudinal data employed in this study has facilitated this differentiation and has permitted examination of possible regional differences in the response. It has also been possible to take into account the inter-animal variability within the two patterns of reflow. Moreover, the changing flows have been mapped with a higher temporal resolution than offered by other techniques that provide serial, quantitative flow measurements. Since the immediate recovery and subsequent decrease in CBF on reperfusion occur over approximately 15 min, the acute phase of recirculation may be difficult to characterise with these other techniques.

A relatively short period of occlusion was utilised in this study since it has been shown that a 4-5 min period of ischaemia is sufficient for morphological damage (Suzuki, 1983) and ATP depletion (Krause, 1988). The initial return, in all cases, of the CBF on reperfusion to values close to the pre-occlusion level precludes the presence of a general no-reflow phenomenon. There was no indication of any immediate focal impairments in CBF on reperfusion even in the striatum, which has been shown to be one of the sub-cortical regions that is susceptible to no-reflow (Kågström, 1983a).

5.4.1 The Group responses

The immediate and permanent recovery of perfusion that was observed unilaterally in a number of animals (Group A response) was unexpected. It has been noted that there is a variability in the number and the size of the small communicating blood vessels between the vertebro-basilar and the carotid circulation in the gerbil (Levy, 1974). The degree of collateral circulation that originates from the unoccluded vertebral supply might therefore be the cause of the observed side-to-side asymmetry on reperfusion. Any residual level flow from this collateral supply during the occlusion would be underestimated due to its longer transit time (see next paragraphs). The low occlusion flows measured for the Group A response cannot, therefore, rule out the possibility of collateral circulation. A previous study has noted the side-to-side variations in the vasculature of the circle of Willis in gerbils (Tamura, 1981). During our study, at the conclusion of a number of the experiments (n=4), the animal was removed from the magnet and the snares were examined. The pulsation of the arterial flow proximal and distal to the snares was checked for consistency. At the end of every study, a post-mortem examination was carried out in order to verify that the snares were fully open and that the external diameter of sections of the carotid arteries proximal and distal to the snares was constant. The mechanical screw system was also inspected and the operation of closing and opening the snares was validated. The internal and external diameters of the arteries were examined post-mortem for indications of wall thickening. No evidence of an unsuccessful occlusion or reperfusion was thereby found.

The post-ischaemic impairment in reperfusion that was observed in this study (Group B response) followed the pattern of an initial recovery of flow, a delayed period of hypoperfusion, reaching a flow of 10 ml/100g/min, and then a slow recovery in the direction of the pre-occlusion level. The diffusion trace(D) measurements after reperfusion suggested a decreasing linear trend with time. The diffusion coefficient and T_1 values are sensitive to temperature (Le Bihan, 1995; Parker, 1983) but the non-selective, T_1-weighted FAIR data provided no evidence of temperature-related changes. The decreasing trend in the trace(D) values was especially apparent in the striatal regions and this may reflect a regional difference in susceptibility to injury. A similar regional pattern was observed in a recent study of hypoxia-ischaemia in the rat (Dijkhuizen, 1998a). During this investigation, an initial incomplete recovery of the ADC was observed in the thalamus and substantia nigra, followed by a subsequent decline in some of the animals, while in the other regions, the ADC displayed an initial

complete recovery. Our laboratory has demonstrated the existence of a flow threshold of approximately 20 ml/100g/min for diffusion changes in the gerbil (Busza, 1992). The apparent slow decline in the trace(D) values observed in our study correspond to recovering CBF values that were close to this threshold and may reflect a process of progressive cell swelling during the phase of hypoperfusion. The magnitude of the decline in the trace(D) values observed in the striatum was substantially smaller than the change typically observed during acute ischaemia. In previous studies of the ADC changes that occur after reperfusion, several distinct responses have been observed. In some investigations, a normalisation of the ADC occurred in most brain regions after 60 min of recirculation although a heterogeneous, "patchy" recovery across the brain slices was often observed (Hossmann, 1994b; Fischer, 1995; Tang, 1997; Schmitz, 1998) (cat model, occlusion, 60 min; cat model, cardiac arrest, 15 min; rat model, 19 minute asphyxial cardiac arrest; rat model, cardiac arrest, 10 min respectively). In another study, although a similar observation was reported in the cortex, the ADC did not recover from its depressed state in the thalamus (Busza, 1992) (gerbil, forebrain 2-vessel ischaemia, 20 min). Another observed pattern is that of an initial recovery of the ADC followed by a later decline at approximately 24 hours following recirculation. This delayed drop in the diffusion coefficient is suggestive of a process of secondary energy failure and has been observed in models of hypoxic-ischaemia in the piglet (Thornton, 1998) (variable durations of ischaemia) and in rat models (Dijkhuizen, 1998a, van Bruggen, 1998) (hypoxia-ischaemia, 20 min, and MCAO, 30 min respectively). It is interesting to note that in the piglet study, the first post-resuscitation diffusion coefficient measurement, (at 2-3 hours after the recovery) was approximately 4% less than the control value in the cortical regions and later displayed a secondary decrease in the ADC (Thornton, 1998). This initial decrease did not however prove to be statistically significant.

5.4.2 Accuracy of flow measurements during hypoperfusion

The CBF during the period of delayed hypoperfusion (Group B response) dropped to an unexpectedly low level based on previous, similar studies (Hossmann, 1985; Pulsinelli, 1982; Todd, 1986a; Miller, 1980). There exists experimental evidence that, paradoxically, shorter periods of ischaemia result in a more pronounced degree of post-ischaemic hypoperfusion (Hossmann, 1985a). For example, 30 min of total forebrain ischaemia in the gerbil resulted in a delayed drop in flow that represented approximately 40% of the control level (Almeida, 1995), while after 5 min of ischaemia in a similar

gerbil model, the CBF fell to a value that was approximately 15% of the pre-occlusion flow (Tomida, 1989). The former investigation employed hydrogen clearance for the flow measurements while the latter study used autoradiography. This relationship between the duration of the period of ischaemia and the severity of hypoperfusion has however, not been verified in a single study.

Due to the limitations of other CBF measurement techniques, longitudinal time-series studies of reperfusion injury in individual animals have not been possible or have been implemented with a relatively low time resolution. In those investigations, it has therefore been necessary to assume a uniform response to reperfusion throughout the brain. In order to simulate the effects of this analytical approach adopted in these investigations to our study of reperfusion, the mean perfusion time-course was obtained by averaging the data over both Group A and Group B patterns (Fig. 5.5). Even though the pre-ischaemic flows are different in the cortical and striatal regions, the flow response during the reperfusion phase in this mean response is remarkably similar in the two regions. The apparent level of the delayed hypoperfusion in the mean response reaches approximately 30% of the pre-ischaemic level in the cortical and striatal regions. By 3 hours post-reperfusion, the CBF in both regions has recovered to approximately 50% of the pre-ischaemic flow values. The pattern that was observed in this mean response more closely resembles that obtained in previous studies of reperfusion injury. This would tentatively suggest that, in these other studies, averaging over a non-uniform pattern of reperfusion has contributed to the apparent discrepancies with our data regarding the severity of the delayed hypoperfusion. However, we believe that during this phase, the lower CBF values measured in our study principally arise as a result of the limitations of the FAIR technique at measuring compromised flows.

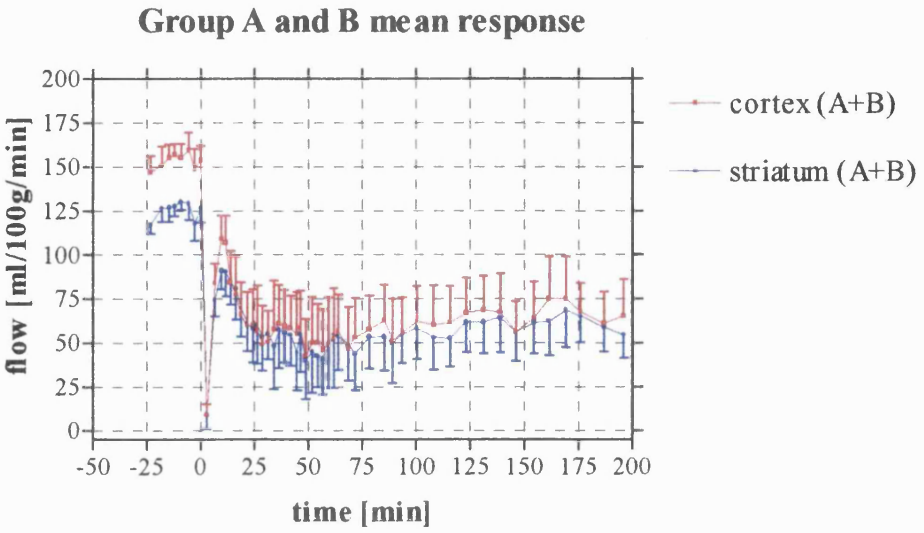

Fig. 5.5 Mean response averaged over Group A and Group B patterns. Data are displayed as mean ± SEM with errors bars shown in one direction only.

The underlying cause of this inaccuracy is the effect of the reduction in the blood flow on the validity of certain assumptions of the FAIR model. In addition to the increase in the inflow time that affects the non-selective image, the reduced blood flow will increase the significance of the transit time, δ, during which blood originating from within the inversion slab will move into the imaging slice (Calamante, 1996). The effects of δ were not considered in the analysis of the data since this time is expected to be insignificant for normal levels of flow. However, the impairment of flow during the period of hypoperfusion will presumably increase the transit and inflow times by a considerable extent. If the increased transit and inflow times are not taken into account in the FAIR quantification model, the technique will provide underestimated flow values. The sensitivity of the flow measurements to a changing transit time or inflow times can be theoretically determined and plotted (see Fig. 4.8 and Section 4.6). For example, with our combination of parameters and for a real flow of 20 ml/100g/min, the transit and inflow times would both need to rise by approximately 300 ms in order to induce an underestimation in the measured flow value of 5 ml/100g/min. Improved inversion and imaging slice profiles have been investigated with a view to reducing the effect of the increased transit times on the quantification (see Section 3.6).

5.4.3 Analysis of non-selective data for blood oxygenation response

The non-selective signal, M_{ns}, possesses a minimal flow component and will be principally T_1-weighted (due to the inversion pulse) and T_2-weighted.(due to the echo time of the EPI sequence, 37.5 ms). With the assumption of unobservable changes in the longitudinal relaxation time at our field strength, the T_2-weighting of the sequence provides information that is principally related to changes in blood oxygenation (see Section 7.4.2). The relatively short echo time provides only a small degree of T_2-weighting but experiments have demonstrated that the gross oxygenation changes should be apparent at an echo time as low as 30 ms (Section 7.3.5).

On occlusion, the non-selective signal intensity declined due to increases in blood volume and the oxygen extraction fraction (OEF) (see Section 7.4.2). On reperfusion, a transient recovery of the signal was usually observed during the period of reactive hyperaemia. In 7 out of the 8 animals that displayed the Group B response in at least one cerebral hemisphere, the signal in this hemisphere subsequently dropped to a relatively stable level below the pre-ischaemic level before beginning to slightly rise at approximately 150 min post-reperfusion (representative data sets are shown in Fig. 5.6). The initial, stable sub-control level indicates the maintenance of a constant level of cerebral metabolism by an increased OEF in response to the decreased delivery of oxygen-carrying blood during the period of hypoperfusion. The metabolism is therefore uncoupled to the blood flow changes in a manner that reflects the wide extraction reserve of the system.

It has been argued that the delayed hypoperfusion is not a pathogenic phenomenon if it is accompanied by a drop in the cerebral metabolism. Even though several studies have found evidence of such coupling (Michenfelder, 1991; Crumrine and LaManna, 1991), the principal body of evidence points to the uncoupling of flow and metabolism during reperfusion. Varied responses have been observed in this respect. In one study, the pathogenic reduction in the cerebral metabolic rate of oxygen has been reported that would result in a decreased degree of oxygen extraction (Singh, 1992). In stark contrast to this result, many studies have demonstrated the manifestation of hypermetabolism during the period of hypoperfusion (see Section 5.1.2). Our observation of an apparent maintenance of the metabolic rate indicates a non-pathogenic response to the reduction in flow. Further work is required to confirm this finding using sequences with a more significant degree of T_2-weighting.

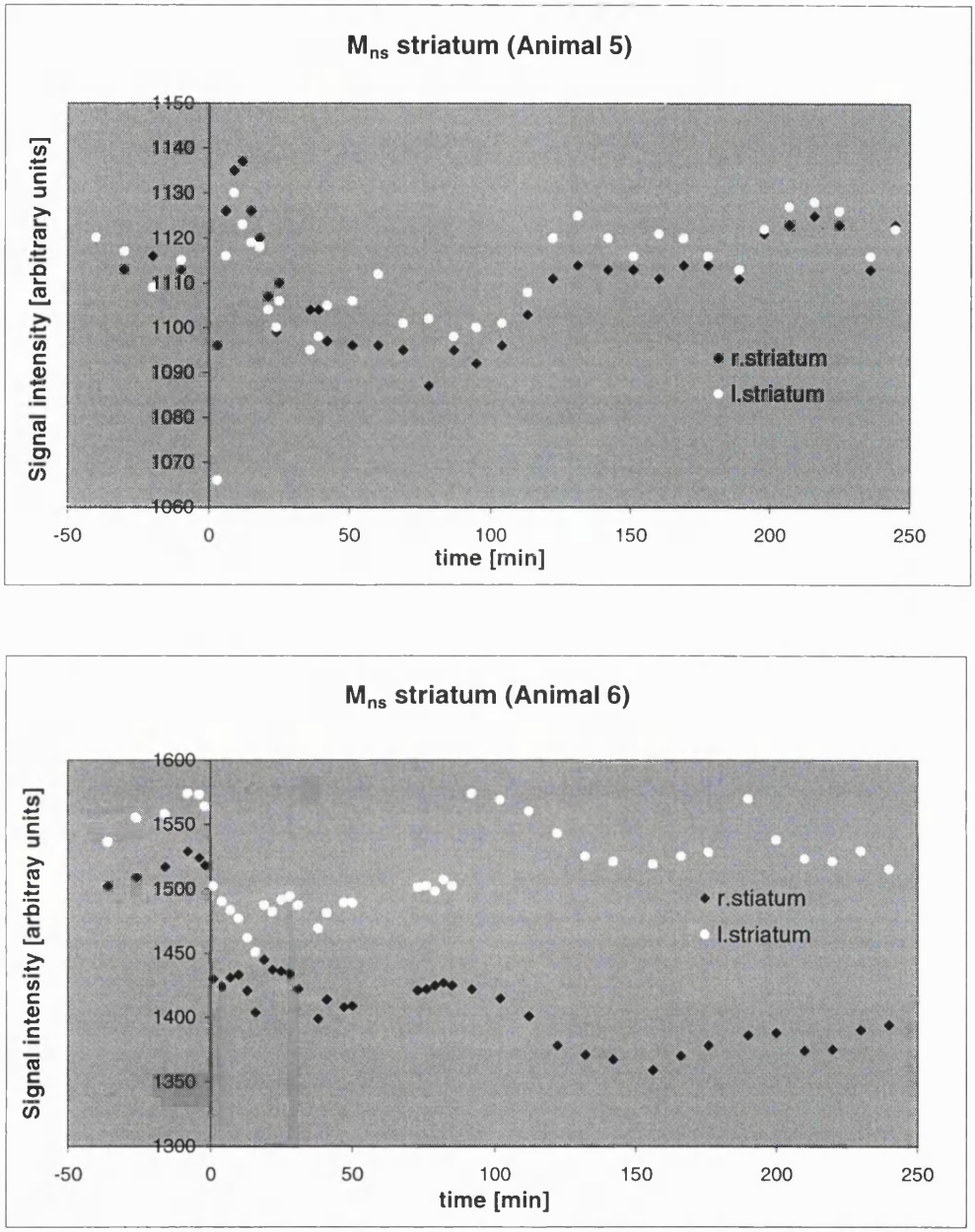

Fig. 5.6 Representative time courses of the non-selective signal intensity (M_{ns}) from two animals. This data will contain information related to blood oxygentation. Animal 5 displayed Group B responses in both hemispheres, while Animal 6 showed a Group A response in the left hemisphere and a Group B response in the contralateral hemisphere.

5.5 Conclusion

In conclusion, we have demonstrated the use of non-invasive FAIR perfusion imaging in following regional CBF changes with a high time resolution in a longitudinal study of reperfusion. On initiation of recirculation after 4 min of total forebrain ischaemia, the blood flow in the cerebral hemispheres either returned to the pre-occlusion level or displayed a pattern of initial recovery followed by hypoperfusion. Further work will need to experimentally examine the effect of the increasing transit and inflow times during flow impairment on the accuracy of flow quantification. Different pulse designs and slice thickness ratios (STRs) can be used to probe the transit time. Through the use of RF transmitter coils with different lengths or by varying the width of the non-selective band, it is possible to examine the inflow time response.

The ability to follow and characterise the time-course of CBF changes is of obvious importance in these and similar studies of cerebral ischaemia and in investigations of therapeutic interventions. Somewhat surprisingly, the CBF during the period of hypoperfusion decreased to a sufficiently low level to compromise the tissue energy status and induce concomitant cell swelling. Further work is, however, required to confirm this response with more animals. The combined measurements of CBF and the diffusion trace suggest a period during the reperfusion phase when intervention may be necessary in order to ameliorate recovery.

VI Implementation of Rapid, Quantitative Diffusion Imaging

Diffusion imaging was introduced in Section 2.1 as a technique that can act as a sensitive probe of tissue status. For practical use in studies of experimental cerebral ischaemia, time efficient implementation of the quantitative measurements are required. This chapter describes the development and optimisation two rapid diffusion pulse sequences, on a high-field system (TurboFLASH) and on a lower-field MRI system (EPI single-shot). Optimisation of both sequences is carried out in order to improve their time efficiency.

6.1 Introduction

Diffusion imaging possesses a unique sensitivity to provide information that other imaging techniques such as relaxometry (the measurement of T_1 and T_2) cannot discern. As with all imaging techniques, it is desirable to acquire the information in as rapid a manner as possible. This is of especial importance in diffusion imaging since the technique is extremely sensitive to the effects of motion in the form of patient movement, breathing and even brain pulsations. The temporal resolution of ADC mapping is, by necessity, limited by the length of the diffusion sensitisation gradients during the magnetisation preparation period. Any rapid technique can be used for the acquisition of the image such as STEAM, U-FLARE and fast spin-echo. EPI can be considered as the sequence of choice but at high magnetic field strengths, the technique is currently difficult to implement satisfactorily due to artefacts caused by inhomogeneity and susceptibility effects.

The goal of accurate diffusion mapping is hampered by several confounding gradient-related effects. Background gradients and the imaging gradients themselves can create unwanted phase dispersion due to their own dephasing effect ("self-talk") or via interactions with the main diffusion gradients ("cross-talk") (Hong, 1992; Conturo, 1995). An important further source of system error is the gradient calibration, and the gradient amplitude, direction and linearity require accurate validation. Errors related to the gradient strength can be further exacerbated in diffusion imaging on account of eddy currents which arise due to the rapid pulsing of the magnetic field gradients (Henkelman, 1987; Ahn, 1991). Eddy current fields are induced in the presence of conducting structures such as cryostat shields, the gradient and shim coils, the NMR probe, and the main magnet windings. The eddy currents will produce magnetic fields

that oppose the main magnetic field in accordance with Lenz's Law of electromagnetic induction. The fields persist, decaying with multi-exponential characteristics whose time constants are associated with the resistance and the inductance of the current path and may be in the order of hundreds of ms. Phase dispersion of the spin system will thereby occur even if the gradient unit is switched off. In the case of diffusion imaging, eddy currents will lead to imbalance between the diffusion sensitising gradients and to variations in the imaging slice width. Hence, additional, unintended dephasing of the signal occurs what will have an adverse effect on the ADC measurement.

A further consideration of diffusion MRI is the directional nature of the diffusion motion. The simple monoexponential model of signal decay that is described by Eq. [2.3] incorporates information about molecular displacements in only one direction even though the motion will be 3-dimensional. For practical implementation of diffusion-weighted imaging, the use of this simple model thereby necessitates the assumption of an isotropic mobility of diffusing spins. However, in biological systems, this is often not the case and diffusion anisotropy must be considered (Section 2.1.2). This chapter describes the practical implementation of rapid quantitative diffusion on two MRI scanners at different field strengths in our laboratory with regard to the aforementioned considerations. On the high field system (8.5T, SMIS console), a TurboFLASH-based sequence was implemented and investigated. The relatively low field scanner (2.35T, SMIS console) was more suitable for EPI imaging but image artefacts due to eddy current effects became readily apparent and had to be eliminated. An isotropic diffusion-weighted sequence for the measurement of the diffusion trace, trace(D), was required for the intended high time-resolution studies on this system and an investigation of sequence parameter optimisation for such a sequence was undertaken.

The implementation of the sequences on each of the two MRI systems will be discussed in turn.

6.2 The High-field system (TurboFLASH diffusion-weighting)

At high magnetic field strengths, EPI becomes technically difficult to implement due to the effects of magnetic field inhomogeneity and susceptibility gradients. The resultant image distortion and spatial misregistration is exacerbated at such fields. In addition, the faster rate of T_2 relaxation at high fields, necessitates the use of faster readout times and appropriately powerful gradient amplifiers. Alternative rapid imaging techniques have

therefore been implemented for diffusion imaging at such field strengths. The TurboFLASH (SNAPSHOT) sequence (Section 1.7.3) is a faster version of FLASH (Haase, 1986) with echo and repetition times, TR,TE << T_1. It can provide images in a few hundred ms with a good degree of spatial and temporal resolution. For diffusion imaging, the sequence can be modified to incorporate a preceding preparation period that creates diffusion sensitisation before the image acquisition. This sequence was implemented on the high field system in our laboratory since it would complement the TurboFLASH sequences that were already being used on the system for quantitative T_1 and perfusion imaging (Section 3.7).;

6.2.1 The TurboFLASH sequence

The cumulative effect of repeated application of low angle RF pulses is to create a steady state of the longitudinal magnetisation in which the amount that has recovered is balanced by the magnetisation that has been nutated into the transverse plane by the RF pulse. Standard FLASH MRI utilises repetition times in the order of 10-100 ms and collects the signal in this steady state. The contrast can be manipulated by different treatments of the evolving transverse magnetisation. In the TurboFLASH sequence, the images are collected during the approach to the steady state. This provides a rapid image acquisition (TR ≈ 5 ms; T_{scan} ≈ 300 ms) but requires a different theoretical treatment (Hänicke, 1990). The optimum flip angle, α_{opt}, is considerably higher than the Ernst angle (Section 1.7.3). Hänicke *et al.* demonstrated that for TR = 5 ms, T_1 = 1sec, and 64 phase encoding steps, α_{opt} is approximately 12° (Hänicke, 1990). The overall signal intensity is therefore significantly enhanced in comparison with that expected from steady state considerations. Considerable decay of the observable transverse magnetisation towards the steady state level, occurs during the phase-encoding excitations. If the longitudinal magnetisation contrast has been prepared with, for example, diffusion sensitisation, it will be beneficial to immediately acquire the low spatial frequencies which determine the bulk appearance of the image. The phase encoding order is consequently optimised with a centric ordering scheme in which the view acquisition is symmetric around $k_y = 0$ (0,-1,+1,...+63,-64) (Holsinger, 1990). The disadvantage of a combined scheme of non-steady state acquisition and a modified phase-encoding strategy, is the resultant application of an effective k-space filter along the phase-encoding direction. The available transverse magnetisation varies from view-to-view and the bulk of the signal is acquired at the time when this change is greatest. The corresponding point-spread-function (PSF) (Haacke, 1987) will therefore deviate

from an ideal sinc function and image artefacts such as edge-enhancement and blurring will consequently be apparent in the image. This effect is exacerbated by T_1 relaxation of the longitudinal magnetisation during the image acquisition. The detrimental effects of the k-space filter can be reduced by the application of dummy cycles of RF before commencing the data acquisition (Holsinger, 1990), variable flip angles to maintain a constant level of transverse magnetisation (Mugler, 1992), or by simply using lower flip angles.

The treatment of the transverse magnetisation from view-to-view will have a significant effect on image contrast. More significantly, banding artefacts across the centre of the image are often observed. This artefact is intensified for higher flip angles and are the result of transverse coherences that develop during the excitation (Frahm, 1987; Crawley, 1988). The coherences can be eliminated by a scheme of incrementing spoilers (Wang, 1990) or alternatively, the use of phase rewinding will incorporate this magnetisation at a constant level (Frahm, 1997).

6.2.1.1 Diffusion preparation

In order to incorporate diffusion-weighting in the TurboFLASH sequence, suitable magnetisation preparation is required. This is provided by a Driven Equilibrium Fourier Transform (DEFT) series of RF pulses [90°-180°-90°] in combination with diffusion sensitising gradients inserted around the 180° pulse (Deimling, 1990). High RF flip angles of the readout pulses and centric order phase encoding schemes are used as described previously.

6.2.1.2 T_1 contamination

Such a sequence is, however, susceptible to T_1 contamination from not only the readout period but also as a result of the magnetisation preparation. This period will be relatively long in order to provide sufficient diffusion weighting and the subsequent spoiling gradients. It can be shown that the expression for the transverse magnetisation, $M_t(n)$, for the nth excitation step, becomes

$$M_t(n) = A(n)e^{-bD} + B(n) \qquad [6.1]$$

where A(n) and B(n) are both functions of sequence parameters during the parameter and readout periods. This expression essentially defines the k-space filter described previously. The diffusion-independent term, B(n), originates from the longitudinal relaxation during the preparation and readout periods. The presence of this term implies that the monoexponential fit of Eq. [2.3] is unrealistic for such a situation (Coremans, 1996). Various correction techniques have been proposed in order to eliminate the B(n) term, such as the collection of a non-phase-encoded data set and thus correcting for T_1 relaxation during the collection period (Coremans, 1997), and the use of a crusher gradient within the preparation period that is rephased during readout (Sinha, 1996). However, the former technique does not account for T_1 contamination during the preparation period. The latter scheme eliminates both contaminating periods but only makes use of 50% of the available signal. A more general elimination scheme is provided by acquiring two images while alternating the phases of both the last 90° RF preparation pulse and the low angle readout pulses. The two are added together so that the diffusion term, A(n)exp(-bD) is reinforced while the B(n) term is eliminated (Coremans, 1997).

6.2.1.3 Eddy currents

The combination of RF pulses during the preparation period should ideally align all the prepared magnetisation along the longitudinal direction. The rephasing effect of the pulses is, however, prevented by magnetic field inhomogeneities and eddy currents. The former effect is common for any preparation scheme and has been considered in other studies (Mansfield, 1992). Improved tolerance to B_1 inhomogeneities is obtained by manipulating the phases of the RF pulses with $[90°_x\text{-}180°_y\text{-}90°_x]$ representing the optimal combination where, for example, $90°_x$ represents a pulse that yields clockwise rotation around the positive x-axis.

Diffusion preparation may result in eddy current-related artefacts that are especially apparent at higher b-values even in systems with active gradient shielding. The eddy currents cause time varying magnetic field inhomogeneities across the sample that act during the application of the diffusion gradients and shift the phase of the refocusing spins. The eddy current induced by the ramp-up and ramp-down of the first diffusion gradient will act both before and after the 180° pulse if the time constant are of sufficient length. The dephasing effect of the eddy current fields are, therefore, not

rephased by those generated by the diffusion gradients applied after the 180° pulse. A phase error ensues and only a proportion of the total magnetisation, Mcosθ, is returned to the z-axis by the second 90° pulse, where θ is the angle between the magnetisation vector, **M**, and the phase axis of the 180° pulse. The angle, θ, will change as the value of the diffusion gradient is varied and the accuracy of the measurement of the diffusion coefficient will, therefore, be compromised. In order to correct for this error, a novel phase-encoding scheme was devised that samples both the Msinθ and Mcosθ components of the magnetisation. This method utilises the acquisition of two images with the 90° flip-back DEFT pulse of the second image phase-shifted by $\pi/2$ radians with respect to the first. A [$90°_x$-$180°_y$-$90°_{-x}$] preparation is thereby succeeded by a [$90°_x$-$180°_y$-$90°_{-y}$] DEFT sequence. The *true* signal, I_T, is obtained by combining the two images in the following manner

$$I_T = \sqrt{(I_{90-x})^2 + (I_{90-y})^2} \qquad [6.2]$$

where, for example, I_{90-x} represents the image acquired after the [$90°_x$-$180°_y$-$90°_{-x}$] combination. In fact, the acquisition of an image at a particular b-value requires the combination of a total of four images in order to take into account the effects of both T_1 contamination and eddy currents. These images can be described as follows:

#1: [$90°_x$-$180°_y$-$90°_{-x}$]-τ-[α_x]$_n$
#2: [$90°_x$-$180°_y$-$90°_x$]-τ-[α_{-x}]$_n$
} phase-cycled addition ⟹ I_{90-x}

#3: [$90°_x$-$180°_y$-$90°_{-y}$]-τ-[α_x]$_n$
#4: [$90°_x$-$180°_y$-$90°_y$]-τ-[α_{-x}]$_n$
} phase-cycled addition ⟹ I_{90-y}

} I_T

where τ is the spoiler gradient delay after the DEFT preparation and [α_x]$_n$ describes the cycle of readout RF pulses.

6.2.2 Implementation of the sequence

The diffusion-weighted TurboFLASH sequence that was implemented on the high-field system is shown in Fig. 6.1 for the phase combination #1 described previously. The 8.5T system has non-shielded gradients and a birdcage coil with an inner diameter of 38 mm was employed to transmit and receive the signal.

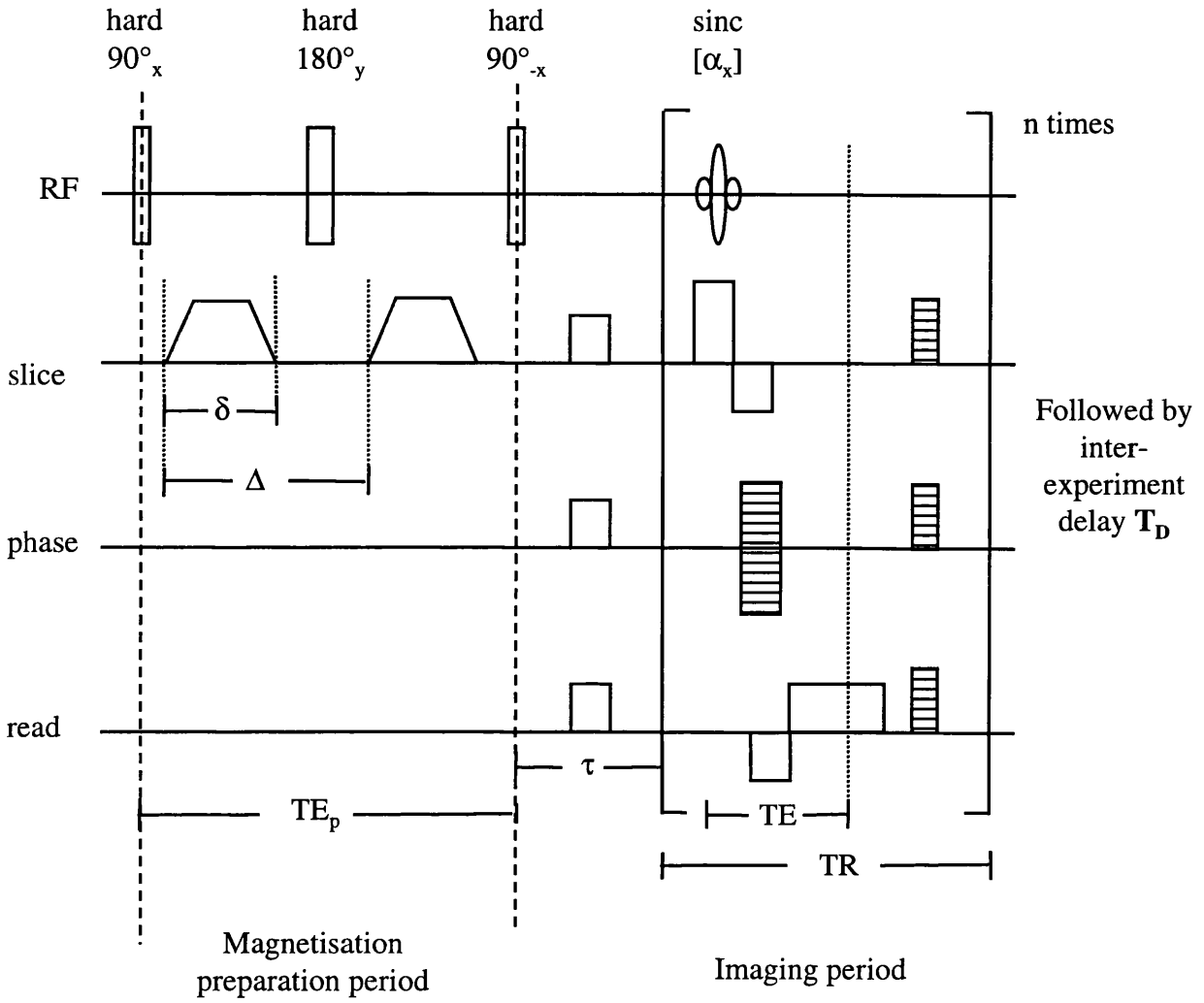

Fig. 6.1 Diffusion weighted TurboFLASH sequence. A diffusion preparation period of length TE_p consists of a 90°-180°-90° RF pulse scheme with diffusion gradients of duration δ and time separation Δ placed around the 180° pulse. Following the preparation period, spoiler gradients are applied during the delay time, τ, to crush residual transverse magnetisation. The imaging sequence is gradient-spoiled TurboFLASH with TE=2 ms and TR=5 ms, which is centre-out phase encoded using 64 phase encoding steps. Rewinding of the phase encoding gradient is not necessary since the theoretical treatment requires no transverse magnetisation to survive between successive low-angle excitations. The inter-experiment delay, T_D, indicates the time allowed for relaxation after the FLASH sequence.

TurboFLASH readout parameters: 64 phase-encoding steps were used with 128 data points acquired during each, and a signal bandwidth of 100 kHz. The FOV was 40 mm and slice-selective excitation was achieved with sinc-shaped RF pulses (T_p=666 μs, bandwidth=6 kHz) with a flip angle of approximately 14°. Other imaging parameters were TE = 2 ms, TR = 5 ms and the total imaging time was 335 ms. The imaging period began with three FLASH dummy cycles and then consisted of centric-ordered phase encoding scheme with an incrementally increasing spoiler in the slice-select and read directions. Spoilers were also applied after the phase-encode direction that decreased and alternated with the phase-encoding gradient.

Preparation parameters: The DEFT pulse train used hard pulses ($T_p(90°)$ = 100 μs, $T_p(180°)$ = 200 μs). The preparation time, TE_p, was 600 ms. The τ delay for post-preparation spoiling was 10 ms.

Background gradients: As described previously, a total of four images are combined to create one data point for the chosen b-value. In addition, in order to minimise the sensitivity to background gradients, the scheme of Jara *et al.* was implented in which alternate averages employed diffusion gradients of the opposite sign (Jara, 1994). On taking the geometrical mean of the two images, the cross-term from the background gradient is eliminated.

6.2.3 Validation of the sequence

6.2.3.1 Phantom experiments

Measurements were performed in two doped agar phantoms with different T_1 values. The temperature of the phantom was monitored continuously throughout the experiment using a chart recorder connected to a thermometer probe. The diffusion coefficients could therefore be corrected for temperature variations by assuming the relationship between ADC and the temperature to be a 2.4% increase per °C (Le Bihan, 1995). Measured diffusion coefficients were, therefore, multiplied by the correction factor $1/(1+0.024\Delta T)$ where ΔT is the temperature variation from a baseline level so that all values would be directly comparable.

In order to validate the TurboFLASH sequence, the diffusion coefficient measured with this technique were compared with the values obtained by a standard spin-echo 2D-FT sequence. Eight b-values from 100-800 sec/mm^2 were employed in order to collect

sufficient data for the diffusion coefficient calculation. A nonlinear monoexponential least squares fit was performed on the data in order to determine the ADC. The sequence diffusion parameters were, $\Delta = 32.4$ ms, $\delta = 24.3$ ms. Diffusion weighting was applied separately along the slice, read and phase-encode directions for both sequences. The imaging slice thickness was 4 mm, and the delay time between the end of each TurboFLASH imaging period and the start of the following preparation period (the inter-experiment time, T_D) was 5 sec in order to allow for almost complete longitudinal relaxation. Images from the TurboFLASH sequence are shown in Fig. 6.2 and the need for the eddy current elimination scheme is clearly apparent in the individual images.

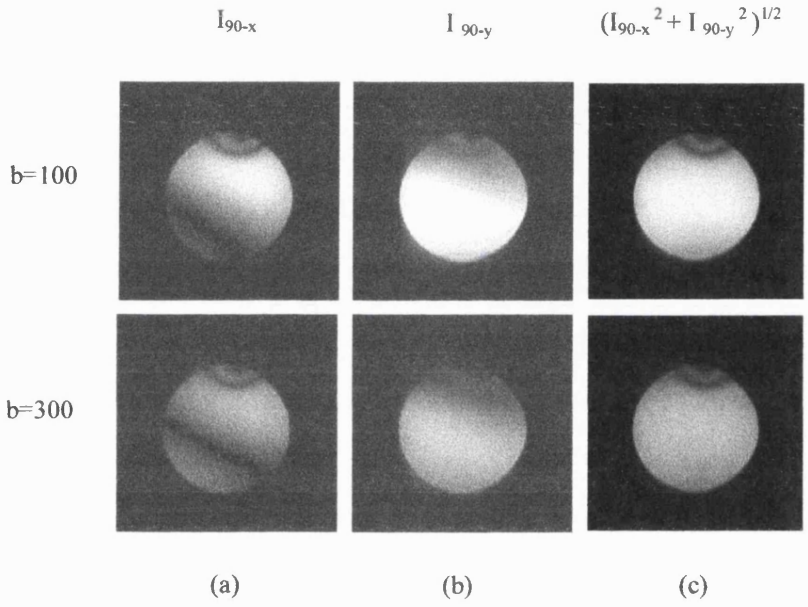

Fig. 6.2 Diffusion weighted images of an agar phantom at two b-values (in sec/mm2) following (a) $90°_x$-$180°_y$-$90°_{-x}$ and (b) $90°_x$-$180°_y$-$90°_{-y}$ magnetisation preparation schemes. The variation of intensity across the images reflects the differing effects of eddy currents at different points in space. Squaring, adding and square rooting pixel intensities yields a much more homogeneous image (c). The dark band at the top of the images is a susceptibility artefact.

In order to compare the ADC values, a statistical analysis was performed on regions drawn on the ADC maps obtained with both imaging techniques. The data from each sequence consisted of measurements of ADC values along the x-, y- and z-gradient directions from five regions that had been repeated four times, resulting in a data set size of 60. The diffusion coefficient measurement was approximately 2.23×10^{-3}

mm^2/sec in every direction. The results of the t-test are shown in Table 6.1 (Section 6.2.4) and confirm the accuracy of the TurboFLASH technique.

6.2.3.2 In-vivo experiments

In order to confirm that the proposed sequence provides accurate ADC measurements under in-vivo conditions, the technique was implemented during an MCAO study (see Section 3.7) in combination with spin-echo 2D-FT diffusion imaging as a reference. Two b-values (31 and 1745 sec/mm^2) were employed for the FLASH measurement and three b-values were used with the spin-echo sequence (Section 3.7). Isotropically-weighted diffusion gradients were incorporated into the TurboFLASH sequence since the MCAO experiments required measurements of the rotationally-independent diffusion trace(D) (see Section 6.3). The spin-echo reference sequence utilised the gradient scheme of (Mori, 1995). The diffusion-weighted images and trace(D) maps from an occluded animal are shown in Fig. 6.3.

The contrast of normal tissue in the maps is minimal due to the anisotropy-independence of the trace(D) measurement. The contrast between ischaemic and non-ischaemic tissues can be clearly observed. The trace(D) values in ROIs (155 pixels) are 8.39×10^{-3} mm^2/sec and 5.18×10^{-3} mm^2/sec in an non-ischaemic and a ischaemic region respectively (TurboFLASH) and 8.47×10^{-3} mm^2/sec and 5.33×10^{-3} mm^2/sec respectively (spin-echo).

6.2.4 The effects of incomplete relaxation between TurboFLASH experiments

The TurboFLASH sequence requires four phase-cycled scans in order to produce a diffusion-weighted image that is free from T_1 and eddy current contamination. The final image is equivalent to two averages of the *true* signal intensity and it is likely that further averaging will be required to boost the SNR of the ADC maps. Hence, it is desirable to reduce the inter-experiment time, T_D, in order to improve the time efficiency of the technique if this case can be achieved without compromising the accuracy of the diffusion coefficient measurement. Previous analyses of FLASH have assumed complete relaxation between acquisitions (Coremans, 1997; Hänicke, 1990). If this is not the case ($T_D<T_1$), it is possible to calculate the longitudinal magnetisation at the end of the first inter-experimental delay by calculation of the corresponding magnetisation at the end of the previous image acquisition, $M_z(64)$ (Coremans, 1997).

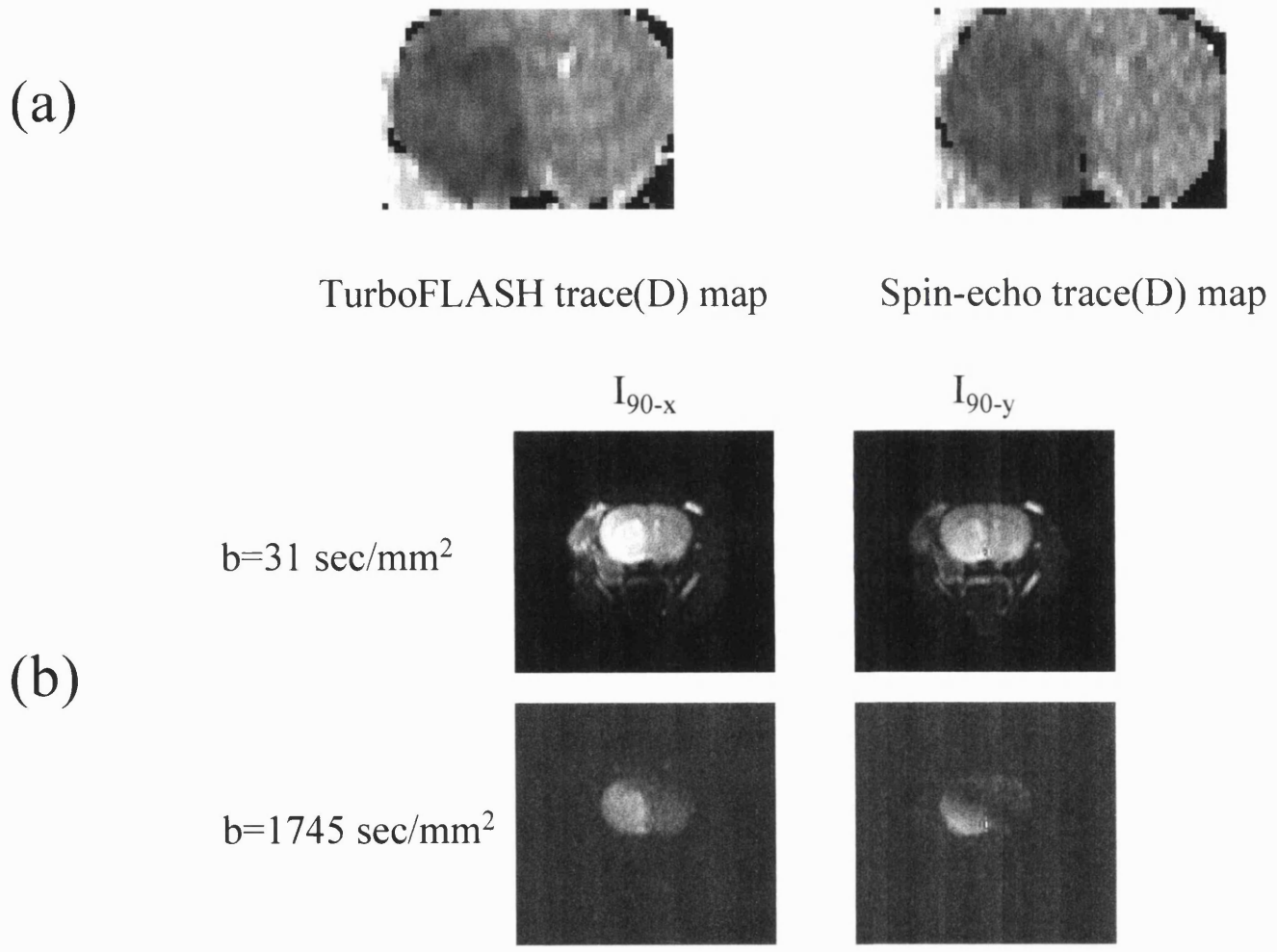

Fig. 6.3 (a) Comparison of trace(D) maps obtained with the two rapid DWI sequences and (b) composite DW-images acquired with the TurboFLASH sequence.

Analysis of the subsequent image acquisition provides the equivalent expression to Eq. [6.1] for the transverse magnetisation for this case,

$$M_t(n) = X(n)e^{-2bD} + Y(n)e^{-bD} + B(n) \qquad [6.3]$$

(see Thomas, 1998 for derivation and complete analysis). It can be seen that the diffusion-independent term, B(n), is independent of the preceding experiment and is therefore not affected by a reduced inter-experimental time. The coefficient Y(n) is the important diffusion monoexponential decay term and is equal to A(n) in Eq. [6.1] with an additional multiplying factor related to $\exp(-T_D/T_1)$. An extra coefficient, X(n), has appeared in the expression that reflects magnetisation that has undergone diffusion preparation during both experiments. This term will introduce biexponential characteristics into the diffusion-related decay of the signal and its relative magnitude with respect to Y(n) must, therefore, be considered. In a similar manner, it is possible to extend the analysis to a third experiment. Equivalent terms are obtained in this case with the addition of an extra coefficient that is related to magnetisation that has been diffusion prepared on three occasions. The significance of these terms will decrease with increasing number of preceding preparations. Fig. 6.4 shows the form of these coefficients for three values of the inter-experiment time, T_D, with T_1 = 1 sec. As T_D shortens, it can be seen that the difference between the Y(n) and the A(n) terms is magnified since inter-experimental T_1 recovery of the magnetisation becomes less complete. The significance of the X(n) term will increase with decreasing T_D and at T_D = 0.75 sec, X(n) represents approximately 2.5% of the monoexponential term, Y(n). The accuracy of the ADC values may therefore be compromised for precise measurements with a high degree of SNR.

In order to demonstrate the practical implications of reduced inter-experimental time on the accuracy of ADC quantification, the phantom measurements described in Section 6.2.3.1 were repeated at T_D = 1.5 sec and 0.75 sec. A similar regional statistical analysis was carried out and the results are displayed in Table 6.1. It can be seen that the accuracy of the measurement with T_D=0.75 sec is compromised to a statistically significant degree. By analysis of the monoexponential decay term, Y(n), it can be shown that the optimal SNR-per-unit-time is obtained for $T_D \approx T_1$ (see Fig. 6.5). The results demonstrate that the sequence can be run using this order of T_D without deleterious effects on the accuracy of the ADC measurement for our level of SNR.

	T_D = 5 sec	T_D = 1.5 sec	T_D = 0.75 sec
P-value from paired t-test	P > 0.05	P > 0.05	P < 0.05
95% confidence interval of differences (lower limit, upper limit) in $mm^2/sec \times 10^{-3}$	(-0.0016, 0.0133)	(-0.0041, 0.0110)	(-0.0254, -0.0071)

Table 6.1 Paired t-test results comparing TurboFLASH diffusion-weighted sequence with a spin-echo sequence on an agar phantom. P-values are two-tailed; difference calculated by subtracting TurboFLASH ADC from method spin-echo ADC. It can be seen that for T_D = 1.5 sec, the error in the ADC measurement is still not noticeable, but when the delay time is reduced to 0.75 sec, the difference between the two values becomes significant.

6.2.5 Discussion

A novel method for fast quantitative diffusion imaging that is tolerant to eddy currents was successfully implemented on the 8.5T high field system. This technique requires multiple scans in order to obtain the corrected image and is, therefore, susceptible to motion artefacts and subsequent image misregistration. It has been demonstrated that the time efficiency can be improved by reducing the inter-experimental delay without compromising the measurement accuracy. Figure 6.5 plots the relative SNR-per-unit-time of the TurboFLASH and standard 2D-FT spin-echo sequences. It can be seen that the TurboFLASH sequence offers a superior combination of temporal and spatial resolution. The effects of T_1 contamination were eliminated with the subtraction scheme proposed by (Yamazaki, 1991). The recovery of the diffusion-prepared spins reduces the efficacy of the TurboFLASH sequence since the available, useable signal is decreased. This will be exacerbated for tissues with a short T_1 when reduced flip angles (Lee, 1994), segmented FLASH schemes (Sinha, 1996), or other correction techniques (Coremans, 1997) should be considered.

6.3 The Low-field system (EPI isotropic diffusion-weighting)

On the lower field, 2.35T magnet, the EPI sequence was suitable for high-speed imaging. A number of problems became apparent upon implementation of the technique

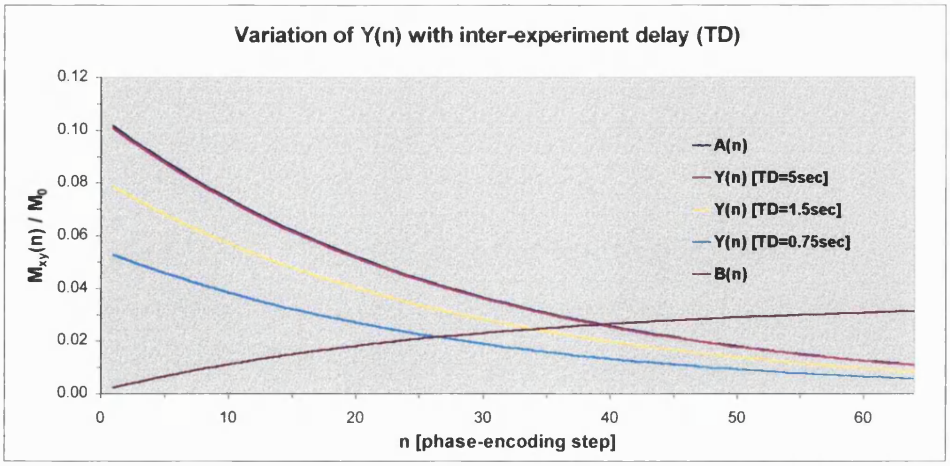

Fig. 6.4 The effect of varying inter-experimental times (TD) on the Y(n) coefficient of Eq. [6.3]. Y(n) describes the mononexponential diffusion decay during the second experiment. The comparable coefficient A(n) from the first experiment, and the diffusion-independent term, B(n), that is unaffected by incomplete inter-experimental relaxation, are also depicted. Parameters are as described in the text. The lines A(n) and Y(n) at TD=5 sec are coincident. The lines A(n) and Y(n) (the latter, for TD = 5 sec) are almost exactly equal.

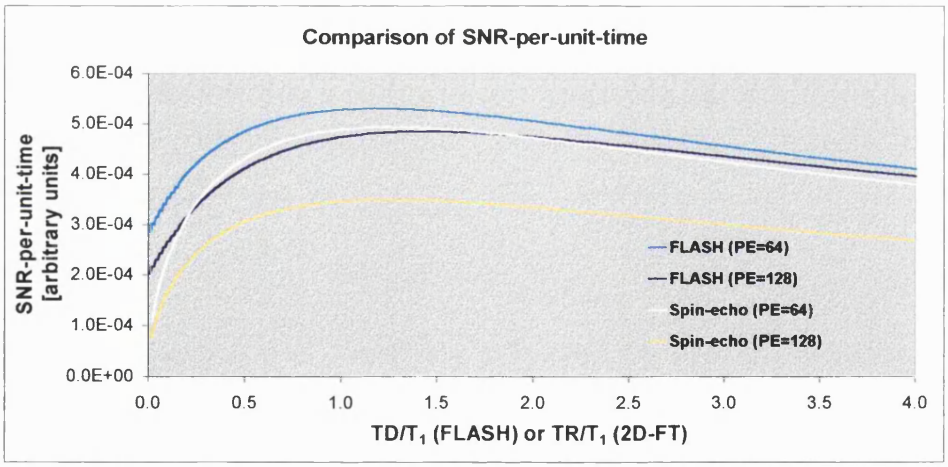

Fig. 6.5 Comparison of SNR-per-unit-time for the centric-order TurboFlash (Eq. [6.1]) and spin-echo sequences. The signal is assumed to originate from the zeroth phase encoding step. The normalised SNR is plotted against the inter-experiment time (TD) for the TurboFLASH sequence, and against the TR time between phase-encoding steps for the 2D-FT sequence. In the case of the latter sequence, 64 or 128 phase encoding steps are assumed for the calculation of the total experiment time, and a TE = 30 ms was also assumed. The flip angle for the FLASH sequence was 17° which is close to the optimal value (Hänicke, 1990); 64 and 128 phase encoding steps were alternatively assumed and the T_1 contribution was eliminated. It can be seen that the optimum TD and TR times for the two sequences are approximately equal to the T_1 time, and that the normalised SNR is of the same order of magnitude for 64 phase encoding steps. The FLASH sequence, however, offers improved spatial resolution with only a small penalty in the corresponding time efficiency.

and these are described in the following sections. A previously-reported single-shot trace(D) sequence was developed and optimised for time-course measurements with improved precision.

6.3.1 Implementation of diffusion-weighted EPI

6.3.1.1 Background gradients

The standard spin-echo EPI diffusion sequence with monopolar diffusion gradients before and after the 180° pulse (Turner, 1990), was modified to reduce the effect of background gradients. Gradients were immediately refocused whenever possible to minimise the possibility of cross-terms. Specifically, the read compensation gradient was applied immediately before the EPI readout rather than before the 180° pulse. Nevertheless, shim-sensitive geometric image distortion was apparent in the images due to the sensitivity of EPI to magnetic field inhomogeneities and susceptibility effects.

6.3.1.2 Eddy currents and gradient calibration

The presence of eddy currents was indicated by the spatial misregistration and intensified geometric distortion of images acquired with and without the application of diffusion gradients (see Fig. 6.6). This artefact was especially visible when the gradient was applied along the x-axis since the anisotropic gradient set was strongest in this direction.

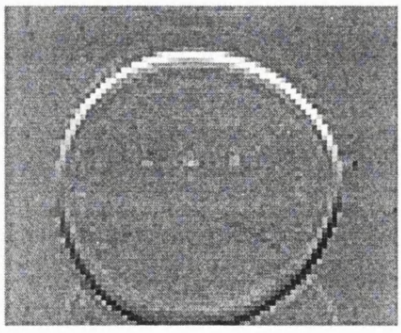

Fig. 6.6 Subtraction of two EPI images of a water phantom acquired with a preceding gradient of, alternately, +550 and –550 Hz/mm applied along the read (x) direction. The two images are shifted in the vertical direction with respect to each other.

As discussed with regard to the TurboFLASH diffusion sequence, quantification of the ADC may be hampered by gradient mismatch induced by the eddy current fields. It was therefore necessary to attempt eddy current compensation with a pre-emphasis unit

(Picker, USA; obtained from an old MRI set-up) (Jensen, 1987) since active gradient shielding (Mansfield, 1987) was not a viable option. The unit uses networks of resistor-capacitor (RC) circuitry in series with the gradient amplifier in order to counter-distort the gradient waveform. The modified waveform nullifies the linear term of the eddy current distortions. The adjustment procedure utilised a pulse sequence with a series of low angle RF pulses applied at various durations after a 500 ms gradient pulse (water phantom as the sample). The resulting series of signal Fourier-transformed echoes, enabled adjustment of the pre-emphasis settings. A representative data set is shown in Fig. 6.7, with and without pre-emphasis. An improvement in gradient performance is observed, but the eddy currents cannot be totally eliminated by pre-emphasis. Non-linear terms are not corrected by the technique. However, the spatial misregistration between EPI images with and without diffusion gradients was significantly reduced.

The gradient calibrations along each axis were then adjusted until a standard 2D-FT diffusion sequence provided accurate temperature-adjusted ADC measurements (water phantom as a sample). The b-value was varied in 8 steps from 8-750 sec/mm^2.

6.3.1.3 The Trace(D) sequence

The confounding effects of anisotropy complicate the interpretation of diffusion images, and a time efficient, EPI-based isotropic method for the measurement of the trace(D) (see Section 2.1.2) was therefore implemented on the 2.35T system. This technique described by Wong *et al.* was chosen (Wong, 1995) since it provides greater gradient efficiency than the alternative technique of Mori *et al.* (Mori, 1995). The authors carried out a numerical search of the parameter space for gradient schemes that eliminated the off-diagonal elements of the diffusion tensor while equalising the diagonal terms ($b_x = b_y = b_z$). The former condition is equivalent to the following condition

$$\int_0^{\tau} k_i(t')k_j(t')dt' = 0 \qquad \{i \neq j\} \qquad [6.4]$$

where k(t′) is the k-space trajectory and the diffusion gradients are applied over an interval $\{0,\tau\}$. Implementation of the single-shot technique was especially suited to the anisotropic gradient set of the 2.35T system (Wong, 1995). The gradient scheme for this situation is shown in Fig. 6.8. The gradient waveforms were applied both before and after the 180° refocusing pulse during the spin-echo preparation period.

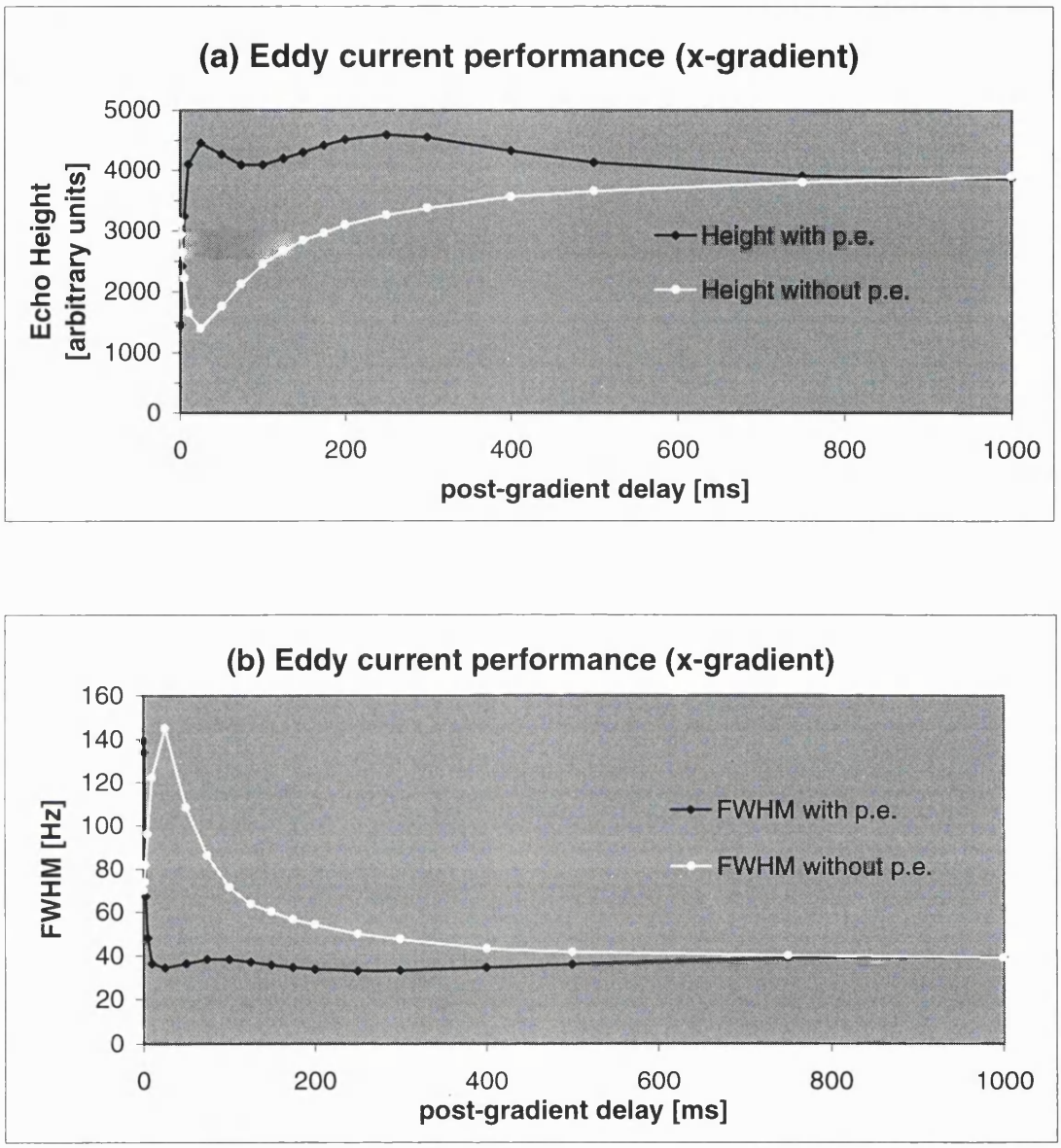

Fig. 6.7 The performance of the 2.35T system in the presence of eddy currents generated by a x-gradient pulse of duration 500 ms. The (a) height and the (b) FWHM of the ehoes are displayed with and without pre-emphasis (p.e.). It can be seen that pre-emphasis eliminates a great deal of the eddy current effect but a residual component remains.

Since the gradients schemes are self-contained and fully refocused, eddy current effects and background gradient cross-terms, should be minimised. The major disadvantage of this technique of isotropic diffusion-weighting is the lack of a well-defined diffusion time (Section 2.1.3) and the complex form of the gradient waveform complicates a complete description of the phase history of the spin system. When deciding the duration of the diffusion gradients, a balance has to be found between the increasing b-value and an associated increase in the echo time. On the 2.35T system, a b-value of 1187 sec/mm^2 was obtained with the maximal gradient strength in the read (x) direction and an echo time TE = 112 ms. The contribution of the imaging gradients to the b-value was calculated and was shown to be negligible.

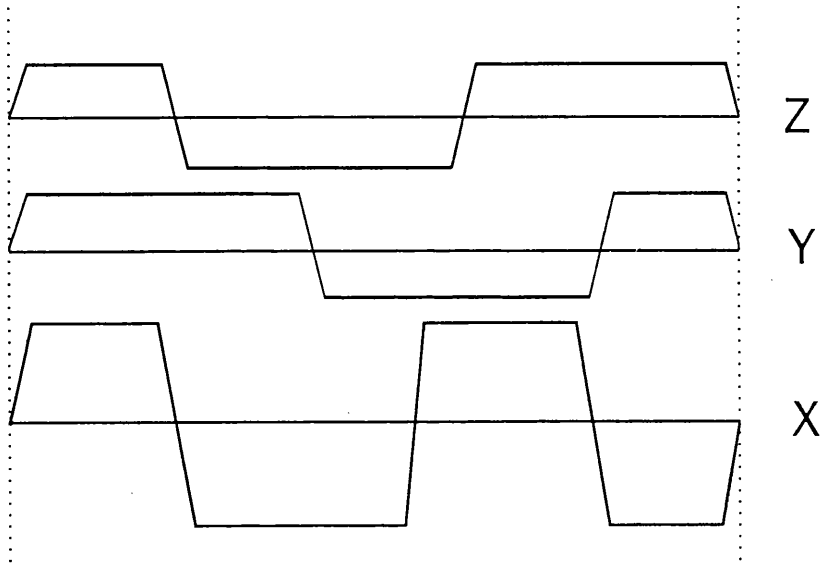

Fig. 6.8 Single-shot diffusion gradients (from Wong (1995), Figure 1(c) for anisotropic gradient sets). X, Y and Z represent the read, phase and slice directions respectively. The diffusion-weighting efficiency of the gradient scheme is 1.048 (in comparison with a single bipolar gradient pulse) of the same duration. The crossing points in order of appearance are 0.111, 0.394, 0.783, 0.217, 0.606, 0.889 and 0.5 in units of τ where τ is the total gradient duration and where gradient ramps are set as 0.024τ.

6.3.2 Optimisation of experimental parameters for the diffusion measurement

For clinical and in-vivo experimental studies, the accuracy and reproducibility of the diffusion measurements is crucial in being able to discern changes of tissue state.

Similarly, the reproducibility or precision is of great importance in a repeated time-course measurement. This objective translates to the minimisation of the coefficient of variation or the maximisation of the SNR of the resultant ADC maps. The aim of the following study was to thereby optimise the set-up parameters of the two-experiment diffusion experiment (i.e. images at two b-values). This was attempted in a theoretical framework and an experimental validation was also performed using the trace(D) sequence.

6.3.2.1 Theoretical optimisation

For the two-experiment scheme, n_1 experiments are carried out at $b=b_1$ in order to measure the diffusion-weighted signal, S_1, and $(n_{tot} - n_1)$ images are acquired at $b=b_0$ to measure the baseline signal, S_0, where n_{tot} is the total number of imaging experiments. The apparent diffusion coefficient, D, is given by a simple manipulation of Eq. [2.3] to provide the following expression

$$D = \frac{\ln S_1 - \ln S_0}{b} \qquad [6.5]$$

If the standard deviation, σ, due to random variation (noise) in an image with measured signal, S_i, then in the limit of large SNR, the standard deviation of $\ln S_i$ is approximately gaussian and of magnitude σ/I_i where $I_i = I'_0 \exp(-bD)$ is the *true* signal intensity. The I'_0 factor is determined by the T_1- and T_2-weighting of the sequence and is, therefore, related to the sequence parameters TE and TR, so that the following relationship applies

$$I'_0 = I_0 e^{-TE/T_2}\left(1 - e^{TR/T_1}\right) \qquad [6.6]$$

The expression for the standard deviation of the diffusion weighted images in the case of image averaging, is provided by the following general expression

$$\sigma_i = \frac{\sigma}{I'_0\sqrt{n_i}} e^{b_i D} \qquad \{i = 0,1\} \qquad [6.7]$$

where n_i is the number of averages at $b=b_i$ and the square-root factor is due to the linear relationship of noise and the number of averages. In MRI, the random noise will usually be independent of the signal. The variance in the ADC map, σ_D^2, can be calculated from

Eq. [6.5] and [6.7] by the propagation of errors (Bevington, 1969). This statistical method for error calculation is valid if the following conditions apply:

1. The SNR in the diffusion-weighted images is sufficiently high that higher order terms can be discarded
2. The error terms associated with the differently weighted images are not correlated, so that cross terms can be eliminated. This should be true for MRI.

With use of this technique, the following general expression for σ_D^2 for an n-point scheme can be obtained (Barlow, 1989)

$$Var(D) = \sigma_D^2 = \left[\sum_{i=0}^{n-1} \frac{x_i^2}{\sigma_i^2} - \frac{\left(\sum_{i=0}^{n-1} \frac{x_i}{\sigma_i^2} \right)^2}{\sum_{i=0}^{n-1} \frac{1}{\sigma_i^2}} \right]^{-1} \qquad [6.8]$$

In the simplest case of a 2-experiment scheme, Eq. [6.7] and [6.8] can be combined to provide the following expression

$$\sigma_D^2 = \frac{\sigma^2}{I_0'^2 (b_1 - b_0)^2} \left(\frac{e^{2b_0 D}}{\left(\frac{T}{TR} - n_1 \right)} + \frac{e^{2b_1 D}}{n_1} \right) \qquad [6.9]$$

where T is the total scan time so that n_{tot} = T/TR. For single averages of the two images ($n_0 = n_1 = 1$), the b_1 dependent terms in the above expression can be collected into a coefficient, $F(b_1 D)$ where

$$F(b_1 D) = \frac{1 + e^{2(b_1 - b_0)D}}{(b_1 - b_0)^2} \qquad [6.10]$$

such that $\sigma_D^2 = (\sigma^2 / I'^2_0).\exp(2b_0 D).[1/(T/TR - n_1) + (1/n_1)].F(B_1 D)$. This expression is depicted in Fig. 6.9 for typical parameter values and is minimised for $(b_1 - b_0)D \approx 1.11$.

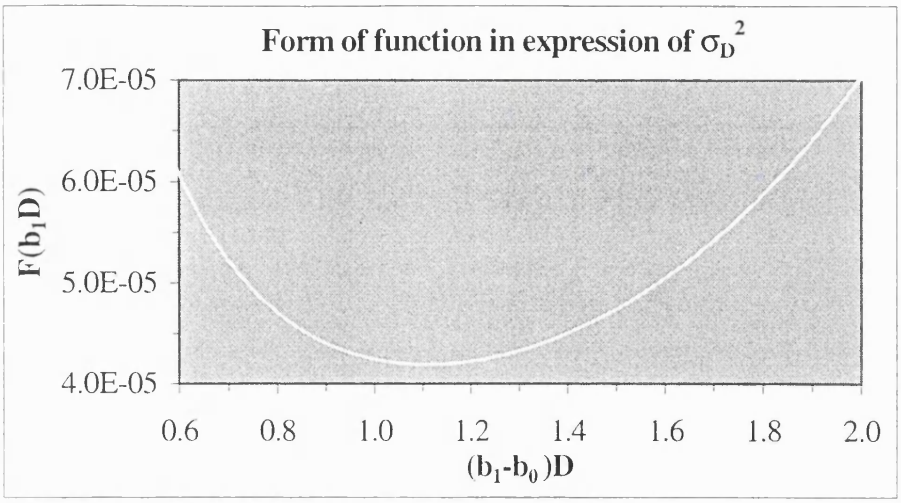

Fig. 6.9 Form of the b_1-dependent coefficients in the expression of the variance of the diffusion coefficient (Eq. [6.10]), plotted against the product, bD (for $D = 2.25\times10^{-3}$ mm^2/sec). It can be seen that the optimal combination of b and D is for a $bD \approx 1.11$.

The number of degrees of freedom of the optimisation was increased to three (b_1, n_1 and TR) for a fixed total scan time and non-diffusion-weighted baseline image (i.e. for $b_0 = 0$) and for a single, fixed diffusion coefficient. The optimisation with respect to the three free parameters was performed using an analytical minimisation algorithm on Eq. [6.9]. The *optimised* set-up parameters can be compared to the so-called *standard* experiment in which the parameters were chosen according to the following formula

- *n*: equal averages so that $n_0 = n_1$
- *b*: A b-value such that bD = 1.0 that has been shown to optimise diffusion discrimination sensitivity (Moran, 1984)
- *TR*: a choice of $TR = 2T_1$

The theoretical optimisation was performed for a fixed total scan time, T = 20 sec, and for typical imaging and NMR parameters for a doped water phantom, and for tissue GM and WM. Figure 6.10 shows representative 1D and 2D plots that depict the relationship of the variance of the ADC map with the three free parameters. A comparison of the values of σ_D^2 obtained with the optimised and standard schemes is listed in Table 6.2. It can be seen that the improvement attained when using the optimised scheme is approximately 33% in all cases.

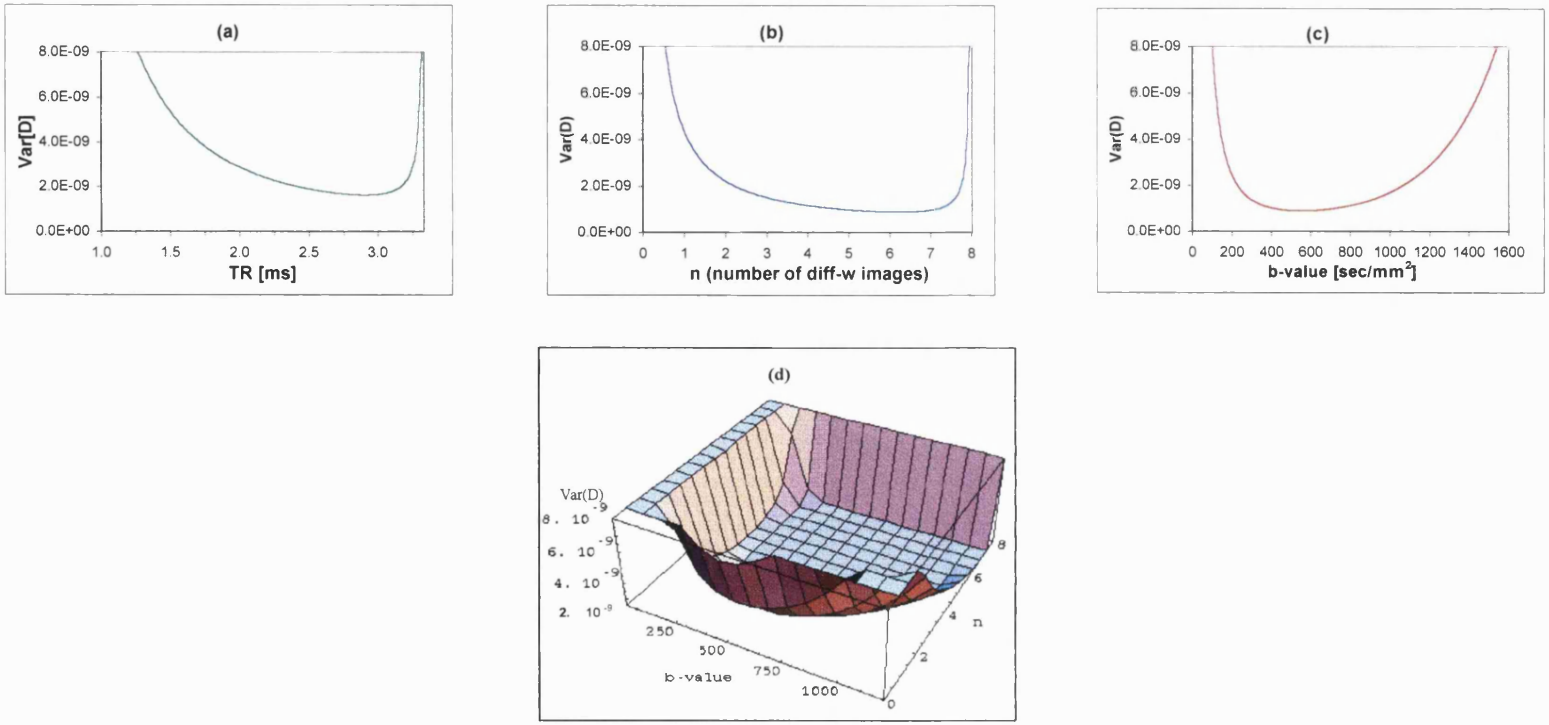

Fig. 6.10 Theoretical relationship of the variance of the diffusion coefficient, Var(D), from Eq. [6.9], with (a) the repetition time between the images, **TR**, (b) the number of diffusion-weighted images, **n**, and (c) the **b**-value for a $CuSO_4$ phantom. Fixed parameters are $T_1 = 2$ sec, $T_2 = 0.93$ sec, $D = 2.25 \times 10^{-3}$ mm^2/sec, an intrinsic SNR of 150:1 (in the b_0 image), and a fixed total scan time of 20 sec. The graphs are created by fixing two of the three free parameters at their optimal values. It can be seen that the relationship of Var(D) with n is relatively flat over the relevant range, but sharp profiles are observed with respect to b and TR. Units of Var(D) are mm^4/sec^2. Plot (d) shows a 2D surface representation of the relationship of Var(D) with b and n.

In the optimal choice of set-up parameters, the ratio of diffusion-weighted to non-weighted images (n_1/n_0) is approximately 3-4, and the product $b_1D \approx 1.3$. This latter figure can be compared to the minimisation of $F(b_1D)$ (Eq. [6.10]) for single equal averages which provided a figure of 1.11 and implies that this product is closely related to the parameter optimisation (Xing, 1997).

	Standard				optimised			
D [mm²/sec]	b_1	n_1 / n_0	TR	σ_D^2	b_1	n_1 / n_0	TR	σ_D^2
0.4×10^{-3} (WM)	2500	5 / 5	2.00	4.81×10^{-8}	3280	9 / 2	1.81	3.6×10^{-8}
0.8×10^{-3} (GM)	1250	5 / 5	2.00	4.48×10^{-8}	1575	10 / 3	1.54	3.4×10^{-8}
2.25×10^{-3} ($CuSO_4$)	444	3 / 3	3.33	1.21×10^{-11}	552	6 / 2	2.50	0.91×10^{-11}

Table 6.2 Comparison of *standard* and *optimised* experiment (with $b_0=0$) for a fixed scan time T = 20 sec and typical imaging and NMR parameters for tissue gray matter and white matter with non-isotropic diffusion-weighting and a copper sulphate ($CuSO_4$) phantom. Units of TR, b and σ_D^2 are sec, sec²/mm and mm⁴/sec² respectively. Minimisation is performed with the use of a computational algorithm.

6.3.2.2 Experimental validation

Experiments were performed with a $CuSO_4$ solution phantom (T_1 = 2 sec, T_2 = 0.93 sec) on the 2.35T system. Images were acquired using a volume transmitter coil of a slotted-tube design and a separate surface coil as the receiver. The 2-experiment single-shot sequence was implemented with the optimised and standard sequence parameters described in the previous section and the trace(D) calculated using Eq. [6.5]. The variance of the trace(D) maps was estimated by repetition of the experiment (n=350) and subsequent regional analysis (282 pixels). The theoretical and experimental results are shown in Table 6.3. A good agreement between theory and experiment was thereby found.

	standard	optimised
b [sec/mm^2]	448	552
n_1 / n_0	3 / 3	6 / 2
TR [sec]	3.33	2.50
Trace(D) [$\times 10^{-3}$ mm^2/sec]	2.265	2.286
σ_D^2 **(calculated)**	273	206
σ_D^2 **(experimental)**	268	210
lower σ_D^2 at 95%	227	177
higher σ_D^2 at 95%	313	245

Table 6.3 Experimental validation with a copper sulphate phantom. Comparison of optimised and standard experiments (n=350). The SNR (I'_0/σ in Eq. [6.7]) was determined from a pair of baseline images. T_1 and T_2 measurements were performed with EPI-based inversion recovery and spin-echo 2D-FT measurements at multiple echo times respectively. Units of σ_D^2 are mm^4/sec^2. These results were reported in (Pell, 1995).

6.3.3 Discussion

This study has presented a means to optimise the set-up parameters of rapid diffusion coefficient quantification. This method is easy to implement and the results of this study demonstrate the benefits of optimal experimental parameters for the 2-experiment scheme of trace(D) measurement. The precision in the value of the diffusion coefficient was described in terms of the variance in the resultant maps and a minimisation was performed with respect to the b-value, the number of weighted images and the repetition time. The accuracy as well as the precision is affected by the imaging scheme. The underestimation of ADCs has been shown to be improved in simulated data by a reduction in the number of different diffusion-weighted images (Eis, 1995). The precision can be increased by signal averaging. A reduction in the repetition time allows this but the increased SNR as a result of signal averaging must be balanced against the reduction in SNR due to the additional T_1-weighting. The optimisation of the b-value is equivalent to sampling in a highly sensitive area of the b-value domain. In the absence of noise, the optimal b-value would be the highest achievable with the available gradient

strength. However, noise is a significant factor in MRI and an appropriate value must, therefore, be chosen that balances the diffusion sensitivity in the image with the resultant SNR.

The results of this study demonstrate the time efficient use of multiple averaging of the diffusion-weighted image at the expense of the baseline image (b_0=0) which possesses a larger inherent SNR. The optimal theoretical b-value scheme for the $CuSO_4$ phantom provides a single-averaged diffusion-weighted image with a SNR that is approximately 30% of the baseline image ($\exp(-b_1D)$) (i.e. in the case of $n_0=n_1=1$). The SNR in the resultant trace(D) image, SNR_D, can be calculated by manipulation of Eq. [6.9] ($SNR_D = D/\sigma_D$) and is approximately 33% of the baseline image. The acquisition of a diffusion-weighted map instead of the interpretation of the diffusion-weighted image, does not, therefore, impair the available SNR.

The optimisation scheme that is described here has been performed for a sample with a known, single, homogeneous value of the ADC. A 2-experiment scheme and a baseline image with b_0=0 are, therefore, natural choices. By extension of Eq. [6.8] to n=3 experiments, it can be shown that multiple experiments will never improve the reproducibility in this situation. This assertion presupposes a linear relationship between $\ln S_i$ and the b-values; if multiexponential behaviour is expected, accurate quantification of the ADC will necessitates multiple experiment and multiexponential fitting. Another study has, however, suggested that 3-experiment schemes are advisable in spite of the resultant reduction in the precision on account of possible random, non-stochastic errors such as those due to motion or hardware imperfections (Eis, 1995).

In the more realistic situation of a sample with a range of unknown diffusion coefficients, the analysis of Eq. [6.8] becomes very complex. A more sophisticated treatment involving the Cramér-Rao theory of lower bounds (van den Bos, 1982) can be used to determine the optimal set-up parameters in this situation, and this theory has been applied to quantitative T_2 relaxometry (Jones, 1996). The graphs in Fig. 6.9 and 6.10 demonstrate that the sensitivity of the optimal response is relatively flat over a range close to turning point of the profiles. In a recent report, it has been proposed that a b-value should be chosen that sensitises the error response of the 2-experiment scheme to the range of ADC values to be measured (Xing, 1997). An interval can be constructed that is related to the combination of b and D values over which a sensitivity response is

achieved that is within specified bounds of the turning point. In this manner, Xing *et al.* describe an optimal 2-experiment scheme for quantitative ADC measurements in the human brain in which the baseline image is slightly diffusion-weighted (b=300 sec/mm^2) in order to reduce contamination from CSF due to the effects of partial volume.

VII The Measurement of the Diffusion Trace and T_2-weighted Signal Intensity in a Study of Repeated Ischaemic Insults

The technique of single-shot trace(D) imaging (see Section 6.3) was implemented in a study of the effects of repeated ischaemia in an animal model. Repetitive ischaemia was induced in both rat and gerbil models of ischaemia and the diffusion coefficient and T_2-weighted signal acquired with a high time resolution. After a discussion of the motivation for such a study, the chapter describes firstly the rat 4-vessel model and secondly, the gerbil 2-vessel model. The trace(D) data are discussed in the light of previous high time-resolution studies of diffusion changes during ischaemia. The T_2-weighted data are then described and the cumulative trends observed in this data are placed in the context of previous studies of repeated ischaemic events.

7.1 Introduction

7.1.1 Transient Ischaemic Attacks (TIAs)

Stroke is a cerebrovascular accident and is usually manifested as a single clinical, ischaemic event of a certain duration and representing either a focal or global phenomenon. The insult is either followed by reperfusion of the effected area, for example, subsequent to resuscitation from cardiac arrest, or, in the case of focal cerebral ischaemia, by maintenance of the occluded state. Transient ischaemic attacks (TIAs) are another common manifestation of clinical stroke. These cause reversible, focal, neurological deficits, lasting from minutes to 24 hours. TIAs are believed to precede the development of brain infarction and, therefore, to increase the risk of the subsequent occurrence of a stroke. The incidence of TIAs is believed to be one in a 1000 per year in the elderly. The attacks can recur but the number suffered by individual patients is variable. One third of patients suffer a single attack but most have between 2 and 10 successive attacks (Russell, 1983). The aetiology of these multiple repetitive ischaemic insults is unknown.

7.1.2 Other motivations for study of repeated ischaemia

A clinical necessity for repeatedly occluding the cerebral arteries presents itself during surgical procedures such as the treatment of cerebral aneurysms (the dilation of the blood vessel due to local faults in the vessel wall caused by disease or injury). During neurosurgery, a temporary occlusion of the cerebral artery is an important tactic in the

control of bleeding or in order to facilitate dissection during operations for conditions such as aneurysms, vascular malformations and highly vascularised tumours (Kimura, 1996). Similarly, some pathological conditions encountered in neonates such as apnea and blood pressure instability have a propensity to be recurrent occurrences (Laptook, 1988).

Previous investigations of the effects of repeated ischaemia in animal models have revealed a possible cumulative injurious consequence. Tomida *et al.* found that 3 periods of 5 min ischaemia separated by delays of an hour had a more damaging effect than one ischaemic episode of 15 min duration (Tomida, 1987). This was hypothesised to be a result of secondary injurious events of morphological or biochemical origin. However, the precise mechanism of the adverse effects of repetitive ischaemia is not well understood.

The aim of this study was to expand on the study of repeated ischaemia in order to further investigate this clinically important pathophysiological syndrome with the use of MRI techniques. The combination of diffusion-weighted and T_2-weighted imaging techniques that were employed in this study offer the ability to detect subtle changes in tissue energy status and blood oxygenation with the high temporal and spatial resolution of MRI. Evidence was sought for any MR visible pathological consequences of the repeated ischaemic events and especially for signs of a progressive effect.

7.2 Material and Methods

7.2.1 Study of trace(D) changes on repeated ischaemia : Animal methods

Two models of ischaemia were employed in this study – total forebrain ischaemia in the gerbil and complete ischaemia in the rat. In man and most animals, the main cerebral and vertebral arteries supply the majority of the blood supply to the brain and the Circle of Willis connects these two principal systems (see Section 2.2.3, Fig. 2.4(a)). In the gerbil, a unique anatomy is found at the base of the brain and there is a lack of significant anastomoses connecting the basilar-vertebral and the carotid supplies (Levine, 1966) (Fig. 2.4(b)). Bilateral common carotid artery occlusion therefore induces virtually complete forebrain ischaemia. The gerbil is a convenient model for the

study of the repeated ischaemia due to the relative simplicity of the surgical procedure (for example, Tomida, 1987; Kato, 1989; Widmann, 1992).

In order to induce global ischaemia in the rat it is necessary to cut off the supply from the vertebro-basilar system since the Circle of Willis is complete, as is the case in humans. A four-vessel occlusion model was implemented in order to induce global ischaemia in Wistar rats (n=4, 100-200 g) (Pulsinelli, 1979). The vertebral arteries were electro-cauterised at the site of the first cervical vertebrae. Anaesthesia induced with 2% halothane and maintained at a level of 1.2 % halothane and 0.4 l/min oxygen. In addition to the 4-vessel study, incomplete ischaemia was induced by occluding the common carotid arteries in the rat without obstructing the flow from the blood supply from the hindbrain (2-vessel rat model, n=1).

Mongolian, adult gerbils (n=5; 60-70g) were used in this study of total forebrain ischaemia (2-vessel model). Anaesthesia was induced with 2% halothane and maintained at a level of 1.2 % halothane, 0.4 l/min oxygen and 0.6 l/min nitrous oxide.

In the two-vessel gerbil and rat models and the four-vessel rat models, the animals were placed into a stereotaxic frame and ear bars were inserted in order to reduce the effects of motion, since diffusion imaging is especially sensitive to such artefacts. The common carotid arteries were visualised with an operating microscope. The arteries were surgically exposed and exposed bilaterally via a ventral mid-cervical incision. Nylon snares were placed around both arteries and attached to individually controlled manual screw system in order to allow remote bilateral occlusion with the animal within the magnet. A rectal thermometer recorded the body temperature which was maintained at 37-38°C by blowing warm air into the magnet bore. The animals were allowed to breathe spontaneously and the respiratory rate and ECG were monitored.

7.2.2 NMR Methods

All experiments were carried out on a 2.35T magnet interfaced to a SMIS console. Details of the asymmetric gradient set and the decoupled transmitter and receiver RF coil set-up are described in Section 4.4. A 2D-FT spin-echo sequence was employed for reproducible positioning of the animal within the magnet. Trace(D) measurements were

obtained with a 1 min time resolution using the isotropically-weighted EPI sequence described in Section 6.3 (TE = 112 ms; TR = 1000 ms; b = 0 & 1187 sec/mm^2; number of averages [NEX] = 30 for each b-value). The optimal scheme according to the analysis described in Section 6.3.2 would have been to use approximately 4 times as many averages for the diffusion-weighted image as for the non-weighted image (providing a scheme with TR = 1540 ms, b = 0 & 1575 sec/mm^2, NEX(b=1575) = 30, NEX(b=0) = 9, see Table 6.2). However, the maximal gradient strength of the system limited the maximum achievable b-value, and, more significantly, it was not possible implement a sequence with unequal number of averages within cycled experiments due to current limitations in the pulse programming software. This problem is currently being investigated, and planned further experiments with this model will aim to use the optimal averaging scheme in order to reduce the coefficient of variation of the data.

Images were obtained in the coronal plane (slth = 2.3 mm; image matrix size = 64×128; field of view = 27.5×55 mm). A two b-value scheme was employed in this study. Multi-exponential behaviour of the different tissue components such as white matter (WM) and grey matter (GM) (Pierpaoli, 1996) will not be reflected in the direction-independent trace(D) measurement. Partial volume effects from the CSF compartment would be expected to increase the measured trace(D) value. However, care was taken to position the regions of interest (ROIs) away from the location of the CSF-containing ventricles and no evidence of an overestimation was found.

7.2.3 Experimental protocol

The experimental protocol consisted of a 20 min control period of trace(D) imaging. Ischaemia was then initiated by tightening the snares and the occlusion was maintained for 10 min. The snares were then opened in order to allow reperfusion for a duration of 30 min. This cycle of 10 min occlusion and 30 min recirculation was repeated up to 4 times. The animal was then sacrificed by exposure to a high concentration of halothane. Trace(D) imaging continued throughout the course of the experiment.

7.2.4 Image and Data Analysis

Four regions of interest (ROIs) were drawn on the trace-weighted (b=1187 sec/mm^2) and non-weighted (b=0 sec/mm^2, here-on denoted as **b0** data) images in the left and the

right cerebral hemispheres of the slice, in both the cortex and the corpus striatum. The regional data were imported into an Excel Spreadsheet and the trace(D) values were calculated according to Eq. [2.3]. Temporal profiles of the trace(D) data and the non-weighted data were created. The non-weighted data are heavily T_2-weighted (T_2 [Grey matter] $\approx$ 65 ms; TE = 112 ms) and, therefore, may reflect local changes in the concentration of deoxyhaemoglobin. Maps of the trace of the diffusion tensor were created by importing the data into IDL (Floating Point Systems, Boulder, Colorado, USA). All values are presented as mean $\pm$ standard error in the mean (SEM). A P-value of <0.05 was considered to indicate statistical significance.

In order to characterise the time response of the trace(D) and the **b0** data, exponential models of decay and recovery were fitted to the data of the form $f(t) = A\exp(-\beta_1 t)$ and $f(t)=A[1-\exp((-\beta_2 t)]$ respectively. Analysis of variance (ANOVA) and t-tests were employed to test for regional differences between group and time responses.

7.2.5 Study of CBF during repeated ischaemia

In a separate study, the time course of cerebral blood flow during the series of 2-vessel occlusions in the gerbil was investigated (n=1). Changes in the diffusion coefficient are thought to be closely related to compromised levels of CBF (Moseley, 1990; Busza, 1992). The purpose of this study was, therefore, to elucidate the physiological changes that occur during the repeated ischaemic events. The technique of FAIR imaging was employed without the acquisition of prior inversion recovery data and, therefore, only qualitative flow information could be obtained from the perfusion subtractions (non-selective image subtracted from the selective image). The animal protocol was the same as previously described for the trace(D) study but with only 3 periods of 10 min occlusion. FAIR images were acquired continuously throughout the experiment with a time resolution of 2 minutes. The animal was then sacrificed with halothane. A gradient-echo EPI sequence rather than a spin-echo implementation was employed (TE = 38 ms) and the pre-saturation pulses were not employed in the sequence so as to increase the SNR of the perfusion subtractions (see Chapter 4). Other changes in the parameters compared to the previously described work with FAIR were TI = 1200 ms, τ = 1200 ms and NEX = 25.

7.2.6 Study of T_2 measurements during repeated ischaemia

The **b0** time course obtained during the acquisition of the trace(D), was used in this investigation to obtain a qualitative understanding of the blood flow and oxygenation changes that occur during repeated ischaemia (see Results). An assumption is thereby made that the **b0** data set is principally T_2-weighted. The validity of this assumption was examined in a separate investigation by obtaining quantitative T_2 measurements during the experimental protocol (n=3). In one of these studies, a 2D-FT sequence at two echo times was employed in order to measure T_2 (TE = 30 ms, 110 ms; number of slices = 2) (n=1; gerbil), while in the other studies, a spin-echo EPI sequence was employed (TE = 35 ms, 110 ms) (n=2; rat). The animal protocol was the same as previously described for the trace(D) study but in the EPI experiments, a reduced occlusion period of 6 min was employed. The relationship of the signal in two spin-echo images obtained at TE = TE_1 and TE_2 (where $TE_2 > TE_1$), denoted $S(TE_1)$ and $S(TE_2)$ respectively, is as follows

$$T_2 = -\frac{TE_2 - TE_1}{\ln[S(TE_2)/S(TE_1)]} \qquad [7.1]$$

7.3 Results

The trace(D) and **b0** data obtained from the 4-vessel occlusion model are displayed in that order, and followed by the results of the gerbil study. The qualitative flow and absolute T_2 measurements are then described.

7.3.1 The four-vessel occlusion model in the rat (n=4)

A variable response to the repeated ischaemic insults was found in the study of 4 animals. The variability in the model was likely caused by inter-animal and inter-experimental differences such as metabolic variations and differences in the induction of ischaemia and reperfusion. A delayed response was often observed in which the trace(D) did not drop during the initial occlusion phases. During the first animal study, the quality of the trace(D) data were adversely affected by motion artefacts. This was especially evident at the time of the occlusion and resulted in high, anomalous trace(D) values. In subsequent animals, care was taken to ensure improved restraining.

The **b0** data showed a very different and more repeatable behaviour on occlusion and reperfusion. Initially, a significant drop in the signal intensity occurred which began to

slowly recover during the 10 min of occlusion. On initiation of recirculation, the signal intensity immediately rose to a value that was significantly higher than the control level. This peak response was followed by a decline in the signal intensity until the start of the subsequent ischaemic insult. The recovery in the signal intensity during the occlusion and the changes in the signal intensity during the peak response on reperfusion both occurred in an apparent exponential pattern. In all but one of the animals, this pattern was repeated with each occlusion-reperfusion phase. An obvious trend in the data became apparent with each phase displaying an overall increase in signal intensity.

The generalised behaviour of each animal to the repeated ischaemic insults in the 4-vessel model are summarised in Table 7.1.

Animal	Notes	Non-weighted (b0) data pattern	Trace(D) data pattern
Animal 1		General increasing trend observed on each phase of occlusion-reperfusion.	Effects of motion artefacts especially apparent as excessive trace(D) values measured during occlusion.
Animal 2	Animal died during the 3rd occlusion	Anomalous decreasing trend observed in the non-weighted data both with regard to the peak response and the pre-occlusion level for each phase.	Trace(D) decline observed on first ischaemic insult. Typical pattern (i.e. decline followed by recovery on occlusion and reperfusion) repeated until 3rd occlusion when animal died.
Animal 3		General increasing trend observed during the 4 occlusion-reperfusion phases.	During first ischaemic insult, the trace(D) declined in all regions except for the right striatum. During subsequent phases, typical response observed.
Animal 4		Increasing trend observed. Peak response was attenuated in the ROIs in the right hemisphere during the 2 initial phases.	Typical response observed in the left hemisphere. In the contralateral hemisphere, delayed response observed and no change in trace(D) on occlusion during the first 2 phases.

Table 7.1 Summary of responses observed during 4-vessel occlusion studies in the rat

7.3.1.1 Trace(D) data

This and subsequent results sections describe, in turn, the data acquired during the phases of occlusion, reperfusion and sacrifice. Figure 7.1 displays a series of representative trace(D) maps obtained during the course of one occlusion/reperfusion phase.

The trace(D) values obtained during the control phase were 0.782±0.003 and 0.771±0.002 ($\times 10^{-3}$) mm^2/sec in the cortical and striatal regions respectively. No significant difference was found between these pre-ischaemic, regional values (paired t-test). In the subsequent analysis, phases that showed no trace(D) decline (a delayed response) during an occlusion were excluded from the analysis of the mean occlusion/reperfusion temporal profiles. On occlusion, in the absence of any delayed response, the trace(D) value rapidly fell in an apparently mono-exponential fashion. The first trace(D) measurement was obtained at 1 min post-occlusion. The trace(D) values at this time were 0.717±0.005 and 0.741±0.012 ($\times 10^{-3}$) mm^2/sec in the cortical and striatal regions respectively. By the second time point (2 min), the mean values were 0.703±0.021 and 0.695±0.03 ($\times 10^{-3}$) mm^2/sec. On examination of the individual trace(D) patterns observed during each ischaemic phase on an animal-by-animal basis, the trace(D) became significantly different from the pre-occlusion level (reduced by > 2SD) by the first time point (1 min) in 35% of all cases and by the second time point (2 min) in 30% of cases.

By approximately 5 min, the trace(D) values had levelled off at a constant value and at 10 min of occlusion, the trace(D) values had reached a level of 0.603±0.05 and 0.605±0.04 ($\times 10^{-3}$) mm^2/sec in the cortex and striatum respectively. These values represent levels that are 77% and 78% respectively of the pre-occlusion values. Percentage minimum levels on occlusion in individual animals varied between 68% and 87% of the control values but did not greatly vary within the same subject. The mean minimal level reached during each successive occlusion phase were: 0.607±0.047, 0.634±0.045, 0.587±0.046 and 0.602±0.044 ($\times 10^{-3}$) mm^2/sec in the cortex, and 0.628±0.048, 0.629±0.038, 0.601±0.047 and 0.602±0.047 ($\times 10^{-3}$) mm^2/sec in the striatum. The average slope of these values with time over all the animals was 3.1±2.2 ($\times 10^{-7}$) [mm^2/sec/min] in the cortex and –3.4±3.1 ($\times 10^{-7}$) [mm^2/sec/min] in the striatum.

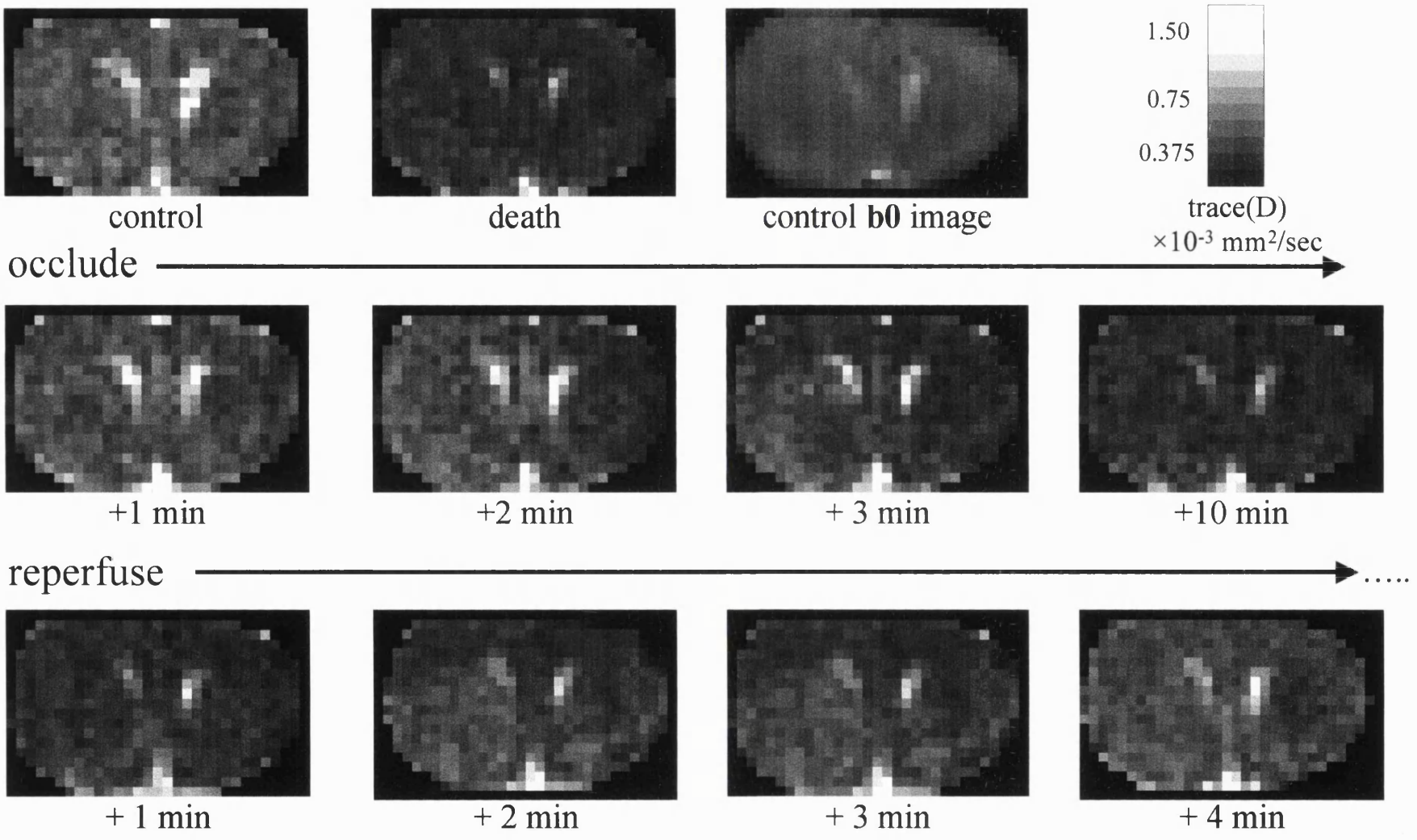

Fig. 7.1 Representative trace(D) maps during one of the occlusion/reperfusion phases in the rat model (Animal 4). Control and post-sacrifice maps and a representative **b0** image are also displayed.

These average values are not significantly different from zero. Figure 7.2(a) shows a plot of the mean trace(D) behaviour.

On reperfusion, the trace(D) recovered in an apparent exponential fashion and by approximately 5 min had reached a plateau level. Since the behaviour of the non-diffusion-weighted, **b0** data on reperfusion suggested a cumulative effect (see Section 7.3.1.2), the trace(D) data during this period was investigated for evidence of similar behaviour. The mean plateau level (taken as the average value of the last 15 min of trace(D) values) reached during each successive reperfusion phases were: 0.805±0.006, 0.781±0.003, 0.770±0.002 and 0.763±0.003 ($\times 10^{-3}$) mm^2/sec in the cortex, and 0.796±0.003, 0.770±0.003, 0.755±0.003 and 0.757±0.002 ($\times 10^{-3}$) mm^2/sec in the striatum. In order to examine the statistical significance of the trend in the recovery trace(D) values, linear regression was performed on the plateau levels in each experiment. A significant negative trend was only found in the cortical region of one animal (Animal 3, cortical region, slope = -0.28±0.09 ($\times 10^{-7}$) $[mm^2/sec]\ min^{-1}$; P=0.05). The mean response over all the animals provided a slope of -0.04±0.1 ($\times 10^{-7}$) $[mm^2/sec]\ min^{-1}$ in the cortex and -0.12±0.1 ($\times 10^{-7}$) $[mm^2/sec]\ min^{-1}$ in the striatum and these values are not significantly different from zero or to each other (P=0.76 and P=0.35 in the two regions). Inspection of Fig. 7.2(a) reveals that the mean recovery level at the end of the first phase reaches a noticeably higher level during the first occlusion/reperfusion phase in comparison with the level reached during the successive phases. This observation is partly due to the bias in the mean response from the first animal in the study which displayed higher trace(D) values as a result of the adverse effects of motion.

In one study, an apparent transient overshoot of the trace(D) was observed on reperfusion in both cortical and striatal regions during all but the last phase of the experiment. Approximately 4 min after initiation of recirculation, the trace(D) had recovered to the pre-occlusion level and then began to rise above this value, reaching a peak that constituted approximately 107% of the initial level. By approximately 15 min post-reperfusion, the trace(D) had fallen to the pre-occlusion level. Figure 7.3 displays this trace(D) data set. A very high signal-to-noise level was obtained for the measurements in this study and this factor might have contributed to this hyper-response being clearly observed.

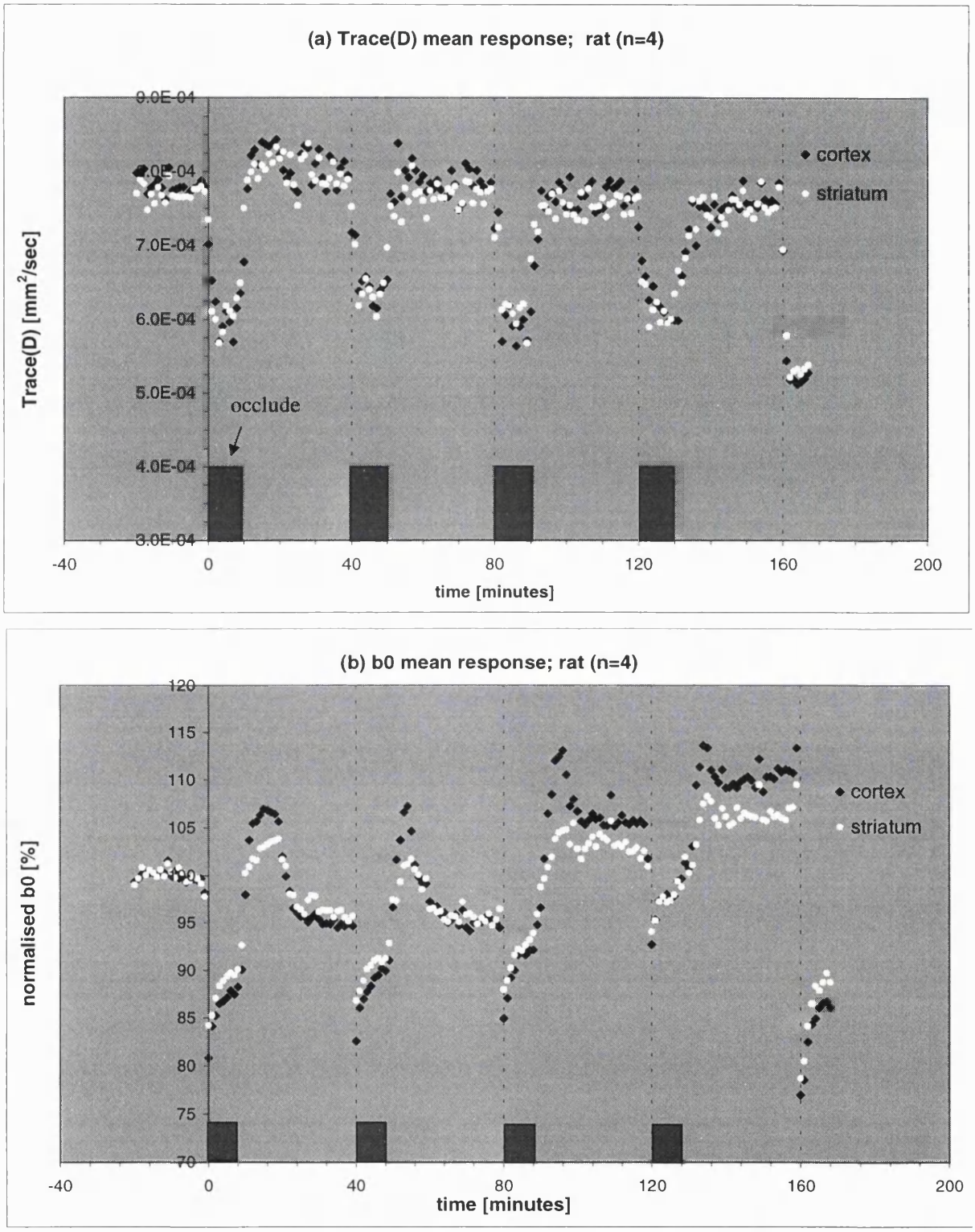

Fig. 7.2 Mean response of the (a) trace(D) and (b) T_2-weighted (**b0**) signal, the in the cortical and striatal regions in the rat 4-vessel occlusion model. Note the rising trend in the **b0** data. Time=0 is the time of the first occlusion. The thick, vertical bars indicate the occlusion phases. At the termination of the experiment, the animal was sacrificed.

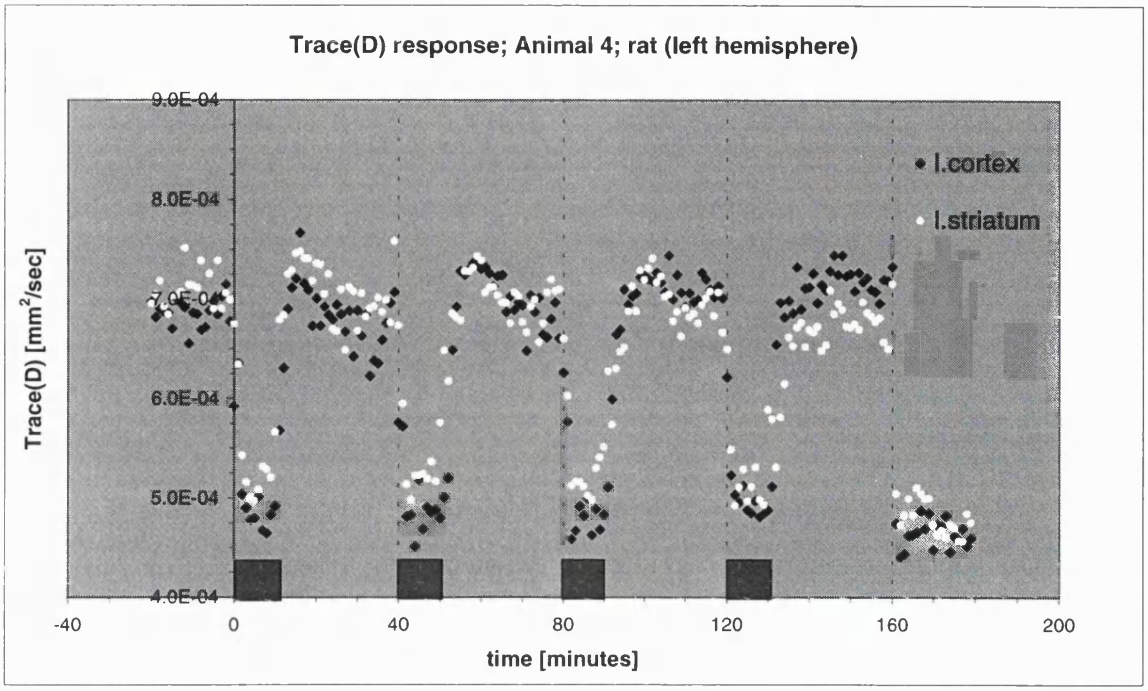

Fig. 7.3 Trace(D) from Animal 4, showing a transient overshoot on reperfusion during the first three phases.

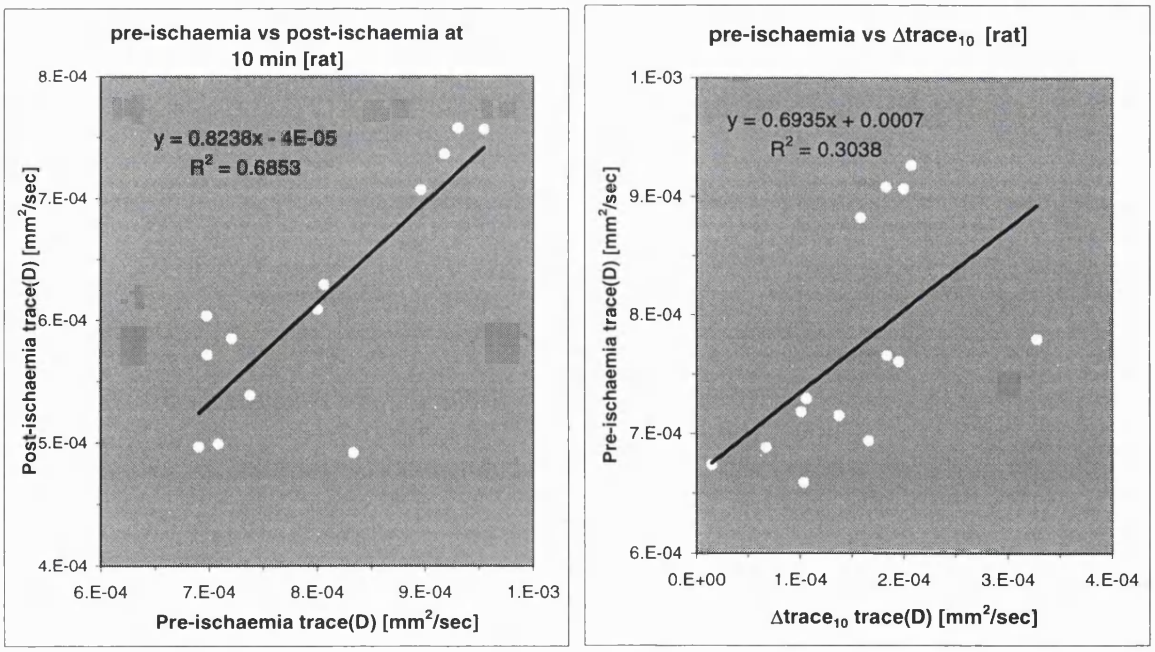

Fig. 7.4 Relationships of pre- and post-ischaemic trace(D) values that displayed a significant correlation. The equations of the fitted regression lines and the corresponding correlation coefficients, R^2, are shown.

Upon sacrifice of the animal by halothane inhalation at the end of the experiment, the immediate decline of the trace(D) followed a similar exponential pattern to the observations during the occlusion phases. The first measurements obtained at 1 min during this procedure were 0.694±0.032 and 0.694±0.036 ($\times 10^{-3}$) mm^2/sec in the cortex and striatum respectively, and by 2 min, the values were 0.545±0.034 and 0.578±0.044 ($\times 10^{-3}$) mm^2/sec. The trace(D) became significantly different from the pre-occlusion level (reduced by > 2SD) by the first minute in 25% of phases and by the second minute in 75% of phases. By 10 min, the trace(D) values had reached levels of 0.523±0.032 and 0.532±0.02 ($\times 10^{-3}$) mm^2/sec in the cortex and striatum respectively. These values represent 67% and 69% of the control level.

On comparing trace(D) values obtained on sacrificing the animal to those obtained during the occlusion phases of the experiment, no significant difference was found between the trace(D) values at 10 min post-occlusion and post-sacrifice. A significant difference was found between the magnitude of the trace(D) change from 0-10 min post-occlusion (denoted $\Delta trace(D)_{10}$) and the same interval post-sacrifice, (P=0.02, paired t-test, cortical and striatal values pooled). A significant correlation was found between the control trace(D) values and the $\Delta trace(D)_{10}$ post-sacrifice (P=0.05, cortical and striatal values pooled) and between the control trace(D) and the terminal value reached 10 min post-sacrifice (P=0.03, cortical and striatal values pooled).

In order to examine the relationship between the pre- and post-ischaemic levels of the trace(D) values, the data were analysed for these correlations (scatter-plots shown in Fig. 7.4). A significant correlation was found between the pre-ischaemic and post-ischaemic (at 10 min) trace(D) values (P<0.001, linear regression, cortical and striatal values pooled) and between the pre- and post-ischaemic $\Delta trace(D)_{10}$ values (P=0.03, cortical and striatal values pooled). This would imply that the variation during the control phase is not of purely physiological origin since one would then have expected the control values to be closely related to the magnitude of the drop on occlusion but not related to the terminal value reached on occlusion. It is also unlikely that the variability in the trace(D) values is due to only stochastic processes since the measurements are correlated. A combination of all these factors is therefore the most likely cause of the baseline variation. Pierpaoli *et al.* (Pierpaoli, 1996) used a similar analysis in a study of

occlusion in a cat model and found no correlation between the initial trace(D) values and $\Delta trace(D)_{10}$.

Time constant analysis : In order to examine the time course of the rapidly changing trace(D) values during the occlusion and reperfusion phases, mono-exponential models were fitted to the data (see Image and Data Analysis). This was carried out on an animal-by-animal basis and only for regions that showed an apparent drop on occlusion. The exponential decay on occlusion is characterised by the time constant, β_1, and the exponential recovery on reperfusion, by the time constant, β_2. The values for these time constants are summarised in Table 7.2.

[min^{-1}]	**Phase 1**	**Phase 2**	**Phase 3**	**Phase 4**	**Death**
β_1 (cortex)	2.3±0.9	0.8±0.4	1.9±0.6	2.1±0.7	1.6±0.2
β_1 (striatum)	2.7±1.2	1.5±0.7	1.8±0.5	2.7±0.6	1.8±0.2
β_2 (cortex)	3.4±1.5	5.5±1.4	2.2±1.2	5.2±1.2	N/A
β_2 (striatum)	3.7±2.3	7.1±4.2	2.7±1.8	2.2±1.4	N/A

Table 7.2 Mean values for the time constants, β_1 and β_2, obtained by fitting the occlusion and reperfusion phases respectively to simple mono-exponential models. Units of these time constants are given in [min^{-1}]. Individual phases that did not drop on occlusion were not included in this analysis and some phases with noise-affected values could not be fitted and, therefore, were also excluded. N/A denotes a non-applicable category.

The average occlusion decay constant, β_1, obtained in the cortex was less than the value obtained in the striatum and the values of the coefficients on death were lower than during the four phases of occlusion and reperfusion (1.8±1.2 min^{-1} and 2.2±1.3 min^{-1} in cortex and striatum respectively during the four phases; 1.6±0.4 min^{-1} and 1.9±0.5 min^{-1} on death). These differences, however, did not achieve statistical significance. For both

of the time constants, no significant difference was found between the successive phases and between regions (ANOVA test).

*7.3.1.2 The **b0** data*

During the first ischaemic insult, an immediate drop in the signal intensity of the non-diffusion-weighted image was observed that represented 20±4% and 15±4% of the pre-ischaemic, control levels in the cortex and striatum respectively but these values are not significantly different from each other (paired t-test). The signal then recovered in an apparent exponential pattern. On reperfusion, a peak response was observed. This peak was 10±2% and 6±3% higher then the control levels in the two regions (and these values are not significantly different), and occurred at 5.0±1.4 and 6.5±1.6 min post-reperfusion. The signal intensity then declined to a value that was significantly lower than the control level in the cortex (94±1% and 97±1% of the control level in the cortex and striatum; P=0.03 and 0.053 respectively, t-test). These values are significantly different from each other (paired t-test; P=0.003).

During subsequent phases, this pattern was repeated (see Table 7.3) with a general increasing trend in the plateau level on reperfusion becoming apparent in 3 out of the 4 animals. In one study, a decreasing trend was observed in the **b0** data. This animal died before the completion of the 4 phase cycle of occlusion/reperfusion. Figure 7.2(b) shows the mean **b0** response.

On sacrificing the animal, the immediate drop in signal intensity (28±14% and 24±12% of the control level in the cortex and striatum respectively) was significantly greater than the fall observed on occlusion (P=0.03 and P=0.02 in the two regions respectively, t-test). The signal then rose in an apparent mono-exponential manner and by 10 min post-sacrifice had reached a level that was 92±15% and 89±14% of the control level in the cortex and striatum respectively.

	Drop (% change w.r.t. control)		**Peak** (% change w.r.t. control)		**Reperfusion plateau level** (% of control)	
	cortex	striatum	cortex	striatum	cortex	striatum
Phase 1	-20±4	-15±4	+10±2	+6±3	94±1 *	97±1 *
Phase 2	-12±2	-9±2	+5±8	+6±4	95±2 *	96±2 *
Phase 3	-11±1	-8±1	+20±2	+11±3	108±3 *	105±2 *
Phase 4	-15±2	-9±1	+24±2	+16±2	114±3 *	110±3 *
Death	-28±14	-25±12	N/A	N/A	N/A	N/A

Table 7.3 Summary of responses in the unweighted (**b0**) data of the 4-vessel occlusion model (n=4). N/A denotes a non-applicable position in the table ; w.r.t. denotes "with respect to". The control level is the pre-ischaemic level of signal intensity. * indicates that the reperfusion plateau level is significantly different from the control level.

In order to examine the statistical significance of the apparent increasing trend in the **b0** data, linear regressions were performed on data from each region in the animals. One animal displayed an anomalous decreasing trend and died before the completion of the experiment. A significant positive slope was found in 3 out of the 4 animals in the cortex (P=0.01, 0.03 and 0.02 for the regions with a positive slope) and in 2 out of the 4 animals in the striatum (P=0.04, 0.02 and 0.08 for the regions with a positive slope). The mean values of the slope were 0.13±0.03 [%/min] and 0.05±0.05 [%/min] in the cortex and striatum respectively. The slope in the cortical region is significantly different from zero (P=0.03). The slope of the mean response (this response is averaged over all the animals and plotted in Fig. 7.2(b)) was similarly significant in the cortex and reached a level close to significance in the striatum (P=0.068 and P=0.05 in the cortical and striatal regions respectively). No correlation was found between the slopes of **b0** trend on reperfusion described here and those values obtained for the trace(D) trend on occlusion (see previous section).

Time constant analysis : In order to characterise the time course of the recovering signal intensity changes after the initial drop immediately on occlusion, a mono-exponential recovery model was fitted to the data (see Image and Data Analysis). This was carried out on an animal-by-animal basis. The exponential recovery on reperfusion is characterised by the time constant, β_2. The mean values of β_2 during the occlusion

phases were 2.9±0.4 min^{-1} in the cortex and 2.6±0.4 min^{-1} in the striatum. On sacrificing the animal, the recovery in the signal intensity provided values for β_2 of 1.7±0.2 min^{-1} and 1.9±0.3 min^{-1} in the two regions. No significant difference was found between these values obtained during occlusion and death.

7.3.2 The two-vessel occlusion model in the rat (n=1)

Incomplete forebrain ischaemia is induced by bilateral occlusion of the carotid arteries without manipulation of the vertebral circulation. The trace(D) did not drop during the occlusion phases but the **b0** data showed the same increasing trend as had been observed in the 4-vessel complete occlusion model. This slope was significant in the cortical region and reached a level close to significance in the striatum; the slope and P-values were 0.03±0.01 [%/min] (P=0.011) and 0.07±0.02 [%/min] (P=0.06) in the cortex and striatum respectively. The 2-vessel model presumably leaves a residual level of blood flow on occlusion which is above the perfusion threshold for tissue energy failure (Busza, 1992) and, therefore, diffusion changes were not observed.

7.3.3 The two-vessel occlusion model in the gerbil (n=6)

A more variable response to the repeated ischaemic insults was found in this study of total forebrain ischaemia than had been observed in the rat model. The variability in the model was likely due to inter-animal and inter-experimental differences. In two gerbils, the repeated ischaemic insults resulted in a terminal drop of the trace(D) values. The gerbil is more susceptible to injury than the rat and the observation of such anomalies might reflect this fact. A delayed response was often observed in which the trace(D) did not drop during the initial occlusion phases. The **b0** data also showed a less repeatable behaviour on occlusion and reperfusion than previously observed with the rat model. The generalised behaviour of each animal to the repeated ischaemic insults in the 4-vessel model are summarised in Table 7.4.

Animal	Notes	non-weighted (b0) data pattern	Trace(D) data pattern
Animal 1		In the right hemisphere, a general increasing trend observed on each phase of occlusion-reperfusion. In the other hemisphere, a decrease was observed between first two phases.	Trace(D) decline observed on first ischaemic insult. The repeated typical pattern (i.e. decline followed by recovery on occlusion and reperfusion) then observed until 3rd phase when slower recovery occurred in some regions. During the 4th phase, recovery was considerably slower and in left cortical region, ADC did not recover.
Animal 2	Data not included in analysis of mean response.	**b0** changes only observed during the first phase of occlusion/reperfusion. Subsequent to this phase, the **b0** remained stable at values close to the control level and displayed only small decreases on occlusion.	Erratic, high trace(D) values observed during first two occlusions due to motion artefacts (incorrect insertion of ear-bars). Trace(D) dropped to a terminally low level (~ 0.55±0.036 ($\times 10^{-3}$) mm^2/sec) on 2nd occlusion.
Animal 3	Data not included in analysis of mean response.	**b0** changes only observed during the first phase of occlusion/reperfusion. Typical recovery on first reperfusion followed by anomalous decline during this phase. Subsequent to this phase, the **b0** remained stable at values close to the control level and displayed only small decreases on occlusion.	Trace(D) dropped to a terminally low level (approx. 0.55±0.036 ($\times 10^{-3}$) mm^2/sec) immediately upon the first occlusion.
Animal 4	Animal died after 4th occlusion	General increasing trend observed	Typical response of decline and recovery except during the first occlusion in the left hemisphere when no trace(D) decline was observed
Animal 5		General response of increasing trend observed in the data during the 4 occlusion-reperfusion phases.	Typical response of decline and recovery observed in both hemispheres. However, general decreasing trend in trace(D) values observed during the cycle of 4 phases.
Animal 6		General response of increasing trend observed in the data during the 4 phases.	Typical response in both hemispheres. However, general decreasing trend observed during the phases.

Table 7.4 Summary of responses observed during 2-vessel occlusion studies in the gerbil

7.3.3.1 Trace(D) data

The trace(D) values obtained during the control phase were 0.741±0.01 and 0.741±0.013 ($\times 10^{-3}$) mm^2/sec in the cortical and striatal regions respectively (with no significant difference). These pre-ischaemic values are not significantly different from the control values measured in the rat, 4-vessel study.

In two animals (animals 2 and 3 described in Table 7.4) a permanent decline in the trace(D) was observed during the second and first occlusion respectively. The trace(D) fell to a level of approximately 0.55 ($\times 10^{-3}$) mm^2/sec in both the cortical and striatal regions on occlusion and remained at this level during the subsequent phases of the experiment. On sacrifice, the trace(D) further decreased to a value of approximately 0.50 ($\times 10^{-3}$) mm^2/sec in both regions. Figure 7.5(a) shows the trace(D) time course of Animal 3. The data from these two animals was not included in the subsequent analysis of the mean trace(D) behaviour. Individual occlusion phases from the other animals in the group that showed no trace(D) decline (a delayed response) were also excluded from the analysis of the mean temporal profiles.

On occlusion, in the absence of any delayed response, the trace(D) value rapidly fell in an apparently mono-exponential fashion. The trace(D) values obtained at 1 min post-occlusion were 0.635±0.021 and 0.671±0.011 ($\times 10^{-3}$) mm^2/sec in the cortical and striatal regions respectively. By the second time point (2 min), the mean values were 0.526±0.027 and 0.562±0.015 ($\times 10^{-3}$) mm^2/sec. The trace(D) became significantly different from the pre-occlusion level (reduced by > 2SD) by the first time point (1 min) in 93% of all cases and by the second time point (2 min) in 7% of cases. By approximately 5 min, the trace(D) values had levelled off at a constant value and at 10 min of occlusion, the trace(D) values had reached a level of 0.529 ±0.007 and 0.532 ±0.01 ($\times 10^{-3}$) mm^2/sec in the cortex and striatum respectively. These values represent level that are 71% and 72% of the pre-occlusion values. Percentage minimum levels on occlusion in individual animals varied between 60% and 80% of the control values. The mean minimal level reached during each successive occlusion phase were: 0.585±0.038, 0.580±0.071, 0.520±0.031 and 0.494±0.031 ($\times 10^{-3}$) mm^2/sec in the cortex, and 0.571±0.031, 0.580±0.050, 0.519±0.025 and 0.498±0.022 ($\times 10^{-3}$) mm^2/sec in the striatum.

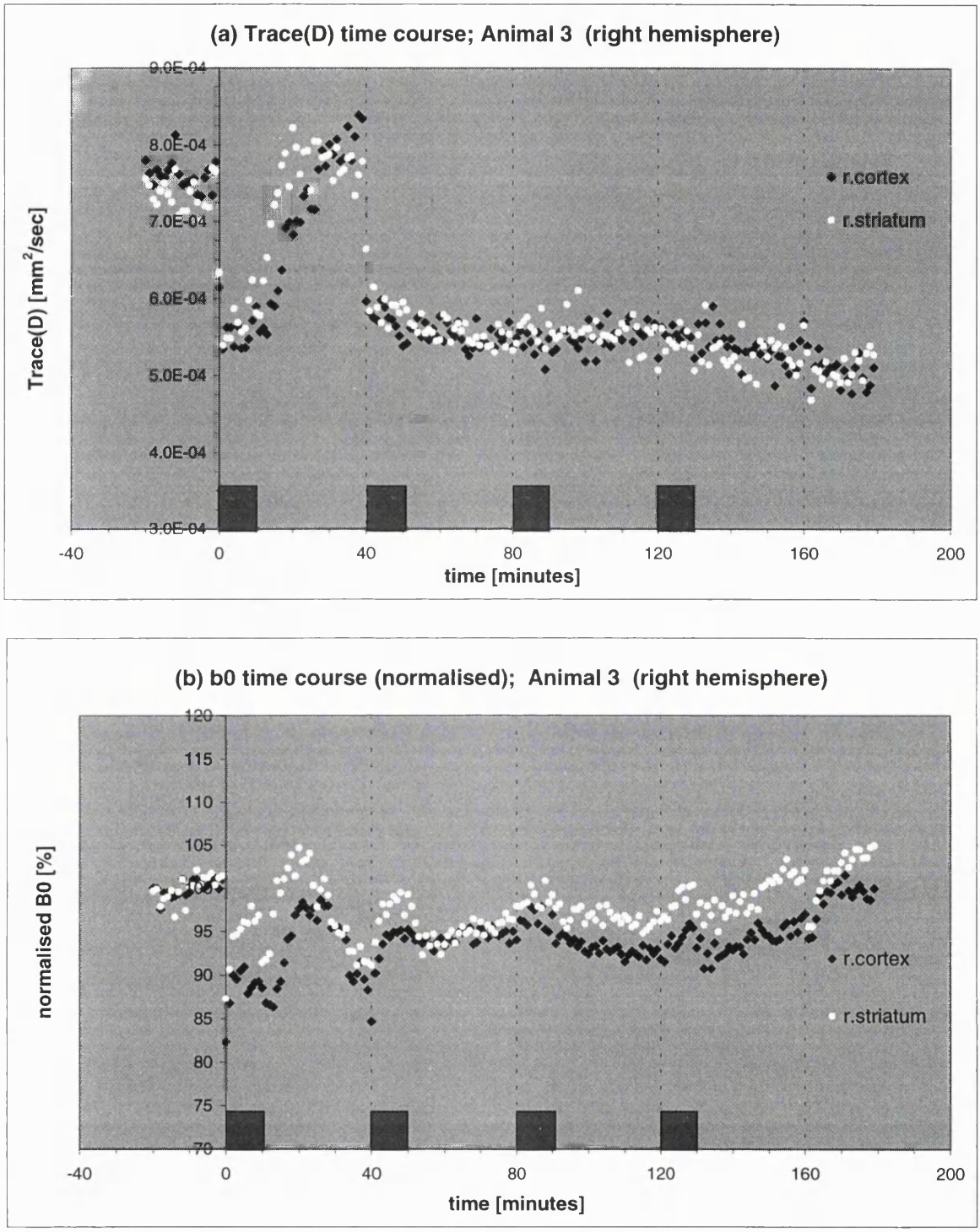

Fig. 7.5 (a) Diffusion and (b) T_2-weighted time-courses from one of the animals that displayed an anomalous response. Note the atypical pattern observed in the **b0** data during the first phase.

A declining trend was observed in the minimum values reached during each of the series of four successive occlusion phases in the complete experiment. The mean slope over all the animals was –4.4±2.2 ($\times 10^{-7}$) [mm^2/sec/min] in the cortex and –5.1±1.0 ($\times 10^{-7}$) [mm^2/sec/min] in the striatum. Neither of these average values are significantly different from zero or each other. Figure 7.6(a) shows a plot of the mean trace(D) behaviour.

On reperfusion, the trace(D) recovered in an apparent exponential fashion and by approximately 15 min had reached a plateau. The mean plateau level (taken as the average value of the last 15 min of trace(D) values) reached during each successive reperfusion phase were: 0.760±0.008, 0.749±0.015, 0.731±0.018 and 0.661±0.032 ($\times 10^{-3}$) mm^2/sec in the cortex, and 0.755±0.008, 0.753±0.013, 0.719±0.011 and 0.678±0.007 ($\times 10^{-3}$) mm^2/sec in the striatum. A significant negative trend was only found in one instance (Animal 4, cortical region, slope = -0.91±0.10 ($\times 10^{-7}$) mm^2/sec/min; P=0.003; linear regression). The mean response over all the animals provided a slope of -0.46±0.17 ($\times 10^{-7}$) [mm^2/sec/min] in the cortex and -0.35±0.19 ($\times 10^{-7}$) [mm^2/sec/min] in the striatum. These values both suggest a negative trend but neither of these values are significantly different from zero (P=0.08 and P=0.16 in the two regions).

On sacrificing the animal by halothane inhalation at the end of the experiment, the immediate decline of the trace(D) followed a similar exponential pattern to the observations during the occlusion phases. The first measurements obtained at 1 min during this procedure were 0.714±0.013 and 0.702±0.006 ($\times 10^{-3}$) mm^2/sec in the cortex and striatum respectively, and by 2 min, the values were 0.462±0.011 and 0.516±0.015 ($\times 10^{-3}$) mm^2/sec. The trace(D) became significantly different from the pre-occlusion level (reduced by > 2SD) by the first minute in 20% of phases and by the second minute in 80% of phases. By 10 min, the trace(D) values had reached a level of 0.410±0.059 and 0.479±0.055 ($\times 10^{-3}$) mm^2/sec. These values represent 55% and 65% of the control level.

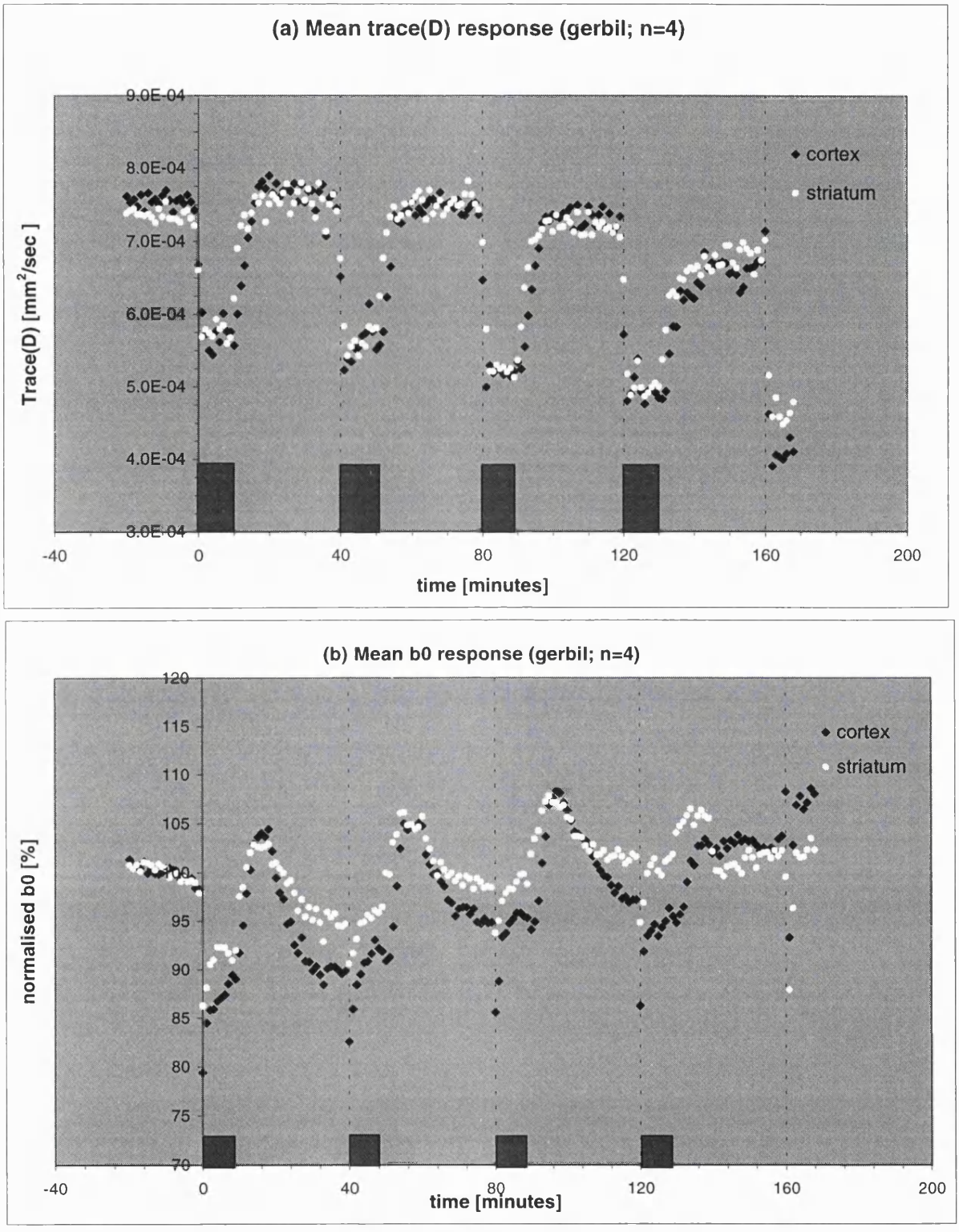

Fig. 7.6 Mean response of the (a) trace(D) and (b) T_2-weighted (**b0**) signal, the in the cortical and striatal regions in the gerbil 2-vessel occlusion model. A cumulative decreasing trend is clearly observable in the trace(D) data and a cumulative rise in the **b0** data.

On comparing trace(D) values obtained on sacrificing the animal to those obtained during the occlusion phases of the experiment, a significant difference was found between the trace(D) values at 10 min post-occlusion and post-sacrifice (P=0.02, paired t-test, cortical and striatal values pooled). No significant difference was found between the trace(D) change between 0-10 min post-occlusion and the same interval post-sacrifice, denoted $\Delta trace(D)_{10}$. No significant correlation was found between the control trace(D) values and the $\Delta trace(D)_{10}$ post-sacrifice or between the control trace(D) and the terminal value reached 10 min post-sacrifice.

The data were analysed for correlations in the same way as described previously in the rat model (Section 7.3.1.1). A significant correlation was found between the pre-ischaemic and post-ischaemic (at 10 min) trace(D) values (P=0.005, linear regression, cortical and striatal values pooled) and between the pre- and post-ischaemic $\Delta trace(D)_{10}$ values (P=0.05, cortical and striatal values pooled). As mentioned in Section 7.3.1.1, this would imply that the variation during the control phase is not of purely physiological origin.

Time constant analysis : Mono-exponential models were fitted to the data in regions that showed an apparent drop on occlusion. The values for the time constants are summarised in Table 7.5.

[min^{-1}]	**Phase 1**	**Phase 2**	**Phase 3**	**Phase 4**	**Death**
β_1 (cortex)	2.4±0.8	1.1±0.2	0.9±0.3	0.8±0.2	2.4±0.5
β_1 (striatum)	2.2±1.2	1.3±0.4	1.8±0.5	1.6±0.06	2.2±0.4
β_2 (cortex)	5.2±1.4	6.1±0.8	5.0±1.5	6.4±1.2	N/A
β_2 (striatum)	2.6±0.9	3.7±1.2	3.6±0.7	4.2±1.8	N/A

Table 7.5 Mean values for the time constants β_1 and β_2 obtained by fitting the occlusion and reperfusion phases respectively to simple mono-exponential models. Units of these time constants are given in [min^{-1}]. Individual phases that did not drop on occlusion were not included in this analysis and some phases with noise-affected values could not be fitted and, therefore, were also excluded.

The average occlusion decay constant, β_1, obtained in the cortex was less than the value obtained in the striatum and the values of the coefficients on death were higher than during the four phases of occlusion and reperfusion (1.3±1.1 min^{-1} and 1.7±1.3 min^{-1} in cortex and striatum respectively during the four phases; 2.4±0.9 min^{-1} and 2.2±0.7 min^{-1} on death). These differences, however, did not achieve statistical significance. For both time constants, no significant difference was found between the successive phases and between the regions (ANOVA test). Also, no significant difference was found between the time constant values obtained in the rat and gerbil models.

*7.3.3.2 The **b0** data*

In 2 of the 6 animals, the trace(D) drop on occlusion remained permanent and significant **b0** changes were only observed during the initial phase of the experiment (see Table 7.4 for details of Animals 2 and 3). These data sets were therefore not included in the subsequent analysis and are discussed at the end of this section.

During the first ischaemic insult, the immediate drop in the signal intensity represented 20±1% and 13±2% of the control levels in the cortex and striatum respectively and these values are significantly different from each other (P=0.003, paired t-test). The signal then recovered and on reperfusion, the peak was 7±2% and 5±1% higher than the control levels in the two regions (and these values are not significantly different), and occurred at 6.3±1.0 and 6.8±0.8 min post-reperfusion. The signal intensity then declined to a value that was significantly lower than the control level in the cortex (90±2% and 95±2% of the control level in the cortex and striatum; P=0.007 and 0.057 respectively, t-test). During subsequent phases, this pattern was repeated (see Table 7.6) with a general increasing trend in the plateau level on reperfusion becoming apparent in all 4 of the animals which displayed a repeating pattern. Figure 7.6(b) shows the mean response.

On sacrificing the animal, the immediate drops in signal intensity (4±1% and 2±1% of the control level in the cortex and striatum respectively) were not significantly different from the decline observed on occlusion (t-test). This immediate decline post-sacrifice were smaller than those values observed in the 4-vessel occlusion model in the rat. The signal then recovered in an apparent mono-exponential manner and by 10 min post-

sacrifice had reached a level that was 109±4% and 103±3% of the control level in the cortex and striatum respectively.

	Drop (% change w.r.t. control)		**Peak** (% change w.r.t. control)		**Reperfusion plateau level** (% of control)	
	cortex	striatum	cortex	striatum	Cortex	striatum
Phase 1	-20±1	-13±2	+7±2	+5±1	91±1 *	95±2 *
Phase 2	-7±2	-4±2	+8±1	+7±2	97±2 *	99±2
Phase 3	-10±2	-5±1	+9±1	+9±3	99±2 *	102±2 *
Phase 4	-10±3	-6±1	+10±2	+11±2	108±4 *	103±4 *
Death	-4±1	-2±1	N/A	N/A	N/A	N/A

Table 7.6 Summary of responses in the non-diffusion-weighted (**b0**) data of the 2-vessel occlusion model (n=4 of 6 animals displaying typical behaviour). The control level is the pre-ischaemic level of signal intensity. * indicates that the reperfusion plateau level is significantly different from the control level.

A significant positive slope was found in 3 out of the 4 animals in the cortex (P=0.18, 0.02 and 0.003 for the regions with a positive slope) and in 2 out of the 4 animals in the striatum (P=0.03, 0.22, 0.9 and 0.4 for the regions with a positive slope). The mean values of the slope were 0.09±0.01 [%/min] and 0.06±0.02 [%/min] in the cortex and striatum respectively (and these values are not significantly different from each other). The values of the slope in the both regions are significantly different from zero (P=0.003 and P=0.03, t-test). The slope of the mean response was similarly significant in both regions (P=0.02 and P=0.03 in the cortical and striatal regions respectively). No correlation was found between the slopes of **b0** trend on reperfusion described here and those values obtained for the trace(D) trend on occlusion (see previous section).

In two animals, Animals 2 and 3 described in Table 7.4, a permanent decline in the trace(D) was observed during the second and first occlusion respectively. Significant **b0** changes (an occlusion drop and a subsequent recovery) occurred during only the first occlusion phase. On reperfusion, an anomalous behaviour was especially apparent in Animal 3 (see Fig. 7.5(b)). Instead of following the pattern of an immediate rise and

peaking response, the **b0** time course displayed a secondary decrease before increasing. The signal then peaked at a level close to the control level before rapidly declining to a level close to the minimum reached during the initial occlusion drop.

Time constant analysis : Mono-exponential recovery model were fitted to the recovering b0 data. The mean values of β_2 during the occlusion phases were 2.0±0.3 min^{-1} in the cortex and 2.7±0.5 min^{-1} in the striatum. On sacrificing the animal, the recovery in the signal intensity provided values for β_2 of 0.9±0.1 min^{-1} and 1.3±0.3 min^{-1} in the two regions. No significant difference was found between values obtained during occlusion and death.

7.3.4 Study of CBF during repeated ischaemia

Perfusion-weighted subtracted images, obtained with a time resolution of 2 min, represented a qualitative measure of CBF. The mean temporal profile of the FAIR subtractions in both cerebral hemispheres are shown Fig. 7.7. During the periods of occlusion, the perfusion-weighted signal drops to a similar level in both hemispheres. However, on comparison with the signal level obtained post-sacrifice, the occlusion values do not indicate a complete cessation of flow during this period. This may signify the effect of collateral circulation.

An immediate side-to-side difference became apparent during each recirculation period. The right cerebral hemisphere displayed an immediate reactive hyperaemic response and a recovery of CBF. The flow in the contralateral hemisphere initially recovered and then dropped to a very low level. In terms of the classifications introduced in Section 5.3, the right hemisphere is displaying a Group A response while the left hemisphere displays a Group B response. These two responses were manifested in the previous study which employed a single 4 min period of occlusion. The data obtained here suggests that the duration and repetition of the occlusion may not be a factor in the occurrence of the Group A response of immediate recovery. The alternative response (Group B) is in accordance with a period of reactive hyperaemia (or more precisely, a return of the flow to a level close to the pre-ischaemic value) followed by delayed hypoperfusion. The level of the subtracted signal intensity at this stage suggests perfusion that is approximately 20-30% of the pre-ischaemic value. This can be compared to the previous study of single 4 min occlusion during which the flow

dropped to a minimal level approximately 10% of the control values. The differing level of compromised flow during this period might reflect the observation by Hossmann mentioned in Section 5.4.2, that a more severe degree of hypoperfusion may result from a shorter duration of ischaemia (Hossmann, 1985a). The level of hypoperfusion does not change significantly during each of the three repeated phases of the experiment. However, the degree of immediate reactive hyperaemia does appear to decrease on each reperfusion phase. This is in agreement with the findings of a study which employed autoradiography to show a similar effect in a model of repeated ischaemia in the gerbil (Tomida, 1987).

7.3.5 Study of T_2 measurements during repeated ischaemia

The mean T_2 measurements in the experiments were 67.0±0.6 ms and 68.9±0.8 ms in the cortical and striatal regions respectively of the rat (2 slices averaged), and 65.1±0.1 ms and 63.7±0.6 ms in the same regions in the gerbil (n=2 animals). In the gerbil experiment, images were acquired with a 2D-FT sequence and the image SNR was poor. Even though variations in the absolute T_2 were observed in this study that approximated the **b0** signal intensity pattern, the analysis of this data was restricted to the cumulative rise in the T_2 which was clearly observed. The T_2 increase was significantly different from zero during the course of the experiment and provided slopes of 0.07±0.01 and 0.04±0.01 ms/min in the cortex and striatum respectively (P=0.01 and P=0.03 in the two regions; linear regression; data from the two slices averaged). This corresponded to an rise in absolute T_2 of approximately 7.5 ms and 3.75 ms in the two regions during the course of the reperfusion phases. These increases in the T_2 values correspond to a signal intensity rise in the T_2-weighted data (TE = 112ms), of approximately +19% and +10% from the control level in the cortex and striatum respectively.

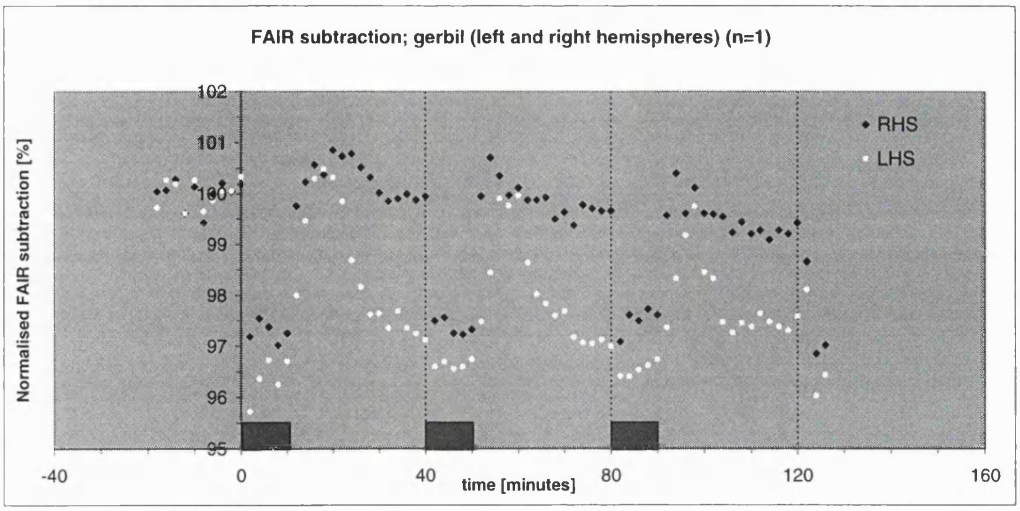

Fig. 7.7 Flow time-course obtained in left (LHS) and right (RHS) cerebral hemispheres in the FAIR perfusion study. Cortical and striatal regions in each hemisphere were averaged together since no difference was observed between them. The subtracted signal is normalised to the control subtraction value. The signal intensity is (to a first order approximation) proportional to the flow. Note the two responses to the reperfusion.The animal died during the third occlusion phase.

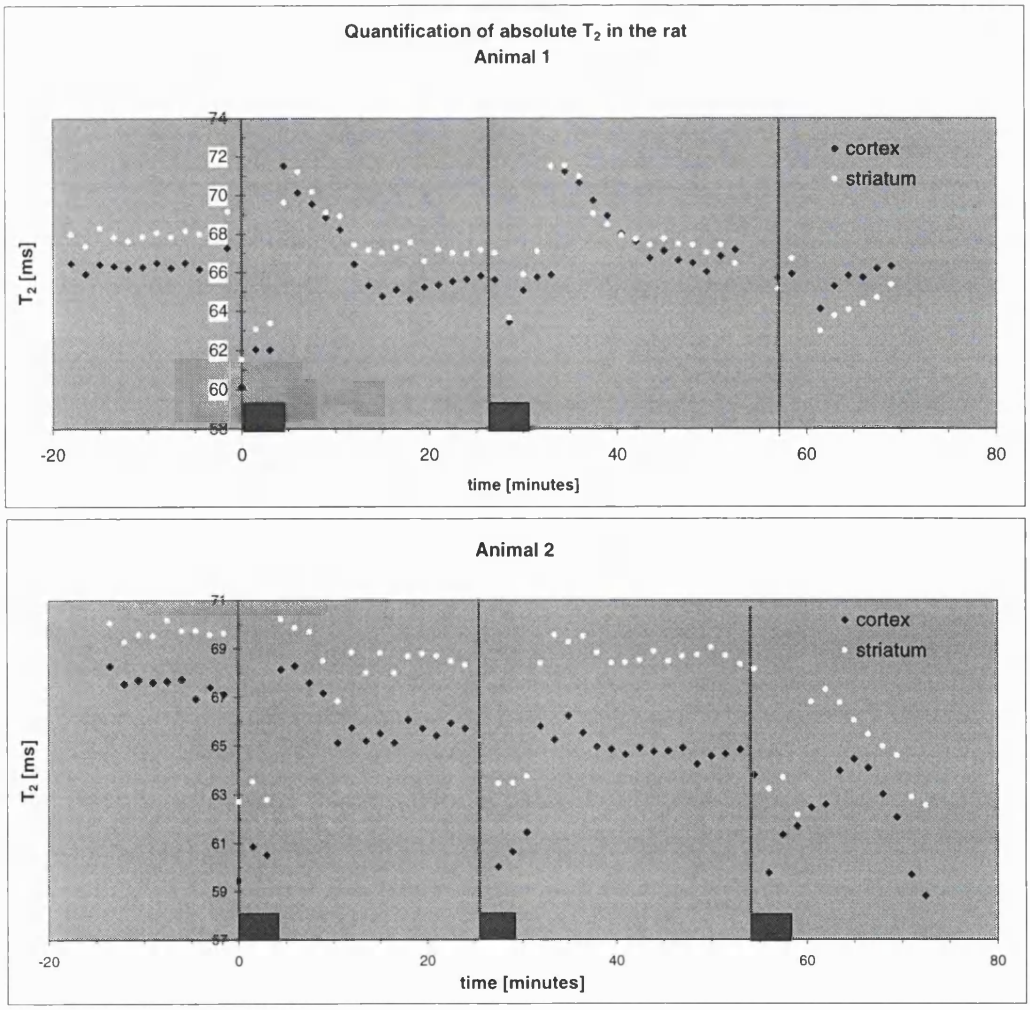

Fig. 7.8 Time-course of absolute T_2 during each of the two experiments in the rat. Both animals died during the third reperfusion phase.

In the rat experiments, spin-echo EPI was employed. Occlusions had a shortened duration of 6 min. Both animals, however, died during the third reperfusion phase and, therefore, the data sets were not analysed for the cumulative rise. The T_2 data clearly displayed the pattern of changes observed in the T_2-weighted data. The underlying pattern was even observed in the acquisition with the smaller echo time. Fig. 7.8 shows the time course of the absolute T_2 from both of the animals. The T_2 immediately declined by approximately 6 ms during the first occlusion in both regions. The hyperaemic overshoot was not clearly visible in one of the animals, but in the other animal constituted an increase of approximately 3.5 ms above the control level in both regions. This variations in the relaxation time during the periods of occlusion and hyperaemia, correspond to a signal intensity change in T_2-weighted data (with TE = 112ms) of approximately -16% and +7% during the occlusion and reperfusion phases respectively.

7.4 Discussion

The experimental model that has been presented here has allowed the effects of repetitive ischaemia to be investigated using high time-resolution diffusion and T_2-weighted MRI. Diffusion coefficient changes indicate alterations in the distribution of cellular water between the intra- and extra-cellular compartments (Moseley, 1990). The non-diffusion-weighted images, **b0** data, obtained during the acquisition of the trace(D) measurement are heavily T_2-weighted. These images should, therefore, reflect changes in blood oxygenation in a comparable manner to the BOLD mechanism (Ogawa, 1990) as well as other possible mechanisms for changes in tissue T_2.

These two imaging contrast mechanisms in concert with each other have provided a unique insight into the consequences of repeated ischaemic episodes. The clinically important pathophysiological syndrome is manifested in conditions such as TIAs, cardiac arrhythmias, neurosurgical surgery and intrapartum events. Previous studies of repetitive ischaemia have demonstrated a progressive degree of cumulative damage. This investigation has provided evidence of a cumulative injurious process using the technique of MRI. The most important finding of the study was the unique sensitivity of T_2-weighted imaging to follow the dynamic pathological events that are occurring. In particular, during the investigation of 4-vessel ischaemia in the rat, the trace(D) images displayed no evidence of a progressive effect, but the **b0** data displayed a distinctive

rising trend that indicates a cumulative process. The gerbil model displayed the same gradual change in the **b0** data that was also evident in the diffusion maps. The gerbil is a more pathologically sensitive animal than the rat and the observation of a clear trend in the trace(D) data as well as the T_2-weighted data may reflect this.

The implications of the trace(D) data (Section 7.4.1) and the **b0** data (Section 7.4.2) will be discussed in turn.

7.4.1 Trace(D) data

7.4.1.1 The sequence

The single-shot sequence provided anisotropy-independent trace(D) values with a time resolution of 1 minute. A high time resolution is of great benefit in studies of ischaemia since the ADC changes occur on a time-scale of seconds and may follow the rapidly varying functional and metabolic events that develop during the insult. Single voxel spectroscopy has been employed in investigations of diffusion imaging during ischaemia with time resolutions of 10 sec (Davis, 1994) and 48 sec (van der Toorn, 1996). This technique does not, however, offer regional differentiation. The imaging sequence, U-FLARE, is based upon a rapid repetition of low angle pulses after an initial $\pi/2$ pulse (Norris, 1991). It has been employed in studies of ischaemia with a time resolution of 2-4 min (Hoehn-Berlage, 1994) but suffers from limitations in SNR. An alternative imaging technique, line scanning, offers a time resolution of 10 sec but only provides limited coverage (one line compared to a normal image containing usually 64 or 128 lines) (Yongbi, 1997; Huang, 1997). The imaging sequence of choice for rapid ADC imaging is EPI (Turner, 1990). This technique can be used with a 12-16 sec time resolution (Pierpaoli, 1992; Latour, 1994; de Crespigny, 1995; Röther, 1996) but is more often employed to obtain ADC maps in approximately 1 min or more (for example, Kucharczyk, 1991; Pierpaoli, 1996; Roberts, 1993).

7.4.1.2 Quantification of trace(D) values

In our study, the control values of the diffusion coefficient in the rat and gerbil models were not significantly different from each other and, as expected for the trace(D), no difference was observed between the values obtained in the cortical and striatal regions. The variation in the baseline values that was observed in the study may be due to partial

volume effects from CSF in the imaging voxel. The higher diffusion coefficient of CSF would introduce a significant variation if present in differing amounts in the chosen voxel (Decanniere, 1995). Comparisons to ADCs obtained in other studies are difficult, since reported measurements are often orientation-dependent and utilise different diffusion times (for example, Moseley, 1990; Mintorovitch, 1991; Knight, 1991; Busza, 1992; Minematsu, 1992). It is further complicated by the lack of a well-defined diffusion time for the single-shot trace(D) sequence used in our study. Our laboratory has reported a drop on occlusion of the diffusion coefficient of approximately 23% by 50 min post-occlusion from a control value of 0.8 ($\times 10^{-3}$) mm^2/sec in a rat model of middle cerebral rat occlusion (MCAO) (trace(D); diffusion time, 5 ms; field strength, 8.5T) (Calamante, 1999). In a time course study of MCAO in the rat, pre-ischaemic cortical ADC measurements of 0.67 ($\times 10^{-3}$) mm^2/sec were obtained (ADC_z, i.e. diffusion gradients applied along slice-select direction) (Röther, 1996). In spite of the difference in baseline measurements which may be due to anisotropy effects, a similar ADC decrease (approximately 28%) was observed in that study by 17 min post-occlusion. In general, trace(D) measurements in grey matter vary between approximately 0.74-0.85 ($\times 10^{-3}$) mm^2/sec in animal studies (van Gelderen, 1994; Miyabe, 1996; Decanniere, 1995; Busch, 1998) and the decline in the trace(D) value on occlusion or cardiac arrest (ΔADC_{trace}) is approximately 20-40% during the first 10 minutes. These values correspond well to those obtained in our study.

The apparent exponential drop of the trace(D) during occlusion, sacrifice and reperfusion, have provided time constants by fitting to an ideal mono-exponential curve. Several groups have reported biphasic behaviour of the ADC decline with an initial rapid decrease and a secondary slower decline which is most likely a temperature effect (Davis, 1994; Hoehn-Berlage, 1994; Decanniere, 1995). However, the period of ADC drop during the 10 min duration of ischaemia employed in our study will likely occur during the first of these phases and a single exponential fit should, therefore, be valid. The calculated time constants displayed a variability due to limited SNR and the very rapid decline. The value of 2.0 min^{-1} and 1.75 min^{-1} in the rat and 1.5 min^{-1} and 2.3 min^{-1} in the gerbil on occlusion and sacrifice respectively can be compared with values obtained during previous studies. Values obtained from some of these other reports are displayed in Table 7.7.

Phase	Time constant [min^{-1}]	Model/ ADC	Notes	Reference
occlusion	~1	rat / ADC_{xyz}	Values computed from figures	Yongbi, 1997
occlusion	6-9	cat / ADC_x	GM variability was 2.3-11.5 min^{-1} over 8 animals	Pierpaoli, 1996
occlusion	11-27	cat / ADC_x	Values computed from figures	Davis, 1994
occlusion	6	rat / ADC_{xyz}	Values computed from figures; 15 sec time resolution; normo-glycaemia, for hypo-, β_1=13 min^{-1}	Huang, 1997
cardiac arrest	9	rat / ADC_{xyz}	Values computed from figures; 15 sec time resolution; normo-glycaemia, for hypo-, β_1=13 min^{-1}	Huang, 1997
cardiac arrest	24-37	rat / ADC_z	Values computed from figures	Van der Toorn, 1996
cardiac arrest	14-20	rat / ADC_x	Values computed from figures	Davis, 1994
cardiac arrest	3-7	cat / ADC_x		Pierpaoli, 1996
reperfusion	3-40	cat / ADC_x	Values computed from figures; great variability in data	Davis, 1994
reperfusion	~2	rat / ADC_{xyz}	Values computed from figures	Yongbi, 1997
reperfusion	~3	cat / ADC_x	Values computed from figures	Pierpaoli, 1996

Table 7.7 Time constants for ADC occlusion changes on occlusion, cardiac arrest and reperfusion from GM regions. ADC_i refers to the application of the diffusion gradients along the read, phase-encoding or slice direction. ADC_{xyz} implies application of gradients along all three directions simultaneously (which is not the same as the trace(D)).

The considerable variation in these values in Table 7.7 probably reflect differences in the degree of the ischaemia and also metabolic variations, the technique of diffusion coefficient measurement, and in the case of cardiac arrest (CA), the concentration and amount of potassium chloride employed. Pierpaoli *et al.* has shown that the diffusion decrease on ischaemia is slower in GM than in WM (Pierpaoli, 1996) and this is presumably due to differing levels in residual perfusion; the placement of ROIs amongst the structural areas of the brain is, therefore, crucial.

7.4.1.3 The relationship of the ADC decline and cerebral metabolism

During our study, the trace(D) value usually had declined by the first time point (1 min) post-occlusion with a significant change occurring usually by the second minute. The similar finding of an almost instantaneous ADC decline on sacrificing the animal (when a more drastic cessation of internal physiological movement occurs), suggests that this observation is not related to motion artefacts. On induction of ischaemia, the most immediate observable response to the suppression of physiological functions is the cessation of spontaneous electrical activity (visible in the EEG). This occurs within approximately 15 sec (Hossmann, 1977).

There have been several investigations of the changing cerebral energy metabolism during ischaemia and reperfusion using phosphorus (^{31}P) NMR (Andrews, 1987; Alger, 1989; Behar, 1989). These investigations have demonstrated an almost immediate change in metabolite concentrations upon induction of ischaemia, and an almost immediate recovery of these metabolites on reperfusion. For example, Behar *et al.* showed that the levels of the metabolites phosphocreatine (PCr) and NTP (nucleotide triphosphate) decreased to noise levels after 4-8 min of global ischaemia in the majority of rats in their study. Following 1 hr of ischaemia, these metabolites were detectable within 4 min of recirculation and NTP and PCr levels had recovered to control values by approximately 30 min and 1 hr respectively. The recovery of tissue pH was found to follow a significantly slower time course (Behar, 1989). Another study reported a similar behaviour on occlusion but a more variable response to reperfusion (Andrews, 1987). The ADC changes observed in our study appeared to approximately parallel the metabolic swings.

Higher time resolution studies of ADC and energy status have enabled a better understanding of these relationships to be obtained. Van der Toorn *et al.* have demonstrated in a CA model in the rat, that ATP starts to decline at a later time and at a slower rate than PCr (a significant decrease was observed by 4 min post-occlusion for ATP compared to 2 min for PCr) (van der Toorn, 1996). This may reflect the early maintenance of ATP levels at the expense of the PCr following a switch from aerobic to anaerobic respiration. The almost immediate decline of the ADC that was observed in our study, is perhaps at odds with this finding since the loss of membrane potential that signals the start of cytotoxic oedema (the generally accepted mechanism for the ADC decline) is likely not to be instantaneous. This process should not occur until the ATP level has dropped below a certain threshold, which as the previous report has indicated, is not an immediate response. This hypothesis is confirmed by direct current (DC) measurement of cell membrane potential that do not indicate a terminal depolarisation until approximately 4-6 min post-ischaemia (Hossmann, 1977; Dijkhuizen, 1998b). Investigations in our laboratory which have monitored ADC and DC potential in an MCAO model in the rat, have, however, reported ADC changes on occlusion that precede the changing membrane potential (Harris, 1998 and unpublished data). In contrast, other reports have described a simultaneous ADC and DC response (de Crespigny; 1997; de Crespigny; 1998). Studies of the penumbral zone that surrounds the ischaemic core have demonstrated that ADC reduction occurs in areas without ATP depletion (Kohno, 1995) and it is clear that ADC changes can arise before the onset of tissue energy failure.

As mentioned previously, a biphasic decrease of ADC has often been observed on induction of ischaemia. One study has shown that the early ADC changes parallel an increase in lactate concentration which is a by-product of anaerobic respiration (Decanniere, 1995). The immediate ADC decline may be related to initial pre-depolarisation trans-membrane ionic shifts (Hansen, 1981), or to an early increase in intracellular tortuosity (Duong, 1998). In fact, recent studies have disputed the generally accepted mechanism of cytotoxic oedema for the ADC decline observed during ischaemia (Neil, 1995; Duong, 1998a; Duong, 1998b) (see Section 2.1.3). Intra- and extra-cellular-specific markers were employed to show that the difference in normal compartmental water mobilities is not sufficient to induce the observed magnitude of the ADC change. Instead, since the large majority of cellular water is in the intracellular compartment (80-90%), ischaemia-induced changes of water mobility in this

compartment must be involved. Suggested mechanisms are a decrease in active intracellular circulation (with the involvement of, for example, cell streaming, axoplasmic flow and organelle movement) or an increase of intracellular viscosity (Duong, 1998b). The latter mechanism might be related to the increase in intracellular sodium ion concentration (see Appendix C, where a substantial ADC difference was observed between water and sodium chloride solutions). The complete explanation of ischaemia-induced ADC changes is likely to be made up of contributions from many of the suggested mechanisms.

7.4.1.4 Sources of variation in the ischaemic trace(D) values

The principal variability in our data was the observation in four out of ten animals of a delayed trace(D) decline, with the trace(D) showing no decrease during the first and occasionally during the second occlusion phase. This delayed response often displayed variation between the cerebral hemispheres. The inter-experimental differences that are responsible for these variations are likely to reflect variability in the reduction of CBF achieved during occlusion. This can be attributed to a number of factors that include differences in the degree of collateral circulation in the brain. In the 2-vessel model of forebrain ischaemia in the gerbil, the significance of collateral flow during the occlusion was indicated by the two flow responses to recirculation (Groups A and B) observed in the study described in Chapter 5. In the 4-vessel occlusion model in the rat, complete occlusion of the vertebral arteries by electrocauterisation is difficult and depends on the technique and position of vertebral occlusion (Furlow, 1982; Todd, 1984). Even if this operation is successful, collateral circulation will remain from the spinal circulation via the lower brainstem into the caudal regions of the brain (Furlow, 1982).

The level of compromised perfusion during the occlusion phase may be above the threshold for diffusion changes (Busza, 1992) as a consequence of the degree of collateral circulation. Previous studies have demonstrated that sustained levels of hypoperfusion that are severe enough to cause T_2-weighted (Pierpaoli, 1996; Gröhn, 1998) and gadolinium-based contrast agent signal changes (Roberts, 1993), have not resulted in visible changes in diffusion-weighted images. This is presumably due to the maintenance of above-threshold flows. A delayed ADC decline may be related to the cumulative effects of repeated exposure to above-threshold hypoperfusion during the repeated occlusions. Eventually, the collateral flow may no longer be able to prevent the

development of the pathophysiological response of cell swelling due to tissue membrane failure which is indicated by a change in the ADC.

7.4.1.5 Severity of occlusion as indicated by the trace(D) values

The degree of ischaemia induced by the occlusion will be indicated by the terminal ADC level during this stage in comparison to the trace(D) level post-sacrifice. The average terminal occlusion values obtained in our study were higher than the corresponding post-sacrifice level at 10 min (but this difference only achieved statistical significance in the striatal region in the gerbil model (P=0.02; paired t-test)). This observation suggests the presence of collateral flow during occlusion and the general variability in the severity of the mechanical method of occlusion.

7.4.1.6 Transient overshoot of the trace(D) values

An overshoot in the trace(D) on reperfusion was apparent in several of the animals in the study and was especially evident in one animal (Fig. 7.3) possibly as a result of the improved SNR of that experiment. A transient overshoot of the ADC on recirculation has been observed in other investigations (Tang, 1997; Fischer, 1995 where the overshoot was observed in the basal ganglia but not in the cortex). A possible mechanism of this transient phenomenon is the increase in the proportion of blood in the voxel during the period of reactive hyperaemia. Blood possesses a higher ADC than tissue. The blood may also cause an artefact-related increase in ADC as a result of its flowing motion.

7.4.1.7 Cumulative changes in the trace(D)

In the study of 4-vessel occlusion in the rat, the trace(D) values on reperfusion remained stable and showed no evidence of a cumulative effect during the cycle of repeated occlusion/reperfusion phases. The recovery and subsequent stabilisation of the ADC on recirculation implies a renormalisation of energy and acid-base homeostasis (Fischer, 1995; Hossmann, 1994). However, in the gerbil study of forebrain ischaemia, the trace(D) value displayed a cumulative decreasing trend during the four phases. This is indicative of a depletion of energy metabolites and a progressive deleterious effect. The mechanism of the progressive change will be discussed in greater detail at a later point in the discussion but specific issues related to the ADC, will be mentioned here.

The FAIR study of perfusion measurements in the gerbil model (see Chapter 5), demonstrated repeated cycles of hyperaemia and delayed hypoperfusion on reperfusion in one of the cerebral hemispheres. This is expected to be the general response. The immediate renormalisation observed in the collateral hemisphere - the Group A response described in Section 5.3 - is not expected to frequently occur especially for a 10 min period of occlusion. The severity of the period of hypoperfusion displayed no gradual change during the cycle of reperfusion phases. An explanation for the cumulative effect observed in the ADC gerbil data based upon a gradual decreasing level of compromised CBF close to the threshold value, is therefore, unlikely. A perfusion threshold for ADC changes was measured in our laboratory to have a value of approximately 20 ml/100g/min (Busza, 1992). Subsequent studies have demonstrated that, in fact, the existence of a single all-or-nothing flow threshold is an oversimplification. The combination of the degree and the duration of the occlusion is likely to play an important role in predicting the level of the threshold and the degree of damage (van Zijl, 1995). One study compared perfusion deficits in flow [^{14}C]-autoradiographs with areas of hyperintensity in diffusion-weighted images after 30 min and 120 min of MCAO in the rat (Kohno, 1995). Flow thresholds of 34 ml/100g/min and 4 ml/100g/min was found for the 30 min and 120 min survival groups respectively. This suggests a strong sensitivity of the tissue to damage as the length of perfusion deficit decreases.

ADC and CBF regional changes in an ischaemic area have been shown to display a radial graduation in severity from the central core to the periphery or penumbral zone (Roussel, 1995; Hoehn-Berlage, 1995) This may be reflected by a similar, gradual decrease in the flow threshold for diffusion changes. These studies imply that a increasing threshold may be the response to repetitive exposure to hypoperfusion during each reperfusion period. This effect would contribute to a developing process of tissue damage that would be reflected by our observation of a decreasing trend in the trace(D) values in the gerbil model.

In addition to the possibility of a changing flow threshold, it is also possible that microscopic, specific regional variations exist in its value. The observation of a cumulative ADC decline may, therefore, be a selective phenomenon related to regional

differences in susceptibility to injury and different durations for maturation-related damage (see Section 5.1.3). Each imaging voxel may contain a range of tissue structures each possessing a different vulnerability to repetitive ischaemia. Even within the so-called selectively vulnerable areas of the brain, a hierarchy of susceptibility is found in the neuronal sub-populations. For example, in the hippocampus, the CA1 subfield is more vulnerable to damage than the CA3 subfield, and in the neocortex, layer 3,5 and 6 are more susceptible than layers 2 and 4 (Kato, 1990b). The voxel may therefore contain a wide variation of such sub-populations and the same level of compromised flow will cause a varying degree of injury throughout that voxel. This effect may be exacerbated by an inhomogeneous distribution of flows within the tissue at the microcirculatory level due to the incomplete ischaemia induced by forebrain ischaemia in the gerbil. In this respect, the 4-vessel model in the rat might well be considered as achieving a more complete level of global ischaemia than the 2-vessel model in the gerbil.

Another possible mechanism for the cumulative trend observed in the gerbil is the development of tissue oedema (see Section 2.1). A study has shown that the later stages of cytotoxic oedema are characterised by osmotically driven increases in the total tissue water content (Hatashita, 1988). At a subsequent stage, the breakdown of the blood brain barrier and the extravasation of intravascular proteins, results in the movement of intravascular water into the tissue (vasogenic oedema). Several studies have demonstrated the aggravated development of tissue oedema during repeated ischaemia as will be discussed later in this Discussion. The effect of an increase in total water content on the diffusion coefficient will depend upon the nature of this water. It is likely that the water will take on the characteristics of the cellular water and thereby will be subject to the same restrictions of the intra- and extra-cellular compartments. Therefore, the ADC should theoretically not change during the period of water movement and an oedema-related mechanism for the trace(D) decreasing trend can be discounted. The later stages of vasogenic oedema are associated with an ADC increase but this is due to the rupturing of cell walls and a consequent increase in water mobility (Knight, 1991).

7.4.2 The b0 (T_2-weighted) data

The use of deoxyhaemoglobin as an intravascular contrast agent has been exploited to great effect in studies of functional activation (for example, Kwong, 1992; Bandettini, 1997) and in investigations of pathological challenges that affect blood oxygenation

levels (for example, Turner, 1991). This technique relies on the powerful paramagnetic nature of deoxyhaemoglobin which increases the magnetic susceptibility of deoxygenated blood relative to oxygenated blood (which essentially possesses the same susceptibility as water). The enhanced magnetic susceptibility is manifested by a shortened T_2 and T_2^* of deoxygenated blood. T_2^* includes contributions from the intrinsic T_2 of the sample and also from macroscopic and microscopic field variations such as inhomogeneities in the static magnetic field (the T_2' component in Eq. [1.18]). Blood oxygenation-related changes in T_2^* are therefore considerably larger than the corresponding variation in T_2 (Bandettini, 1994). However, quantitative imaging of T_2^* is sensitive to susceptibility-induced artefacts that are especially evident at high-field and is facilitated with the use of modified imaging techniques (Howseman, in Press). T_2 is less dependent on experimental conditions and is sensitised to changes in compartments with a smaller dimension than the larger intravoxel spin dephasing that accounts for changes in T_2^*. Factors that account for the T_2 change include diffusion of spins through susceptibility induced gradients (Bandettini, 1994) and chemical exchange of water between different magnetic states inside and outside the red blood cells (Bryant, 1990; van Zijl, 1998).

Our study has used the strongly T_2-weighted **b0** data to probe the blood oxygenation changes during the cycle of repeated occlusion/reperfusion phases. These images also contain a contribution due to T_1-weighting because of the short repetition time of the single-shot trace(D) sequence. T_1 changes are, however, expected to be insignificant at our field strength (see Section 5.2.3.1).

The variations in signal intensity in the **b0** images during the occlusion and reperfusion phases, are comparable to observations reported during similar studies of vascular challenges with hypoxia (Turner, 1991; Dijkhuizen, 1996) and reversible occlusions (de Crespigny, 1993). The observed patterns of the T_2-weighted data will reflect not only direct changes in blood oxygenation but also any factor that affects the total density of deoxyhaemoglobin in the voxel. The interaction of cerebral blood volume (CBV), CBF and the oxygen extraction fraction (OEF) will therefore contribute to the observed pattern of T_2-weighted signal intensity. The OEF is the demand:supply relationship for oxygen and is defined as the ratio of the rate of oxygen metabolism ($CMRO_2$) to the oxygen delivery (see Appendix B).

7.4.2.1 Occlusion

The immediate signal decline on occlusion reflects the response of the vasculature to a drop in the cerebral perfusion pressure (CPP) that had been initiated by the intervention. The blood vessels dilate in order to maintain the autoregulatory function of brain tissue (for example, Papatta, 1993). Vasodilation occurs principally in the vessels in the arterial blood supply but also, to a certain extent, within the venous and pial circulations (Auer, 1987). When the vessels become maximally vasodilated, the maintenance of a constant CBF becomes compromised and extraction of oxygen from the delivered blood will increase. A greater proportion of oxygen is extracted from the decreased delivery of oxygen as the system attempts to maintain the rate of oxygen metabolism (see Situation II(i) in Appendix B). In the **b0** data of this study, the decline in signal intensity occurred by the first time point post-occlusion (1 min) in the majority of cases. This indicates the immediate reaction of the blood circulation to the changing CPP. De Crespigny *et al.* demonstrated the immediacy of the CBV response relative to the slightly delayed drop in ADC and DC potential (de Crespigny, 1997). The decrease in T_2-weighted signal intensity displayed no significant contrast that might have been expected due to the different degrees of vascularity present in GM and WM tissue-types. Another study found a 2:1 difference in the magnitude of the GM/WM signal drop (de Crespigny, 1993). However, the regions used in our study are expected to contain predominately GM.

The subsequent recovery of the **b0** signal intensity towards the control level during the period of occlusion, can be attributed to a number of possible factors. A decrease in the OEF has been reported in several studies of ischaemia (Wise, 1983; Papatta, 1990; Baron, 1991) and reflects a reduced demand for oxygen as the tissue down-regulates in response to the reduced supply of oxygen. The $CMRO_2$ can no longer be maintained due to the sustained decrease in blood flow which delivers the oxygen. A reduction in the CBV would also result in a T_2-weighted signal increase. Swelling of the tissue parenchyma as a result of cytotoxic oedema (Little, 1975) and perivascular glial cell enlargement (Arsenio-Nunes, 1973) will compress the microcirculation. Microcirculatory defects may also develop during the period of occlusion with similar mechanisms that contribute to recirculation deficits in the reperfusion model (see Section 5.1). Such factors include increased blood viscosity (Fischer, 1973), formation of endothelial microvilli (Dietrich, 1984) and platelet aggregation (Dougherty, 1979).

Roussel *et al.* suggested that the recovery of gradient-echo signal intensity (T_2^*-weighted) may be able to delineate areas of reversibly and irreversibly damaged damage (Roussel, 1995). In an MACO model in the rat, peripheral areas surrounding the ischaemic core, possibly representing the penumbra and misery perfusion, displayed a non-recovering decline in signal intensity which implicates a stable, increased level of the OEF. The recovery observed in the core of the lesion in their study (and observed globally in our study) indicates a decline in the OEF. This may either reflect a pathological response or it may be a subtle reflection of the tissue's ability to adapt to such potentially injurious events by reducing its metabolic requirements in line with a decreased delivery of blood.

By the end of the 10 min occlusion period, the **b0** signal recovered to a level slightly below the pre-ischaemic signal intensity (Tables 7.4 and 7.8). For a longer period of ischaemia, it is expected that the signal intensity would increase back to the baseline level. In the previously described study of Roussel *et al.*, the recovery of signal intensity in the core of the lesion took place over 1-2 hr (Roussel, 1995). The changes observed in our study are quicker and this reflects differences between the models of focal and global ischaemia.

7.4.2.2 Recirculation

On reperfusion, the immediate overshoot in the **b0** data is due to the phase of reactive hyperaemia oxygenation (Haggendal, 1970, Kågström, 1983a) that rapidly changes the state of blood. Ischaemia-induced accumulation of extracellular $[K^+]$ (Dixon, 1949) and $[H^+]$ due to lactic acid formation (Lowry, 1964), and changes in partial pressures of oxygen and carbon dioxide, will contribute to relaxation of cerebrovascular smooth muscle. Cerebral arteries will dilate and a sudden rush of blood through the expanded vasculature will occur. In a similar manner to Roussel's previously mentioned hypothesis, de Crespigny *et al.* stated that the appearance of the overshoot of the signal intensity indicates the maintained capacity of viable tissue to autoregulate and, hence, delineates tissue that is capable of recovery. In that study, the degree of tissue ischaemia was indicated by the reduced size of the overshoot and its delayed appearance after recirculation (de Crespigny, 1993; Dijkhuizen, 1996).

The subsequent decline of the signal intensity reflects the stabilisation of the blood oxygenation status. The FAIR flow study indicated the appearance of a period of delayed hypoperfusion. The CBV will also decrease during this period (Todd, 1986b; Xu, 1987; Pluta, 1989). The stabilisation of the **b0** signal at values below the control level during the initial reperfusion phases is significant in that it implies that during these phases, the reduced blood flow and, therefore, reduced oxygen delivery, is accompanied by a compensatory increase in the extraction of oxygen. This will be discussed in further detail at a later stage when discussing the cumulative trend in the **b0** data.

The **b0** signal changes observed during the course of the study have been explained solely in terms of changes in blood T_2 as a result of blood oxygenation levels. Confirmation of the significance of the T_2 change was provided by the experiments during which absolute T_2 values were obtained. A T_2 decline on occlusion of approximately 9% and an overshoot of approximately 5% with respect to pre-ischaemic values were observed. These changes account for all of the T_2-weighted signal intensity variations that are observed at the echo time, TE, of 112 ms, of our sequence.

7.4.2.3 Anomalous observations

In our study, the appearance in the majority of phases of a repeated pattern (with a decline and partial recovery of signal intensity during occlusion and a subsequent hyperaemic response on recirculation) indicates the repeatability of the recovery from transient occlusion in the animal models. In a few of the phases, this pattern was not observed but the **b0** changes that did occur are able to offer additional insights into the developing state of the tissue. These anomalous **b0** signal changes were always accompanied by atypical patterns in the trace(D) data. An example of this behaviour, is shown in Fig. 7.5. A permanent trace(D) decline during the first occlusion phase is not accompanied by a hyperaemic overshoot on reperfusion in the **b0** data. Instead, the **b0** signal recovers towards the pre-ischaemic level and then declines significantly below this level. This seems to indicate an accumulation of deoxygenated blood that would be expected to occur during an unsuccessful reperfusion which leaves the tissue in a continued ischaemic state. The absence of significant **b0** changes during subsequent phases reflects the inability of the reperfusion to have any effect on improving the tissue status.

In the case of animals which displayed a delayed trace(D) decline (with the diffusion coefficient displaying no drop on occlusion during the initial phases), the T_2-weighted signal usually displayed the typical response of decline followed by recovery and overshoot on reperfusion. The hyperaemic response was often, however, reduced in magnitude in comparison with successive phases which were accompanied by a decline in the trace(D). This indicates that comprehensive failure of the mechanical procedure of occlusion is unlikely to be responsible for the appearance of a delayed response.

An interesting further observation of anomalous data sets was with regard to the cumulative **b0** trend observed during the cycle of repeated events. As will be discussed in the next section, an increasing trend was observed as the typical response. However, in animals that died prematurely during the second or third phases of the experiment (n=2), an anomalous decreasing trend was observed in a majority of the regions in the analysis. These responses indicate the sensitivity of the T_2-weighted data in comparison with the diffusion images in reflecting underlying processes and requires further investigation.

7.4.2.4 Cumulative changes in the b0 data

A general rising trend in the **b0** data was observed during the course of the repeated phases (Fig. 7.2(b) and 7.6(b)). The trend in the T_2-weighted data, unlike the trace(D) data, was observed in both the rat and gerbil models. This trend suggests a cumulative effect that develops during the repeated transient ischaemic episodes. Single periods of brief ischaemia have been previously shown to produce no apparently significant T_2-weighted signal increase (see Section 5.4.3).

The progressive pathogenic response to repeated ischaemia has not been a universal observation. In previous studies, variability has been observed in the response of the cerebral metabolism and glutamate levels. In particular, one investigation has demonstrated a neuroprotective effect of multiple ischaemic events but a very short reperfusion interval was employed in this study (Steinberg, 1994). In fact, a phenomenon of ischaemic preconditioning has been described in several studies in which a prior period of brief ischaemia, which is not lethal in itself, has induced significant protection to subsequent ischaemic events (ischaemic tolerance). This phenomenon was first demonstrated in the gerbil (Kitagawa, 1990; Kirino, 1991) and

subsequently in rat models of global and focal ischaemia (Kitagawa, 1991; Liu, 1992, Simon, 1993). For example, Liu *et al.* reported that preconditioning with 3 min of ischaemia in the rat, followed by 3 days of reperfusion, protected against hippocampal neuronal damage that followed a subsequent 8 min period of ischaemia (Liu, 1992). Cortical spreading depressions may also have a neuroprotective action (Matsushima, 1996). Mechanisms that may contribute to ischaemic tolerance include modified gene expression and the synthesis of heat shock proteins (HSPs). These proteins are produced in response to serious forms of stress such as heat, trauma and physical or chemical agents (Brown, 1989; Lindquist, 1986; Simon, 1991). The production of HSPs has been demonstrated in ischaemic preconditioning (Nishi, 1993). Ischaemic preconditioning was not, however, expected to be a relevant factor in studies of repetitive ischaemia as in the case of our investigation, since reperfusion intervals of at least 24 hr are probably required for manifestation of this phenomenon.

Various studies have investigated the metabolic, functional, biochemical and morphological responses to repetitive ischaemia (for example, Mrsulja, 1977; Andrews, 1987; Alger, 1989; Hossmann, 1990; Bizzi, 1996). Many investigations have reported a cumulative deleterious response to the repeated ischaemic episodes. This has been reflected in progressive changes during successive periods of ischaemia in their measurements of tissue oedema, neuronal cell damage, glutamate and metabolite levels, protein synthesis and the microcirculation. A number of principal mechanisms have been implicated in the pathogenesis of the cumulative effect. These can be summarised as follows:

1. The development of tissue oedema during the repeated ischaemic events indicating an imbalance of the ion homeostasis and resulting in increased intracranial presence and compression of the circulation (Vass, 1988)
2. The gradual inhibition of protein synthesis (Widmann, 1992)
3. The development of secondary tissue hypoxia due to an imbalance between impaired circulation during the intervals between ischaemic events, and cerebral metabolism during the reperfusion intervals (Xu, 1987; see later in the Discussion)
4. Progressive damage of the mitochondrial respiration (LaManna, 1977)
5. Modified selective gene expression (Hermann, 1998)
6. A gradual release of excitatory amino acids (EAAs) such as glutamate. This will trigger calcium accumulation which is considered a major contributing factor in excitotoxic neuronal cell damage (Ueda, 1992).

These mechanisms are not mutually exclusive and some of them are more likely to be symptoms rather than reasons for the cumulative trend. The following section discusses how the trend in the **b0** data may reflect some of these mechanisms.

7.4.2.5 Possible mechanisms for the trend in the b0 data

The trend in the T_2-weighted data reflects an increasing tissue spin-spin relaxation time. This has been confirmed by the T_2-quantification experiment in which the observed change in the relaxation time (approximately +7.5%) is of sufficient magnitude to explain this trend. As previously discussed, the contribution of a changing T_1 to the data are expected to be non-observable at our field strength. The rising trend in the **b0** data would, in fact, be countered by a T_1 increase which would induce a decline of the weighted signal. Its influence is, therefore, not expected to be a significant factor in the typical response of the **b0** data. It may, however, contribute to the decreasing trend observed in the two animals that died before the four phases were completed (Section 7.4.2.3). In these cases, a significant T_1 increase may have occurred.

A possible mechanism for the T_2 rise is the development of tissue oedema. Cytotoxic oedema is not implicated since it will not change the total tissue water content and upon induction of ischaemia, T_2 changes are significantly delayed in comparison to ADC changes (Moseley, 1990). These changes, therefore, could only be assumed to be reflected by the development of vasogenic oedema (Knight, 1991; Calamante, 1999). Many studies have demonstrated the aggravation of tissue oedema during repetitive ischaemia using the technique of specific gravity. Its appearance has been suggested as early as 1 hr post-occlusion (Vass, 1988). Oedema development may reflect an increase in the osmotically-driven water uptake at the time when the blood brain barrier is still intact (Hatashita, 1988). This was previously mentioned as a possible cause for the cumulative decrease of the trace(D) observed in the gerbil (see Section 7.4.1.7). A biphasic opening of the BBB has been shown to occur during recirculation, and the immediate opening observed on recirculation associated with hyperaemia, may allow small amounts of water into the tissue at this stage (Suzuki, 1983; Ting, 1985). However, the **b0** rising trend is not associated with a decreasing trend in the diffusion coefficient in the rat model. Therefore, a mechanism for the T_2 rise that is solely based upon the development of oedema is unlikely. Nevertheless, the associated swelling of

the tissue may have an indirect effect as will be discussed shortly. A more probable source of the cumulative effect is the blood circulation. Changes in blood volume and oxygen extraction are implicated and these factors will be discussed in turn.

A progressively impaired cerebral blood volume would contribute to a rising T_2 due to the resulting decrease in the concentration of deoxyhaemoglobin in the voxel. Physical alterations in blood circulation have been observed during repetitive ischaemia. Vass *et al.* demonstrated a progressive decline in the number of perfused capillaries that would be associated with a gradual decrease in the CBV (Vass, 1988). The tissue parenchyma will be gradually swelling due to the development of oedema, and the resultant compression of the circulation would have a similar, exacerbated effect on the blood volume. A progressive decreasing trend of the CBV during the course of the repeated ischaemic events, would be at odds with the observation during CBF studies of a constant level of hypoperfusion during this period (Tomida, 1987). This flow response may reflect the redistribution of the microcirculation that Vass *et al.* observed, with a compensatory dilation of the larger blood vessels. This redistribution of flow is, however, non-nutritional and will contribute to an increasing level of secondary tissue hypoxia (Xu, 1987).

The **b0** data provides subtle information concerning the oxygenation status of the circulation. The oxygen extraction fraction (OEF) is a parameter that describes the fundamental interrelationship of the blood flow and the cerebral metabolism. During the initial reperfusion phases, the recovering **b0** signal reaches a level that is lower than the control range (Tables 7.3 and 7.6). This indicates an uncoupling of flow and metabolism (see Appendix B). When an impaired flow during the period of delayed hypoperfusion is accompanied with a maintained level of $CMRO_2$ (i.e. cerebral metabolism) (Situation II(i) in Appendix B). The trace(D) has usually completely recovered by this stage and this may reflect the ability of the brain to maintain normal metabolic status. During the course of the subsequent reperfusion phases, the gradual rise in the plateau level of the **b0** signal, indicates a down-regulation of the brain's requirement for oxygen and a decline in the metabolic demand for oxygen (hypometabolism) (Situation II(iii) in Appendix B). This is a pathogenic response even though the metabolism is now more closely coupled to the compromised blood flow during hypoperfusion. It indicates that the wide reserve of oxygen extraction that normally allows the brain to maintain a

normal $CMRO_2$, has been exceeded. This will likely result in the development of secondary tissue hypoxia and, as a consequence, tissue injury. The mechanism for the progressive reduction of the capacity of normal oxygen extraction, may involve mitochondrial damage as the system is "stunned" by the repetition of the ischaemic event with an insufficient interval available for the recovery of normal tissue function.

7.5 Conclusion

The principal findings of this study have been the high time-resolution investigation of combined trace(D) and T_2-weighted changes during occlusion and reperfusion, the general increased sensitivity of the T_2-weighted (**b0**) signal to follow underlying events in comparison with the trace(D) data, the confirmation of the solely T_2-based nature of the signal intensity changes, and the cumulative, deleterious effects of repetitive ischaemia observed in the T_2-weighted signal.

An EPI-based single-shot sequence was used to provide a temporal resolution for combined trace(D) and T_2-weighted measurements of 60 sec with use of the same sequence. On occlusion, the trace(D) decline was observed within the first 2 min and this suggests an initial phase of intracellular changes in water mobility that occurs before the terminal loss of ion homeostasis. The complete recovery of the trace(D) values within approximately 5 min post-reperfusion, reflects the almost immediate renormalisation of the cerebral metabolism.

The **b0** signal displayed changes during occlusion and reperfusion that are directly related to variations in transverse relaxation time of the tissue. T_2-weighted imaging has the ability to follow alterations in blood flow, volume and oxygen extraction. Van Zijl *et al.* has derived expressions for the relationship between T_2 and these vascular parameters (van Zijl, 1998). However, in the case of the conditions imposed by ischaemia, an analytical treatment becomes very complicated. It is, nevertheless, possible to use the T_2-weighted data to gain a clear, system-independent and qualitative understanding of the blood oxygenation changes that are evolving. Susceptiblity-induced artefacts associated with T_2^* imaging are avoided and this technique is therefore especially attractive to studies at high-field. The sensitivity of this data in providing information concerning pathological changes was evident on examination of the atypical responses in the study. This information is often difficult to interpret and

requires further investigation but may offer an early indication of the outcome of an intervention.

The cumulative, pathological effect of repeated episodes of ischaemia has been demonstrated and has been placed in the context of the considerable amount of relevant, previous work. A decreasing trend in the trace(D) was observed in the gerbil model but not in the rat model of 4-vessel occlusion. This difference reflects the increased susceptibility of the gerbil to ischaemic damage in comparison to the more resilient rat model. In both animal models, however, the **b0** data displayed an increasing trend that corresponded to an absolute change in tissue T_2. The possible mechanisms of the cumulative response have been discussed and are most likely directly related to a progressive deleterious changes in the blood circulation. The increased sensitivity of the **b0** signal in manifesting the cumulative effects, especially in the rat model, is a significant finding of this study. Diffusion imaging has made a major impact on the study of ischaemia as a result of its unique sensitivity in detecting the initial stages of cell damage that are not observable by T_2-weighted imaging. Interestingly, in the study of repetitive ischaemia, the underlying pathomechanisms apparently induce a greater sensitivity of T_2-weighted images than DW images to observing their effects.

The relevance of such studies of repeated ischaemia is especially applicable to the field of cerebrovascular surgery. Deliberate temporary occlusion of the intracranial arteries is often used in the treatment of complex cerebral aneurysms and vascularised tumours, in order to control bleeding and facilitate dissection during operations. It remains controversial among neurosurgeons whether it is best to employ a single period of occlusion (Jabre, 1987, Samson, 1994) or to interrupt the arterial occlusion with intervals of reperfusion (Suzuki, 1979; Peerless, 1990). Typically, this latter approach utilises periods of temporary occlusion of 2-5 min separated by intervals of up to 10 min (Peerless, 1990) and is implemented with the rationale that these interruptions allow time for recovery from the detrimental effects of ischaemia. The animal studies of repetitive ischaemia described in this chapter would dispute the recommendation of this approach. In fact, one neurosurgical investigation has reported a suggestive relationship between increased frequency of temporary arterial clipping and post-operative ischaemia (Samson, 1994). Care must, however, be taken when extrapolating such results to the clinical situation and further investigation is required in order to aid this process.

Further work with the animal models described in this chapter will also need to examine the effects of differing durations of ischaemia and reperfusion on the degree of the cumulative effect. Single periods of ischaemia will need to be better investigated in order to aid these comparisons. Different approaches to create ischaemia warrant further investigation, such as the 2-vessel rat model attempted in this study, focal models, and unilateral forebrain ischaemia in the gerbil.

In conclusion, non-invasive, high time-resolution trace(D) and T_2-weighted imaging have enabled investigation of the clinically relevant condition of repetitive ischaemia. Such techniques offer a unique insight into the dynamic, pathological events that are rapidly evolving.

CONCLUSIONS OF THE THESIS

This thesis has described the development of quantitative perfusion and diffusion imaging techniques and their subsequent implementation in the study of experimental cerebral ischaemia. Perfusion is a quantifiable, direct measure of the ability of the vascular supply to meet the metabolic demands of the tissue. It may be argued that the perfusion measurement on its own, is an imperfect indicator of the viability of brain tissue compromised by insufficient perfusion. The diffusion coefficient is a sensitive indicator of the extent of tissue damage, and in combination with the measurement of perfusion provides a considerably more powerful tool for the investigation of ischaemia. MRI offers the opportunity to non-invasively measure and co-register these parameters with a high temporal and spatial resolution. The combined implementation of these techniques in the studies described in this thesis (Chapters 3-7) has, thereby, provided important insights into the mechanisms of changing tissue viability.

The clinical evaluation of cerebral perfusion has obvious utility but has been hampered by the relatively invasive nature of most of the currently implemented methods of blood flow measurement. Furthermore, most methods of CBF determination are based on the pioneering work of S.S. Kety who formulated the basic flow expression based on the kinetics of a single compartment for animal autoradiography work rather than human measurements (Kety, 1951). A single compartment is a homogeneous tissue element for which the assumption of a well-mixed compartment is valid (so that the residual function - r(t) in Eq. [3.4] - is of the form $\exp(-ft/\lambda)$). Only high resolution imaging techniques such as MRI can approach the spatial resolution required to satisfy Kety's formulation in this respect. The methods of arterial spin labelling such as FAIR and continuous spin tagging, described in Sections 3.3 and 3.4, have tremendous potential for routine clinical use. However, their implementation for the accurate evaluation of precisely the range of flows that are the most interesting to the clinician or experimenter, is currently subject to a number of concerns. These issues are tackled in this thesis by the implementation of improved sequence designs and the optimisation of the labelling RF pulses that are intrinsic to the methodology of these techniques. The FAIR technique has warranted special attention in this work since, by its nature, it has the potential of being the least affected by the transit time sensitivity. Improved pulse design of the inversion and imaging pulses (Section 3.6) has allowed the potential realisation of the ideal, theoretical FAIR experiment. A significant degree of transit time

insensitivity should then be achievable without the decay of the label that is a consequence of the alternative use of the post-labelling modification employed in QUIPSS (Wong, 1997) or the modified CASL technique (Alsop, 1996) in order to achieve this aim. The double adiabatic pulse refocusing scheme has the additional effect of contributing to the elimination of vascular signal in a similar manner to diffusion gradients by virtue of its rephasing/dephasing mechanism within the intervening delay.

Chapters 4 and 5 described the design and implementation of a FAIR sequence with improved temporal resolution. The influence of the inflow time on perfusion quantification was demonstrated and it is shown that the contribution to measurement inaccuracy may be as significant as the transit time unless it is incorporated into the analysis. The use of this technique combined with diffusion imaging in the study of reperfusion injury has provided important information concerning the pathophysiology of this syndrome and has also demonstrated some of the potential inadequacies of the arterial spin labelling methods. Chapter 6 has discussed the design and optimisation of two variants of time efficient quantitative diffusion imaging. The MRI systems in our laboratory, on which these pulse sequences were implemented, provided different potential pitfalls that had to be considered. Finally, Chapter 7 has described the application of one of these diffusion techniques in the study of repeated ischaemia with the additional finding of a cumulative change apparent in the T_2-sensitive component of the images.

The ultimate goal of stroke imaging is the ability to distinguish between reversibly and irreversibly damaged tissue. Studies of the ischaemic penumbra (see Hoehn-Berlage, 1995b) and the tissue state of misery perfusion (see Section 3.7) have demonstrated the promise of MRI in achieving this aim but it is likely that a combination of MR and other techniques will be required. However, MRI readily allows the evaluation of the condition of tissue and can thereby provide information as to the state of tissue injury or recovery in the clinical or experimental setting. The multi-parametric nature of MRI is one of the great strengths of the imaging method. The principally physiological emphasis of the perfusion and diffusion studies described in this thesis can be enhanced in future investigations with the functional and metabolic information provided by functional MRI and NMR spectroscopy respectively. Time is a decisive factor in studies of the rapidly evolving ischaemic cascade that occur during the onset of acute stroke and in investigations of the development of reperfusion injury. The implementation of

high time-resolution imaging with Turbo FLASH and EPI sequences has enabled the performance of time efficient, longitudinal investigations of these conditions. These and similar studies have largely been directed towards gaining a better understanding of the pathophysiology of cerebral ischaemia and in the assessment of therapeutic strategies; their utility in aiding clinical diagnosis will be enhanced as the techniques develop and the animal models are further refined. However, it must be kept in mind that care is to be taken when extrapolating data from the experimental to the clinical setting. The clinical diagnosis and prognosis of stroke has benefited greatly from the increasingly widespread implementation of multi-parametric MRI techniques (Baird, 1998). The combined clinical use of diffusion and perfusion imaging has displayed potential as a powerful predictive tool (Rordorf, 1998). The continued investigation and application of these techniques in the clinical setting is, therefore, of significant clinical relevance.

The work described in this thesis can be regarded as laying the groundwork for future investigations. Further studies will need to focus on a number of principal issues that are summarised here:

(1) Comparative investigations between the different ASL techniques are required in order to further understand the characteristics of the spin tagging methodology especially during situations of compromised flow. This would expand upon the initial study described in Section 3.8 comparing the continuous to the FAIR technique in the same animal.

(2) Multi-point fitting to the theoretical perfusion expressions predicted by the perfusion models allows quantification of the transit time (Chapter 3). A more extensive investigation of the differing sensitivities to the transit time of the ASL techniques at varying levels of flow, is also required. A comparison with the corresponding values of the mean transit time (MTT) provided by tracer techniques such as dynamic susceptibility contrast imaging would be advantageous in the understanding of these techniques.

(3) The change in the diffusion coefficient observed during the relatively early stages of recirculation (Chapter 5) is potentially of significant importance since it implies a time when intervention may be beneficial in order to ameliorate recovery. Further work is required to substantiate this finding and to further follow the evolving time course. Implementation of the optimised pulse scheme for FAIR described in Chapter 3 would enable improved characterisation of the flow response.

(4) The sensitivity of the perfusion quantification to the inflow time (Chapter 4) requires additional investigation especially in conditions of low flows. Clinical imaging usually utilises head coils and the significance of the inflow time on the measurement accuracy of the FAIR experiment in this case may be as important as the transit time.

(5) The time efficient TurboFLASH diffusion sequence (Chapter 6) offers the opportunity to combine high resolution quantitative imaging with ^{1}H and ^{31}P NMR spectroscopy at high magnetic field strengths. This would be especially suitable for the study of the perfusion threshold for diffusion changes (Chapters 5 and 7).

(6) Further experiments using the model of repeated ischaemia would need to directly compare the effects of single and repeated ischaemic events. The additional implementation of metabolite spectroscopy would offer insights into the cumulative effect, and the combined use of CBF and gradient-echo imaging (Kim, 1997b) would allow non-invasive determination of the changes in oxygen extraction that are believed to contribute to the manifestation of the cumulative trend.

APPENDIX A : ANALYSIS OF THE T_1 MODEL IN THE CASE OF SHORT REPETITION TIMES

A1 Integrated form of the Bloch equation

All calculations are based on the solution of the flow-modified Bloch equation (Detre, 1992) under the relevant initial conditions that are defined by the situation. Integration and rearrangement of this equation yields the following expression that relates magnetisation at time $t = t_1$ to the magnetisation at a later time $t = t_2$

$$M(t_2)\, e^{t_2/T_{1app}} - M(t_1)\, e^{t_1/T_{1app}} = \int_{t_1}^{t_2} \left(fM_a(t) + \frac{M_0}{T_1} \right) e^{t/T_{1app}}\, dt \qquad [A1]$$

where $M_a(t)$ is the arterial magnetisation per unit volume (ml) of blood and other terms are defined in Section 3.2.1.

A2 Transit time effects

Incorporation of the effects of the transit time (see Section 3.5.1 and Eq. [4.5]) into the FAIR model, modifies $\Delta M(TI)$ so that $\Delta M(TI) = 0$ for $TI < \delta$ and the following expression for $TI \geq \delta$

$$\Delta M(TI) = M_{ss}(TI) - M_{ns}(TI) = 2M_0\alpha_0 \frac{f}{\lambda} e^{-\delta/T_{1a}} \left[\frac{e^{-(TI-\delta)/T_{1app}} - e^{-(TI-\delta)/T_{1a}}}{\frac{1}{T_{1a}} - \frac{1}{T_{1app}}} \right] \qquad [A2]$$

The transit time can therefore be determined from the biexponential relationship from the intercept of the $\Delta M(TI)$ curve on the TI time axis. No evidence was found for a significant non-zero intercept in the control biexponential data (Chapter 3 and 4) and the transit time was, therefore, not considered in the analysis.

A3 Short TR FAIR : (no pre-saturation)

Implementation of FAIR with a short repetition time introduces a modified set of initial conditions that are dependent upon the relaxation during the recovery time (see Section 4.2.1). The repeated application of non-selective inversion pulses results in a build-up of a steady state level of inflowing blood magnetisation described by the factor *X(TR)* (Eq.

[4.3]). The expression for this factor is obtained by calculation of the magnetisation state that builds up after applying a series of inversion pulses to a spin system that starts from a state of thermal equilibrium. Analysis of ΔM(TI) in this case necessitates splitting the analysis into components in order to calculate the magnetisation at the start and the end of the recovery period and at the start and the end of the subsequent inversion pulse. The initial conditions of the latter phase are defined by the final state of the former phase and vice versa. Figure A1 depicts the state of the magnetisation in the z-direction (M_z) at various stages of the analysis. The initial conditions at four of these stages, denoted (a) - (d) on Fig. A1, are as follows (with transit time effects neglected):

non-selective image

start of recovery time of preceding selective image: ***(a)*** *see Fig. A1*

$$M_a(t) = \frac{M_0}{\lambda}\left(1 - 2X(TR)\,\alpha_0\, e^{-(TR+TI+t)/T_{1a}}\right)$$
$$M_{ns}(t=0) = 0$$

start of inversion time (assume inverted when reached steady state): ***(b)***

$$M_a(t) = \frac{M_0}{\lambda}\left(1 - 2X(TR)\,\alpha_0 e^{-t/T_{1a}}\right)$$
$$M_{ns}(t=0) = (1-2\alpha_0)M_{ns}(t'=\tau)$$

selective image

start of recovery time of preceding non-selective image: ***(c)***

$$M_a(t) = \frac{M_0}{\lambda}\left(1 - 2X(TR)\,\alpha_0\, e^{-(t+TI)/T_{1a}}\right)$$
$$M_{ss}(t=0) = 0$$

start of inversion time (assume inverted when reached steady state): ***(d)***

$$M_a(t) = \frac{M_0}{\lambda}\left(1 - 2X(TR)\,\alpha_0\, e^{-(t+TR)/T_{1a}}\right)$$
$$M_{ss}(t=0) = (1-2\alpha_0)M_{ss}(t'=\tau)$$

[A3]

where $M_{ss}(t'=\tau)$ is the tissue magnetisation at the end of the previous recovery time. The resulting expression for ΔM(TI) is then derived by inclusion of these conditions into Eq. [A1] and the resulting expression is given by Eq. [4.2].

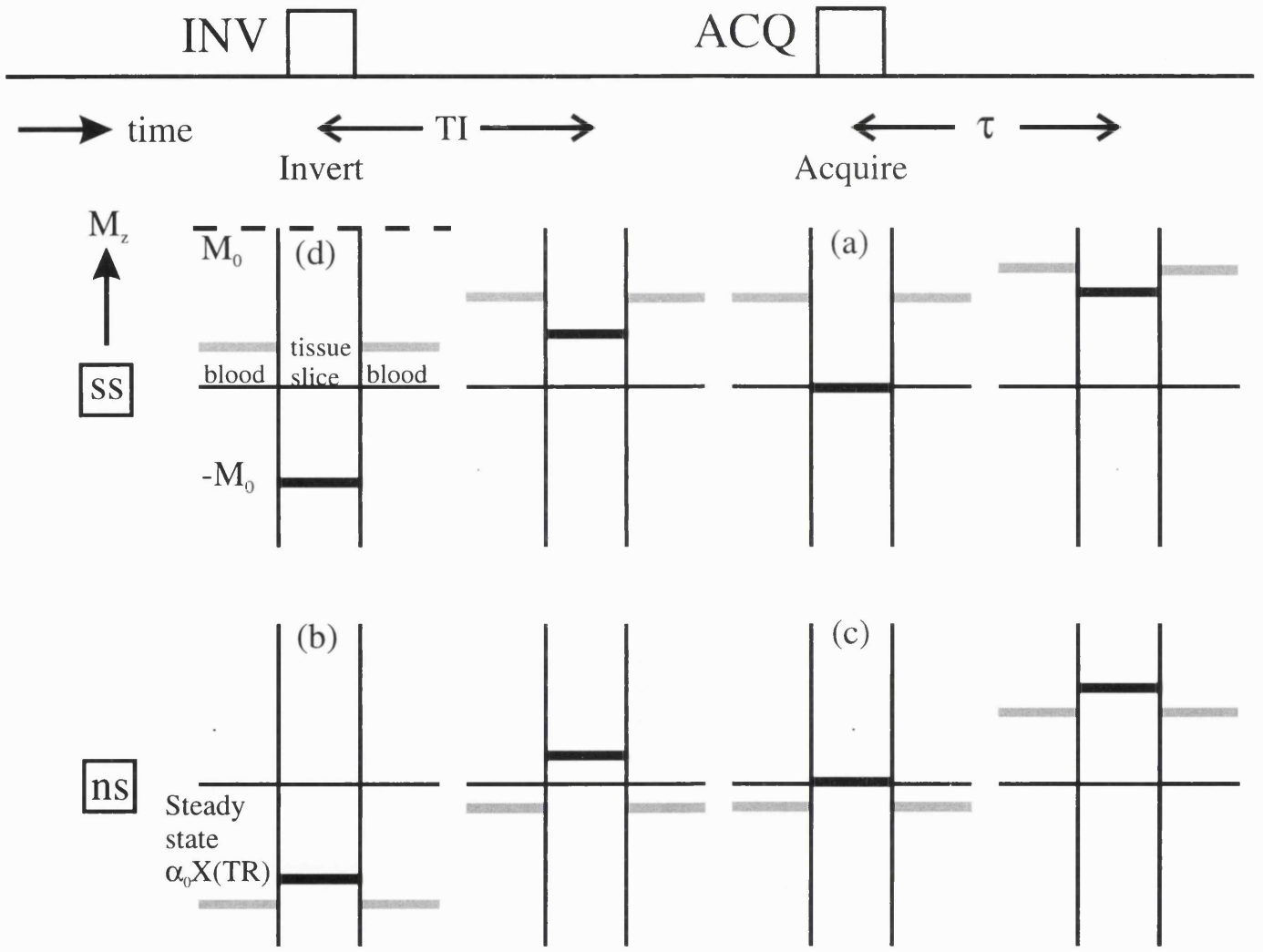

Fig. A1 Schematic representation of the tissue and inflowing blood magnetisation states (M_z) in the selective (ss) and non-selective (ns) images, for short TR FAIR without a saturation pulse.The tissue magnetisation of the selected slice is shown in the central band and the inflowing blood magnetisation is depicted in the outer zones, proximal and distal to the slice of interest. The magnetisation of these external blood spins is depicted since only these spins will enter the slice and influence the measured signal.

A4 Short TR FAIR (with pre-saturation)

In order to simplify the quantification of short repetition time FAIR, global pre-saturation pulses can be applied at the beginning of each experiment (see Section 4.2.2). This destroys the build up of any steady-state magnetisation or any complicating magnetisation difference that has evolved during the previous experiment. The selective and non-selective acquisitions can be considered in isolation and the flow-related signal in each experiment develops only during the inversion time but not during the recovery time. The tissue magnetisation is then modified during the inversion time by inflowing blood spins that are still relaxing from the initial saturation pulse in the case of the selective image and by blood spins relaxing after inversion from this state in the case of the non-selective image. The initial conditions in this situation are as follows (with transit time effects neglected and assuming a perfect saturation):

non-selective and selective images

start of recovery time of preceding image:

$$M_a(t=0)=0$$
$$M_{ns/ss}(t=0)=0$$

start of inversion time:

$$M_a(t)=\frac{M_0}{\lambda}\left[1+\left((1-2\alpha_0)\left(1-e^{-\tau/T_{1a}}\right)-1\right)e^{-t/T_{1a}}\right] \quad (non-selective)$$

$$M_a(t)=\frac{M_0}{\lambda}\left(1-e^{-(t+\tau)/T_{1a}}\right) \quad (selective)$$

$$M_{ns/ss}(t=0)=(1-2\alpha_0)\left[M_0\left(1-e^{-\tau/T_{1app}}\right)-M_0\frac{f}{\lambda}\left(\frac{e^{-\tau/T_{1app}}-e^{-\tau/T_{1a}}}{\frac{1}{T_{1a}}-\frac{1}{T_{1app}}}\right)\right] \quad [A4]$$

The tissue magnetisation at the start of the TI time is the same in the case of both the selective and non-selective images since both experiments start from a state of global saturation. The expression for the difference in magnetisation, ΔM(TI), is given by Eq. [4.2].

A5 Short TR FAIR (with pre-saturation and coil inflow effects)

Inflow of fresh arterial spins from outside the coil can occur during both the recovery time and the inversion time (see Section 4.2.3). Use of pre-saturation pulses is assumed in this situation as coil inflow effects would otherwise significantly complicate the quantification. A number of situations need to considered in the analysis of the effects of coil inflow on quantification. These regimes depend upon the choice of experimental parameters and the value of the inflow time (see Table 4.1). If the chosen recovery time is less than the coil inflow time ($\tau < \Delta$), the coil volume fills with uninverted spins that will flow into the imaging slab during the subsequent inversion at a time ($\Delta - \tau$). The blood magnetisation during the TI time in such a case therefore fulfils the following conditions:

non-selective image

$$M_a(t) = \frac{M_0}{\lambda}\left[1+\left((1-2\alpha_0)\left(1-e^{-t/T_{1a}}\right)-1\right)e^{-t/T_{1a}}\right] \qquad 0<t<(\Delta-\tau)$$

$$M_a(t) = \frac{M_0}{\lambda}\left(1-2\alpha_0 e^{-t/T_{1a}}\right) \qquad (\Delta-\tau)\le t<\Delta$$

$$M_a(t) = \frac{M_0}{\lambda} \qquad t\ge\Delta$$

selective image

$$M_a(t) = \frac{M_0}{\lambda}\left[1+\left((1-2\alpha_0)\left(1-e^{-t/T_{1a}}\right)-1\right)e^{-t/T_{1a}}\right] \qquad 0<t<\delta$$

$$M_a(t) = \frac{M_0}{\lambda}\left(1-e^{-(t+\tau)/T_{1a}}\right) \qquad \delta\le t<(\Delta-\tau)$$

$$M_a(t) = \frac{M_0}{\lambda} \qquad t\ge(\Delta-\tau) \qquad \text{[A5]}$$

Considering for example the non-selective image, while the inversion time is less than this *secondary* inflow time, ($\Delta - \tau$), blood spins entering the imaging slice have been inverted during their recovery from the pre-saturation (Fig. 4.2). Once this time has been reached, fresh spins that have entered the coil during the previous recovery time, arrive at the slice after having been inverted from their equilibrium state. Subsequent to the *principal* inflow time, Δ, fresh, uninverted, spins that have entered the coil during the inversion time, reach the imaging slice.

Expressions for ΔM(TI) in each of the regimes shown in Table 4.1 are shown here. An approximate form for each equation can be obtained by assuming equal T_1 values (T_1=T_{1a}) and that (f/λ)TI << 1 and this simplified expression is shown if it reduces to a simple form.

(a) **Case (i)** $TI < \Delta$ and $\tau \geq \Delta$

$$\Delta M(TI) = \frac{2M_0\alpha_0 \frac{f}{\lambda}}{\left(\frac{1}{T_{1app}} - \frac{1}{T_{1a}}\right)}\left[\left(e^{-TI/T_{1a}} - e^{-TI/T_{1app}}\right) - e^{-(TI-\delta)/T_{1app}}\left(e^{-\delta/T_{1a}} - e^{-\delta/T_{1app}}\right)\right] \quad [A6]$$

With approximations :

$$\Delta M(TI) = 2M_0\alpha_0 \frac{f}{\lambda} e^{-TI/T_1}(TI - \delta) \quad [A7]$$

(b) **Case (ii)** $TI \geq \Delta$ and $\tau \geq \Delta$

$$\Delta M(TI) = \frac{2M_0\alpha_0 \frac{f}{\lambda} e^{-TI/T_{1app}}}{\left(\frac{1}{T_{1app}} - \frac{1}{T_{1a}}\right)}\left[e^{\tau/T_{1app}}\left(e^{-\tau/T_{1a}} - e^{-\tau/T_{1app}}\right) - e^{\delta/T_{1app}}\left(e^{-\delta/T_{1a}} - e^{-\delta/T_{1app}}\right)\right] \quad [A8]$$

With approximations :

$$\Delta M(TI) = 2M_0\alpha_0 \frac{f}{\lambda} e^{-TI/T_1}(\Delta - \delta) \quad [A9]$$

(c) **Case (iii)** $TI < (\Delta - \tau)$ and $\tau < \Delta$

$$\Delta M(TI) = \frac{2M_0\alpha_0 \frac{f}{\lambda} e^{-\delta/T_{1a}}}{\left(\frac{1}{T_{1app}} - \frac{1}{T_{1a}}\right)}\left(e^{-(TI-\delta)/T_{1a}} - e^{-(TI-\delta)/T_{1app}}\right)\left[1 - e^{-\tau/T_{1a}}\right] \quad [A10]$$

(d) **Case (iv)** $(\Delta - \tau) \leq TI < \Delta$ and $\tau < \Delta$

$$\Delta M(TI) = \frac{M_0 \frac{f}{\lambda}}{\left(\frac{1}{T_{1app}} - \frac{1}{T_{1a}}\right)} \left[e^{-TI/T_{1app}} \left(e^{-(\Delta-\tau)(1/T_{1a}-1/T_{1app})} - e^{-\delta(1/T_{1a}-1/T_{1app})} \right) \left(2\alpha_0 \left(1 - e^{-\tau/T_{1a}} \right) \right) \right.$$
$$\left. + 2\alpha_0 e^{-(\Delta-\tau)/T_{1a}} \left(e^{-(TI-\Delta+\tau)/T_{1a}} - e^{-(TI-\Delta+\tau)/T_{1app}} \right) \right]$$

[A11]

(e) **Case (v)** $TI \geq \Delta$ and $\tau < \Delta$

$$\Delta M(TI) = \frac{M_0 \frac{f}{\lambda}}{\left(\frac{1}{T_{1app}} - \frac{1}{T_{1a}}\right)} \left[e^{-TI/T_{1app}} \left(e^{-(\Delta-\tau)(1/T_{1a}-1/T_{1app})} - e^{-\delta(1/T_{1a}-1/T_{1app})} \right) \left(2\alpha_0 \left(1 - e^{-\tau/T_{1a}} \right) \right) \right.$$
$$\left. + 2\alpha_0 e^{-(TI-\Delta)/T_{1app}} e^{-(\Delta-\tau)/T_{1a}} \left(e^{-\tau/T_{1a}} - e^{-\tau/T_{1app}} \right) \right]$$

[A12]

APPENDIX B : RELATIONSHIP OF CBF, $CMRO_2$, OEF AND THE T_2-WEIGHTED SIGNAL INTENSITY

(see Sections 3.7.3 and 7.4.2)

Definition:

OEF = $CMRO_2$ / (O_2 delivery) [units of numerator and denominator: μM/100g/min]

Assumptions:

(1) $CMRO_2$ is proportional to the rate of rate of cerebral metabolism

(2) O_2 delivery is proportional to the CBF

If the flow is reduced, for example, during occlusion or, on recirculation, during the period of delayed hypoperfusion, the response of the $CMRO_2$ can either be to remain coupled or become uncoupled to the CBF. Four situations need to be considered for the consequences of a reduction in flow (with notation derived from (Baron, 1991) and its suggested mechanism given after each heading):

I Coupled CBF and $CMRO_2$

(Pure metabolic depression, mechanism: neuronal shutdown, (Baron, 1991))

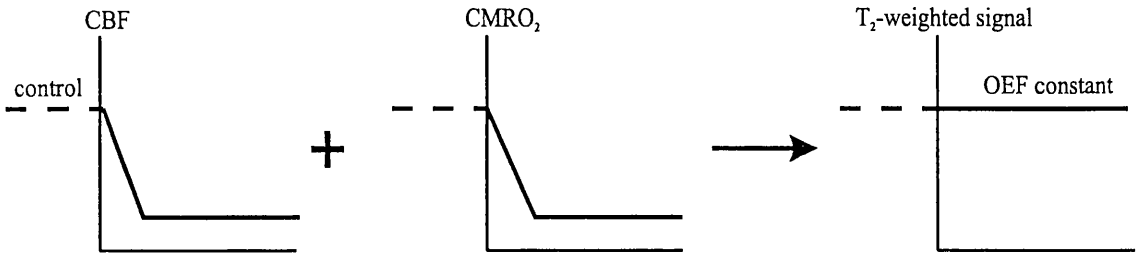

II (i) Uncoupled CBF and $CMRO_2$ with metabolic rate maintained at the initial level (*oligaemic misery perfusion, mechanism: oxygen extraction reserve, (Baron, 1991)*)

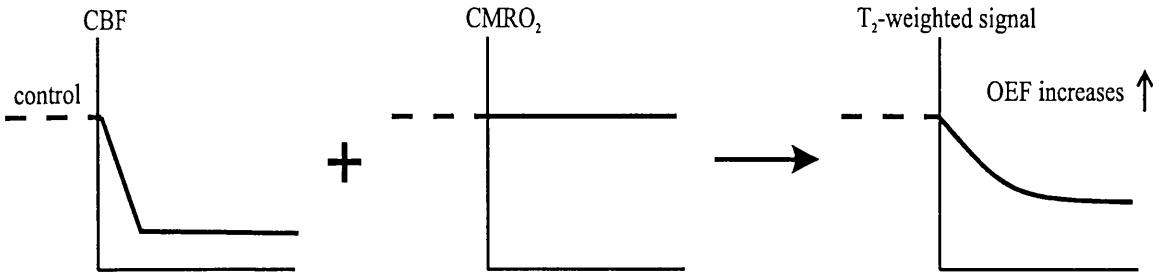

Note: It is suggested in this study that this situation occurs during the initial reperfusion phases in the repeated ischaemia model and is manifested by a T_2-weighted signal that does not completely recover. It also arises during the initial stages of ischaemia (our repeated ischaemia data; also see Roussel, 1995).

II (ii) Uncoupled CBF and $CMRO_2$ with metabolic rate depressed from the initial level (*ischaemic misery perfusion, mechanism: metabolic, neuronal shutdown, (Baron, 1991)*)

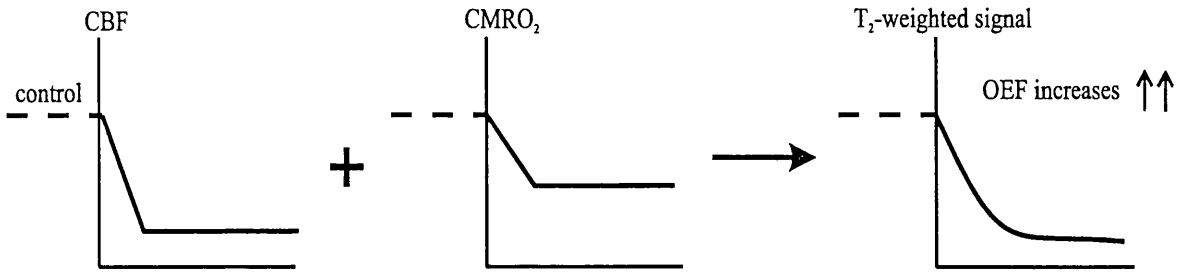

Note: OEF increase is greater than in the case of oligaemic misery perfusion and the depressed metabolism indicates likely tissue injury that is reflected in clinical studies (Baron, 1987). Diffusion imaging should be able to delineate areas of oligaemic and ischaemic misery perfusion since the ADC is unlikely to decline in the former situation.

II (iii) Uncoupled CBF and $CMRO_2$ with a more severe hypometabolism

(relative luxury perfusion, mechanism: ischaemic necrosis, (Baron, 1991))

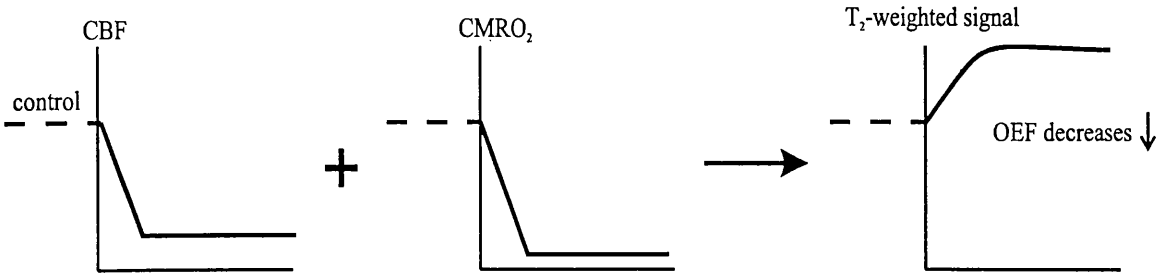

Note: It is suggested in this study that the above situation occurs during the cycle of repeated ischaemic events and accounts for the general, increasing trend in the T_2-weighted signal. This situation also arises in the core of an ischaemic lesion after the initial drop in signal (our repeated ischaemia data; also see Roussel, 1995). The oxygen supply exceeds the demand and this is likely to indicate a developing pathological mechanism.

APPENDIX C : INVESTIGATION OF THE NATURE OF WATER IN HYDROGELS AND IN FLUFF-PULP WITH NMR

This study was undertaken with the aims of utilising the NMR techniques, such as rapid EPI imaging and diffusion measurements, that had been developed during the course of the investigations described in this thesis. The area of application was the study of the absorbent properties and the dynamics of molecular motion in the principal constituents of incontinence pads. This is an area of research that is of significant medical and industrial relevance.

The work was carried out in conjunction with the Incontinence Group of the Department of Medical Physics in University College London (UCL). This Group works in collaboration with several other UCL departments, notably the Division of Geriatric Medicine which is based at St. Pancras Hospital, London. The work involves the clinical evaluation of incontinence products (mostly through the Continence Product Evaluation Network); the creation of International Standards for incontinence products; the design of novel incontinence products; and research projects focusing on the science and technology of absorbency and wider continence issues like skin health and nursing practice.

C1 Introduction

Disposable incontinence pads have become surprisingly complex structures with the layering of different absorbent materials. The introduction of laminated structure is attractive from a manufacturing point of view but assessing the functional performance of such composite products is difficult.

Urinary incontinence – the unintentional release of urine – is a surprisingly common condition which, unless properly managed, can cause a great deal of physical discomfort and psychological distress. Despite advances in the medical treatment of this condition, it is likely that there will always be a need for simple, retentive, patient-worn pads to contain escaped urine. The design of these products is very similar to that of infant disposable diapers. Currently, there exists a plethora of absorbent incontinence pads on the market. The mechanisms of fluid absorption and movement in these pads is not well understood and a means of assessing the different varieties of pads would be great benefit.

Methods such as capacitance mapping, electrical impedance tomography (ECT) and resistive mapping have been employed in order to monitor the spread of fluid through the pad. However, these techniques suffer from poor sensitivity and quantification-related issues. Such methods are cumbersome and may disrupt the structure of the pad. This study has used the technique of MRI which offers the opportunity to gain a better understanding of the mechanisms of water absorption, permeability and mobility within the pads. NMR has the ability to distinguish between difference mobility states of water – *free* or *bound* – and this is exploited in this investigation by measurements of proton density (PD) and magnetisation transfer contrast (MTC) (Section 1.6.3). The information gained from such a study is of potential importance since pad design can only be optimised if the mechanisms of liquid absorption and retention can be better understood.

This investigation was carried out in two stages. Firstly, a simple form of MR spectroscopy was employed in order to evaluate the mechanisms of fluid absorption in the constituent materials of a pad. Quantitative relaxometry, proton density, MTC and diffusion-weighted spectra were acquired. Secondly, high time-resolution MR-imaging was used in order to monitor in real-time, the absorption of water in the pad and its constituent layers.

C2 NMR investigation of the nature of water in material samples

The absorbent layer in incontinence pads consists principally of superabsorbant polymer (SAP) grains scattered through a fluff-pulp material. SAP is a hydrogel, a swollen polymer that possesses the unique attribute of being able to absorb huge quantities of liquid – up to 70 times their own weight of water. In addition to their use in pads and diapers, superabsorbent polymers are utilised in the manufacture of contact lenses, burn wound dressings and membranes. In addition, they are employed for biochemical separation, including gel permeation chromatography and gel electrophoresis, and their application as an NMR tissue phantom has been described (Gore, 1989). Fluff-pulp is a porous material that is derived from wood-pulp. The aim of this study was to investigate the absorptive mechanism of water transport and retention in the constituent materials of the pads – SAP, fluff-pulp and a 50%:50% mixture – using a combination of proton density-weighted and MTC-weighted NMR, diffusion measurements and also T_1/T_2

relaxometry. The liquids used in these experiments were varying concentrations of sodium chloride (NaCl) solution. Urine is approximately 0.9wt% of NaCl.

The proton density-weighted profiles provide information on the amount of water in a free state since the linewidth of bound water is too great to be detected by the spin-echo sequence (TE = 30 ms). The MTC data provides an indication of the relative proportion of the free and bound water pools in the absorbed liquid. The bound compartment will cross-relax with the mobile water pool and reduce the MTR (see Introduction, Section 1.6.3). The diffusion coefficient reflects the random, translational motion of water within the material and will affected by viscosity changes and compartmental restriction. Relaxometry supplies further information regarding water translational and rotational mobility via the interplay of inter- and intra-molecular magnetic dipole forces between the water protons. Relaxation times are related to the correlation times (τ_c) of the water protons in the observed system which reflects the time between *jumps* in the orientation of their individual magnetic fields. The theory of Bloembergen, Purcell and Pound (BPP) expresses the T_1 and T_2 relaxation times in terms of the correlation times and the resonant frequency, ω_0 (Bloembergen, 1948). The relaxation time data should therefore be able to provide information concerning the correlation time regimes of the state of absorbed water within the different materials. It must be taken into consideration, however, that BPP theory is limited in its scope in explaining the relaxation characteristics of multi-compartment solutions such as tissue. It has been pointed out that even if a very small fraction of cellular water is highly immobilised on a macromolecular surface, its correlation time may significantly affect the overall T_1 and T_2 values (Daskiewicz, 1963).

C2.1 Methods

All experiments were carried out on a 2.35T magnet interfaced to a SMIS console. The RF pulses were transmitted with a birdcage, volume coil of length 6.5 cm. The SAP used in this study was a mixture of crosslinked polyacrylic acid and sodium polyacrylate with varying ratios and a principal particle size of 300 μm (50 mesh) (Stockhausen GmBH, Krefeld, Germany).

Proton density (PD) and MTC measurements (n=3 experiments corresponding to 42 measurements): 1 g of (a) SAP, (b) fluff-pulp and (c) a mixture of 50% SAP and 50% fluff-pulp, were added to 10 ml of each of the following liquids: (i) distilled water, (ii)

0.5wt% sodium chloride/water solution [0.086M], (iii) 1wt% NaCl solution; (iv) 10% NaCl solution. After a period of control imaging with both fluid and substrate separate, they were mixed together. Transverse, 1-D profiles of the entire volume were acquired with a standard spin-echo sequence (TR = 15 sec; TE = 30 ms; 6 or 30 repeated acquisitions before and after addition of liquid) with an RF top-hat pre-pulse for MTC (B1 strength = 60 mG (255Hz); pulse length, T_p = 5 sec). Interleaved acquisition of proton-density (frequency offset, Δf = 100 kHz) and MTC spectra (Δf = 2 kHz). It was necessary to apply the MTC pulse at a large frequency offset during the PD-weighted acquisition because the 5 sec pre-pulse affected the subsequent RF amplifier characteristics. Profiles were analysed by integrating for the area.

T_1, T_2 and ADC measurements (n=4 experiments): After a period of control imaging, 1 g of (a) SAP and (b) fluff-pulp, were added to 10 ml of (i) distilled water and (ii) 10wt% NaCl solution. A similar sequence as described previously was implemented. For measurements of the spin-lattice relaxation time, T_1, the TR was varied in 8 steps from 0.5-5 sec (500, 100, 1500, 2000, 2500, 3000, 3500 and 5000 ms) and the data fitted to saturation recovery curve. For measurements of the spin-spin relaxation time, T_2, the TE was varied in 8 steps from 30-900 ms (30, 60, 100, 200, 400, 500, 700 and 900 ms). For ADC measurements, a spin-echo sequence with bipolar diffusion gradients alternatively applied along read and phase directions, was employed (TE = 90 ms; Δ = 44 ms; δ = 22 ms; b-value = 700 sec/mm^2). The two diffusion coefficients (ADC_x and ADC_y) were averaged together since the mixtures are homogeneous. Profiles were analysed by integrating for the area.

C2.2 Results

Proton density and MTC measurements

A representative data series from one of the experiments is shown in Fig. C1 and the overall results are shown in Fig. C2 with the PD-weighted signal and the MTC ratio (MTR) normalised to the control level. The MTR is defined as

$$MTR = \frac{M_S(\Delta f = 2kHz)}{M_0(\Delta f = 100kHz)} \qquad [C1]$$

where M_0 and M_S are the interleaved PD-weighted and MTC-weighted profiles respectively.

PD: The proton density-weighted signal always declined on mixing together the fluid and material sample but in varying degrees in each case. This indicates different degrees of water binding in these samples. Between the materials, the magnitude of the PD change increased in the order, SAP, 50%:50% mixture and fluff-pulp. Between the different solution concentrations, the magnitude of the PD change decreased with increasing concentration of the NaCl solution. In the SAP, there was not a statistically significant difference.

MTC: The change in the MTR was minimal and non-significant when mixing the superabsorber with the liquids. In the other material combinations, a decrease in the MTR was observed. Between materials, the magnitude of the MTR change increased in the order, SAP - mixture - fluff-pulp. Between solutions, the change of the ratio decreased with increasing concentration of the NaCl solution, but in the SAP, this was not a statistically significant difference.

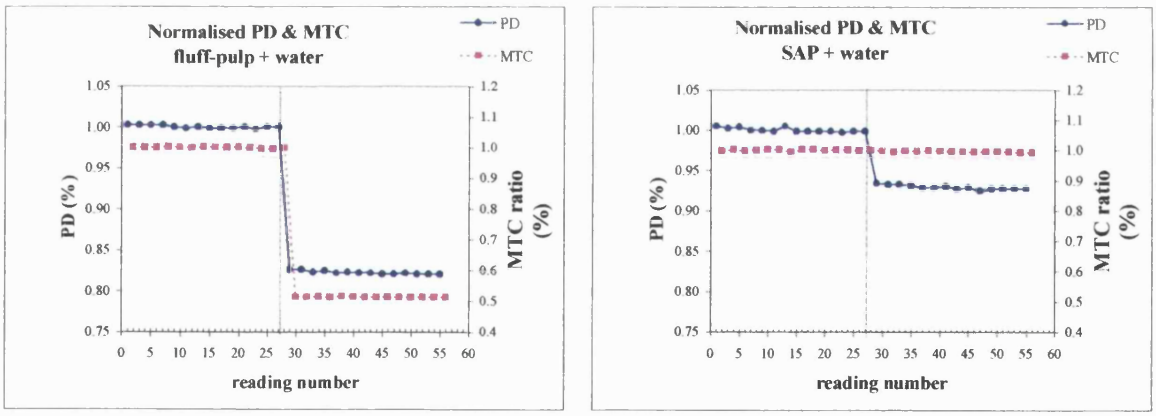

Fig. C1 Representative experimental data series from PD / MTC experiments in SAP and fluff-pulp. The vertical dotted line indicates the instant of water addition to the sample.

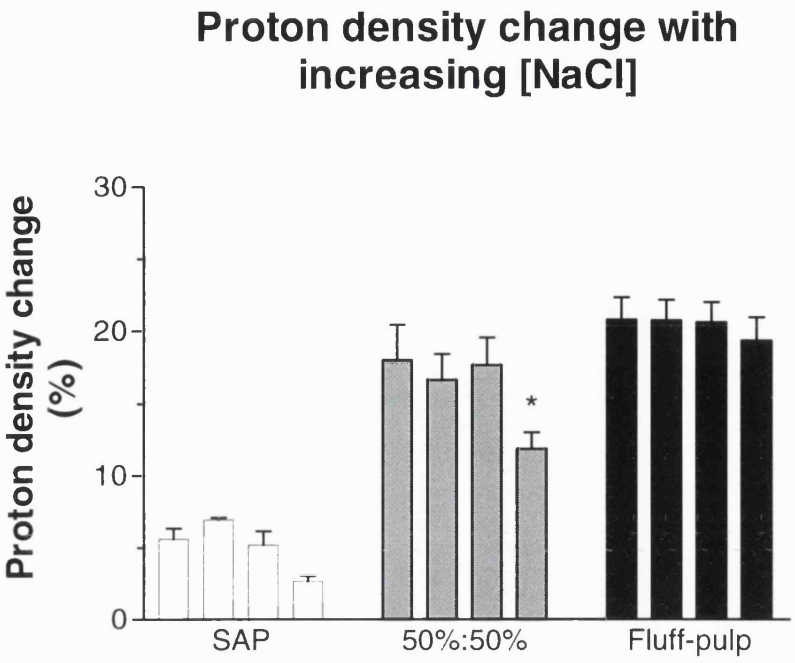

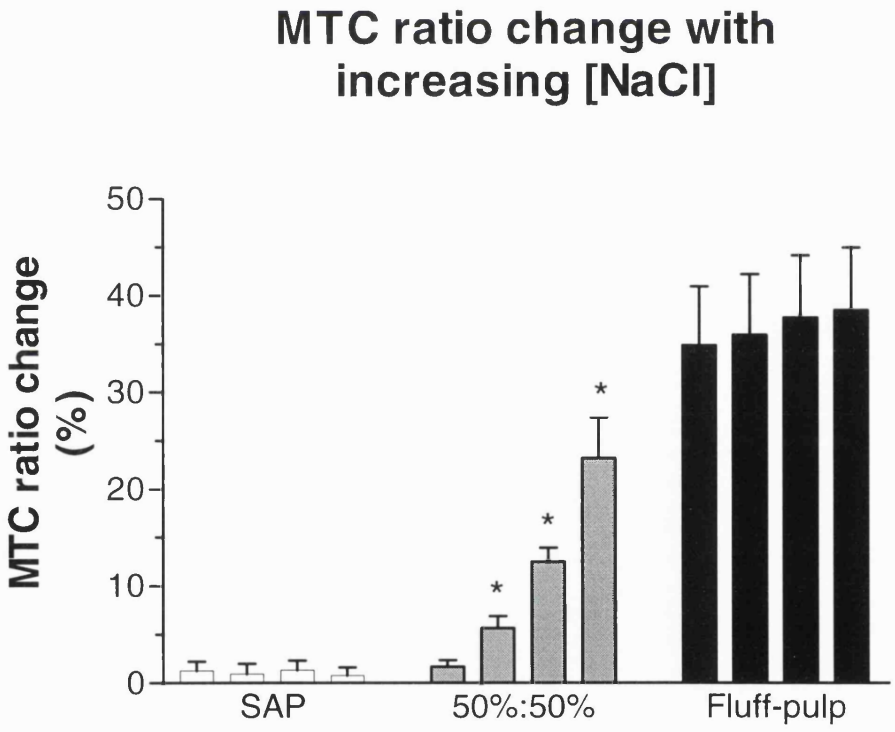

Fig. C2 Proton density and MTC ratio changes with increasing concentration of NaCl (0%, 0.5%, 1% and 10% by weight). * indicates a significant difference with respect to the values obtained with water ($P < 0.05$). A positive percentage change indicates a decrease in the parameter after mixing the liquid and material. Error bars are ±SEM.

T_1, T_2 and ADC measurements

Results are shown in Fig. C3 which depicts the percentage ratio of parameter changes. For example, in the case of T_1 and the fluff-pulp/water combintation, this ratio becomes

$$\Delta T_1(\%) = \left[\frac{T_1(water) - T_1(fluff + water)}{T_1(water)}\right] \times 100 \qquad [C2]$$

where T_1(fluff-pulp+water) is the relaxation time of the mixture. A decline in all the parameters was observed on mixing the material and fluids together.

T_1 : The T_1 decline of water in the presence of fluff-pulp was of a significantly greater magnitude than for SAP (P=0.02, paired t-test). In the case of NaCl solution, the difference between the relaxation time of the solution in the two materials did not achieve statistical significance. The data suggested that the 10% NaCl solution possesses a lower T_1 than water (control data) but this did not achieve statistical significance.

T_2 : The T_2 decline was far greater when adding either liquid to fluff-pulp in comparison to the same change observed in the presence of SAP (P<0.001). It can be clearly seen in Fig. C3 that the ratio in T_2 changes between the two materials (i.e. $\Delta T_2(\%)$[fluff-pulp]/$\Delta T_2(\%)$[SAP]) is greater than the corresponding T_1 decline (P=0.01, paired t-test on SAP:fluff-pulp ratios)

ADC : The ADC of the NaCl solution was significantly lower than water (control data) (P<0.0001). On mixing the liquid and material substrates, a decline in the diffusion coefficient was observed that was characterised by the absence of a significant variation between SAP and fluff-pulp and between water and NaCl solution.

C2.4 Discussion

In light of the results, the conclusions that were drawn from the two experiments regarding the state of absorbed water in the different materials, are described in turn.

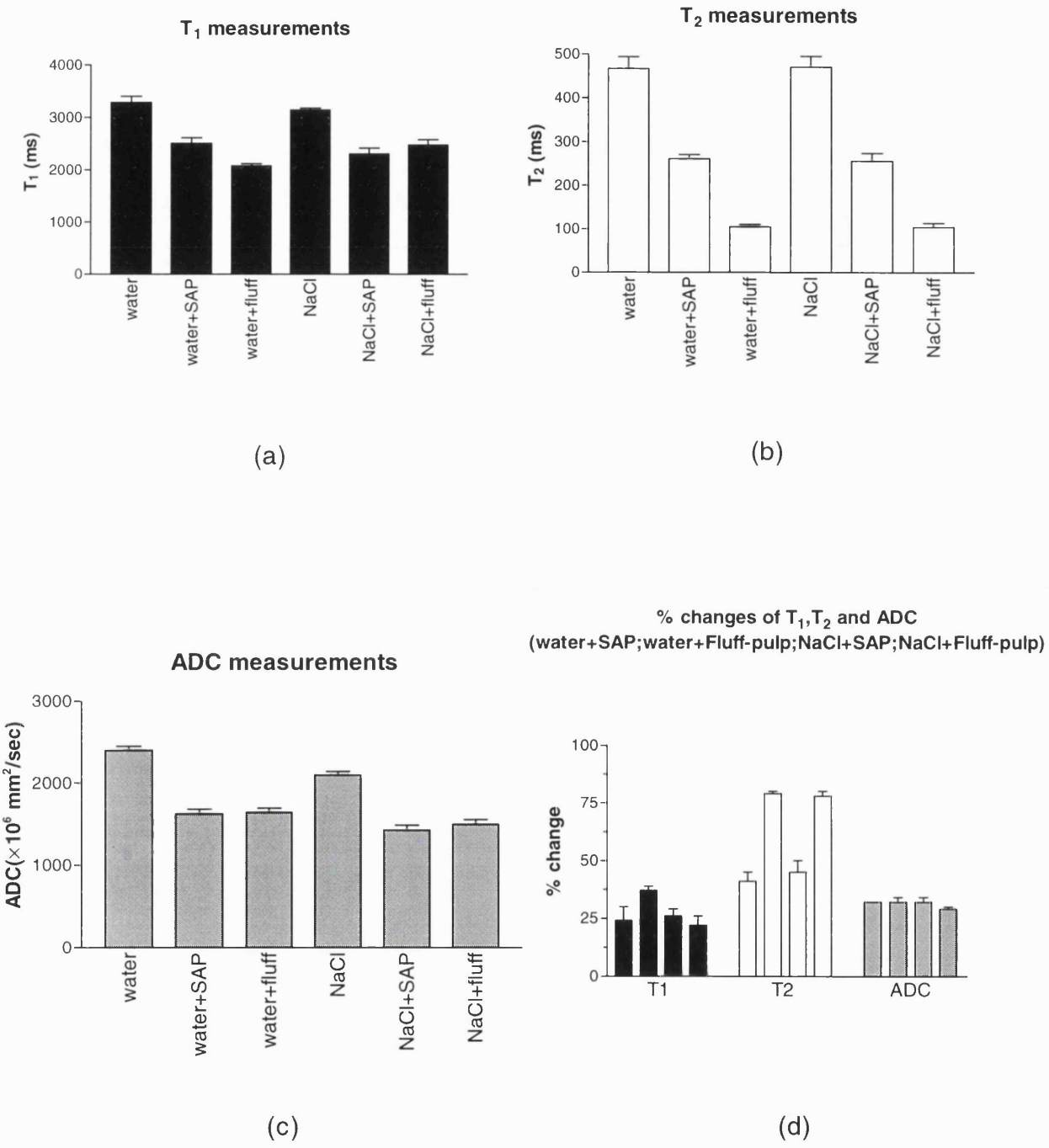

Fig. C3 Summary of T_1, T_2 and ADC data.

Measurements of (a) T_1, (b) T_2 and (c) the ADC, in SAP and fluff-pulp with water and 10wt% NaCl solution
(d) Percentage change (before addition / after addition). For each parameter, ratios are displayed for, in order, water+SAP, water+fluff-pulp; 10%NaCl+SAP; 10%NaCl+fluff-pulp.

A positive percentage change indicates a decrease of the parameter. Error bars are ±SEM.

C2.4.1 Proton density and MTC measurements

The somewhat surprising finding of only a relatively small proton density decline on mixing the water and the SAP, indicates important information regarding the state of water in these superabsorbent materials. It is apparent that water is not principally being tightly bound by the polymer. It is presumably being absorbed via driving forces such as osmotic pressure and electrostatic mechanisms through the porous structure of the hydrogel. The principal mode of water transport through the SAP grains is believed to be a diffusive mechanism (Buchholz, 1998). The water moves to a lower energy state within the ploymer network and the associated slower diffusion of the polymer contributes to granular swelling. The fibre-like polymer elements are crosslinked with chemicals so that the polymer gains rigidity and remains insoluble, and form numerous interconnections. A haphazard network configuration thereby results (Fig. C4).

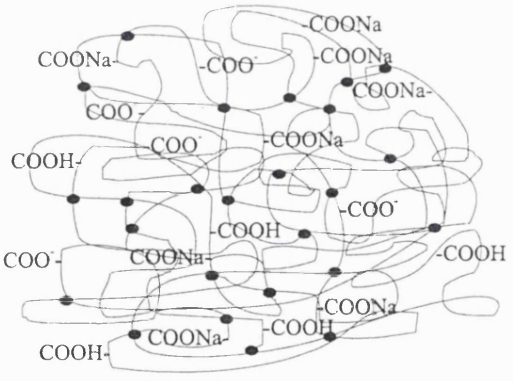

Fig. C4 Schematic representation of a crosslinked polymer network. The dots represent the crosslinks between the coiled polymer chains, which have carboxylate functional groups spaced along their length

The water molecules are free to diffuse through the pores that exist between these complex chains driven by osmotic and electrostatic mechanisms. The minimal change of the MTC ratio in SAP is a further indication of the absence of a *tight* water binding mechanism. It has been suggested that the principal binding site of water in SAP are the electric dipoles (-COOH) or fixed charges ($-COO^-$) of carboxyl groups (Rajamohanan, 1995; Stockhausen, personal communication). This, however, appears to be a secondary mechanism to that of hydration of the sodium ions and a significant PD change is, therefore, not expected. The resulting hydrogen bond is apparently of

insufficient strength or in insufficient numbers, for the water to be considered bound in the NMR sense. Other likely sources for water binding in SAP are the sodium ions associated with the carboxyl groups ($-COO^-Na^+$). Water will bind to the fixed charge (Na^+) via its OH^- group. The water molecule's remaining proton is electropositive and attracts surrounding water molecules. The resulting electric dipole bonds are not as strong as the hydrogen bond (and therefore will not cause a significant PD decrease) but may participate in the water-mediated linking of the polymer chains.

With an increasing concentration of NaCl solution, the PD and MTC changes decreased and increased respectively, but both only to a small extent. This reflects the reduced ability of hydrogels to absorb fluid in the presence of salt solutions. This is due to the polyelectrolytic nature of the SAP. The polymer chains can be considered as a polyelectrolytic macro-ion whose positive charge is balanced by bound sodium ions within the polymer (from the sodium polyacrylate component). In the presence of a dissolved sample electrolyte such as NaCl, the Coulomb potential of the macro-ion's charge is diminished and the apparent charge of the macro-ion is therefore decreased. The attachment of mobile Na^+ from the simple electrolyte will also act to reduce the absorptive capacity of the polymer by diminishing the osmotic pressure that drives the process of water absorption.

In the fluff-pulp, the proton density-weighted signal decreased to a far greater extent in comparison to SAP, and a larger MTC effect was also observed. The fibrous fluff-pulp material has a porous structure (Fig. C5(a)) and the absorption of water will occur by flow and convective mechanisms driven by capillary pressure through the pores (Buchholz, 1998). The dimensions of these pores are relatively large in comparison to those in SAP. The principal constituents of fluff-pulp are cellulose fibres. Cellulose molecules are relatively long and flat with a large surface area that offers many suitable hydroxyl ($-OH^-$) binding sites to water. The resultant hydrogen bonds are strong enough to cause the large PD change in the fluff-pulp material. The cellulose molecule will offer a large interfacial area for cross-relaxation between the bulk, mobile water and the absorbed, bound component. The MTC effect is therefore significantly larger for fluff-pulp than in the case of SAP.

The MTC effect decreased with increasing NaCl concentration. A suggested mechanism for this response is the ability of the sodium ions in the simple electrolyte to bind to the

hydroxyl sites in the cellulose molecule. The hydrophilic nature of the sodium ion is also be reflected in the formation of hydration shells.

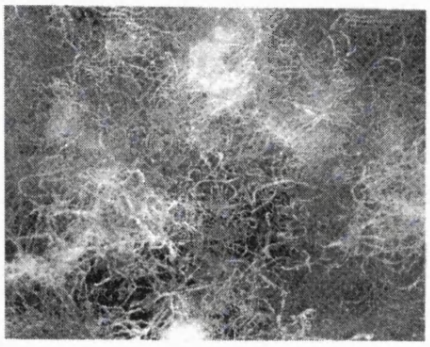

(a)

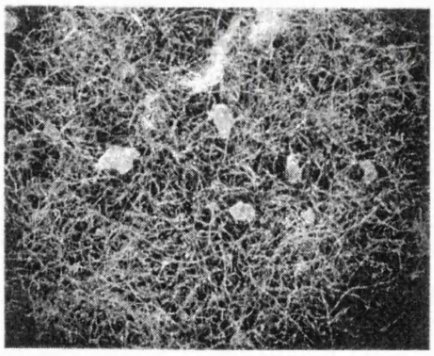

(b)

Fig. C5 Optical images of (a) fluff-pulp, and (b) a composite of fluff-pulp and superabsorbent polymer granules (magnification ×10) (from Buchholz, 1998).

A hydration number of 5-6 has been demonstrated (Kang, 1883) although presumably, secondary shells will also form. The newly bound sodium ion in the cellulose molecule will therefore be surrounded by water molecules. The $-Na^{+}-H_2O$ bond (via the hydroxyl group in water rather than a hydrogen-bond) is of insufficient *strength* to be observed as a further decrease in the proton density signal. However, the increased size of the *superstructure* formed by the combination of the polymer/sodium/hydration-shell, may result in the larger MTC effect either (i) by increasing the size of the macromolecular structure that can cross-relax with the mobile, bulk water, or (ii) by providing a greater opportunity for the relatively free protons in the hydration shells themselves to cross-relax with the bound compartment within the polymer.

The 50%:50% mixture of SAP and fluff-pulp would be expected to display an intermediate response. However, on addition of water to the combined materials, the MTC data implies a significant component absorbed in the SAP but the PD decline implies a greater than expected proportion of water within the fluff-pulp component (Fig. C2). This requires further investigation. The increasing MTC effect with increasing NaCl concentration may signify a further increase in water within the fluff-pulp component as the SAP becomes gradually less effective. A possible mechanism for this observation is extensive absorption by the SAP but with an increased MTC effect due to the close proximity of the hydrogel polymer and the cellulose molecules in the fibrous fluff-pulp. Fig. C5(b) displays a magnified image of SAP grains distributed in fluff-pulp.

In a separate experiment, a 1 g piece from a standard complete pad (Paul Hartmann GmBH, Germany) was investigated with the PD- and MTC-weighted sequence (n=2, data not shown) On addition of 10 ml of water, the PD decrease (22±1%) and the MTR decrease (22±3) (cf. Fig. C2), and the T_1 and T_2 decreases (28% and 62% respectively) (cf. Fig. C3), are an indication of an even greater proportion of the water within the fluff-pulp compartment. The pad was cut open at the end of the experiment. The SAP grains had swollen but the surrounding fluff-pulp was damp. A variable response is, however, expected from different pads, even from the same manufactured batch, because of different characteristics and distributions of the SAP grains.

In an additional experiment, samples of SAP and fluff-pulp were mixed with vegetable oil. No changes in the PD or the MTC effect were observed (data not shown). This is a further indication of the hydrophilic nature of the absorbent process in both materials.

C2.4.2 T_1 and T_2 measurements

Mono-exponential exponential recovery curves were fitted to all the T_2 data. This treatment relies upon the mono-phasic character of water in these materials within the exchange time defined by the measurement time of our experiments ($\approx$ 30 ms). However, biexponential behaviour is expected especially in fluff-pulp in which a substantial bound water component has been predicted. The limited SNR of our study and the number of data points (minimum TE = 30 ms) are insufficient to confirm this hypothesis. Further investigation of potentially multi-exponential behaviour is required. The division of water into free and bound compartments is a simplification and intermediate components, known as, for example, hydration water and structured water (Fullerton, 1992) need to be considered.

The relaxation times both declined on mixing the water and the samples of SAP and fluff-pulp (ΔT_1 : -23% and -36% and ΔT_2 = -40% and -78%, in SAP and fluff-pulp respectively). The reduction in the spin-spin relaxation time is sufficient to account for the PD-weighted signal changes (for TE = 30 ms) described previously. The reduction in both relaxation times reflects a decreasing water mobility that is associated with an increased water proton correlation time in the liquid/sample mixture. A greater change in correlation times occurs in the more tightly bound fluff-pulp system. In the SAP mixture, the rising correlation time is presumably simply due to a decreased water mobility as the hydrogel expands, while in the fluff-pulp, the hydrogen-bonded water molecules will contribute to a larger change. The decreasing relaxation times, also reflects the porous nature of the two materials. Previous studies have employed relaxometry to investigate porosity and permeability in different porous materials (for example, Hollewand, 1994; Kleinberg, 1994). The pores affect the relaxation characteristics since the relaxation rate of the water on the pore surface is faster then that of the bulk water inside the pore and in the surrounding fluid (Brownstein, 1979). An NMR study of the porosity of hydrogels has analysed the volume-to-surface-area ratios of the pores (in the order of nm) using a fibre-cell model of fast diffusion (Chui, 1995).

In terms of the BPP relationship, the data assigns the range of relevant correlation times to the region close to the T_1 minimum in Fig. C6 (where $\tau_c = 1/\omega_0$) since both relaxation times declined but to different extents in the two materials. This is the area of the BPP curve that optimally describes the properties of viscous liquids such as oil and fat ($\tau_c \approx 10^{-9}$), and it can be seen that in this range, the rate of change of T_2 with correlation time is much greater than the corresponding change of T_1. In fluff-pulp, the magnitude of the decline of the spin-spin relaxation time was significantly larger than the change of this relaxation time in SAP. This reflects a greater change in correlation time for water during absorption in fluff-pulp. In the central region of the BPP curve, a more substantial τ_c increase will further enhance the rate of T_2 relaxation. Its affect on T_1 relaxation is more complex but if, as Fig. C6 shows, the correlation time shift is sufficient to take the proton over the T_1 minimum, then the increase in the spin-lattice relaxation time will be comparable to that induced by the significantly smaller correlation time change that occurs in the presence of SAP.

The difference in the relaxation time responses can also be understood in terms of the frequency components that contribute to the two modes of relaxation (see Section 1.6). Both T_1 and T_2 are induced by magnetic field fluctuations at the Larmor frequency, ω_0, but T_2 relaxation is also affected by an extra component, at zero frequency (in the rotating frame of reference). This significance of this additional term is apparent in the data where magnetic field variations at a frequency, ω=0, are enhanced in the case of absorbed water within fluff-pulp but not within the superabsorbent.

On changing the fluid from water to NaCl solution, the pattern in the relaxation time data does not appear to significantly change. As previously described, the mechanism of absorption in the presence of a salt solution is unlikely to involve any major structural changes that would be expected to affect the correlation time (and presumably reflects an osmotic response).

C2.4.3 ADC measurements

The diffusion coefficient of sodium chloride solution is approximately 15% less than the ADC of pure water. This indicates the increased viscosity of 10% NaCl solution due to the accumulation of hydrated sodium ions.

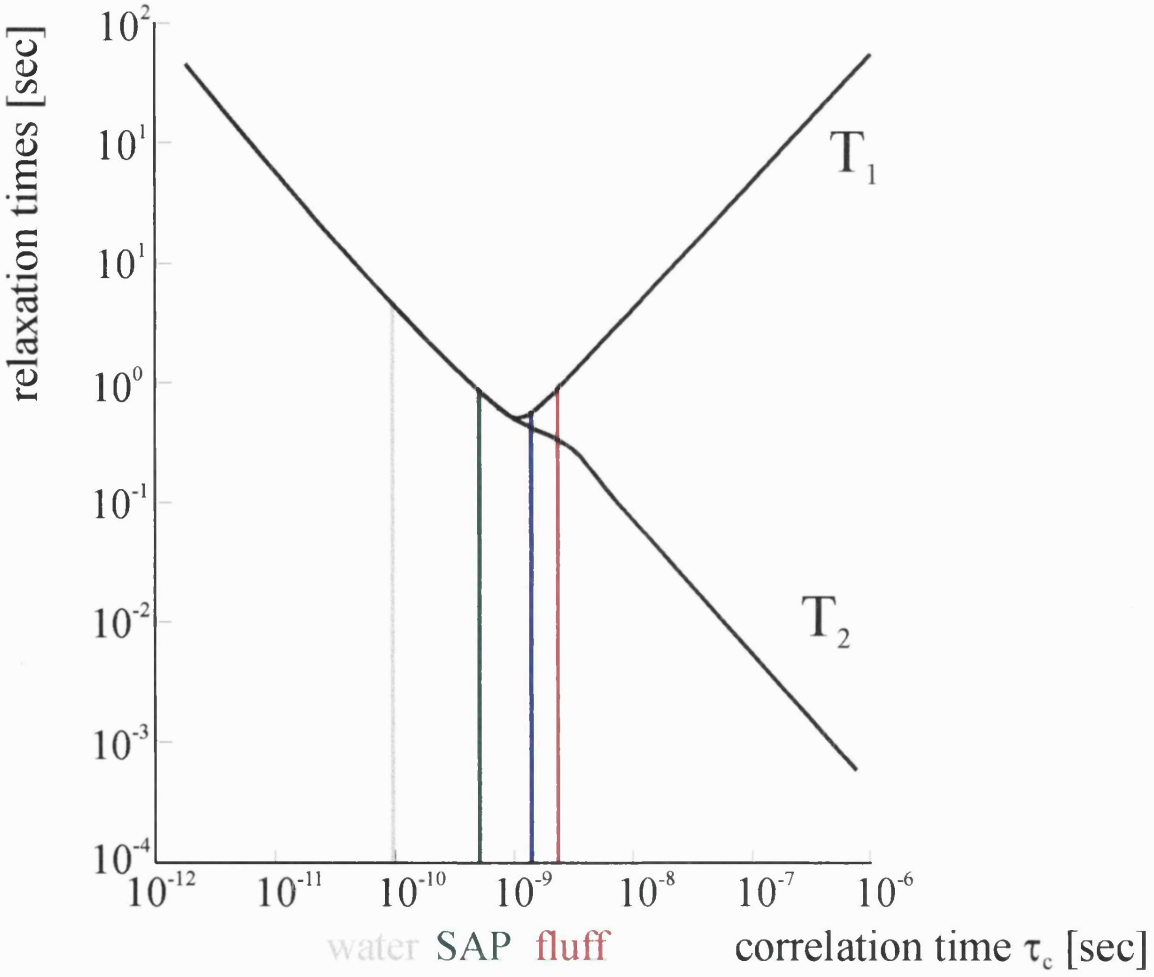

Fig. C6 A schematic depiction of the BPP relationship. The point at which the blue line crosses the curves, depicts the point at which $\omega_0\tau_c=1$, and the grey line is the approximate position of pure water. The green and red lines are a schematic representation of the relative correlation times of SAP and fluff-pulp respectively. The greater correlation time increase in the case of water absorption in fluff in comparison with SAP is manifested by a similar T_1 relaxation time, but by a significantly reduced value of T_2.

(The T_1 data also suggested a reduction in this relaxation time due to an increased correlation time but this was not statistically significant, but should be enhanced for greater salt concentrations). The Stokes-Einstein diffusion coefficient relates viscosity to diffusion according to

$$D = \frac{kT}{6\pi\eta R_{HD}} \qquad [C3]$$

where D is the diffusion coefficient, η is the viscosity and R_{HD} is the hydrodynamic radius of the spherical particle.

A further decline in the ADC was measured on mixing the liquid and material together, indicating a further restriction in translational water mobility. No significant difference was found in these changes when using different liquid or material combinations. It has been suggested that the addition of salt to a hydrogel will reduce, rather than increase, the viscosity of the mixture due to the interaction of the electric potential of the macro-ion and the simple electrolyte (Chaterjee, 1975). The contrary observation was however observed in our study.

C2.5 Conclusion

This study has employed NMR to investigate the state of water in the different components that constitute the absorbent layer in an incontinence pad. Quantitative measurements of relaxation times, proton density, MTC and ADC measurements have provided information related to the state of the absorbed water. Relaxation times are controlled by a number of processes operating in parallel, such as bulk relaxation, compartmental relaxation rates, and relaxation by diffusion through field gradients. Nevertheless, by examining the relative changes in these times on varying the liquid and material combinations, it has been possible to infer properties of water mobility and environment.

It has been shown that the unique absorbent properties of SAP are not characterised by a *tight* water bond. Instead, the water molecules are more likely to be absorbed and transported by diffusive and osmotic forces into the interior of the polymer structure where it remains relatively mobile. This is in stark contrast to fluff-pulp in which a considerable proportion of the water becomes tightly hydrogen-bonded to the cellulose molecules where it can cross-relax to a great extent with the surrounding bulk water.

The observation of different water mobilities in SAP and fluff-pulp is somewhat surprising since SAP can absorb approximately 80 times more water than fluff-pulp. Similarly, unlike the behaviour of wetted fluff-pulp, the swollen superabsorbent polymer will not release the water when squeezed between one's fingers.

The relatively mobile nature of water in the hydrogel has been implied by a low-temperature NMR study that reported a substantial free water signal obtained at sub-zero temperatures (Yasuda, 1972). Many other studies have described a contrary, response – the multi-phasic character of water in these polymers with bound, free and intermediate components (Krishnamurthy, 1973; Lee, 1975; Taniguchi, 1975). Techniques employed in these investigations have included ultrasound (Koda, 1994) and differential scanning calorimetry (DSC). The latter technique measures the heat enthalpy changes as frozen hydrogels are thawed but the relevance of data obtained during the low temperature, non-equilibrium state, has been disputed (Roorda, 1994). An NMR study with ^{17}O-labelled water reached similar conclusions to those described in our investigation (Roorda, 1994). The use of labelled oxygen rather than hydrogen within the water molecule allowed closer investigation of the intra-molecular state of the molecule (the relaxation rate of the oxygen is on the order of ms). In this study, no evidence of a bound component was obtained and the mobile state of the water was demonstrated.

By substituting water with sodium chloride solution, it has been possible to demonstrate the effect of simple electrolytes on the absorptive abilities of the material substrates. A chemical rather than a structural change has been implicated. In SAP, the detectable change on substituting the fluids was unexpectedly small considering the weakened absorbent capability in a salt solution. In the aforementioned ^{17}O NMR study, the results were similarly unchanged by the substitution of water with sodium chlorate ($NaClO_4$) solution (Roorda, 1994).

C3 Imaging study of water absorption in the constituent layers of a pad

The aim of this study was to follow the time course of water absorption in the pads, with the use of rapid, MR-imaging with EPI, while the water was being remotely directed onto the material. In addition to testing the pad in this way, its constituent layers were separately analysed. A composite, layered pad was also constructed using water-filled capillary tubes to delineate the layers.

C3.1 Methods

All experiments were carried out on a 2.35T magnet interfaced to a SMIS console. The RF pulses were transmitted with a birdcage, volume coil of length 6.5 cm. Time course studies were carried out on the following materials, (a) 4×4×1 cm^3 (width×length×height) section of a layered pad (n=2), (b) 4×4×1 cm^3 section of the bottom layer, which is made up fluff-pulp (see next section) (n=2), (c) 4×4×1 cm^3 section of the middle layer which consists of SAP and fluff-pulp (see next section) (n=2), (d) 5 g of SAP (polyacrylic acid + sodium polyacrylate) (n=1), and (e) 4×4×1 cm^3 section of a home-made composite pad with capillary tube markers between the layers (n=2).

The samples were individually placed in the RF coil and during imaging, 10 ml of distilled water was remotely added via a plastic tube connected to a syringe.

A spin-echo EPI sequence with a 1 sec time resolution was used to obtain transverse images (TE = 37.5 ms; TR = 1 sec; slice thickness = 2.5 mm; FOV = 55 mm; image matrix size = 64×128). Imaging was continued for 2-5 min. Multi-slice proton density-weighted images with a high degree of spatial resolution were subsequently obtained with a 2D-FT spin-echo sequence (TE = 30 ms, TR = 15 sec; image matrix = 128×128 or 256×256; slice thickness = 1 mm; transverse and coronal planes).

C3.2 The structure of a layered pad

Incontinence pads are usually made up of three principal layers. These layers are as follows:

Top layer: This layer sits under a thin coverstock. The top layer consists of short, curly fibres. The intention is that this layer will rapidly receive liquid, and because of its relatively open structure, allow it to pass into the middle layer. Furthermore, this layer should retain its open structure and resist wet collapse.

Middle layer (*Basis Matte*): This layer in intended to form the bulk of the absorbent function of the pad. It contains superabsorbent particles and fluff-pulp. Rapid fluid absorption by SAP grains is hindered by their swelling since the particles make contact with each other and *gel blocking* results. It is therefore necessary to embed the SAP grains in the wettable fluff-pulp material. The absorbent layer takes in the fluid and

distributes it to distal regions. This layer extends over a larger surface area than the top layer, but does not cover the entire area of the pad.

Bottom layer (*Grunde Matte*): This layer consists of a relatively thin layer of fluff-pulp, and serves principally to act as a reservoir and to deal with any fluid that is not handled by the middle layer. This layer extends over the majority of the pad area. It sits above a thin, non-porous waterproof backing.

C3.3 Results and Discussion

The EPI images of the wetted pad and its layers were of relatively poor quality. This is because of the porous nature of the constituent materials and the resulting water/air/material susceptibility-related artefacts. This was especially apparent in the pads containing SAP when the significant swelling introduces large air cavities within the sample and increases the susceptibility differences. Figure C7 displays a transverse EPI image together with a 2D-FT spin-echo image of a swollen pad. EPI images of the bottom layer and the SAP sample are also shown.

The high time resolution imaging allowed investigation of the *activation time* of the SAP within the pad, which reflects the time it takes the SAP to become fully swollen. It was possible to distinguish the presence of water in the fluff-pulp and the SAP compartments in the pad, by examination of the images obtained during the single sample experiments (samples (b) and (d) in the Methods section). Figure C8 displays the images obtained during a time-course experiment in which water was added to the complete pad (sample (a)). The initial images show a high region of signal intensity in the top layer that acts as an early reservoir of fluid. The signal in the rest of the pad is relatively homogeneous and this indicates the rapid, initial wetting of the fluff-pulp component in the middle layer. After approximately 10-15 sec, the appearance of the image became more diffuse. This reflects the initial activation of the SAP particles during this stage. The images became gradually more diffuse as the pad swells. By approximately 70 sec, the images have stabilised in overall signal intensity. These measurements were consistent with results from experiments performed on similar samples of complete pad (sample (a)), the middle layer (sample (c)) and on the separate sample of superabsorber (sample (d)). A representative time-course from the sample of SAP is shown in Fig. C9. It can be seen that the signal distribution in the images remains constant after approximately 80 sec.

Proton density-weighted images of the different samples are shown in Fig. C10. In the image of the complete pad, the particulate nature of the images reflects the presence of the water within the swollen SAP grains (cf. EPI images of SAP in Fig. C9). The image of the bottom, fluff-pulp layer displays a uniform pattern of water absorption. In the image of the composite, home-made pad, the signal intensity is confined to the middle layer. This confirms the absorption of all the water by the middle layer of SAP and fluff-pulp.

C3.4 Conclusion

This study has demonstrated the utility of using MR-imaging in following the absorption of fluid by the constituent materials of a pad. A determination of the SAP activation time of approximately 70 sec for hydrogel swelling has been obtained. Other values quoted for this measurement are 100 sec (Stockhausen, personal communication) and 85 sec (Cutié, 1998) using the standard, vortex technique.

Such MRI studies offer the opportunity to provide information that can aid pad designers in such matters as ideal distribution of the superabsorber particles, and the optimal design of the composite layers that make up a standard incontinence pad.

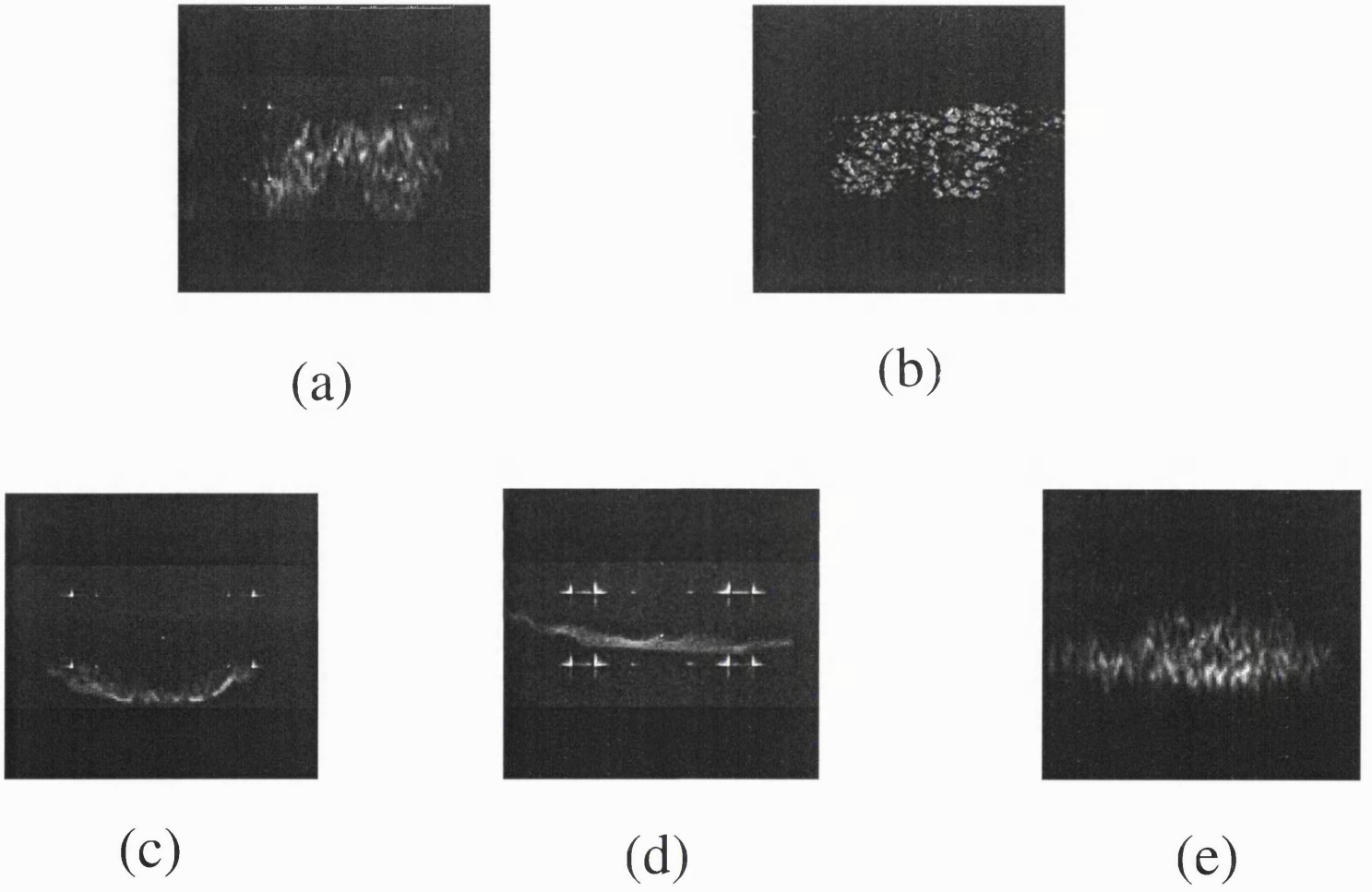

Fig. C7 Comparison of (a) an EPI image (TR=15 sec) and (b) a 2D-FT SE image of a complete pad. EPI images of (c) SAP grains, (d) fluff-pulp and (e) the middle layer are also shown for comparison.

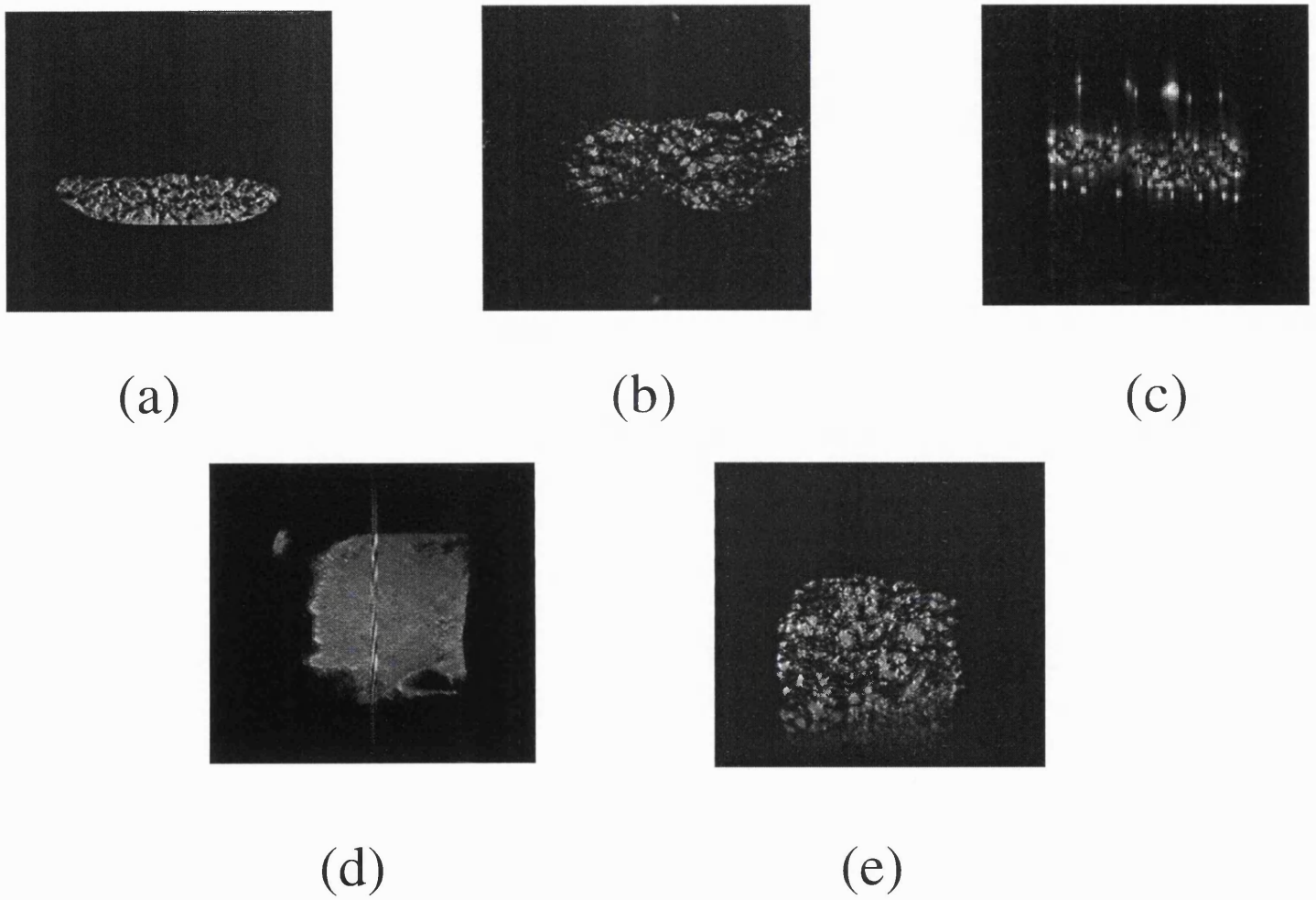

Fig. C10 Spin-echo 2D-FT transverse images of (a) SAP, (b) pad and (c) the composite pad. Coronal images of (d) fluff-pulp and (e) the middle layer are also shown.

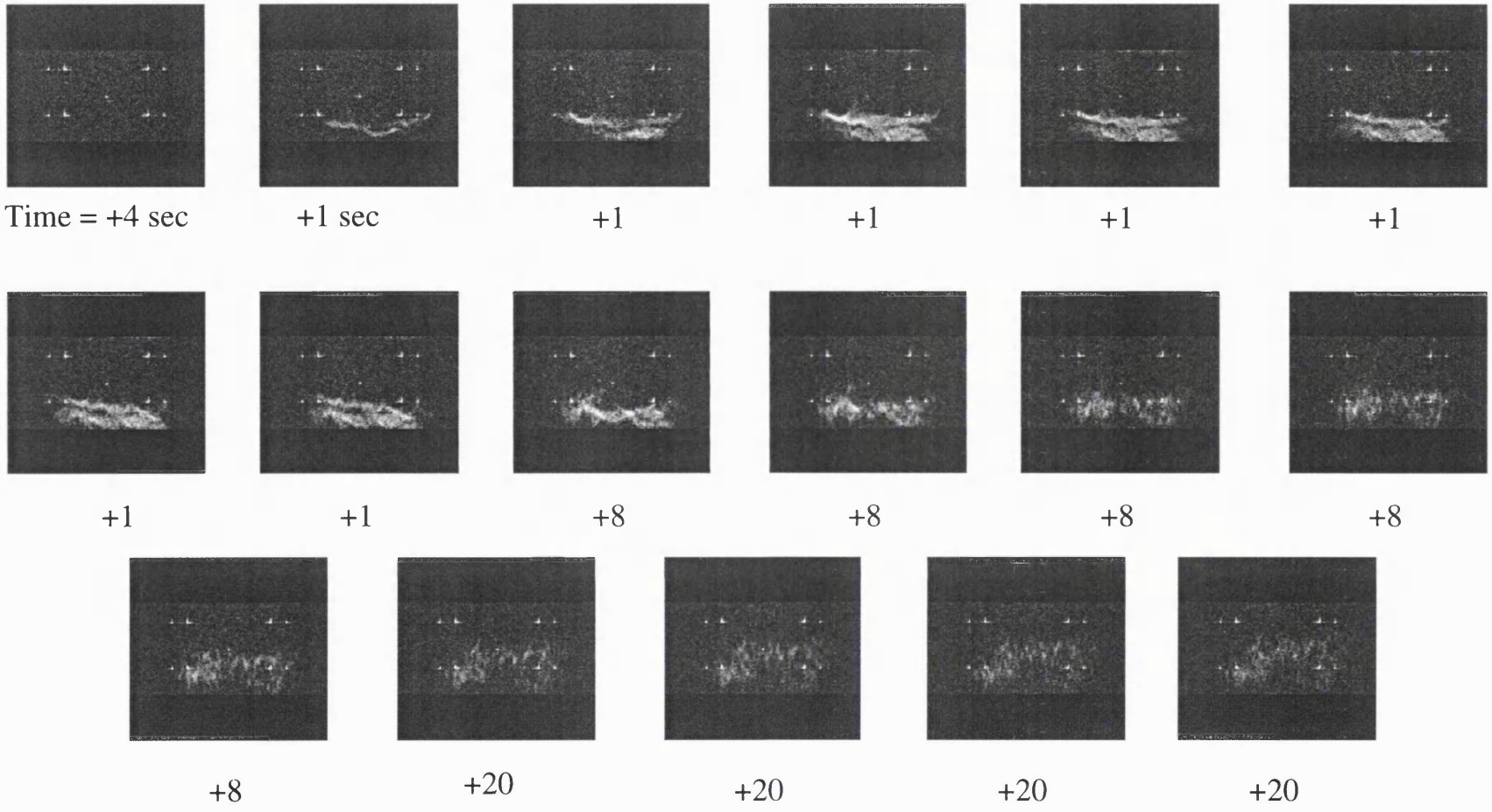

Fig. C8 EPI time course of water absorption in a piece of complete pad material. Time=0 sec is the moment of water addition, and increments in seconds are measured from this point. EPI images were collected with a 1 sec time resolution and a selection of the images are shown here.

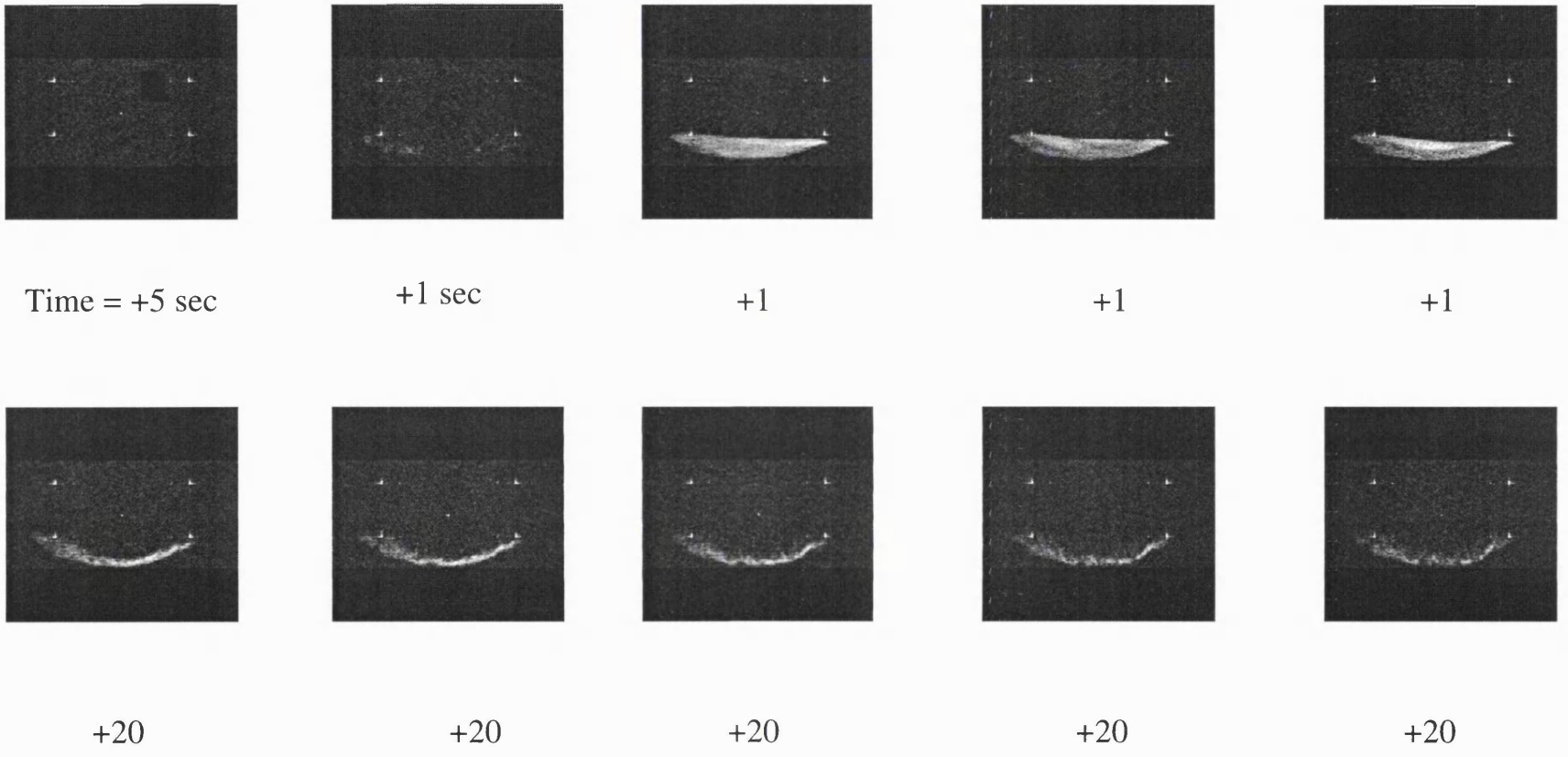

Fig. C9 EPI time course of water absorption in SAP grains. Time=0 sec is the time of water addition. EPI images were collected with a 1 sec time resolution and a selection of images are shown here.

REFERENCES

Ahn, C.B., Cho, Z.H., Analysis of eddy currents in nuclear magnetic resonance imaging. *Magn. Reson. Med.* **17**, 149-163 (1991)

Alger, J.R., Brunetti, A., Nagashima, G., Hossmann, K.A., Assessment of postischemic cerebral energy metabolism in cat by ^{31}P NMR : The cumulative effects of secondary hypoxia and ischemia. *J. Cereb. Flow Metab.* **9,** 506-514 (1989)

Allen, K.L., *Studies of experimental cerebral ischaemia using NMR and hydrogen clearance*, PhD Thesis (1992)

Allen, K. L., Busza, A. L., Proctor, E., King, M. D., Williams, S. R., Crockard, H. A., Gadian, D. G., Controllable graded cerebral-ischemia in the gerbil - studies of cerebral blood-flow and energy-metabolism by hydrogen clearance and ^{31}P NMR-spectroscopy. *NMR Biomed.* **6**, 181-186 (1993)

Almeida, A., Allen, K.L., Bates, T.E., Clark, J.B., Effect of reperfusion following cerebral ischaemia on the activity of the mitochondrial respiratory chain in the gerbil brain. *J. Neurochem.* **65**, 1698-1703 (1995)

Alsop, D. C., Detre, J. A., Reduced transit-time sensitivity in non-invasive magnetic-resonance-imaging of human cerebral blood-flow. *J. Cereb. Blood Flow Metab.* **16**, 1236-1249 (1996)

Alsop, D.C., Detre, J.A., Multisection cerebral blood flow MR imaging with continuous arterial spin labelling. *Radiology* **208**, 410-416 (1998a)

Alsop, D.C., Li, L., Detre, J.A., Multi-slice activation imaging with arterial spin tagging: The effects of flow and transit time changes, *in* "Proc., ISMRM 6th Annual Meeting, Sydney, 1998", p. 1196 (1998b)

Ames, A., III., Wright, R.L., Kowada, M., Thurston, J.M., Majno, G., Cerebral Ischemia. II. The no-reflow phenomenon. *Am. J. Pathol.* **52**, 437-453 (1968)

Andrews, B.T., Weinstein, P.R., Keniry, M., Pereira, B., Sequential in vivo measurement of cerebral intracellular metabolites with phosphorus-31 magnetic resonance spectroscopy during global cerebral ischemia and reperfusion in rats. *Neurosurgery* **21**, 699-707 (1987)

Arsenio-Nunes, M.L., Hossmann, K.A., Farkas-Bargeton, E., Ultrastructural and histochemical investigation of the cerebral cortex of cat during and after complete ischaemia. *Acta Neuropathol.* **26**, 329-344 (1973)

Auer, L.M., Pucher, R., Leber, K., Ischiyama, N., Autoregulatory response of pial vessels in the cat. *Neurol. Res.* **9**, 245-248 (1987)

Aukland, K., Bower, B.F., Berliner, R.W., Measurement of local blood flow with H_2 gas. *Circ. Res.* **14**, 164 (1964)

Avery, S., Crockard, H.A., Ross, Russell, R.R., Evolution and resolution of oedema following severe temporary cerebral ischaemia in the gerbil. *J. Neurol. Neurosurg. Psych.* **47**, 604-610 (1984)

Back, T., Hoehn-Berlage, M., Kohno, K., Hossmann, K.A., Diffusion nuclear magnetic resonance imaging in experimental stroke: correlation with cerebral metabolites. *Stroke* **25**, 494-500 (1994)

Baird, A.E., Warach, S., Magnetic resonance imaging of acute stroke. *J. Cereb. Blood Flow Metab.* **18**, 583-609 (1998)

Bandettini, P.A., Wong, E.C., Jesmanowicz, R., Hinks, R.S., Hyde, J.S., Spin-echo and gradient-echo EPI of human brain activation using BOLD contrast: a comparative study at 1.5T. *NMR Biomed.* **7**, 12-20 (1994)

Bandettini, P. A., Kwong, K. K., Davis, T. L., Tootell, R. B. H., Wong, E. C., Fox, P. T., Belliveau, J. W., Weisskoff, R. M., Rosen, B. R., Characterization of cerebral blood oxygenation and flow changes during prolonged brain activation. *Human Brain Mapping* **5**, 93-109 (1997)

Barlow, R., In: *Statistics : a guide to the use of statistical methods in the physical sciences*, Wiley, Chichester, UK (1989)

Baron, J.C., Samson, Y., Pantano, P., Chiras, J., Derouesne, C., Boussier, M.G., Inter-relationship of local CBF, OEF, $CMRO_2$ in ischemic areas with variable outcome: Further PET studies in humans. *J. Cereb. Flow Metab.* **7** (suppl1), 41 (1987)

Baron, J.C., Pathophysiology of acute cerebral ischemia: PET studies in humans. *Cerebrovasc. Dis.* **1** (suppl 1), 22-31 (1991)

Basser, P.J., x, In: *Magnetic resonance imaging* (Stark, D.D., Bradley, W.G., eds.), Vol. 1, Chap. x, Mosby, St Louis (1992)

Basser, P.J., Mattiello, J., Le Bihan, D., MR diffusion tensor spectroscopy and imaging. *Biophys. J.* **66**, 259-267 (1994)

Basser, P.J., Inferring microstructural features and the physiological state of tissues from diffusion-weighted images. *NMR Biomed.* **8**, 333-344 (1995)

Bazán, N.G. Jr., Effects of ischemia and electroconvulsive shock. *Biochim. Biophys. Acta* **218**, 1 (1970)

Beckstead, J.E., Tweed, W.A., Lee, J., MacKeen, W.L., Cerebral blood flow and metabolism in man following cardiac arrest. *Stroke* **9**, 569-573 (1978)

Behar, K.L., Rothman, D.L., Hossmann, K.A., NMR spectroscopic investigation of the recovery of energy and acid-base homeostasis in the cat brain after prolonged ischemia. *J. Cereb. Flow Metab.* **9,** 5655-665 (1989)

Bell, B.A., A history of the study of the cerebral circulation and the measurement of cerebral blood flow. *Neurosurgery* **14**, 238-246 (1984)

Bendall, M.R., Connelly, A., Mckendry, J.M., Elimination of coupling between cylindrical transmit coil and surface-receive coils for in vivo NMR. *Magn. Reson. Med.* **3**, 157-163 (1986)

Benveniste, H., Hedlund, L.W., Johnson, G.A., Mechanism of detection of acute cerebral ischemia in rats by diffusion-weighted magnetic resonance microscopy. *Stroke* **23**, 746-754 (1992)

Betz, E., Ingvar, D.H., Lassen, N.A., Schmal, F.W., Regional blood flow in the cerebral cortex, measured simultaneously by heat and inert gas clearance. *Acta Phsyiol. Scand.* **7**, 1-9 (1966)

Bevington, P.R., In: *Data reduction and error analysis for the physical sciences*, McGraw-Hill, New York, p. 56-65 (1969)

Bizzi, A., Righini, A., Turner, R., Le Bihan, D., Bockhorst, K.H., Alger, J.R., Imaging focal reperfusion injury following ischemia with diffusion-weighted magnetic resonance imaging and 1H-magnetic resonance spectroscopy. *Mag. Reson. Imag.* **14**, 581-592 (1996)

Bloembergen, N., Purcell, E.M., Pound, R.V., Relaxation effects in nuclear magnetic resonance absorption. *Phys. Rev.* **73**, 679-712 (1948)

Bloch, F., Hansen, W.W., Packard, M.E., Nuclear induction. *Phys. Rev.* **69**, 127 (1946)

Bolas, N.M., Petros, A.J., Bergel, D., Radda, G.K., Use of 19F magnetic resonance spectroscopy for measurement of cerebral blood flow, *in* "Proc., SMR 5th Annual Meeting, 1985 ", p. 315

van den Bos, A., In: *Handbook of measurement science*, (Sydenham, P.H., ed.), Wiley, New York (1982)

Branch, C.A., Hernandez, L., Yongbi, M., Helpern, J.A., Estimation of arterial arrival time and cerebral response characteristics of perfusion measurement with arterial spin labeling, *in* "Proc., ISMRM 6th Annual Meeting, Sydney, 1998 ", p. 375

Brierly, J.B., Excell, B.J., The effects of profound systemic hypotension upon the brain of M. Rhesus. Physiological and pathological observations. *Brain* **89**, 269-298 (1966)

Brierly, J.B., Cerebral hypoxia, In: *Greenfield's Neuropathology*, (W. Blackwood and J.A.N. Corsellis (Eds.)), 3rd Edn., Edward Arnold, London, p. 41-85 (1976)

Brown, I.R., Rush, S., Ivy, G.O., Induction of heat shock gene at the site of tissue injury in the rat brain. *Neuron* **2**, 1559-1564 (1989)

Brownstein, K.R., Tarr, C.E., Importance of classical diffusion in NMR studies of water in biological cells. Phys. Rev. A 19, 2446-2453 (1979)

Bryant, R.G., Marill, K., Blackmore, C., Francis, C., Magnetic relaxation in blood and blood clots. *Magn. Reson. Med.* **13**, 133-144 (1990)

Buchholz, F.L., Absorbency and superabsorbency, In: *Modern superabsorbent polymer technology*, (Buchholz, F.L., Graham, A.T., eds.), John Wiley, London, Chp. 1 (1998)

Busch, E., Beaulieu, C., de Crespigny, A., Moseley, M.E., Diffusion MR imaging during acute subarachnoid hemorrhage in rats. *Stroke*, **29**, 2155-2161 (1998)

Busza, A. L., Allen, K. L., King, M. D., van Bruggen, N., Williams, S. R., Gadian, D. G., Diffusion-weighted imaging studies of cerebral ischemia in gerbils - potential relevance to energy failure. *Stroke* **23**, 1602-1612 (1992)

Buxton, R.B., Frank, L.R., Siewart, B., Warach, S., Edelman, R.R., A Quantitative model for EPISTAR perfusion imaging, in "Proc., ISMRM 3rd Annual Meeting, Nice, 1995 ", p. 132

Buxton, R.B., Frank, L.R., Wong, E.C., Siewart, B., Warach, S., Edelman, R.R., A general kinetic model for quantitative perfusion imaging with arterial spin labeling. *Magn. Reson. Med.* **40**, 383-396 (1998)

Calamante, F., Williams, S. R., van Bruggen, N., Kwong, K. K., Turner, R., A model for quantification of perfusion in pulsed labeling techniques. *NMR Biomed.* **9**, 79-83 (1996)

Calamante, F., Lythgoe, M.F., Pell, G.S., Thomas, D.L., King, M.D., Busz, A.L., Williams, S.R., Ordidge, R.J., Gadian, D.G., Early changes of water diffusion, perfusion, T_1 and T_2 during focal cerebral ischemia in the rat studied at 8.5T. *Magn. Reson. Med.* (1999)

Cameron, I.R., Segal, M.B., The effect on pial arteriole diameter of local changes in potassium concentration. *Eur. Neurol.* **6**, 100-106 (1971-72)

Chaterjee, P.K., In: *Absorbency*, Elsevier, Oxford, p. 198-203 (1975)

Chen, Q., Siewert, B., Bly, B. M., Warach, S., Edelman, R. R., STAR-HASTE: perfusion imaging without magnetic susceptibility artifact. *Magn. Reson. Med.* **38**, 404-408 (1997)

Cheung, J.Y., Bonventre, J.V., Malis, C.D., Leaf, A., Calcium and ischemic injury. *N. Engl. J. Med.* **314**, 1670-1676 (1986)

Chiang, J., Kowada, M., Ames, A., III, Cerebral ischemia. III. Vascular changes. *Am. J. Pathol.* **52**, 455-476 (1968)

Chui, M.M., Philipps, R.J., McCarthy, M.J., Measurement of the porous microstructure of hydrogels by nuclear magnetic resonance. *J. Colloid Interface Sci.* **174**, 336-344 (1995)

Conolly, S., Glover, G., Nishimura, D., Macovski, A., A reduced power selective adiabatic spin-echo pulse sequence. *Magn. Reson. Med.* **18**, 28-38 (1991)

Conturo, T.W., McKinstry, R.C., Aronovitz, J.A., Neil, J.J., Diffusion MRI: Precision, accuracy and flow effects. *NMR Biomed.* **8**, 307-332 (1995)

Coremans, J., Spanoghe, M., Sterckx, J., Luypaert, R., Eisendrath, H., Osteasux, M., *in* "Proc., ISMRM 4th Annual Meeting, New York, 1996 ", p. 1340

Coremans, J., Spanoghe, M., Budinsky, L., Sterckx, J., Luypaert, R., Eisendrath, H., Ostwaux, M., A comparison between different imaging strategies for diffusion measurements with the centric phase-encoded TurboFLASH sequence. *J. Magn. Reson.* **124**, 323-342 (1997)

Cramer, S.C., Nelles, G., Benson, R.R., Kaplan, J.D., Parker, R. A., Kwong, K.K., Kennedy, D.N., Finklestein, S.P., Rosen, B.R, Simultaneous measurement of cerebral blood flow and functional MRI signal in the evaluation of stroke recovery mechanisms. *Neurology* **48**, 6050 (1997)

Crawley, A.P., Wood, M.L., Henkelman, R.M., Elimination of transverse coherences in FLASH MRI. *Magn. Reson. Med.* **8**, 248-260 (1988)

de Crespigny, A.J., Wendland, M.F., Derugin, N., Vexler, Z.S., Moseley, M.E., Rapid MR imaging of a vascular challenge to focal ischemia in cat brain. *J. Magn. Reson. Imag.* **3**, 475-481 (1993)

de Crespigny, A.J., Röther, J., D'Arceuil, H.E., Yoshikawa, J., Iwai, K., Seri, S., Moseley, M.E., High speed MRI of very early diffusion changes in focal cerebral ischemia, *in* "Proc., ISMRM 3rd Annual Meeting, Nice, 1995 ", p. 1369

de Crespigny, A.J., Röther, J., Beaulieu, C., Moseley, M.E., Correlation of diffusion, blood volume and DC potential changes in rat brain after cardiac arrest, *in* "Proc., ISMRM 5th Annual Meeting, Vancouver, 1997 ", p. 394

de Crespigny, A., Röther, J., van Bruggen,_N., Beaulieu,_C., Moseley,_M.E., Magnetic resonance imaging assessment of cerebral hemodynamics during spreading depression in rats. *J. Cereb. Blood Flow Metab.* **18**, 1008-1017 (1998)

Crumrine, R.C., LaManna, J.C., Regional cerebral metabolites, blood flow, plasma volume and mean transit time in total cerebral ischemia in the rat. *J. Cereb. Blood Flow Metab.* **11**, 272-107 (1991)

Cutié, S.C., Smith, P.B., Reim, R.E., Graham, A.T., Analysis and cahracterization of superabsorbent polymers, In: *Modern superabsorbent polymer technology*, (Buchholz, F.L., Graham, A.T., eds.), John Wiley, London, Chp. 4 (1998)

Cuypers, J., Matakas, F., The effect of post-ischemic hyperemia on intracranial pressure and the no-reflow phenomenon. *Acta Neuropathol.* **29**, 73-84 (1974)

Damadian, R., Goldsmith, M. , Minkoff, L., NMR in cancer: XVI.FONAR images of the live human body. *Physiol. Chem. Phys.* **9**, 97-100 (1977)

Daskiewicz, O.K., Hennel, J.W., Lubas, B., Szczepkowski, T., W., Proton magnetic relaxation and protein hydration. *Nature* **200**, 1006-1007 (1963)

Davis, D., Ulatowski, J., Eleff, S., Izuta, M., Mori, S., Shungu, D., van Zijl, P.C.M., Rapid monitoring of changes in water diffusion coefficients during reversible ischemia in cat and rat brain. *Magn. Reson. Med.* **31**, 454-460 (1994)

Decanniere, C., Eleff, S., Davis, D., van Zifl, P.C.M., Correlation of rapid changes in the average water diffusion constant and the concentration of lactate and ATP breakdown products during global ischemia in cat brain. *Magn. Reson. Med.* **34**, 343-352 (1995)

Deimling, M., Mueller, E., Lamb, G., Diffusion-weighted imaging with TurboFLASH, in "Proc., SMRM 9th Annual Meeting, 1990 ", p. 387

Del Zoppo, G.J., Schmid-Schönbein, Mori, E., Copeland, B.R., Chang, C.M., Polymorphonuclear leukocytes occlude capillaries following middle cerebral artery occlusion and reperfusion in baboons. *Stroke* **22,** 1276-1283 (1991)

Detre, J. A., Eskey, C. J., Koretsky, A. P., Measurement of cerebral blood-flow in rat-brain by ^{19}F NMR detection of trifluoromethane washout. *Magn. Reson. Med.* **15**, 45-57 (1990)

Detre, J.A., Subramanian, V.H., Smith, M.D., Smith, D.S., Kobayashi, A., Zaman, A., Leigh, J.S. Jr., Measurement of regional cerebral blood flow in cat brain using intracarotid $2H_2O$ and ^{2}H NMR imaging. *Magn. Reson. Med.* **14**, 389-395 (1990)

Detre, J. A., Subramanian, V. H., Mitchell, M. D., Smith, D. S., Kobayashi, A., Zaman, A., Leigh, J. S., Measurement of regional cerebral blood-flow in cat brain using intracarotid (H_2O)-H_2 and H_2 NMR imaging. *Magn. Reson. Med.* **14**, 389-395 (1990)

Detre, J. A., Leigh, J. S., Williams, D. S., Koretsky, A. P., Perfusion imaging. *Magn. Reson. Med.* **23**, 37-45 (1992)

Detre, J.A., Alsop, D.C., Vives, L.R., Maccotta, L., Teener, J.W., Raps, E.C., Noninvasive MRI evaluation of cerebral blood flow in cerebrovascular disease. *Neurology*. **50**, 633-641 (1998)

Dietrich, W.D., Busto, R., Ginsberg, M.D., Cerebral endothelial microvilli: formation following global forebrain ischemia. *J. Neuropathol. Exp. Neurol.* **43**, 72-83 (1984)

Dijkhuizen, R.M., Brandsma, D., de Graaf, R.A., Berkelbach van der Sprenkel, J.W., Tulleken, C.A.F., Nicolay, K. Bold MRI during MCAO-occlusion, reperfusion and serial respiratory challenges in focal ischemic rat brain, *in* "Proc., ISMRM 4th Annual Meeting, New York, 1996", p. 499

Dijkhuizen, R.M., Knollema, S., van der Worp, H.B., Horst, G.J.T., De Wildt, D.J., van der Sprenkel, J.W.B., Tulleken, K.A.F., Nicolay, K., Dynamics of cerebral tissue injury and perfusion after temporary hypoxia-ischemia in the rat. *Stroke* **29**, 695-704 (1998a)

Dijkhuizen, R.M., *Magnetic resonance imaging and spectroscopy in experimental cerebral ischemia*, PhD thesis (1998b)

Ding, G., Li, L., Du, Y., Ye, C., NMR microscopy of polyacylamide hydrogel. *Magn. Reson. Imag.* **14**, 947-948 (1996)

Dirnagl, U., Cerebral ischemia : the microcirculation as trigger and target. *Progr. Brain Res.* **96**, 49-64 (1993)

Dixon, K., Anaerobic leakage of potassium from brain. *Biochem. J.*, **44**, 187-190 (1949)

Dixon, W.T., Du, L.N., Faul, D.D., Gado, M., Rossnick, S., Projection angiograms of blood labeled by adiabatic fast passage. *Magn. Reson. Med.* **3**, 454-462 (1986)

Dougherty, J.H., Levy, D.E., Weksler, B.B., Experimental cerebral ischemia produces platelet aggregates. *Neurology* **29**, 1460-1465 (1979)

Drayer, B.P., Wolfson, S.K. Jr., Reinmuth, O.M., Dujovny, M., Boehake, M., Cook, E.E., Xenon enhanced computed tomography for the analysis of cerebral integrity, perfusion and blood flow. *Stroke* **9**, 123 (1978)

Duong, T.Q., Ackerman, J.H., Yablonskiy, Neil, J.J., Extracellular and intracellular apparent diffusion in normal and focally-ischemic rat brain via ^{1}H MRS, *in* "Proc., ISMRM 6th Annual Meeting, Sydney, 1998 ", p. 342 (1998a)

Duong, T.Q., Ackerman, J.H., Ying, H.S., Neil, J.J., Evaluation of extra- and intracellular apparent diffusion in normal and globally ischemic rat brain via ^{19}F NMR. *Magn. Reson. Med.* **40**, 1-13 (1998b)

Edelman, R.R., Siewert, B., Darby, D.G., Thangaraj, V., Nobre, A.C., Mesulam, M.M., Warach, S., Qualitative mapping of cerebral blood-flow and functional localization with echo-planar MR-imaging and signal targeting with alternating radio-frequency. *Radiology* **192**, 513-520 (1994)

Edelman, R.R., Chen, Q., EPISTAR MRI: Multislice mapping of cerebral blood flow. *Magn. Reson. Med.* **40**, 800-805 (1998)

Edelstein, W.A., Hutchison, J.M.S., Johnson, G., Redpath, T., Spin-warp NMR imaging and applications to human whole-body imaging. *Phys. Med. Biol.* **25,** 751-756 (1980)

Edwards, A.D., Richardson, C., van der Zee, P., Elwell, C., Wyatt, J.S., Cope, M., Delpy, D.T., Reynolds, E.O., Measurement of hemoglobin flow and blood flow by near infrared spectroscopy. *J. Appl. Phyiol.* **75**, 1884-1889 (1993)

Eichling, J., Raichle, M., Grubb, R., Ter-Porgossian, M., Evidence of the limitations of water as a freely diffusable tracer in brain of the Rhesus monkey. *Circ. Res.* **35**, 358-364 (1974)

Eis, M., Hoehn-Berlage, M., Correction of gradient cross-talk and optimization of measurement parameters in diffusion MR imaging. *J. Magn. Reson. Ser. B* **107**, 222-234 (1995)

Ernst, R.R., Anderson, W.A., Applications of FT spectroscopy to magnetic resonance. *Rev. Sci. Instrum.* **37**, 93-98 (1966)

Fischer, E.G., Ames, A. III, Lorenzo, A.V., Cerebral blood flow immediately following brief circulatory stasis. *Stroke*, **10**, 423-427 (1979)

Fischer, E.G., Impaired perfusion following cerebrovascular stasis. *Arch. Neurol.* **29**, 361-366 (1973)

Fischer, M., Bockhorst, K., Hoehn-Berlage, M., Schmitz, B., Hossmann, K.A., Imaging of the apparent diffusion coefficient for the evaluation of cerebral metabolic recovery after cardiac arrest. *Magn. Reson. Imag.* **13**, 781-790 (1995)

Frahm, J., Hänicke, W., Comparative study of pulse sequences for selective excitation in NMR imaging. *J. Magn. Reson.* **60**, 320-332 (1984)

Frahm, J., Hänicke, W., Merboldt, K.D., Transverse coherence in rapid FLASH NMR imaging. *J. Magn. Reson.* **72**, 307-314 (1987)

Frank, L. R., Wong, E. C., Buxton, R. B., Slice profile effects in adiabatic inversion: application to multislice perfusion imaging. *Magn. Reson. Med.* **38**, 558-564 (1997)

Fujioka, M., Okuchi, K., Miyamoto, S., Sakaki, T., Hiramatsu, K., Tominaga, M., Kamada, Y., Iwasaki, S., Changes in the basal ganglia and thalamus following reperfusion after complete ischaemia. *Neuroradiol.* **36**, 605-607 (1994)

Fullerton, G.D., Physiologic basis of magnetic relaxation, In: *Magnetic resonance imaging* (Stark, D.D., Bradley, W.G., eds.), Vol. 1, Chap. 4, Mosby, St Louis (1992)

Furlow, T.W., Cerebral ischemia produced by four-vessel occlusion in the rat: A quantitative evaluation of cerebral blood flow. *Stroke* **13**, 852-855 (1982)

Gadian, D.G., Frackowiak, R.S.J., Crockard, H.A., Proctor, E., Allen, K., Williams, S.R., Ross Russell, R.W., Acute cerebral ishaemia : concurrent changes in cerebral blood flow, energy metabolites, pH, and lactate measured with hydrogen clearance and 31P and 1H nuclear magnetic resonance spectroscopy. I. Methodology. *J. Cereb. Blood Flow Metab.* **7**, 199-206 (1987)

Gadian, D. G., Allen, K., van Bruggen, N., Busza, A. L., King, M. D., Williams, S. R., Applications of NMR-spectroscopy to the study of experimental stroke in-vivo. *Stroke* **24**, I 57-I 59 (1993)

Gärtner, G., Wagner, J., Uber den Hirnkreislauf. *Wien. Med. Wochenschr.* **37**, 601, 640 (1887)

van Gelderen, P., de Vleeschouwer, H.M., DesPres, D., Pekar, J., van Zijl, P.C.M., Moonen, C.T.W., Water diffusion and acute stroke. *Magn. Reson. Med.* **31**, 154-163 (1994)

Go, I.G., Lammertsma, A.A., Paans, A.M.J., Vaalburg, W., Woldring, M.G., Extraction of water labeled with oxygen 15 during single-capillary transit. *Arch. Neurol.* **38**, 581-584 (1981)

Gore, J.C., Brown, M.S., Zhong, J., Mueller, K.F., Good, W., NMR relaxation of water in hydrogel polymers: A model for tissue. *Magn. Reson. Med.* **9**, 325-332 (1989)

Gröhn, O.H., Lukkarunen, J.A., Oja, J.M.E., van Zijl, P.C.M., Ulatowski, J.A., Traystman, R.J., Kauppinen, R.A., Non-invasive detection of cerebral hypoperfusion and reversible ischemia from reductions in the magnetic resonance imaging relaxation time T_2. *J.Cereb. Blood Flow Metab.* **18**, 911-920 (1998)

Haacke, E.M., The effects of finite sampling in spin-echo or field-echo magnetic resonance imaging. *Magn. Reson. Med.* **4**, 407-421 (1987)

Haase, A., Frahm, J., Matthaei, W., Hanicke, W., Merboldt, K.D., FLASH imaging. Rapid NMR imaging, using low-flip angle pulses. *J. Magn. Reson.* **67,** 258-266 (1986)

Haggendal, E., Löfgren, N.J., Nilsson, N.J., Zwetnow, N.N., Prolonged hyperemia after periods of increased cerebrospinal fluid pressure in dogs. *Acta Physiol. Scand.* **79**, 272-279 (1970)

Hänicke, W., Merboldt, K.D., Chien, D., Gyngell, M.L., Bruhn, H., Frahm, J., Signal strength in subsecond FLASH magnetic resonance imaging: The dynamic approach to steady state. *Med. Phys.* **17**, 1004-1010 (1990)

Hansen, A.J., Zeuthen, T., Extracellular ion concentration during spreading depression and ischemia in the rat cortex. *Acta Physiol. Scand.* **113**, 437-445 (1981)

Harris, N.G., Houseman, J., Zilkha, E., Obrenovitch, T.P., Williams, The temporal relationship between ADC , DC potential and extracellular glutamate in the rat brain following cardiac arrest: Simultaneous MRI, electrophysiology and microdialysis, *in* "Proc., ISMRM 5th Annual Meeting, Vancouver, 1997 ", p. 339

Hatashita, S., Hoff, J.T., Salamat, S.T., Ischemic brain edema and the osmotic gradient between blood and brain. *J.Cereb. Blood Flow Metab.* **8**, 552-559 (1988)

Heiss, W., Hayakawa, T., Patterns of changes in blood flow and relationships to infarction in experimental cerebral ischemia. *Stroke* **5,** 454-459 (1976)

Helpern, J.A., Ordidge, R.J., Knight, R.A., The effect of cell membrane water permeability on the apparent diffusion coefficient of water, in "Proc. SMR, 11th Annual Meeting, 1992", p. 1201

Helpern, J.A., Branch, C.A., Yongbi, M.N., Huang, N.C., Perfusion imaging by un-inverted flow sensitive alternating inversion recovery (UNFAIR). *Magn. Reson. Imaging* **15**, 135-139 (1997)

Henkelman, R.M., Bronskill, M.J., *Rev. Magn. Reson. Med.* **2**, 1 (1987)

Henkelman, R.M., Neil, J.J., Xiang, Q.S., A quantitative interpretation of IVIM measurements of vascular perfusion in the rat brain. *Magn. Reson. Med.* **32**, 464-469 (1994)

Hermann, D.M., Kuroiwa, T., Ito, U., Mies, G., Expression of c-*jun*, *hsp*72 and *gfap* following repeated repeated unilateral common carotid artery occlusion in gerbils – correlates of delayed ischemic injury. *Brain Res.* **799**, 35-43 (1988)

Hernandez, L., Branch, C.A., Helpern, J.A., Measurement of CBF with arterial spin labelling: Correlate with microspheres, *in* "Proc., ISMRM 6th Annual Meeting, Sydney, 1998 ", p. 1193

Herscovitch, P., Raichle, M.E., What is the correct value for the brain-blood partition coefficient for water?. *J.Cereb. Blood Flow Metab.* **5**, 65-69 (1985)

Hill, L.E., *The physiology and pathology of the cerebral circulation*, Churchill, London (1896)

Hoehn-Berlage, M., Back, T., Norris, D.G., Early changes in apparent diffusion coefficient of rat brain following total circulatory arrest. *MAGMA* **2**, 39-42 (1994)

Hoehn-Berlage, M., Norris, D.G., Kohno, K., Mies, G., Leibfritz, D., Hossmann, K.A., Evolution of regional changes in apparent diffusion coefficient during focal ischemia in rat brain: the relationship of quantitative diffusion NMR imaging to reduction in cerebral blood flow and metabolic disturbances. *J. Cereb. Blood Flow Metab.* **15**, 1002-1011 (1995a)

Hoehn-Berlage, M., Diffusion-weighted NMR imaging: Application to experimental focal cerebral ischemia. *NMR Biomed.* **8**, 345-358 (1995b)

Hollewand, M.P., Gladden, L.F., Probing the structure of porous pellets: An NMR study of drying. *Magn. Reson. Imag.* **12**, 291-294 (1994)

Holman, L., Hill, T.C., Perfusion imaging with single-photon emission computed tomography, in Cerebral Blood Flow: Physiologic and Clinical Aspects, McGraw-Hill, New York, Chp. 14 (1987)

Holsinger, A.E., Riederer, S.J., The importance of phase-encoding order in ultra-short TR SNAPSHOT MR Imaging. *Magn. Reson. Med.* **16**, 481-488 (1990)

Hong, X., Dixon, W.T., Measuring diffusion in inhomogeneous systems in imaging mode using antisymmetric sensitizing gradients. *J. Magn. Reson.* **99**, 561-570 (1992)

Hossmann, K.A., Lechtape-Grüter, H. and Hossmann, V., The role of cerebral blood flow for the recovery of the brain after prolonged ischemia. *Z. Neurol.* **204**, 281-299 (1973)

Hossmann, K.A., Total ischemia of the brain, In: *Brain and heart infarct*, (Zulch, K.J., Kaufmann, W., Hossman, K.A., Hossmann, V., eds.), Berlin, Springer, p. 107-122 (1977)

Hossmann, K.A., Post-ischemic resuscitation of the brain: Selective vulnerability versus global resistance. *Progr. Brain Res.* **63**, 3-17 (1985a)

Hossmann, K.A., Mies, G., Paschen, W., Csiba, L., Bodsch, W., Rapin, J.R., Le Poncin-Lafitte, M., Takahashi, K., Multiparametric imaging of blood flow and metabolism after middle cerebral artery occlusion in cats. *J. Cereb. Blood Flow Metab.* **5**, 97-107 (1985b)

Hossmann, K.A., Nagashima, G., Klatzo, I., Repetitive ischaemia of cat brain: pathophsyiological observations. *Neurolog. Res.* **12**, 158-164 (1990)

Hossmann, K.A., Animal models of cerebral ischaemia. 1. Review of literature. *Cererbrovasc. Dis.* , 1 (suppl 1), 2-15 (1991)

Hossmann, K.A., Viability thresholds and the penumbra of focal ischemia. Ann. Nuerol. 36, 557-566 (1994a)

Hossmann, K. A., Fischer, M., Bockhorst, K., Hoehnberlage, M., NMR imaging of the apparent diffusion-coefficient (ADC) for the evaluation of metabolic suppression and recovery after prolonged cerebral-ischemia. *J. Cereb. Blood Flow Metab.* **14**, 723-731 (1994b)

Howseman, A. M., Thomas, D.L., Pell, G.S., Williams, S.R., Ordidge, R.J., Rapid interleaved T_2^* imaging. *Magn. Reson. Med.* (in Press)

Huang, N.C., Yongbi, M.N., Helpern, J.A., The influence of preischemic hyperglycemia on acute changes in the apparent diffusion coefficient of brain water following focal and global ischemia in rats, *in* "Proc., ISMRM 5th Annual Meeting, Vancouver, 1997 ", p. 396

Ingvar, D.H., Lassen, N.A., Quantitative determination of regional cerebral blood flow in man. *Lancet* **2,** 806-807 (1961)

Ito, U., Spatz, M., Walker, J.T., Klatzo, I., Experimental cerebral ischemia in Mongolian gerbils. I. Light microscopic observations. *Acta Neuropathol. (Berl.)* **32**, 209-223 (1975)

Jabre, A., Symon, L., Temporary vascular occlusions during aneurysm surgery. *Surg. Neurol.* **27**, 47-93 (1987)

Jara, H., Wehrli, F.W., Determination of background gradients with diffusion MR imaging. *J. Magn. Reson. Imaging* **4**, 787-797 (1994)

Jensen, D.J., Brey, W.W., Delayre, J.L., Narayana, P.A., Reduction of pulsed gradient settling time in the superconducting magnet of a magnetic resonance instrument. *Med. Phys.* **14**, 859-862 (1987)

Jones, J.A., Hodgkinson, P., Barker, A.L., Hore, P.J., Optimal sampling strategies for the measurement of spin-spin relaxation times. *J. Magn. Reson. Ser. B* **113**, 25-34 (1996)

Kågström, E., Smith, M.L., Siesjö, B.K., Local cerebral blood flow in the recovery period following complete cerebral ischemia in the rat, *J. Cereb. Blood Flow Metab.* **3**, 170-182 (1983a)

Kågström, E., Smith, M.L., Siesjö, B.K., Recirculation in the brain following incomplete ischemia in the rat, *J. Cereb. Blood Flow Metab.* **3**, 183-192 (1983b)

Kaneko, Z., First steps in the development of the Doppler flowmeter. *Ultrasound Med. Biol.* **12,** 1877 (1986)

Kang, S.K., Jhon, M.S., Ionic mobility and contact ion pairing study by ^{23}Na, ^{35}Cl, and ^{39}K nuclear magnetic resonance in a poly[methacrylic acid-*co*-(N,N-dimethylamino)ethyl methacrylate] hydrogel. *Macromolecules* **26**, 171-176 (1993)

Kao, Y., Wan, X., MacFall, J.R., Simultaneous multislice acquisition with arterial-flow tagging (SMART) using echo planar imaging (EPI). *Magn. Reson. Med.* **39**, 662-665 (1998)

Kaplan, B., Brint, S., Tanabe, J., Jacewicz, M., Wang, X.J., Pulsinelli, W., Temporal thresholds for neocortical infarction in rats subjected to reversible focal cerebral ischemia. *Stroke* **22**, 1032-1039 (1991)

Kato, H., Kogure, K., Nakano, S., Neuronal damage following repeated brief ischemia in the gerbil. *Brain Res.* **479**, 366-370 (1989)

Kato, H., Araki, T., Kogure, K., Murakami, M., Uemura, K., Sequential cerebral blood flow changes in short-term cerebral ischemia in gerbils. *Stroke* **21**, 1346-1349 (1990a)

Kato, H., Kogure, K., Neuronal damage following non-lethal but repeated cerebral ischemia in the gerbil. *Acta Neuropathol.* **79**, 494-500 (1990b)

Katz, L.N., Kolin, A., The flow of blood in the carotid artery of the dog under various circumstances as determined with the electromagnetic flowmeter. *Am. J. Physiol.* **122**, 788 (1938)

Kawai, K., Nakagomi, T., Kirino, T., Tamura, A., Kawai, N., Preconditioning in vivo ischemia inhibits anoxic long-term potentiation and functionally protects CA1 neurons in the gerbil. *J. Cereb. Blood Flow Metab.* **18**, 288-296 (1998)

Kety, S.S., Schmidt, C.F., The nitrous oxide method for the quantitative determination of cerebral blood flow in man : theory, procedure and normal values. *J. Clin. Invest.* **27**, 475-483 (1948)

Kety, S.S., The theory and applications of the exchange of inert gas at the lungs and tissues. *Pharmacol. Rev.* **3**, 1-41 (1951)

Kim, S.G., Quantification of relative cerebral blood-flow change by flow-sensitive alternating inversion-recovery (FAIR) technique - application to functional mapping. *Magn. Reson. Med.* **34**, 293-301 (1995)

Kim, S.G., Tsekos, N.V., Ashe, J., Multi-slice perfusion-based functional MRI using the FAIR technique: comparison of CBF and BOLD effects. *NMR Biomed.* **10**, 191-196 (1997a)

Kim, S. G., Tsekos, N. V., Perfusion imaging by a flow-sensitive alternating inversion recovery (FAIR) technique: application to functional brain imaging. *Magn. Reson. Med.* **37**, 425-435 (1997b)

Kim, S. G., Ugurbil, K., Comparison of blood oxygenation and cerebral blood flow effects in fMRI: estimation of relative oxygen consumption change. *Magn. Reson. Med.* **38**, 59-65 (1997c)

Kim, S.G., Tsekos, N.V., Lee, S.P., Silva, A.C., Merkle, H., Echo-planar imaging at ultra-high fields (9.4T) "Proc., ISMRM 6th Annual Meeting, Sydney, 1998 ", p. 1964

Kimura, R., Shiino, A., Matsuda, M., Handa, J., Morikawa, S., Inubushi, T., Acute focal cerebral ischemia in rats studied by diffusion-weighted magnetic resonance imaging – an experimental study. *Surg. Neurol.* **46**, 67-74 (1996)

Kirino, T., Suzuki, R., Laursen, H., Yamaguchi, T., Klatzo, I., Effects of a brief cerebral-ischemia in the gerbil hippocampus. *Stroke* **13**, 117 (1982)

Kirino, T., Tsujita, Y., Tamura, A., Induced tolerance to ischemia in gerbil hippocampus neurons. *J.Cereb. Blood Flow Metab.* **11**, 299-307 (1991)

Kitagawa, K., Matsumoto, M., Tagaya, M., Hata, R., Ueda, H., Niinobe, M., Handa, N., Fukunaga, R., Kimura, K., Mikoshiba, K., Kamada, T., "Ischemic tolerance" phenomenon found in the brain. *Brain Res.* **528**, 21-28 (1990)

Kitagawa, K., Matsumoto, M., Kuwabara, K., Tagaya, M., Ohtsuki, T., Ueda, H., Handa, N., Kimura, K., Kamada, T., "Ischemic tolerance" phenomenon detected in various brain regions. *Brain Res.* **561,** 203-211 (1991)

Klatzo, I., Pathophysiologic aspects of cerebral ischemia. In: *The Nervous System Vol.1*, (Tower, D.B., ed.), New York, Raven Press, p. 313-322 (1975)

Klatzo, I., Disturbances of the blood-brain-barrier in cerebrovascular disorders. *Acta Neuropath.* **S8**, 81-88 (1983)

Kleinberg, R.L., Pore size distributions, pore coupling, and transverse relaxation spectra of porous rocks. *Magn. Reson. Imag.* **12**, 271-274 (1994)

Kloiber, O., Miyazawa, T., Hoen-Berlage, M., Hossmann, K.A., Simultaneous ^{31}P NMR spectroscopy and laser doppler flowmetry of rat brain during global ischemia and reperfusion. *NMR Biomed.* **6**, 144-152 (1993)

Knight, R.A., Ordidge, R.J., Helpern, J.A., Chopp, M., Rodolosi, L.C., Peck, D., Temporal evaluation of ischemic damage in rat brain measured by proton nuclear magnetic resonance imaging. *Stroke* **22**, 802-808 (1991)

Koda, S., Yamashita, K., Iwai, S., Nomura, H., Iwata, M., Ultrasonic investigation of the states of water in hydrogels. *Polymer* **35**, 5626-5629 (1994)

Kohno, K., Back, T., Hoehn-Berlage, M., Hossmann, K.A., A modified rat model of middle cerebral artery thread occlusion under electrophysiological control for magnetic resonance investigations. *Magn. Reson. Imag.* **13**, 65-71 (1995)

Krishnamurthy, S., McIntyre, D., Santlee, E.R. Jr., Nature of water in hydrogels. J. Polym. Sci. 11, 427-440 (1973)

Kucharczyk, J., Mintrovitch, J., Asgari, H.S., Moseley, M.E., Diffusion/perfusion MR imaging of acute cerebral ischemia. *Magn. Reson. Med.* **19**, 311-315 (1991)

Kumar, A., Welti, D., Ernst, R.R., NMR zeugmatography. *J. Magn. Reson.* **18**, 69-83 (1975)

Kwong, K. K., Belliveau, J. W., Chesler, D. A., Goldberg, I. E., Weisskoff, R. M., Poncelet, B. P., Kennedy, D. N., Hoppel, B. E., Cohen, M. S., Turner, R., Cheng, H. M., Brady, T. J., Rosen, B. R., Dynamic magnetic-resonance-imaging of human brain activity during primary sensory stimulation. *Proc. Natl. Acad. Sci. USA* **89**, 5675-5679 (1992)

Kwong, K. K., Chesler, D. A., Weisskoff, R. M., Donahue, K. M., Davis, T. L., Østergaard, L., Campbell, T. A., Rosen, B. R., MR perfusion studies with T_1-weighted echo-planar imaging. *Magn. Reson. Med.* **34**, 878-887 (1995)

LaManna, J.C., Jöbsis, F.F., Austin, G.M., Schulen, W., Changes in brain metabolism in the cat in response to multiple brief transient ischemic episodes. *Exp. Neurol.* **55**, 304-317 (1977)

Laptook, A.R., Hassan, A., Peterson, J., Corbett, R.J.T., Nunnally, R.L., Effects of repeated ischemia on cerebral blood flow and brain energy on metabolism. *NMR Biomed.* **2**, 74-79 (1988)

Latour, L.L., Svoboda, K., Mitra, P., Sotak, C.H., Time-dependent diffusion of water in a biological model system. *Proc. Natl. Acad. Sci.* **91,** 1229-1233 (1994)

Lauterbur, P.C., Image formation by induced local interactions: Examples employing nuclear magnetic resonance. *Nature (Lond.)* **242,** 190-191 (1973)

St. Lawrence, K.S., Lee, T.Y., Tracer kinetic modelling analysis for the arterial spin tagging technique, *in* "Proc., ISMRM 5th Annual Meeting, Vancouver, 1997", p. 1750

Le Bihan, D., Turner, R., Moonen, C.T.W., Pekar, J., Effects of intra-voxel incoherent motions (IVIM) in steady-state free precession (SSFP) imaging: application to molecular diffusion imaging. *Magn. Reson. Med.* **10**, 324 (1989)

Le Bihan, D., Temperature imaging by NMR. In: *Diffusion and Perfusion Magnetic Resonance Imaging: Applications to Functional MRI*, (Le Bihan, D., ed.), New York, Raven Press, p. 181-187 (1995)

Lee, H.B., Jhon, M.S., Andrade, J.D., Nature of water in synthetic hydrogels 1. Dilatometry, specific conductivity, differential scanning calorimetry of polyhydroxyethyl methacrylate. *J. Colloid Interface Sci.* **51**, 225-231 (1975)

Lee, H., Proce, R., Diffusion imaging with MP-RAGE sequence. *J. Magn. Reson. Imaging* **4**,837-842 (1994)

Lei, H., Buist, R., Peeling, J., Incomplete saturation of macromolecule spins caused an underestimation of perfusion in the one-coil spin tagging approach, *in* "Proc., ISMRM 5th Annual Meeting, Vancouver, 1997", p. 1751

Levine, S., Payan, H.M., Effects of ischaemia and other procedures on the brain and retina of the gerbil (Meriones unguiculatus). *Exp. Neurol.* **16**, 255-262 (1966)

Levine., S., Shon, D., Cerebral ischemia in infant and adult gerbils, relation to incomplete circle of Willis. *Arch. Pathol.* **87**, 315-317 (1969)

Levy, D.E., Brierly, J.B., Communications between vertebro-basilar and carotid arterial circulations in the gerbil. *Exp. Neurol.* **45**, 503-508 (1974)

Levy, D.E., Brierly, J.B., Plum, F., Ischaemic brain damage in the gerbil in the absence of "no-reflow". *J. Neurol. Neurosurg. Psychiat.* **38**, 1197-1205 (1975)

Levy, D.E., Duffy, T.E., Cererbal energy metabolism during transient ischemia and recovery in the gerbil. *J. Neurochem.* **28**, 63-70 (1975)

Levy, D.E., Van Uitert, R.L., Pike, C.L., Delayed postischemic hypoperfusion: A potentially damaging consequence of stroke. *Neurology* **29**, 1245-1252 (1979)

Lin, L.I-K., A concordance correlation coefficient to evaluate reproducibility. *Biometrics* **45**, 255-268 (1989)

Little, J.R., Kerr F.W.L., Sundt, T.M., Microcirculatory obstruction in focal cerebral ischemia. Relationship to neuronal alterations. *Mayo Clin. Proc.* **50**, 264-270 (1975)

Little, J., Kerr, F., Sundt, T., Microcirculatory obstruction in focal cerebral ischemia: an electron microscope investigation in monkeys. *Stroke* **7**, 25-30 (1976)

Lindquist, S., The heat-shock response. *Annu. Res. Biochem.* **55**,1151-1191 (1986)

Liu, Y., Kato, H., Nakata, N., Kogure, K., Protection of rat hippocampus against ischemic neuronal damage by pretreatment with sublethal ischemia. *Brain Res.* **586**, 121-124 (1992)

Lowry, O., Passonneau, J., Hasselberger, F., Schulz, D., Effect of ichemia on known substrates and cofactors of the glycolytic pathway in brain. *J. Biol. Chem.* **239**, 18-30 (1964)

Lythgoe, M.F., Busza, A.L., Calamante, F., Sotak, C.H., King, M.D., Bingham, A.C., Williams, S.R., Gadian, D. G., Effects of diffusion anisotropy on lesion delineation in a rat model of cerebral ischemia. *Magn. Reson. Med.* **38**, 662-668 (1997)

Lythgoe, M.F., Calamante, F., Thomas, D.L., Pell, G.S., King, M.D., Busza, A.L., Sotak, C.S., Williams, S.R., Ordidge, R.J., Gadian, D.G., A novel rat model of oligaemic misery perfusion using partial occlusion in the middle cerebral artery: Acute changes in MRI diffusion, perfusion, T_1 and T_2. *Stroke* (submitted)

McLaughlin, A.C., Ye, F. Q., Pekar, J. J., Santha, A. K. S., Frank, J.A., Effect of magnetization transfer on the measurement of cerebral blood flow using steady-state arterial spin tagging approaches: a theoretical investigation. *Magn. Reson. Med.* **37**, 501-510 (1997)

Maccotta, L., Detre, J. A., Alsop, D. C., The efficiency of adiabatic inversion for perfusion imaging by arterial spin labeling. *NMR Biomed.* **10**, 216-221 (1997)

Mancuso, A.M., Karibe, H., Rooney, W.D., Zarow, G.J., Graham, S.H., Weiner, M.W., Weinstein, P.R., Correlation of early reduction in the apparent diffusion coefficient of water with blood flow reduction during middle cerebral artery occlusion in rats. *Magn. Reson. Med.* **34**, 368-377 (1995)

Mansfield, P., Multiplanar image formation using NR spin echoes. *J. Phys. C Sol. State Phys.* **10**, L55-L58 (1977)

Mansfield, P., Morris, P.G., In: *NMR imaging in biomedicine*, Orlando, Florida, Academic Press, p. 41-46 (1982)

Mansfield, P., Chapman, B. Multishield active magnetic screening of coil structures in NMR. *J. Magn. Reson.* **72**, 211-223 (1987)

Matsushima, K., Hogan, M.J., Hakim, A.M., Cortical spreading depression protects against subsequent focal cerebral ischemia in rats. *J. Cereb. Blood Flow Metab.* **16**, 221-226 (1996)

Meier, P., Zierler, K.L., On the theory of the indicator-dilution method for measurement of blood flow and volume. *J. Appl. Physiol.* **6**, 731-744 (1954)

Merboldt, K., Hanicke, W., Bruhin, H., Gyngell, M.L., Frahm, J., Diffusion imaging of the human brain in vivo using high-speed STEAM MRI. *Magn. Reson. Med.* **23**, 179-192 (1992)

Michenfelder, J.D., Milde, J.H., Katušic, Z.S., Postischemic canine cerebral blood flow is coupled to cerebral canine metabolic rate. *J.Cereb. Blood Flow Metab.* **11**, 611-616 (1991)

Miller, J.R., Myers, R.E., Neuropathology of systemic circulatory arrest in adult monkeys. *Neurology (Minneap.)* **22**, 888-904 (1972)

Miller, C.L., Lampard, D.G., Alexander, K., Brown, W.A., Local cerebral blood flow following transient cerebral ischemia. I. Onset of impaired reperfusion within the first hour following global ischemia. *Stroke* **11**, 534-541 (1980)

Minematsu, K., Li, L., Sotak, C.H., Davis, M.A., Fisher, M., Reversible focal ischemic injury demonstrated by diffusion-weighted magnetic resonance imaging in rats. *Stroke* **23**, 1304-1311 (1992)

Mintorovitch, J., Moseley, M.E., Chileuitt, L., Shimizu, Y., Cohen, Y., Weinstein, P.R., Comparison of diffusion and T_2-weighted MRI for the early detection of cerebral ischemia and reperfusion in rats. *Magn. Reson. Med.* **18**, 39-50 (1991)

Miyabe, M., Mori, S., van Zijl, P.C.M., Kirsch, J.R., Eleff, S.M., Koehler, R.C., Traystman, R.J., Correlation of the average water diffusion constant with cerebral blood flow and ischemic damage after transient middle cerebral artery occlusion in cats. *J. Cereb. Blood Flow Metab.* **16**, 881-891 (1996)

Mommaerts, W.F.H.M., In: *Essentials of human phyiology*, (Ross, G., ed.), Year Book (1978)

Moran, P.R., A general approach to T_1, T_2 and spin density discrimination sensitivity in NMR imaging. *Magn. Reson. Imag.* **2**, 17-22 (1984)

Mori, S., van Zijl, P.C.M., Diffusion weighting by the trace of the diffusion tensor within a single scan. *Magn. Reson. Med.* **33**, 41-52 (1995)

Moseley, M.E., Cohen, Y., Mintorovitch, J., Chileuitt, L., Shimizu, H., Kucharczyk J., Wendland, M.F., Weinstein, P.R., Early detection of regional cerebral ischemia in cats : Comparison of diffusion- and T_2-weighted MRI and spectroscopy. *Magn. Reson. Med.* **14**, 330-346 (1990)

Mrsulja, B., Lust, W.D., Mrsulja, B.J., Passonneau, V., Effect of repeated cerebral ischemia on metabolites and metabolic rate in gerbil cortex. *Brain Res.* **119**, 480-486 (1977)

Mugler III, J.P., Epstein, F.H., Brookeman, J.R., Shaping the signal response during the approach to steady state in three-dimensional magnetization-prepared rapid gradient-echo imaging using variable flip angles. *Magn. Reson. Med.* **28**, 165-185 (1992)

Nadasy, G.L., Greenberg, J.H., Reivich, M., Kovach, A.G.B., Local cerebral blood flow during and after bilateral carotid artery occlusion in unanesthetized gerbils. *Stroke* **21**, 901-907 (1990)

Nakano, S., Kato, H., Kogure, K., Neuronal damage in the rat hippocampus in a new model of repeated reversible transient cerebral ischemia. *Brain Res.* **490**, 1780180 (1989)

Nakata, N., Kato, H., Kogure, K., Effects of repeated cerebral ischemia on extracellular amino acid concentations measured with intracerebral micodialysis in the gerbil hippoccampus. *Stroke* **24**, 458-464 (1993)

The National Institute of Neurological Disorders and Stroke rt-PA Stroke Study Group, *N. Eng. J. Med.* **333**, 1581-1587 (1996)

Neil, J.J., Duong, T.Q., Ackerman, J.J.H., Evaluation of intracellular diffusion in rat brain via ^{133}Cs NMR, *in* "Proc., ISMRM 3rd Annual Meeting, Nice, 1995 ", p. 33

Nemoto, E.M., Snyder, J.V., Carroll, R.G., Morita, H., Global ischemia in dogs : Cerebrovascular CO_2 reactivity and autoregulation. *Stroke* **6**, 425-431 (1975)

Nemoto, E.M., Hossmann, K.A., Cooper, H.K., Postischemic hypermetabolism in cat brain. *Stroke* **12**, 666-676 (1981)

Nishi, S., Taki, W., Uemura, Y., Higashi, T., Kudoh, H., Satoh, M., Nagata, K., Ischemic tolerance due to the induction of HSP70 in a rat ischemic reciculation model. *J. Cereb. Blood Flow Metab.* **615**, 281-288 (1993)

Nordström, C.H., Rehncrona, S., Siejsö, B.K., Restitution of cerebral energy state after complete energy state after complete and incomplete ischemia of 30 min duration. *Acta. Physiol. Scand.* **97**, 270-272 (1976)

Norris, D.G., Ultrafast low angle RARE: U-FLARE. .*Magn. Reson. Med.* **17**, 539-542 (1991)

Norris, D.G., Niendorf, T., Hoehn-Berlage, M., Kohno, K., Schneider, E.J., heinz, P., Hropot, M., Leibfritz, D., Incidence of apparent restricted diffusion in three different models of cerebral infarction. *Magn. Reson. Imag.* **12**, 1175-1182 (1994)

Nowak, T. S., Tomida, S., Wagner, H. G., Klatzo, I., Effect of acute electrode placement on blood-flow measured by hydrogen clearance and tracer diffusion methods in the gerbil. *Stroke* **19**, 137 (1988)

Ogawa, S., Lee, T.M., Nayak, A.S., Glynn, P., Oxygenation-sensitive contrast in magnetic resonance imaging of rodent brain at high magnetic fields. *Magn. Reson. Med.* **14**, 68-78 (1990)

Olney, J.W., Inciting excitotoxic cytocide among central neurons. *Adv. Exp. Biol.* **203**, 631-645 (1986)

Ordidge, R.J., Helpern, J.A., Knight, R.A., Qing, Z., Welch, K.M.A., Investigation of cerebral ischemia using magnetisation transfer contrast (MTC) MR imaging. *Magn. Reson. Imag.*, **9**, 895-902 (1991)

Ordidge, R.J., Wylezinska, M., Hugg, J.W., Butterworth, E., Franconi, F., Frequency offset corrected inversion (FOCI) pulses for use in localised spectroscopy. *Magn. Reson. Med.* **36**, 562-566 (1997)

Osburne, R.C., Halsey, J.H. Jr., Cerebral blood flow : A predictor of recovery from ischemia in the gerbil. *Arch. Neurol.* **32**, 457-461 (1975)

Østergaard, L., Sorensen, A.G., Kwong, K. K., Weisskoff, R. M., Gyldensted, C., Rosen, B.R., High-resolution measurement of cerebral blood-flow using intravascular tracer bolus passages: 1. mathematical approach and statistical analysis. *Magn. Reson. Med.* **36**, 726-736 (1996)

Østergaard, L., Johannsen, P., Høst-Poulson, P., Vestergaard-Poulson, P., Asboe, H., Gee, A.D., Hansen, S.B., Cold, G.E., Gjedde, A., Gyldensted, C., Cerebral blood flow measurements by magnetic resonance imaging with bolus tracking: Comparison with [15O]H2O positron emission tomography in humans. *J. Cereb. Blood Flow Metab.* **18**, 935-940 (1998)

Papatta, S., Fiorelli, M., Rommel, T., Hartmann, A., Dettmers, C., Yamaguchi, T., Chabriat, H., Poline, J.B., Crouzel, C., Di Giamberardino, L., Baron, J.C., PET study of chnages in local brain hemodynamics and oxygen metabolism after unilateral middle cerebral occlusion in baboons. *J. Cereb. Blood Flow Metab.* **13**, 416-424 (1993)

Parker, D.L., Smith, V., Sheldon, P., Crooks, L.E., Fussel, L., Temperature distribution measurements in two-dimensional NMR imaging. *Med. Phys.* **10**, 321-325 (1983)

Pauli, W., Communication, 1212 (1924); or *Naturwissenschaften* **12**, 741 (1924)

Payne, G.S., Leach, M.O., Threshold voltages for the hyperbolic secant inversion pulse. *NMR Biomed.* **5**, 142-144 (1992)

Payne, G.S., Leach, M.O., Implementation and evaluation of frequency offset corrected inversion (FOCI) pulses on a clinical MR system. *Magn. Reson. Med.* **38**, 828-833 (1997)

Peerless, S.J., Drake, C.G., Management of aneurysms of the posterior circulation, In: *Neurological Surgery ed. 3*, (Youmans, J.R., ed.), WB Saunders, Philadelphia, p. 1764-1806 (1990)

Pekar, J., Jezzard, P., Roberts, D.A., Leigh, J.S., Frank, J. A., Mclaughlin, A.C., Perfusion imaging with compensation for asymmetric magnetization-transfer effects. *Magn. Reson. Med.* **35**, 70-79 (1996)

Pell, G.S., Thomas, D.L., Howseman, A.M., Houseman, J., Gadian, D.G., Ordidge, R.J., Optimisation of experimental parameters for diffusion weighted single-shot trace measurement, *in* "Proc., ISMRM 3rd Annual Meeting, Nice, 1995 ", p. 1627

Pell, G.S., Thomas, D.L., Lythgoe, M.F., Calamante, F., Howseman, A.M., Williams, S.R., Gadian, D.G., Ordidge, R.J., Measurement of perfusion using arterial spin tagging with the FOCI pulse, *in* "Proc., ISMRM 6th Annual Meeting, Sydney, 1998 ", p. 1190

Pell, G.S., Thomas, D.L., Lythgoe, M.F., Calamante, F., Howseman, A.M., Gadian, D.G., Ordidge, R.J., The implementation of quantitative FAIR perfusion imaging with a short repetition time in time-course studies. *Magn. Reson. Med.* (In Press)

Pell, G.S., Lythgoe, M.F., Thomas, D.L., Calamante, F., King, M.D., Gadian, D.G., Ordidge, R.J., A study of reperfusion in a gerbil model of forebrain ischemia using serial magnetic resonance FAIR perfusion imaging. *Stroke* (submitted)

Pierpaoli, C., Righini, A., Barnet, J., Matietiello, J., Alger, J.R., Chiro, D., Simultaneous measurement of BOLD signal intensity and ADC changes during global brain ischemia using diffusion-weighted EPI, in "Proc., SMRM 12th Annual Meeting, 1992", p. 314

Pierpaoli, C., Alger, J.R., Righnin, A., Mattiello, J., Dickerson, R., des Pres, D., Barnett, A., di Chiro, G., High temporal resolution diffusion MRI of global cerebral ischemia and reperfusion. *J. Cereb. Blood Flow Metab.* **16**, 892-905 (1996)

Pluta, R., Tomida, S., Ikeda, J., Nowak, T.S. Jr., Klatzo, I., Cerebral vascular volume after repeated ischemic insults in the gerbil: Comparisons with changes in CBF and brain edema. *J. Cereb. Blood Flow Metab.* **9**, 163-170 (1989)

Powers, W.J., Raichle, M.E., Positron-emission tomography and its application to the study of cerebrovascular disease in man. *Stroke* **16**, 361 (1985)

Pulsinelli, W.A., Brierly, J., Plum, F., Temporal profile of neuronal damage in a model of transient forebrain ischemia. *Ann. Neurol.* **11**, 491-498 (1982a)

Pulsinelli, W.A., Levy, D.E., Duffy, T.E., Regional cerebral blood flow and glucose metabolism following transient forebrain ischemia. *Ann. Neurol.* **11**, 499-509 (1982b)

Purcell, E.M., Torrey, H.C., Pound, R.V., Resonance absorption by nuclear magnetic moments in a solid. *Phys. Rev.* **69**, 37-38 (1946)

Quarles, R.P., Mintun, M.A., Larson, K.B., Markham, J., MacLeod, A.M., Raichle, M.E., Measurement of regional cerebral blood flow with positron emission tomography: a comparison of [^{15}O]-water to [^{11}C]-butanol with distributed-parameter and compartmental models. *J. Cereb. Blood Flow Metab.* **13**, 733-747 (1993)

Rajamohanan, P.R., Gunapathy, S., Ray, S.S., Badiger, M.V., Mashelkar, R.A., Cross relaxation and exchange in poly(acrylamide) hydrogel studied through ^{1}H MASS NMR and 2D nuclear Overhauser enhancement spectroscopy. *Macromolecules* **28**, 2533-2536 (1995)

Rein, H., Verber Besonderheiten der Blutzcirculation in der Arteria carotis. *Z. Biol.* **89**, 307 (1929)

Rempp, K.A., Brix, G.B., Wenz, F., Becker, C.R., Gückel, F., Lorenz, W.J., Quantification of regional cerebral blood flow and volume with dynamic susceptibility contrast-enhanced MR imaging. *Radiology* **193**, 637-641 (1994)

Roberts, T.P.L., Vexler, Z., Derugin, N., Moseley, M.E., Kucharczyk, J., High-speed MR imaging of ischemic brain injury following stenosis of the middle cerebral artery. *J. Cereb. Blood Flow Metab.* **13**, 940-946 (1993)

Roberts, D.A., Detre, J.A., Bolinger, L., Insko, E. K., Leigh, J.S., Quantitative magnetic-resonance-imaging of human brain perfusion at 1.5T using steady-state inversion of arterial water. *Proc. Natl. Acad. Sci. USA* **91**, 33-37 (1994)

Roberts, D.A., Rizi, R., Lenkinski, R.E., Leigh, J.S., Magnetic resonance imaging of the brain:blood partition coefficient for water: Application to spin-tagging measurement of perfusion. *J. Magn. Reson. Imaging.* **6**, 363-366 (1996)

Roorda, W., Review: Do hydrogels contain different classes of water?. *J. Biomater. Sci. Polymer Edn.* **5**, 383-395 (1994)

Rordorf, G., Koroshetz, W.J., Copen, W.A., Cramer, S.C., Schaefer, P.W., Budzik, R.F. Jr., Schwamm, L.H., Buananno, F., Sorenson, A.G., Gonzalez, G., Regional ischemia and ischemic injury in patients with acute middle cerebral artery stroke as defined by early diffusion-weighted and perfusion-weighted MRI. *Stroke* **29**, 939-943 (1998)

Rosen, B.R., Belliveau, J.W., Chien, D., Perfusion imaging by nuclear magnetic resonance. *Magn. Reson. Q.*, **5**, 263 (1989)

Rosen, B.R., Belliveau, J.W., Vevea, J.M., Brady, T.J., Perfusion imaging with NMR contrast agents. *Magn. Reson. Med.* **14**, 249-265 (1990)

Rosen, B.R., Belliveau, J.W., Aronen, H.J., Kennedy, D., Buchbinder, B.R., Fischman, A., Gruber, M., Glas, J., Weisskoff, R.M., Cohen, M.S., Hochberg, F.H., Brady, T.J., Susceptibility contrast imaging of cerebral blood volume: human experience. *Magn. Reson. Med.* **22**, 293-299 (1991)

Rosenblum, W.I., Regional cerebral blood flow in the anesthetized mouse as measured by local hydrogen clearance. *Stroke* **8**, 103-106 (1977)

Röther, J., de Crespigny, A.J., D'Aceuil, H., Moseley, M.,E., MR detection of cortical spreading depression immediately after focal ischemia in the rat. *J. Cereb. Blood Flow* **16**, 214-220 (1996)

Rothman, S.M., Olney, J.W., Glutamate and the pathophysiology of hypoxic-ischemic brain damage. *Ann. Neurol.* 19, 105-111 (1986)

Rottenberg, D.A., Lu, H.C., Kearfott, K.J., The in-vivo autoradiographic measurement of regional cerebral blood flow using stable xenon and computerized tomography : The effect of tissue heterogeneity and computerized tomography noise. *J. Cereb. Blood Flow* **2**, 173-178 (1982)

Roussel, S.A., van Bruggen, N., King, M.D., Gadian, D.G., Identification of collaterally perfused areas following focal cerebral ischemia in the rat by comparisons of gradient echo and diffusion-weighted MRI. *J. Cereb. Blood Flow Metab.* **15,** 578-586 (1995)

Russell, R.W.R., Transient cerebral ischemia, In: *Vascular disease of the central nervous system*, (Russell, R.W.R., ed.), Churchill Livingstone, Edinburgh, Chp. 11 (1983)

Sakurada, O., Kennedy, C., Jehle, J., Brown, J.D., Carbin, G.L., Sokoloff, L., Measurement of local cerebral blood flow with iodo-[^{14}C]-antipyrine. *Am. J. Physiol.* **234**, H59 (1978)

Samson, D.S., Batjer, H.H., Bowman, G. *et al.*, A clinical study of the parameters and effects of temporary occlusion in the management of intracranial aneurysms. *Neurosurgery*, **34**, 22-29 (1994)

Sandor, P., Cox van Put, J., de Jong, W., de Wied, D., Continuous measurement of cerebral blood volume in rats with the photoelectric technique: effect of morphine and naloxone. *Life Sci.* **39**, 1657-1665 (1986)

Sapirstein, L.A., Regional blood flow by fractional distribution of indicators. *Am. J. Phyiol.* **193**, 161-169 (1958)

Schmitz, B., Hoehn-Berlage, M., Kerskens, C.M., Böttiger, B.W., Hossmann, K.A., Recovery of the rodent brain after cardiac arrest: A functional MRI study. *Magn. Reson. Med.* **39**, 783-788 (1998)

von Schulten, M.W., Untersuchungen über den Hirndruck, mit besonder rucksicht auf sine einwirkung auf die Circulation-verhaltnisse des Avges. *Arch. Klin. Chir.* **32**, 455,733,947 (1885)

Schwarzbauer, C., Morrissey, S.P., Haase, A., Quantitative magnetic resonance imaging of perfusion using magnetic labeling of water spins within the detection slice. *Magn. Reson. Med.* **35**, 540-546 (1996)

Siesjö, B.K., Cell damage in the brain : a speculative synthesis. *J. Cereb. Blood Flow Metab.* **1,** 155-185 (1981)

Siesjö, B.K., A new perspective on ischemic brain damage?. *Progr. Brain Res.* **96**, 1-9 (1993)

Siewert, B., Schlaug, G., Edelma, R.R. Warach, S. Comparison of EPISTAR and T_2*-weighted gadolinium-enhanced perfusion imaging in patients with acute cerebral ischaemia. Neurology. 48, 673-679 (1997)

Silva, A. C., Zhang, W. G., Williams, D. S., Koretsky, A. P., Estimation of water extraction fractions in rat brain using magnetic resonance measurement of perfusion with arterial spin labeling. *Magn. Reson. Med.* **37**, 58-68 (1997a)

Silva, A. C., Williams, D. S., Koretsky, A. P., Evidence for the exchange of arterial spin-labeled water with tissue water in rat brain from diffusion-sensitized measurements of perfusion. *Magn. Reson. Med.* **38**, 232-237 (1997b)

Simon, R.P., Cho, H., Gwinn, R., Lowenstein, D.H., The temporal profile of 72-kDa heat-shock protein expression following global ischemia. *J. Neurosci.* **11**, 881-889 (1991)

Simon, R.P., Niiro, M., Gwinn, R., Prior ischemic stress protects against experimental stroke. *Neurosci. Lett.* **163**, 135-137 (1993)

Sinha, U., Sinha, S., High-speed diffusion imaging in the presence of eddy currents. *J. Magn. Reson. Imaging* **6**, 657-666 (1996)

Steinberg, G.K., Panahian, N., Sun, G., Maier, C.M., Kunis, D., Cerebral damage caused by interrupted, repeated arterial occlusion versus uninterrupted occlusion in a focal ischemic model. *J. Neurosurg.* **81**, 554-559 (1994)

Stejskal, E.O., Tanner, J.E., Spin diffusion measurements: spin echoes in the presence of a time-dependent field gradient. *J. Chem. Phys.* **42**, 288-292 (1965)

Stewart, G.N., Researches on the circulation time in organs and on the influences which affect it. Parts I-III. *J. Physiol. (London)* **15**, 1 (1894)

Styles, P., Passive electrical isolation of double coil probes for localized spectroscopy and imaging. *NMR Biomed.* **2**, 61-66 (1988)

Suzuki, J., Kwak, R., Okudairo, Y., The safe time limit of temporary clamping of cerebral arteries in the direct surgical treatment of intracranial aneurysms under moderate hypothermia. *Tohoku J. Exp. Med.* **127**, 1-7 (1979)

Suzuki, R., Yamaguchi, T., Kirino, T., Orzi, F., Klatzo, I., The effects of 5-minute ischemia in Mongolian gerbils. I. Blood-brain-barrier, cerebral blood-flow, and local cerebral glucose-utilization changes. *Acta Neuropath.* **60**, 207-216 (1983)

Tadamura, E., Hatabu, H., Li, W., Prassad, P.V., Edelman, R.R., Effect of oxygen inhalation on relaxation times in various tissues. *J. Magn. Reson. Imag.* **7**, 220-225 (1997)

Tagaki, S., Cocito, L., Hossmann, K.A., Blood recirculation and pharmacological responsiveness of the cerebral vasculature following prolonged ischemia of cat brain. *Stroke* **8**,707-712 (1977)

Tamura, A., Horizoe, H., Fukada, T., Relationship of cerebral vasculature to infarcted areas following unilateral common carotid artery ligation in the Mongolian gerbils. *J. Cereb. Flow Metab.* **1** (Suppl 1), S194-195 (1981)

Tang, T., Liachenko, S., Yan, B., Zha, L., Xu, Y., Protracted and scattered abnormality of brain ADC after resuscitation from asphyxial cardiac arrest, *in* "Proc., ISMRM 5th Annual Meeting, Vancouver, 1997", p. 392

Taniguchi, Y., Horigome, S., *J. Appl. Polym. Sci.* **19**, 2743-2752 (1975)

Thomas, D.L., Pell, G.S., Lythgoe, M.F., Gadian, D.G., Ordidge, R.J., A Quantitative method for fast diffusion imaging using magnetisation-prepared TurboFLASH. *Magn. Reson. Med.* **39**, 950-960 (1998)

Thornton, J.S., Ordidge, R.J., Penrice, J., Cady, E.B., Amess, P.N., Punwani, S., Clemence, M., Wyatt, J.S., Temporal and anatomical variations of brain water apparent diffusion coefficient in perinatal cerebral hypoxic-ischemic injury: Relationships to cerebral energy metabolism. *Magn. Reson. Med.* **39**, 920-927 (1998)

Ting, P., Masaoka, H., Kuroiwa,_T., Klatzo,_I., The role of early blood-brain-barrier opening in post-ischemic neuronal injury. *Acta Neurol. Scand.* **72**, 119 (1985)

Todd, N.V., Crockard, H.A., Russel, R.W.R., Picozzi, P., Cerebral blood flow in the four-vessel occlusion rat model. *Stroke* **15**, 579 (letter) (1984)

Todd, N.V., Picozzi, P., Crockard, H. A., Russell, R. R., Reperfusion after cerebral-ischemia - influence of duration of ischemia. *Stroke* **17**, 460-466 (1986a)

Todd, N.V., Picozzi, P., Crockard, H.A., Quantitative measurement of cerebral blood flow and cerebral blood volume after cerebral ischaemia. *J. Cereb. Blood Flow Metab.* **6**, 338-341 (1986b)

Tomida, S., Nowak, T. S., Vass, K., Lohr, J. M., Klatzo, I., Experimental-model for repetitive ischemic attacks in the gerbil - the cumulative effect of repeated ischemic insults. *J. Cereb. Blood Flow Metab.* **7**, 773-782 (1987)

Tomida, S., Wagner, H. G., Klatzo, I., Nowak, T. S., Effect of acute electrode placement on regional CBF in the gerbil - a comparison of blood-flow measured by hydrogen clearance, [^{3}H]-nicotine, and [^{14}C]-iodoantipyrine techniques. *J. Cereb. Blood Flow Metab.* **9**, 79-86 (1989)

Tominaga, T., Ohnishi, S.T., Ion movements and edema formation in CNS injury, In: *Central nervous system trauma: research techniques*, (Ohnishi, S.T., ed.), CRC Press, New York, USA (1995)

van der Toorn, A., Verheul, H.B., van der Sprenkel, J.B., Tulleken, C.A.F., Nicolay, K., Changes in metabolites in focal ischemia in car brain assessed with localized MR spectroscopy. *Magn. Reson. Med.* **32**, 685-691 (1994)

van der Toorn, A., Sykovà, E., Dijkhuizen, R.M., Voříšek, I., Vargovà, L., Škobisovà, E., van Lookeren Campagne, M., Reese, T., Nicolay, K., Dynamic changes in water ADC, energy metabolism, extracellular space volume and tortuosity in neonatal rat brain during global ischemia. *Magn. Reson. Med.* **36**, 52-60 (1996)

Traupe, H., Kruse, E., Heiss, W.D., Reperfusion of focal ischemia of varying duration : postischemic hyper- and hypo- perfusion, *Stroke* **13**, 615-622 (1982)

Tsekos, N.V., Urgubil, K., Kim, S.G., Effect of sequence parameters in assessment of tissue perfusion, *in* "Proc., ISMRM 4th Annual Meeting, New York, 1996 ", p. 1310

Tsekos, N.V., Zhang, F.Y., Merkle, H., Nayayama, M., Iadecola, C., Kim, S.G., Quantitative measurements of cerebral blood flow in rats using FAIR technique : Correlation with previous iodoantipyrine autoradiographic studies. *Magn. Reson. Med.* **39**, 564-573 (1998)

Tsuchidate, R., He, Q.P., Smith, M.L., Siesjo, B.K., Regional cerebral blood flow during and after 2 hours of middle cerebral artery occlusion in the rat. *J. Cereb. Blood Flow Metab.* **17**, 1066-1073 (1997)

Turner, R., Le Bihan, D., Single-shot diffusion imaging at 2.0 Tesla. *J. Magn. Reson.* **86**, 445-452 (1990)

Turner, R., le Bihan, D., Moonen, C.T.W., Despres, D., Frank, J., Echo-planar time course MRI of cat brain oxygenation changes. *Magn. Reson. Med.* **22**, 159-166 (1991)

Twieg, D.B., The k-trajectory formulation of the NMR imaging process with applications in analysis and synthesis of imaging methods. *Med. Phys.* **10**, 610-621 (1983)

Ueda, Y., Obrenovitch, T.P., Lok, S.Y., Sarna, G.S., Symon, L., Changes in extracellular glutamate concentration produced in the rat striatum by repeated ischemia. *Stroke* **23**, 1125-1130 (1992)

van Uitert, R.L., Levy, D.E., Regional blood flow in the conscious gerbil. *Stroke.* **9** 67-72 (1978)

Vass, K., Tomida, S., Hossmann, K. A., Nowak, T. S., Klatzo, I., Microvascular disturbances and edema formation after repetitive ischemia of gerbil brain. *Acta Neuropath. (Berl)* **75**, 288-294 (1988)

Verhaegen, M. J., Todd, M. M., Warner, D. S., James, B., Weeks, J. B., The role of electrode size on the incidence of spreading depression and on cortical cerebral blood-flow as measured by H_2 clearance. *J. Cereb. Blood Flow Metab.* **12**, 230-237 (1992)

Verheul, H.B., Balasz, R., Berkelbach van der Sprenkel, J.W., Tamminga, K.S., Nicolay, K., Tulleken, C.A.F., Comparison of diffusion-weighted MRI with changes in cell volume in a rat model of brain injury. *NMR Biomed.* **7**, 96-100 (1994)

Wade, J.G., Amtorp, O., Sorenson, S.C., No-reflow state following cerebral ischemia. *Arch. Neurol.* **32**, 381-384 (1975)

Walsh, E.G., Minematsu, K., Leppo, J., Moore, S.C., Radioactive microsphere validation of a volume localized continuous saturation perfusion measurement. *Magn. Reson. Med.* **31**, 147-153 (1994)

Wang, H.Z., Riederer, S.J., A spoiling sequence for suppression of residual transverse magnetization. *Magn. Reson. Med.* **15**, 175-191 (1990)

Warner, D.S., Kassell, N.F., Boarini, D.J., Microsphere cerebral blood flow determination, in *Cerebral Blood Flow: Physiologic and Clinical Aspects*. McGraw-Hll, New York, Chp. 17 (1987)

Weiskoff, R.M., Chesler, D., Boxerman, J.L., Rosen, B.R., Pitfalls in MR measurement of tissue blood flow with intravascular tracers: Which mean transit time?. *Magn. Med. Reson.* **29**, 553-559 (1993)

White, B.C., Grossman, L.I., Krause, G.S., Brain injury by global ischemia and reperfusion: a theoretical perspective on membrane damage and repair. *Neurology* **43**, 1656-1665 (1993)

Widmann, R., Weber, C., Bonnekoh, P., Schlenker, M., Hossmann, K.A., Neuronal damage after repeated 5 minutes of ischemia in the gerbils is preceded by prolonged impairment of protein metabolism. *J. Cereb. Blood Flow Metab.* **12**, 425-433 (1992)

Williams, D. S., Detre, J. A., Leigh, J. S., Koretsky, A. P., Magnetic-resonance-imaging of perfusion using spin inversion of arterial water. *Proc. Natl. Acad. Sci. USA* **89**, 212-216 (1992)

Willis, T., Wren, C., Cerebri Anatome: Cui Accessit Nervorum Descriptio et Usus, Flesher, J., London (1664)

Wise, RJ.S., Bernardi, S., Frackowiak, R.S.J., Leg, N.J., Jones, T., Serial observations on the pathophysiology of acute stroke: The transition from ischaemia to infarction as reflected in regional oxygen extraction. *Brain* **106**, 197-222 (1983)

Wolff, S.D., Balaban, R.S., Magnetic transfer contast (MTC) and tissue water relaxation in vivo. *Magn. Reson. Med.* **10**, 135-144 (1989)

Wong, E.C., Cox, R. W., Song, A. W., Optimized isotropic diffusion weighting. *Magn. Reson. Med.* **34**, 139-143 (1995)

Wong, E.C., Buxton, R.B., Frank, L.R., Quantitative perfusion imaging using EPISTAR and FAIR, *in* "Proc., ISMRM 4th Annual Meeting, New York, 1996 ", p. 13

Wong, E.C., Buxton, R. B., Frank, L. R., Implementation of quantitative perfusion imaging techniques for functional brain mapping using pulsed arterial spin labeling. *NMR Biomed.* **10**, 237-249 (1997)

Wong, E.C., Buxton, R.B., Frank, L.R., Quantitative imaging of perfusion using a single subtraction (QUIPSS and QUIPSS II). *Magn. Reson. Med.* **39**,702-708 (1998a)

Wong, E.C., Buxton, R.B., Frank, L.R., A theoretical and experimental comparison of continuous and pulsed arterial spin labeling techniques for quantitative perfusion imaging. *Magn. Reson. Med.* **39**,702-708 (1998b)

Xing, D., Papadakis, N.G., Huang, C.L.H., Lee, V.M., Carpenter, T.A., Hall, L.D., Optimised diffusion-weighting for measurement of apparent diffusion coefficient (ADC) in human brain. *Magn. Reson. Imaging* **15**, 771-784 (1997)

Xu, S., Wagner, H., Tomida, S., Vass, K., Nowak, T.S. Jr., Pluta, R., Cumulative brain injury in repeated ischemic insults. *Soc. Neurosci.Abstr.* **13**, 1688 (1987)

Yamazaki, T., Miyazaki, T., Toyoshima, H., Maki, T., Incremental flip angle subtraction TurboFLASH, in "Proc., SMRM 10th Annual Meeting, 1991 ", p. 852

Yasuda, H., Olf, H.G., Crist, B., Lamaze, C.E., Peterlin, A., Movement of water in homogeneous water-swollen polymers, In: *Water structure at the water-polymer interface*, (Jellinek, H.H.G., ed.) Plenum Press, New York, p. 39-55 (1972)

Ye, F.Q., Mattay, V.S., Jezzard, P., Frank, J.A.,Weinberger, D.R., Mclaughlin, A.C., Correction for vascular artifacts in cerebral blood flow values measured by using arterial spin tagging techniques. *Magn. Reson. Med.* **37**, 226-235 (1997a)

Ye, F.Q., Berman, K.F., Ellmore, T., Esposito, G., van Horn, J.D., Yang, Y., Duyn, J., Salustri, C., Smith, A., Frank, J.A., Weinberger, D.R., McLaughlin, A.C., $H_2{}^{15}O$ PET validation of arterial spin tagging measurements of cerebral blood flow in humans. *in* "Proc., ISMRM 5th Annual Meeting, Vancouver, 1997 ", p. 87

Yongbi, M.N., Huang, N.C., Branch, C.A., Helpern, J., The application of diffusion-weighted line-scanning for the rapid assessment of water ADC changes in stroke at high magnetic fields. *NMR Biomed.* **10**, 79-86 (1997)

Yongbi, M.N., Branch, C.A., Helpern, J.A., Perfusion imaging using FOCI RF pulses. *Magn. Reson. Med.* **40**, 938-943 (1998)

Young, W., H_2 clearance measurement of blood flow: a review of technique and polagrographic principles. *Stroke.* **11**, 552-564 (1980)

Zaleska, M.M., Floyd, R.A., Regional lipid peroxidation in rat brain in vitro: possible role of endogenous iron. *Neurochem. Res.* **10**, 397-410 (1985)

Zaharchuk, G., Bogdanov, A.A. Jr., Marota, J.J.A., Shimizu-Sasamata, M., Weiskoff, R.M., Kwong, K.K., Jenkins, B.G., Weissleder, R., Rosen, B.R., Continuous assessment of perfusion by tagging including volume and water extraction (CAPTIVE): A steady-state contrast agent technique for measuring blood flow, relative blood volume fraction, and the water extraction fraction. *Magn. Reson. Med.* **40**, 666-678 (1998)

Zea-Longa, E., Weinstein, P.R., Carlson, S., Cummins., R., Reversible Middle Cerebral Artery Occlusion without Craniectomy in Rats. *Stroke* **20**, 84-91 (1989).

Zhang, W. G., Williams, D. S., Detre, J. A., Koretsky, A. P., Measurement of brain perfusion by volume-localized NMR-spectroscopy using inversion of arterial water spins - accounting for transit-time and cross-relaxation. *Magn. Reson. Med.* **25**, 362-371 (1992)

Zhang, W. G., Williams, D. S., Koretsky, A. P., Measurement of rat-brain perfusion by NMR using spin labeling of arterial water – in-vivo determination of the degree of spin labeling. *Magn. Reson. Med.* **29**, 416-421 (1993)

Zhang, W. G., Silva, A. C., Williams, D. S., Koretsky, A. P., NMR measurement of perfusion using arterial spin-labeling without saturation of macromolecular spins. *Magn. Reson. Med.* **33**, 370-376 (1995)

Zhou, J., Mori, S., van Zijl, P.C.M., FAIR excluding radiation damping (FAIRER). *Magn. Reson. Med.* **40**, 712-719 (1998)

Zhu, X.H., Kim, S.G., Andersen, P., Ogawa, S., Ugurbil, K., Chen, W., Simultaneous oxygenation and perfusion imaging study of functional activity in primary visual cortex at different visual stimulation frequency: Quantitative correlation between BOLD and CBF changes. *Magn. Reson. Med.* **40**, 703-711 (1998)

van Zijl, P.C.M., Miyabe, M., Mori, S., Kirsch, J.R., Eleff, S.M., Koehler, R.C., Traystman, R.J., Correlation of water diffusion, cerebral blood flow and ischemic damage after middle cerebral artery in cats. *J. Cereb. Blood Flow Metab.* **15**, S59 (1995)

van Zijl, P.C.M., Eleff, S.M., Ulatowski, J.A., Oje, J.M.E., Ulug, A.M., Traystman, R.J., Kauppinen, R.A., Quantitative assessment of blood flow, blood volume and blood oxygenation effects in functional magnetic resonance imaging. *Nature Med.* **4**, 159-167 (1998)

GLOSSARY

(including commonly used acronyms and abbreviations)

α	RF pulse flip angle
α_0	degree of inversion
β	hyperbolic secant pulse truncation factor
β_1, β_2	rate constants fitted to changing trace(D) and b0 signal (Chapter 7)
δ	transit time to the tissue bed; diffusion gradient duration
δa	transit time to the vascular bed
ϕ	magnetisation phase
γ	gyromagnetic ratio
λ	blood:brain partition coefficient
μ	magnetic moment vector; hyperbolic secant pulse parameter
υ	frequency
π pulse	RF pulse designed to rotate magnetisation by π radians in the rotating frame
ρ	proton density
σ	standard deviation
τ	inter-experiment time (short repetition time FAIR)
τ_c	correlation time
ω	precessional angular frequency
ω_0	Larmor precessional frequency
ω_1	RF pulse precessional frequency
Δ	inflow time; inter-diffusion-gradient time
$\Delta\omega$	frequency offset (ω_0-ω_1)
ΔM	subtraction of flow-sensitive and flow-insensitive images (for FAIR, $\Delta M=M_{ss}-M_{ns}$)
A(n),B(n),X(n),Y(n)	terms relating to magnetisation during nth phase encoding step (FLASH, Chapter 6)
A(t)	multiplication factor (FOCI pulse, Chapter 3)
ADC	apparent diffusion coefficient
ADC_i	ADC measured along x,y or z direction
AFP	adiabatic fast passage
AIF	arterial input function
ASL	arterial spin labelling
ATP	adenosine triphosphate
b	factor describing the diffusion-weighting of gradients
b0	non-diffusion-weighted, T_2-weighted data from trace(D) sequence
B	magnetic induction field vector
B_0	static magnetic induction field
B_1	RF magnetic induction field
B_{eff}	effective magnetic induction field

BBB blood brain barrier

BOLD blood oxygenation level dependent

CASL continuous arterial spin labelling

CBF cerebral blood flow

CBV cerebral blood volume

$CMRO_2$ cerebral metabolic rate of oxygen consumption

CPP cerebral perfusion pressure

CSF cerebrospinal fluid

CT computerised tomography

D diffusion tensor; scalar diffusion coefficient

DC direct current

DSC-MRI dynamic susceptibility contrast MRI

DWI diffusion weighted imaging

E(f) extraction fraction

EPI echo planar imaging

EPISTAR echo planar imaging with signal targeting using alternating RF

f perfusion flow (usual units: [ml/100g/min])

FAIR flow-sensitive alternating inversion recovery

FLASH fast low angle shot sequence

fMRI functional magnetic resonance imaging

FOCI frequency offset correction inversion

FT Fourier transform

G magnetic field gradient; Gauss unit ($1G=10^{-4}T$)

G_x,G_y,G_z components of the gradient in the laboratory frame

GM grey matter

Group A group response of immediate renormalisation of flow on reperfusion (Chapter 5)

Group B group response of flow recovery followed by hypoperfusion on reperfusion (Chapter 5)

HS hyperbolic secant

IR inversion recovery

k Boltzmann's constant

k-space tern used when describing the effects of a pulse sequence in frequency space

k_f, k_r forward and reverse magnetisation transfer rates between free and bound water pools

M macroscopic magnetisation vector

$M^1(t)$, $M^2(t)$ dynamic control and tagged (respectively) tissue magnetisation (CASL)

M_0 equilibrium magnetisation per unit mass along the static magnetic field

M_a arterial magnetisation per unit volume

M_m macromolecular magnetisation per unit mass

M_{ns} non-selective tissue magnetisation (FAIR)

M_{ss} slice-selective tissue magnetisation (FAIR)

M_{ss}^1 steady state control tissue magnetisation (CASL)

M_{ss}^2 steady state tagged tissue magnetisation (CASL)

M_x,M_y,M_z components of **M** in the laboratory frame

$M_{x'}$,$M_{y'}$,$M_{z'}$ components of **M** in the rotating frame

M_{xy} transverse magnetisation at right angles to B_0

MCAO middle cerebral artery occlusion

MRI magnetic resonance imaging

MTC magnetisation transfer contrast

MTT mean transit time

NMR nuclear magnetic resonance

OEF oxygen extraction fraction

PASL pulsed arterial spin labelling

PCr phosphocreatine

PET positron emission tomography

PICORE proximal inversion with a control for off-resonance effects

Q(t) quantity of tracer uptake (Kety's tracer kinetic theory, Chapter 2)

QUIPSS quantitative imaging of perfusion using a single subtraction

ramp[A(t)] fraction of A(t) over which the waveform ramps down (FOCI pulse, Chapter 3)

RF radio-frequency

ROI region of interest

SAP superabsorbent

SAR specific absorption rate

SD standard deviation

SE spin-echo

SEM standard error in the mean

slth slice thickness

SNR signal-to-noise

SNR-unit-time signal-to-noise with respect to time

SPECT single photon emission computerised tomography

STR slice thickness ratio

T Tesla (SI unit of magnetic flux density)

T_1 longitudinal, spin-lattice relaxation

T_{1a} T_1 value of blood

T_{1app} T_1 in the presence of flow

T_{1sat} T_1 in the presence of off-resonance irradiation

T_{1t} T_1 of intrinsic tissue

T_2 intrinsic transverse, spin-spin relaxation

T_2' extrinsic contribution of field inhomogeneities

T_2^* effective T_2 relaxation time incorporating T_2 and T_2'

T_D inter-experiment time (TurboFLASH)

T_s scan duration

TE echo time

TI interval time

TIA transient ischaemic attack

TR repetition time

Trace(D) (a third) of the trace of the diffusion tensor

TurboFLASH FLASH sequence with $TR<T_2$

Var variance

w post-labelling delay (CASL)

WM white matter

X(TR) steady state factor (short repetition time FAIR)